A Measurement of the CP Parameter sine two beta using Fully Reconstructed b to ccbar Decays at the BABAR Experiment

Eric Charles

Stanford Linear Accelerator Center
Stanford University
Stanford, CA 94309

SLAC-Report-620
April 2003

Prepared for the Department of Energy
under contract number DE-AC03-76SF00515

Printed in the United States of America. Available from the National Technical Information Service, U.S. Department of Commerce, 5285 Port Royal Road, Springfield, VA 22161.

A Measurement of the $\mathcal{CP}$ Parameter $\sin 2\beta$ Using Fully Reconstructed $b \to c\bar{c}$ Decays at the *BABAR* Experiment

by

Eric Charles

A dissertation submitted in partial fulfillment of

the requirements for the degree of

Doctor of Philosophy

(Physics)

at the

UNIVERSITY OF WISCONSIN-MADISON

2002

"I measure time by how a body sways"
— T. Roethke

Acknowledgements

For many, many reasons the first thanks on this dissertation must go to my "boss", Damon Fasching. In addition to having always patient and hilarious officemate, a great friend, and repeated lending my huge sums of money so that I could make it to the end of the month, Damon has been the best example of everything I should like to be as a scientist.

Also, I would like to thank my advisor, Sau Lan Wu, for having given me so many opportunities; to work in Geneva, to work in Berkeley and most importantly, the freedom to work on the subjects that I felt were important with the colleagues of my choosing.

I also want to acknowledge how lucky I was to have had the privilege to work with so many brilliant colleagues. On the Atlas Pixel project with Khang Dao, Damon, Kevin Einsweiller and John Richardson I had the pleasure of being part of an excellent research team, and appreciating the rare joy of trusting and respecting my co-workers. Likewise, working with John Walsh, Peter Elmer, Gerry Lynch, Gerhard Raven, Ian Scott and David Brown on the *BABAR* tracking software; and again with Phil Strother and Steve Gowdy on the *BABAR* physics analysis software. Finally, I particularly want to thank Shahram Rahatlou, Riccardo Faccini, Gerhard Raven and David Kirkby for all the help with the work described in this dissertation.

It would be hard to underestimate the importance that the numerous long phone conver-

sations with my friends Kate Gundersen, Anita Chakravarti and Maryll Feild had in giving me the patience to continue with my studies and the perspective to realize how lucky I was to be allowed to do so. Likewise the numerous pleasant hours spent exploring the bars and concert halls of the Bay Area and inventing novel drinking games with Damon, Tom Dignan and Michelle Bland.

The best reward of graduate school has been the privilege of meeting and working with so many kind and interesting people from so many different countries. In particular, I would like to acknowledge all those friends and colleagues who have housed and fed me while I was working on this dissertation, to wit: Richard Sloane, Tom Dignan, Stephen Gowdy, Jesse Wood, Wahid Bhimji, Helene and Patrick Lemaitre, Jamie Boyd, Nicole Chevalier, Philip Strother, Giulia Belodi, Jim Weatherall, Micheal George, Karina Oddoux, Charles Metzger, Aidje Tafial, Maurice Frank, Oliver Miller, Marcella Bona, Cristina Bulfon, Shahriar Rahatlou, Francesca Pastore, Jane Tinslay, Rostyslav Boutchko and Julia Velikina.

Lastly, I want to thank my family and particularly my mother, Margo Chavez-Charles for all support and love without which I would not be sitting here, writing the last sentence of my dissertation.

Contents

List of Figures

List of Tables

Abstract

This dissertation presents a measurement of the time-dependent $\mathcal{CP}$-violating asymmetries in the neutral B-meson system performed with data collected with the *BABAR* detector at the PEP-II asymmetric-energy B Factory at the Stanford Linear Accelerator Center. The data sample used consists of 29.7 fb^{-1} collected at the $\Upsilon(4S)$ resonance and 3.9 fb^{-1} collected off-resonance. We analyze three samples of fully-reconstructed B-meson decays: a sample of decays to $\mathcal{CP}$ eigenstates in the modes J/ψ K^0_S, $\psi(2S)$ K^0_S, χ_{c1} K^0_S, and J/ψ K^{*0} (822 events); as well as both charged (14304 events) and neutral (10457 events) B decays to flavor-eigenstates including $D^{(*)}$ and $\pi/\rho/a_1$. In all cases, the proper decay time difference between the reconstructed B-meson and the recoiling B-meson is determined by measuring the separation of the two decay vertices. Furthermore, the flavor of the recoiling B-meson is tagged using a neural network algorithm. We use the flavor-eigenstate samples to calibrate both the vertexing and tagging performance. We measure the amplitude of the $\mathcal{CP}$ asymmetry, $\sin 2\beta = 0.61 \pm 0.14(stat) \pm 0.06(syst)$. These results indicate the existence of indirect $\mathcal{CP}$ violation in the B-meson system.

Contributions of the Author

Be realistic; there is not a single person who is essential to the experiment.
— D. Fasching

Simply put, any significant results achieved in experimental High Energy Physics represent the combined work of literally hundreds of people. Therefore, when presenting results it is only fair to distinguish clearly between the author's contribution and the work of others. Put more frankly, this author would be tremendously embarrassed to be given sole credit for what is largely the work of esteemed colleagues.

The entire theoretical discussion of Chapter 1 follows the standard set forth in many primers, review articles and especially the excellent "*BABAR* Physics Book[1]". Likewise discussion of the general method for measuring time-dependent $\mathcal{CP}$ violation given at the end of the Chapter, although the particular formalism is the author's own.

Chapter 2 is simply a description of the *BABAR* detector. The author was in no way involved in the design of the detector, and allow slightly involved in the final stages of the construction of the SVT. On the other hand, the author did significant work on the use of the SVT for tracking purposes [2].

The choice of cuts for the event selections in Chapter 3 were entirely the work of the relevant *BABAR* working groups, with minimal contribution from the author. On the other hand, the particular implementation of those cuts for the analysis presented here was the sole work of the author, who accepts blame for any discrepancies with the standard selections.

The vertexing and flavor tagging algorithms described in Chapters 4 and 5 are also *BABAR* standards, and the author did not participate in their implementation or design.

The primary individual contribution of the author was in extending the technique for extracting sin2β from the selected, vertexed and tagged event samples. Specifically in the use of the kernel estimation technique for background modeling, the use of a probability-based (rather than a cut-based) method for flavor tagging, changes in the choice of resolution function parameterization, and of course all the systematic error studies related to these modifications.

Finally, all of the discussion and results in Chapter 7 are courtesy of the excellent `CKMFitter` group [3].

Chapter 1

$\mathcal{CP}$ Violation in the B-Meson System

"Saying that you're trying to discover why the universe is made of matter and not antimatter is a great pick-up line."
— T. Dignan.

Asymmetries of the $\mathcal{CP}$ transformation, which simultaneously exchanges particles for their anti-particles and reverses their momenta and helicities, are among the least well measured aspects of the Standard Model of Particle Physics. [1] In fact, although the 1964 observation of the $\mathcal{CP}$ violating decay $K_L^0 \to \pi^+\pi^-$ [6] was generally unexpected, it has since led to a well formulated theory of $\mathcal{CP}$ violation in the context of the Standard Model. However, despite the general confidence in the theory, many aspects have yet to be confirmed experimentally.

This chapter details the theoretical motivation and context for the work described in the remainder of this dissertation; the end goal of which is a measurement of the parameter sin2β using the time-structure of B-meson decays observed at the *BABAR* experiment. The most important point is that sin2β is a parameter of Standard Model of Particle Physics (henceforth simply Standard Model) which quantifies $\mathcal{CP}$ violation in certain types of decays.

---

[1] For a brief summary of the salient features of the Standard Model I refer the reader to any particle physics textbook. In the body of this dissertation I will only discuss those features of the Standard Model which directly relate to the results presented. Furthermore, unless stated otherwise, charge-conjugate reactions are implied throughout and all numerical values are taken from Refs. [4, 5].

So, we begin with a catalog of facts pertaining to $\mathcal{CP}$ violation, the Standard Model, and Cosmology.

1. The Standard Model accurately describes all extant measurements from nuclear, high-energy and particle physics with a small set of axioms and some twenty-odd input parameters.
2. For all its success, the Standard Model is *NOT* mathematically self-consistent, but requires arbitrary integration cut-offs to avoid divergent results for many calculations.
3. There is a manifest baryon asymmetry in the observable universe. Furthermore, the Sakharov conditions [7] state that violation of the combined charge conjugation - parity $\mathcal{CP}$ symmetry is a necessary condition for said baryon imbalance.
4. The only source of $\mathcal{CP}$ violation in the Standard Model is in the electroweak sector, and is fully described by complex terms in the Cabbibo-Kobayashi-Maskawa (CKM) mass mixing matrix [8].
5. Until recently, $\mathcal{CP}$ violation had only been observed in the neutral kaon system [6, 9, 10]. However, advances in experimental techniques have made it possible to study $\mathcal{CP}$ violation in the neutral B-meson system.

From these points it immediately follows that any knowledge of the $\mathcal{CP}$-violating parameters obtainable by study of the B-meson system is very useful as it enables progress in several issues.

1. Making more accurate predictions within the Standard Model and testing the Standard Model more stringently with said predictions.

2. Constraining any theories which claim to derive or approximate to the Standard Model.
3. Developing more precise cosmological models explaining the matter anti-matter imbalance.

The philosophical justifications having been made, the remainder of this chapter will describe $\mathcal{CP}$ violation in the Standard Model. Secs. 1.1, 1.2 and 1.3 will detail various sources of $\mathcal{CP}$ violation and examine the necessary conditions for their existence. Sec. 1.4 will show the existence of such conditions in the electroweak sector of the Standard Model, quantify the expected resultant $\mathcal{CP}$ violation and introduce sin2β as a measure of $\mathcal{CP}$ violation. Finally, Sec. 1.5 will give a simple overview to the method we use to measure sin2β.

Chapter 2 will give an overview of the experimental apparatus, namely the PEP-II accelerator complex and the *BABAR* detector. Chapters 3 through 6 will the detail the various steps of the analysis and present a measurement of sin2β as well as several calibration measurements. Finally, in Chapter 7 we will conclude with an interpretation of our results in the context of the Standard Model.

1.1 $\mathcal{CP}$ Violation in Field Theories

> *"Particles are defined by their Poincare Invariants. . ."*
> — C. Goebel, Physics 711 Lecture.

At its core, the Standard Model is a quantum field theory. That is to say, in the Standard Model, the time-evolution of systems are described by the action of the Lagrangian on the quantum field. Furthermore, the observable particle spectra are simply the eigenstates of the associated Hamiltonian. For our purposes, the most important consequence of these statements is that the Standard Model exhibits the same symmetry properties as underlying Lagrangian.

Since most of the remainder of this chapter describes how $\mathcal{CP}$ violation arises in the Standard Model, is is best to start by:

- defining the discrete transformations $\mathcal{C}$, $\mathcal{P}$, and $\mathcal{T}$, as well as the combined transformations, $\mathcal{CP}$ and $\mathcal{CPT}$;
- Summarizing the operation of those transformation on the quantum field and the Standard Model Lagrangian;
- Discussing the circumstances under which the combined $\mathcal{CP}$ symmetry can be broken in any quantum field theory.

The main point of this section is that the existence of irreducible complex coupling constants in the Lagrangian are an necessary condition for $\mathcal{CP}$ violation.

1.1.1 Definitions of the Discrete Symmetries

For an operator on the quantum field to be physically meaningful to any inertial observer it must preserve the Minkowski interval $t^2 - \boldsymbol{x}^2$. Such quantities are known as Lorentz-invariants.

In addition to the continuous (Lorentz) transformations which preserve this interval, three independent discrete transformations preserve $t^2 - \boldsymbol{x}^2$. Namely, the charge conjugation operator ($\mathcal{C}$), the parity operator ($\mathcal{P}$), and the time-reversal operator ($\mathcal{T}$). In fact, in the Standard Model, these three operators form a complete set of discrete Lorentz-invariant

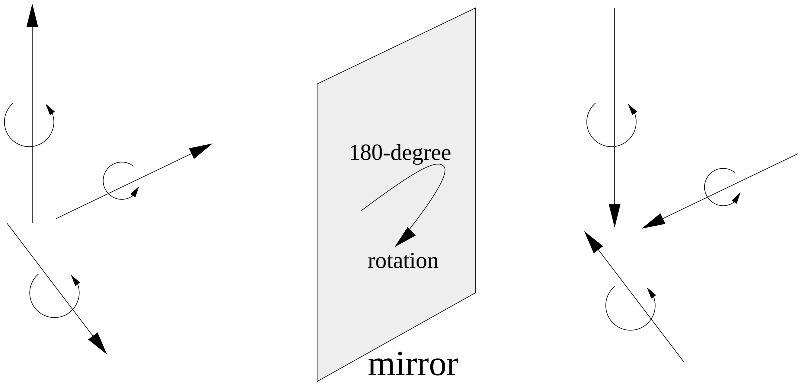

Figure 1.1: *The parity operation:* $(t, \boldsymbol{x}) \to (t, -\boldsymbol{x})$.

operators. All other discrete interval-preserving transformations extant in the Standard Model can be formed from $\mathcal{C}$, $\mathcal{P}$, $\mathcal{T}$, and the group of continuous Lorentz and gauge rotations.

Without further ado we give formal definitions of these operators.

1.1.1.1 Parity: $\mathcal{P}$

The parity operator $\mathcal{P}$ reverses the signs of the 3 spatial elements of a four-vector: $(t, \boldsymbol{x}) \to (t, -\boldsymbol{x})$ and $(E, \boldsymbol{p}) \to (E, -\boldsymbol{p})$. This is equivalent to a mirror-image followed by an 180-degree rotation normal to the plane of the mirror. The parity operator reverses the momentum of a particle but leaves its angular momentum unchanged. This transformation is show schematically in Fig. 1.1.

Parity violation was predicted in 1954 by Yang and Lee [11], and subsequently observed by C.S.Wu in nuclear β decays [12].

1.1.1.2 Time Reversal: $\mathcal{T}$

The time reversal operator $\mathcal{T}$ flips the sign of the time component of a state vector while leaving the space components unchanged, $(t, \boldsymbol{x}) \to (-t, \boldsymbol{x})$. This reverses both the momentum

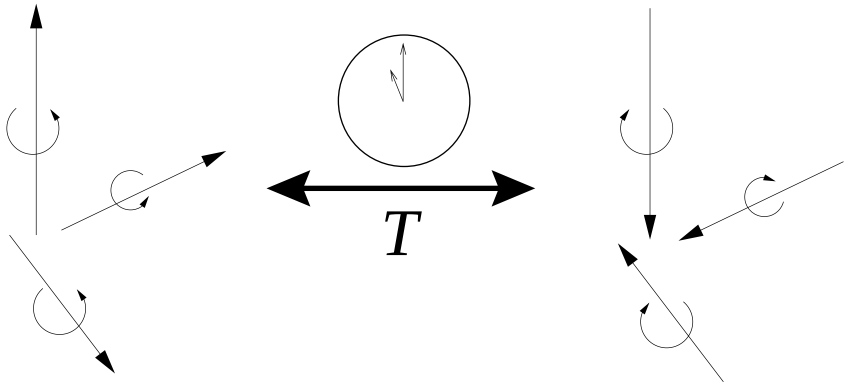

Figure 1.2: *The time reversal operation:* $(t, \boldsymbol{x}) \rightarrow (-t, \boldsymbol{x})$.

and angular momentum. This transformation is shown schematically in Fig. 1.2.

1.1.1.3 Charge Conjugation: $\mathcal{C}$

The charge conjugation operator $\mathcal{C}$ is defined to be the transformation of a particle into its anti-particle without changing position or momentum.

1.1.2 Field Transformations of $\mathcal{C}$, $\mathcal{P}$, $\mathcal{T}$

As a Lorentz scalar, the Lagrangian can only be composed of terms proportional to field bilinears – scalar, vector, tensor, pseudo-vector, pseudo-scalar quantities. Since the Lagrangian describes the time-evolution of the field, it is sufficient to observe how these field bilinears transform under the various symmetry operations to understand under which cases particular symmetries should be conserved.

So as a (very relevant) example, we summarize in Tab. 1.1.2 the action of the discrete symmetry operators on the Dirac field for spin $\frac{1}{2}$ particles and the various bilinears of that field. Furthermore, since $\mathcal{C}$, $\mathcal{P}$, and $\mathcal{T}$ are independent and discrete, they can be combined and commute. At this point we are particularly interested in two of four possible combination

Term (form)	$\mathcal{C}$	$\mathcal{P}$	$\mathcal{T}$	$\mathcal{CP}$	$\mathcal{CPT}$
Coefficients (c)	1	1	c^*	1	c^*
Scalar ($\bar{\phi}\phi$)	1	1	1	1	1
Pseudo-scalar ($\bar{\phi}\phi$)	1	-1	-1	-1	1
Vector ($\bar{\phi}\gamma^\mu\phi$)	-1	$G_{\mu\nu}$	$G_{\mu\nu}$	$-G_{\mu\nu}$	-1
Pseudo-vector ($\bar{\phi}\gamma^\mu\gamma^5\phi$)	1	-$G_{\mu\nu}$	$G_{\mu\nu}$	$-G_{\mu\nu}$	-1
Tensor ($\bar{\phi}[\gamma^\mu, \gamma^\nu]\phi$)	-1	$G_{\mu\alpha}G_{\mu\beta}$	$-G_{\mu\alpha}G_{\nu\beta}$	$-G_{\mu\alpha}G_{\nu\beta}$	1
Derivative Operator (∂_μ)	-1	$G^{\mu\nu}$	$-G^{\mu\nu}$	$-G^{\mu\nu}$	1

Table 1.1: *Summary of the action of the $\mathcal{C}$, $\mathcal{P}$, and $\mathcal{T}$ operators on bilinears of the Dirac field; $G_{\mu\nu}$ is (1,-1,-1,-1) across the diagonal and 0 elsewhere.*

operations: $\mathcal{CP}$ and $\mathcal{CPT}$.

Remembering that the Lagrangian $\mathcal{L}$ is a Lorentz scalar, and noting that any contraction of indices to form a Lorentz scalar must result in an eigenstate with a +1 $\mathcal{CPT}$ eigenvalue we conclude $\mathcal{CPT}$ is an exact symmetry for the special case of Dirac fields. If fact, under the basic assumptions of Lorentz invariance, locality, causality, positive energies and norms, the combination $\mathcal{CPT}$ operator is guaranteed to be a fundamental symmetry of nature [13]. Furthermore, $\mathcal{CPT}$ has been tested to extremely stringent levels and no credible results have indicated any violation [14].

This is not quite the case for the $\mathcal{CP}$ transformation. As we shall see in the next section, under particular circumstances $\mathcal{CP}$ violation is possible and in fact occurs.

1.1.3 $\mathcal{CP}$ Violation From Coupling Terms

Complex quantities such as particle masses and coupling constants do not transform under $\mathcal{CP}$ but only under $\mathcal{T}$. Therefore, if any of these quantities is not purely real, it will suffer a phase shift relative to the quantities that are transformed by $\mathcal{CP}$, potentially violating $\mathcal{CP}$ symmetry.

To manifest as $\mathcal{CP}$ violation, such phase differences must be robust against gauge modifications. If redefinitions of the fields phases can remove overall phases in each couplings, the theory remains $\mathcal{CP}$-conserving. With sufficient coupling, however, irreducible phases can remain, and how such phases effect observable $\mathcal{CP}$ violation will be shown in the following sections.

1.2 Time Evolution of Neutral Meson States

> *"It isn't a mass eigenstate; it doesn't have a well defined rest frame."*
> — C. O'Dell

The results discussed in this section are treated in significantly more detail in several places, most notably Ref. [15].

Before we continue with our discussion of $\mathcal{CP}$ violation, we must introduce a bit of background about the systems in which we propose to measure it – the heavier neutral mesons: $q\overline{q}$ bound states having at least one /, c or b quark, such as K^0, D^0, B^0, and B_s^0. Such systems exhibit particular phenomena that are very relevant to any measurements of $\mathcal{CP}$ violation.

1. They decay via the weak interaction with a lifetime on the order of $10^{-12}s$, implying that such particles travel about $c\tau \sim 300\,\mu$m. (The K^0 lifetime is somewhat longer, as described in Sec. 1.4.4.)

2. They can decay to $\mathcal{CP}$ eigenstates such as $\pi^0\pi^0$ from which it is not possible to determine the flavor of the initial state.

3. They are able to mix with their respective anti-particles via the W-boson box diagrams Fig. 1.3.

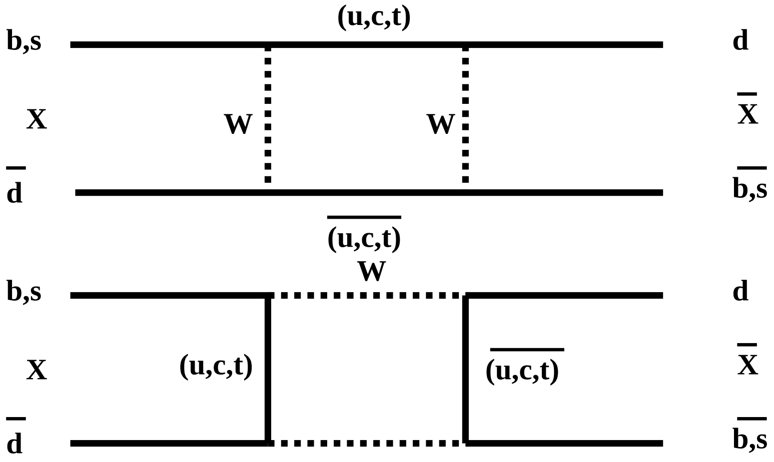

Figure 1.3: *The "ladder" (top) and "box" (bottom) diagrams for neutral meson mixing.*

4. It is possible to pair-produce them in coherent states, such that the pair time evolve in phase.

Although there is nothing particularly unusual or surprising about the manner in which neutral mesons decay weakly, the other three points have some involved implications, which we will now discuss.

d

1.2.1 Tagging and $\mathcal{CP}$ Final States

In order to proceed with a full fledged discussion of $\mathcal{CP}$ violation, it is useful to distinguish between two types of final states in neutral meson decays.

1. "Flavored" final states, f_{flav}, are not $\mathcal{CP}$ self-conjugate, and generally have very different amplitudes compared to decays to $\mathcal{CP}$ conjugate final states. $A_{X\to f_{flav}} \gg A_{X\to \bar{f}_{flav}}$ and $A_{\bar{X}\to \bar{f}_{flav}} \gg A_{\bar{X}\to f_{flav}}$.

2. "CP" final states, f_{cp}, are $\mathcal{CP}$ self conjugate, and have related amplitudes from either $\mathcal{CP}$ conjugate initial state. $A_{X\rightarrow f_{cp}} = \eta_{CP} A_{\bar{X}\rightarrow f_{cp}}$, where η_{CP} is the $\mathcal{CP}$ eigenvalue of the final state f_{cp}.

In fact, there are many decays, where to an excellent, $\mathcal{O}(10^{-3})$ or better, approximation:

$$A_{X^0\rightarrow f_{flav}} = 0 \quad or \tag{1.1}$$

$$A_{X^0\rightarrow f_{\bar{flav}}} = 0$$

Such decays greatly simplify the discussion in the next few sections, in particular the decay amplitude given in Eq. (1.16), and as such, are instrumental in isolating particular phenomena in neutral meson decay.

1.2.2 Mixing of a Neutral Mesons

Flavor mixing has been studied in the decays of neutral mesons into conjugate flavor-specific final states. A classic example of such decays are semi-leptonic B decays via virtual W bosons:

$$B^0 \rightarrow D^+\mu^-\bar{\nu_\mu} \quad and \tag{1.2}$$

$$\bar{B}^0 \rightarrow D^-\mu^+\nu_\mu.$$

In these decays, the leptons's charge is the same as the charge of the virtual W, which is in turn defined by the flavor of the b quark, and thus the B-meson flavor. It is said that the lepton "tags" the B as being either B^0 or $\overline{B}^0$. By studying associated production of neutral mesons, "flavor tagging" can be used identify events in which flavor mixing has or has not occurred.

The correct technical description of flavor mixing is that neutral mesons time-evolve as mass eigenstates which are linear combinations of the flavor eigenstates, $|X_{mass}\rangle = \mathcal{M}|X_{flav}\rangle$.

Consider a weakly-decaying neutral meson X^0. It is an arbitrary linear combination of the flavor eigenstates:

$$\alpha|X^0\rangle + \beta|\bar{X}^0\rangle \tag{1.3}$$

and mixes with its conjugate according to the time-dependent Schrödinger equation:

$$i\frac{\partial}{\partial t}\begin{pmatrix}\alpha\\ \beta\end{pmatrix} = \mathcal{H}\begin{pmatrix}\alpha\\ \beta\end{pmatrix} \equiv \begin{pmatrix} m_{11}-\frac{1}{2}i\gamma_{11} & m_{12}-\frac{1}{2}i\gamma_{12}\\ m_{21}-\frac{1}{2}i\gamma_{21} & m_{22}-\frac{1}{2}i\gamma_{22}\end{pmatrix}\begin{pmatrix}\alpha\\ \beta\end{pmatrix} \tag{1.4}$$

The m and γ terms represent the mixing and decay features of the time behavior of the state. The off-diagonal elements are potentially complex: the angle in the complex plane of m_{12} corresponding the phase of the mixing, and γ_{12} representing coupling to common decay modes of the X^0 and $\bar{X}^0$ (for example, $B^0 \to J/\psi\ K^0_S$ or $\pi^+\pi^-$). Furthermore, $\mathcal{CPT}$ invariance guarantees that $m_{11} = m_{22} \equiv m$, $\gamma_{11} = \gamma_{22} \equiv \gamma$, $m_{21} = m^*_{12}$ and $\gamma_{21} = \gamma^*_{12}$.

Therefore, Eq. (1.4) becomes

$$i\frac{\partial}{\partial t}\begin{pmatrix}\alpha\\ \beta\end{pmatrix} = \begin{pmatrix} m-\frac{1}{2}i\gamma & m_{12}-\frac{1}{2}i\gamma_{12}\\ m^*_{12}-\frac{1}{2}i\gamma^*_{12} & m-\frac{1}{2}i\gamma\end{pmatrix}\begin{pmatrix}\alpha\\ \beta\end{pmatrix} \tag{1.5}$$

The mass eigenstates are the eigenvectors of the Hamiltonian. Namely

$$|X_L\rangle = p|X^0\rangle + q|\bar{X}^0\rangle \tag{1.6}$$

$$|X_H\rangle = p|X^0\rangle - q|\bar{X}^0\rangle$$

where:

$$q = \left(\frac{\sqrt{2(m+\frac{1}{2}i\gamma)^2 + (m_{12}-\frac{1}{2}i\gamma_{12})(m^*_{12}-\frac{1}{2}i\gamma^*_{12})}}{m_{12}-\frac{1}{2}i\gamma_{12}}\right) \tag{1.7}$$

$$\text{and} \qquad |p|^2 + |q|^2 = 1 \tag{1.8}$$

The mass difference and decay width difference can be obtained by diagonalizing the mixing matrix. Let

$$\alpha = |m_{12}|^2 - \frac{1}{4}|\gamma_{12}|^2, \qquad \beta = \mathcal{R}e(m_{12}\gamma_{12}^*) \tag{1.9}$$

Then,

$$\Delta m = \sqrt{2\alpha - 2\sqrt{\alpha^2 - \beta^2}} \quad \text{and} \tag{1.10}$$

$$\Delta\Gamma = 4\beta/\Delta m \tag{1.11}$$

For this we see that an initially pure $|X^0\rangle$ state will time evolve as a superposition of the mass eigenstates $|X_L\rangle$ and $|X_H\rangle$. Furthermore, the time-evolution can be fully expressed in terms of the physically intuitive quantities m, Γ, Δm, and $\Delta\Gamma$.

$$\begin{aligned} |X^0(t)\rangle &= g_+(t)|X^0\rangle + (q/p)g_-(t)|\bar{X}^0\rangle, \qquad (1.12) \\ |\bar{X}^0(t)\rangle &= (p/q)g_-(t)|X^0\rangle + g_+(t)|\bar{X}^0\rangle, \end{aligned}$$

where

$$\begin{aligned} g_+(t) &= e^{-imt}e^{-\Gamma t/2}(e^{-i\Delta mt/2}e^{-\Delta\Gamma t/2} + e^{+i\Delta mt/2}e^{+\Delta\Gamma t/2}) \qquad (1.13) \\ g_-(t) &= e^{-imt}e^{-\Gamma t/2}(e^{-i\Delta mt/2}e^{-\Delta\Gamma t/2} - e^{+i\Delta mt/2}e^{+\Delta\Gamma t/2}). \end{aligned}$$

1.2.3 Neutral Mesons in Coherent States

Consider the associated production of a pair of interchangeable or mix-able particles. For example, two photons from positron annihilation, or two B-mesons from the decay of an $\Upsilon(4S)$. Both are produced at the same time and place. Therefore, until either particle decays, scatters or otherwise interacts, both particles must have exactly the same phase in their mutual center of mass frame.

This is the origin of the classic Einstein-Poldosky-Rosen situation [16]. Each particle propagates as a mixture of available eigenstates (spin states in the case of photons, flavor states in the case of B-mesons), allowing the expectation values for observable (spin, flavor) for that particle to vary, however the expectation values for the pair of particles remains constant. That is to say, *until one of the particles decay, there is always exactly one* X^0 *and one* $\bar{X}^0$

In fact, after the decay of one of the particles, the other continues to evolve. Thus, the probability to observe, for example, two X decays or two $\bar{X}$ decays, is a function of the time difference between the two decays.

If we consider states where two coherent mesons which decay to states f_1 and f_2 at proper times t_1 and t_2, we can write the coherent state as,

$$\begin{aligned} S(t_1, t_2) = & \frac{1}{\sqrt{2}} e^{-(\Gamma/2+im)(T)} \\ & \{[e^{(i\Delta m+\Delta\Gamma)(\Delta t/2)} + e^{-(i\Delta m+\Delta\Gamma)(\Delta t/2)}](|X_1^0\rangle|\bar{X}_2^0\rangle - |\bar{X}_1^0\rangle||X_2^0\rangle) \\ & -[e^{(i\Delta m+\Delta\Gamma)(\Delta t/2)} + e^{-(i\Delta m+\Delta\Gamma)(\Delta t/2)}](\tfrac{p}{q}|X_1^0\rangle|X_2^0\rangle - \tfrac{q}{p}|\bar{X}_1^0\rangle|\bar{X}_2^0\rangle)\} \end{aligned} \tag{1.14}$$

Which can in turn can be used to calculate the decay amplitude

$$\begin{aligned} A(t_1, t_2) = & \frac{1}{\sqrt{2}} e^{-(\Gamma/2+im)(T)} \\ & \{[e^{(i\Delta m+\Delta\Gamma)(\Delta t/2)} + e^{-(i\Delta m+\Delta\Gamma)(\Delta t/2)}](A_1\bar{A}_2 - \bar{A}_1 A_2) \\ & -[e^{(i\Delta m+\Delta\Gamma)(\Delta t/2)} + e^{-(i\Delta m+\Delta\Gamma)(\Delta t/2)}](\tfrac{p}{q}A_1 A_2 - \tfrac{q}{p}\bar{A}_1\bar{A}_2)\} \end{aligned} \tag{1.15}$$

Where $T \equiv t_1 + t_2$ and $\Delta t \equiv t_1 - t_2$.

1.3 Three Types of $\mathcal{CP}$ Violation in Neutral Meson Systems

"So I made of list of all the things I am angry at him about."
— A. Chakravarti

The results discussed in this section and the next are treated in significantly more detail in several places, notably Refs. [17] and [18]. Here we merely summarize the most relevant points.

It is useful at this point to categorize and describe various ways in which $\mathcal{CP}$ violation can occur and how it can be measured by studying decay asymmetries. The core of this discussion is the observation that if $\mathcal{CP}$ were an exact symmetry of nature, the rate from any pair of $\mathcal{CP}$ conjugates processes must be equal at all times.

Furthermore, since phase space is $\mathcal{CP}$ invariant, the only possibility for $\mathcal{CP}$ violating terms to appear in decay rates is via the matrix elements themselves. If we admit the possibility of flavor mixing, and consider the decay from an initial state i to final state f, $i \to f$, and its $\mathcal{CP}$ conjugate process $i \bar{\to} f$, having amplitudes $A_{i\to f}$ and $\bar{A}_{i\bar{\to}f}$ respectively, the quantity

$$\lambda \equiv (q/p)(\bar{A}_{i\bar{\to}f}/A_{i\to f}) \tag{1.16}$$

summarizes all possible sources of $\mathcal{CP}$ violation.

CP violation in decay occurs when a decay process and its $\mathcal{CP}$ conjugate process have different magnitudes owing to differences in phases from several intermediate states. This form of $\mathcal{CP}$ violation is also known as "direct" $\mathcal{CP}$ violation.

Direct $\mathcal{CP}$ violation could potentially be observed by comparing the total rate for any processes to the rate for its $\mathcal{CP}$ conjugate:

$$a_f = \frac{\Gamma(X \to f) - \Gamma(\bar{X} \to \bar{f})}{\Gamma(X \to f) + \Gamma(\bar{X} \to \bar{f})}. \tag{1.17}$$

However, the effect usually small, and although it has not yet been measured, there is compelling evidence for it in the kaon system [9, 10].

CP violation in mixing occurs when the mass eigenstates differ from the $\mathcal{CP}$ eigenstates. This form of $\mathcal{CP}$ violation is also known as "indirect" $\mathcal{CP}$ violation. Indirect $\mathcal{CP}$ violation can be observed by comparing time variation of the rates for a pair of $\mathcal{CP}$ conjugate decays from states that are able to mix with each other:

$$a_f(t) = \frac{\Gamma(X^0(t) \to f) - \Gamma(\bar{X}^0(t) \to \bar{f})}{\Gamma(X^0(t) \to f) + \Gamma(\bar{X}^0(t) \to \bar{f})}. \tag{1.18}$$

where X^0 and $\bar{X}^0$ are able to mix. In fact, this form of $\mathcal{CP}$ violation has been unambiguously observed in the neutral kaon system [6].

CP violation in the interference between mixing and decay occurs when $\mathcal{CP}$ conjugate decays to the same final state contribute different phases. This can only be observed by comparing the decays of $\mathcal{CP}$ conjugate states which are able to mix with each other into the same final $\mathcal{CP}$ eigenstates:

$$a_f(t) = \frac{\Gamma(X^0(t) \to f_{CP}) - \Gamma(\bar{X}^0(t) \to f_{CP})}{\Gamma(X^0(t) \to f_{CP}) + \Gamma(\bar{X}^0(t) \to f_{CP})}. \tag{1.19}$$

Although this form of $\mathcal{CP}$ violation occurs in combination with the other types, there are certain circumstances under which it is, to an excellent approximation, the only effect. It is in fact, this type of $\mathcal{CP}$ violation that we measure in this dissertation. This type of $\mathcal{CP}$ violation has only been observed in the past year [19, 20]. Previous measurements ([21, 22]) were ambiguous at best.

1.3.1 $\mathcal{CP}$ Violation in Decay

Consider the decay amplitudes for $\mathcal{CP}$ conjugate states X and $\bar{X}$ to decay into final states f and $\bar{f}$. If we call these amplitudes A_f and $\bar{A}_{\bar{f}}$, the quantity $|\frac{\bar{A}_{\bar{f}}}{A_f}|$ is phase-convention independent.

Two types of phases are present in the amplitudes A_f and $\bar{A}_{\bar{f}}$.

1. Those arising from complex parameters in the Lagrangian. In the Standard Model, such phases enter only via the electroweak CKM mass mixing matrix, and are often called "weak" phases. Such phases appear in A_f and $\bar{A}_{\bar{f}}$ with opposite signs.

2. Those arising from contributions of intermediate on-shell states. Since such contributions usually dominated by strong interactions, these are often called "strong" phases. Since they do not intrinsically violate $\not{C}\not{P}$ such phases appear in A_f and $\bar{A}_{\bar{f}}$ with like signs.

If we separate each decay channels contribution to the amplitude into magnitude A_i, "weak-phase" term $e^{i\phi_i}$ and "strong-phase" term $e^{i\delta_i}$ we obtain:

$$|\frac{\bar{A}_{\bar{f}}}{A_f}| = |\frac{\sum_i A_i e^{i\delta_i - \phi_i}}{\sum_i A_i e^{i\delta_i + \phi_i}}|. \tag{1.20}$$

From this we can set that "direct" $\not{C}\not{P}$ violation only occurs if two terms with differing weak phases acquire different strong phases:

$$|A|^2 - |\bar{A}|^2 = -2\sum_{i,j} A_i A_j \sin(\phi_i - \phi_j)\sin(\delta_i - \delta_j). \tag{1.21}$$

Furthermore the rate asymmetry can be expressed in terms of the decay amplitudes:

$$a_f = \frac{1 - |\bar{A}/A|^2}{1 + |\bar{A}/A|^2} \tag{1.22}$$

Since the magnitude and "strong phase" of any amplitude involving strong interactions at long distances is non-perturbative, it is effectively impossible to calculate such quantities model independently, Thus it remains very difficult to relate observable "direct" $\not{C}\not{P}$ violation asymmetries to the underlying Standard Model parameters.

1.3.2 $\mathcal{CP}$ Violation Purely in Mixing

As mentioned above, $\mathcal{CP}$ eigenstates are not identical to mass eigenstates. Or, in terms of mixing parameters q and p:

$$|\frac{q}{p}|^2 = |\frac{M_{12}^* - \frac{i}{2}\Gamma_{12}^*}{M_{12} - \frac{i}{2}\Gamma_{12}}. \tag{1.23}$$

In analogy with Eq. (1.22), the rate asymmetry for $\mathcal{CP}$ violation in mixing can be expressed in terms of the mixing coefficients:

$$a_{mix} = \frac{1 - |q/p|^4}{1 + |q/p|^4}. \tag{1.24}$$

In order to relate "indirect" $\mathcal{CP}$ violation to fundamental CKM parameters it is necessary to calculate Γ_{12} and M_{12}. This involves large theoretical uncertainties, in particular those owing to the hadronization models in the calculation of Γ_{12}.

1.3.3 $\mathcal{CP}$ Violation in Interference Between Decays of Mixed and Unmixed Mesons

In the case of neutral meson decays to $\mathcal{CP}$ eigenstates, the final state is accessible in both X_0 and $\bar{X}_0$ decays. Thus, both mixing and decay amplitudes must be taken into account. The quantity of interest is the λ of Eq. (1.16). If we re-write λ in terms of the magnitudes and phases of the complex quantities q/p and $\bar{A}_{f_{CP}}/A_{f_{CP}}$ we get:

$$\lambda = |q/p||\bar{A}_{\bar{f}_{CP}}/A_{f_{CP}}|e^{i\phi_{CP}}. \tag{1.25}$$

Where ϕ_{CP} is the relative phase between q/p and $\bar{A}_{\bar{f}_{CP}}/A_{f_{CP}}$.

In fact, as shown in Sec. 1.2.3 the time-dependent asymmetry for coherent neutral mesons can be expressed in terms of λ as:

$$a_{f_{CP}} = \frac{(1 - |\lambda_{f_{CP}}|^2)\cos(\Delta M t) - 2\mathcal{I}\lambda_{f_{CP}}\sin(\Delta M t)}{1 + |\lambda_{f_{CP}}|^2}. \tag{1.26}$$

Clearly it is possible to have $\mathcal{CP}$ violation with:

$$|\lambda| = 1, \mathcal{I}\lambda \neq 0. \tag{1.27}$$

In which case, Eq. (1.26) reduces considerably to:

$$a_{f_{CP}} = -\mathcal{I}\lambda_{f_{CP}} \sin(\Delta M t). \tag{1.28}$$

Or, in terms of the $\mathcal{CP}$ violating phase ϕ_{CP} we have:

$$a_{f_{CP}} = -\sin(\phi_{CP}) \sin(\Delta M t). \tag{1.29}$$

Since ϕ_{CP} is simply the phase shift between the mixing and decay terms in the process amplitude and is independent of their magnitudes it can be cleanly related to electroweak parameters of the Lagrangian.

Thus, observation of $\mathcal{CP}$ violation in interference between decays and mixing with no contribution from $\mathcal{CP}$ violation in decay offer the best hope for directly extracting information about the CKM matrix. Examples of such decays are modes dominated by a single $\mathcal{CP}$-violating phase.

We should also note that it is possible to decay to states that have $\mathcal{CP}$ self-conjugate particle content, but are not $\mathcal{CP}$ eigenstates because the contain admixtures of various angular momenta and hence different parity. In some cases the amplitudes for each $\mathcal{CP}$ contribution can be separated by means of angular analyses. Otherwise, we must average over the various contributions.

1.4 Quark Mixing and $\mathcal{CP}$ Violation in the Standard Model

"I still think it looks more the tree of the Cabbalah than a physics theory."
— C. Shalizi

As stated in the introduction, the only source of $\mathcal{CP}$ violation in the Standard Model is in the electroweak sector. We will proceed now with a brief summary of the important features of the electroweak sector of the standard model and describe how they give rise to $\mathcal{CP}$ violation.

1.4.1 Weak Interactions and the CKM Matrix

In the Standard Model, each quark generation consists of three multiplets:

$$\begin{aligned} {Q_L}^I = (\begin{matrix} {U_L}^I \\ {D_L}^I \end{matrix}) &= (3,2)_{+1/6} \\ {u_R}^I &= (3,1)_{+2/3} \\ {d_R}^I &= (3,1)_{-1/3}. \end{aligned} \tag{1.30}$$

Here, for example $(3,1)_{+2/3}$ signifies an SU$(3)_C$ triplet, SU$(1)_L$ singlet, with hyper-charge $Y = Q = T_3 = +1/3$. In the Standard Model, the interaction of quarks with the primordial SU$(1)_L$ fields, A^a, are describe by:

$$\mathcal{L}_W = -\frac{1}{2} g \bar{{Q_L}}^I \gamma^\mu \tau^a {Q_L}^I {A_\mu}^a. \tag{1.31}$$

Furthermore, the interaction of quarks with the Standard Model Higgs scalar doublet ϕ are described by:

$$\mathcal{L}_Y = -G \bar{{Q_L}}^I \phi {d_R}^I - F \bar{{Q_L}}^I \tilde{\phi} {u_R}^I + H.C.. \tag{1.32}$$

In general F and G are 3×3 *complex* matrices. As described in Sec. 1.1.3, their complex nature can introduce $\mathcal{CP}$-violating terms into the coupling constants in the electroweak sector.

Spontaneous symmetry breaking, because of the non-zero Higgs vacuum expectation value ($\langle\phi\rangle \neq 0$), causes $SU(2)_L X U(1)_Y \rightarrow U(1)_{EM}$. The result of which is that various members of quark doublet become distinguishable. Similarly, the primordial vector Bosons become the more familiar electroweak carriers, W^+, W^-, Z^0, γ.

After this transformation the charged current interactions in Eq. (1.31) are given by:

$$\mathcal{L}_W = -\sqrt{\frac{1}{2}} g \bar{u}_L{}^I \gamma^\mu d_L{}^I W_\mu{}^+ + H.C.. \tag{1.33}$$

Furthermore, mass-type (of the form $-m\phi\bar{\phi}$) terms arise from the replacement $Re(\phi^0) \rightarrow \sqrt{\frac{1}{2}}(v + H^0)$:

$$\mathcal{L}_M = -M_d \bar{d}_L{}^I d_R{}^I - M_u \bar{u}_L{}^I u_R{}^I, \tag{1.34}$$

where we have defined:

$$\begin{aligned} M_d &\equiv \sqrt{\frac{1}{2}} vG \\ M_u &\equiv \sqrt{\frac{1}{2}} vF. \end{aligned} \tag{1.35}$$

Finally, if we want to transform to the mass eigenbasis, we must introduce a group of unitary matrices V_{dR}, V_{uR}, V_{dL}, and V_{uL} such that:

$$\begin{aligned} M_d^{diag} &= V_{dL} M_d V_{dR}^\dagger \\ M_u^{diag} &= V_{uL} M_u V_{uR}^\dagger. \end{aligned} \tag{1.36}$$

Thus, in the mass eigenbasis, the charged current interaction is given by:

$$\mathcal{L}_W = -\sqrt{\frac{1}{2}} g \bar{u}_L{}^I \gamma^\mu \bar{V} d_L{}^I W_\mu{}^+ + H.C.. \tag{1.37}$$

where $\bar{V} = V_{uL} V_{dL}^\dagger$ is the mass mixing matrix or Cabbibo-Kobayashi-Maskawa (henceforth CKM) matrix [8]. The order ($N = 3$) of the CKM matrix is given by the number of quark generations, and in general it has complex coefficients, for a total of $2N^2 = 18$ parameters.

However, the unitarity requirements constrain $N^2 = 9$ of those parameters. Furthermore, we are free to redefine all but one $(2N-1=5)$ of the quark phases. Therefore, the CKM matrix has a total of $18-9-5=4$ free parameters. As a 3×3 matrix, these can be defined as three real rotations and a single complex phase. It is in fact, the irreductability of this complex phase that permits $\mathcal{CP}$ violation.

1.4.2 Unitarity Conditions and Unitarity Triangles

As discussed above, the description of the CKM matrix requires 4 independent parameters. Although many such descriptions are possible, two parameterizations occur in most of the literature.

1. The "Standard" parameterization in terms of three Euler rotations [23], $\theta_{12}, \theta_{13}, \theta_{23}$ and a complex phase δ.
$$V = \begin{pmatrix} c_{12}c_{13} & c_{12}c_{13} & s_{13}e^{-i\delta} \\ -s_{12}c_{23} - c_{12}s_{23}s_{13}e^{i\delta} & c_{12}c_{23} - s_{12}s_{23}s_{13}e^{i\delta} & s_{23}c_{13} \\ s_{12}s_{23} - c_{12}c_{23}s_{13}e^{i\delta} & -c_{12}s_{23} - s_{12}c_{23}s_{13}e^{i\delta} & c_{23}c_{13} \end{pmatrix} \tag{1.38}$$

2. The Wolfenstein parameterization [24]. Basically an expansion in terms of the sin of the Cabbibo angle [25], $\lambda \equiv \sin(\theta_{12})$, which uses the feature that $s_{23} = \mathcal{O}(\lambda^2)$ and $s_{13} = \mathcal{O}(\lambda^3)$, to define expansion co-efficients of order unity, A and ρ and complex phase η,
$$V = \begin{pmatrix} 1-\lambda^2/2 & \lambda & A\lambda^3(\rho - i\eta) \\ -\lambda & 1-\lambda^2 & A\lambda^2 \\ A\lambda^3(1-\rho i\eta) & -A\lambda^2 & 1 \end{pmatrix}, \tag{1.39}$$
which is accurate to $\mathcal{O}(\lambda^4)$.

The unitarity of the CKM matrix, $VV^\dagger = 1$, implies a some very useful relations.

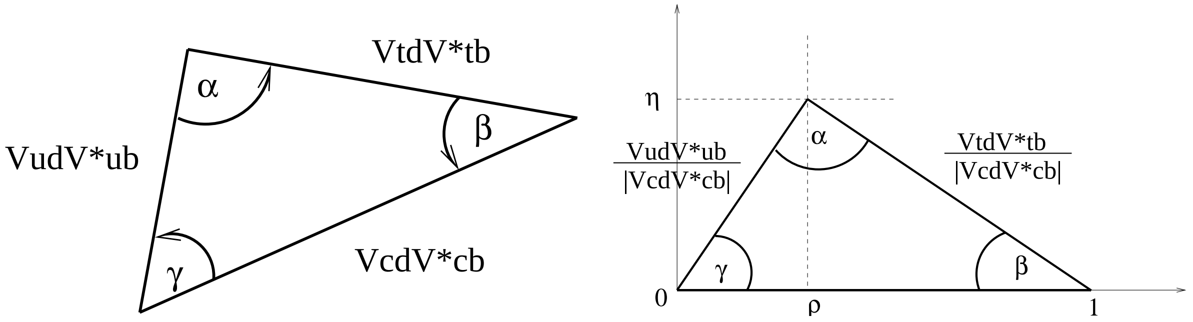

Figure 1.4: *The unitarity triangle for the B-meson system. The bottom figure has been rotated, all the sides have been divided by* $V^*_{cb}V_{cd}$.

1. $V_{ij}V_{kj} = 0$ for $i \neq k$. In terms of the various matrix elements:

$$\begin{aligned} V_{ud}V^*_{us} + V_{cd}V^*_{cs} + V_{td}V^*_{ts} &= 0 \\ V_{us}V^*_{ub} + V_{cd}V^*_{cb} + V_{td}V^*_{tb} &= 0 \\ V_{ud}V^*_{ub} + V_{cd}V^*_{cb} + V_{td}V^*_{tb} &= 0. \end{aligned} \tag{1.40}$$

   Each of these expressions require three complex numbers to sum to zero, and can thus be geometrical expressed as triangles in the complex plane. Such triangles are called “unitarity triangles”. The unitary triangle for the B-meson systems is shown in Fig. 1.4.

2. A quantity J, the Jarlskog Parameter, exists such that

$$\mathcal{I}[V_{ij}V_{kl}V^*_{il}V^*_{kj}] = J\sum m,n = 13\epsilon_{ikm}\epsilon_{jln} \tag{1.41}$$

   for all $i,j,k,l = 1,2,3$. In fact, by construction, the area of any of the unitarity triangles is equal to J/2 [26, 27, 28].

1.4.3 Measurements of the CKM Matrix Elements

Several constraint on the CKM matrix exist and we will summarize them here [29]. The magnitude of five of the nine CKM matrix elements have been measured directly.

1. $|V_{ud}| = 0.9736 \pm 0.0010$ has been measured using nuclear β decays.
2. $|V_{us}| = 0.2205 \pm 0.0018$ has been measured using semi-leptonic kaon and hyperon decays.
3. $|V_{cd}| = 0.224 \pm 0.016$ has been measured via charm production in ν and $\bar{\nu}$ scattering off valence d quarks.
4. $|V_{cs}| = 1.01 \pm 0.18$ has been measured using semi-leptonic D decays.
5. $|V_{cb}| = 0.041 \pm 0.003$ has been measured using semi-leptonic B decays.

Additionally, two elements have been indirectly measured.

1. The ratio $\frac{|V_{ub}|}{|V_{cb}|} = 0.08 \pm 0.02$ has been measured by observing the B semi-leptonic decay spectrum near the kinematic end-point.
2. The quantity $|V_{tb}^{*} V_{td}| = 0.009 \pm 0.003$ has been measured using $B^0\overline{B}^0$ mixing.

Finally, we note that unitarity conditions allow us to constrain some of the unmeasured CKM terms, as well as to narrow the possible ranges for others. A global fit to current data gives the following ranges.

$$|V_{ij}| = \begin{pmatrix} 0.9742 - 0.9757 & 0.219 - 0.262 & 0.002 - 0.005 \\ 0.219 - 0.225 & 0.9734 - 0.9749 & 0.037 - 0.43 \\ 0.004 - 0.014 & 0.035 - 0.043 & 0.9990 - 0.9993 \end{pmatrix} \tag{1.42}$$

1.4.4 The Neutral Kaon System

Neutral kaons are mesons with quark content $K^0 = s, \bar{d}$, $\bar{K}^0 = \bar{s}, d$. As discussed above, the K^0 and $\bar{K}^0$ are able to mix with each other. In fact, since in the kaon system, decays to $\mathcal{CP}$ eigenstates vastly dominate over "tagging" decays, the lifetimes differ hugely between the mass eigenstates, and it is more convenient to define "long" and "short" mass eigenstates in terms of their lifetimes:

$$\begin{aligned} \tau_S &= (8.927 + -0.009) \times 10^{-11} s \\ \tau_L &= (5.17 + -0.04) \times 10^{-8} s, \end{aligned} \tag{1.43}$$

where the subscripts S and L refer to the short and long-lived mass eigenstates:

$$\begin{aligned} |K_S\rangle &= p|K^0\rangle + q|\bar{K}^0\rangle, \\ |K_L\rangle &= p|K^0\rangle - q|\bar{K}^0\rangle, \end{aligned} \tag{1.44}$$

such that $\Delta\Gamma_K < 0$ by construction. Furthermore, the kaon mass difference has been measured to be:

$$\Delta m_K \equiv M_L - M_S = (3.491 + -0.009) \times 10^{-15}\,\mathrm{GeV}/c^2. \tag{1.45}$$

From Eqs. (1.43 and 1.45) we see that:

$$\Delta\Gamma_K \approx -2\Delta m_K. \tag{1.46}$$

Furthermore, since the $\mathcal{CP}$-violating effects in the kaon system are known to be small, it is useful to work in terms of a series expansion of the phase ϕ_{12}, and to note that to first order,

$$\begin{aligned} \Delta m_K &= 2|M_{12}| \\ \Delta\Gamma_K &= 2|\Gamma_{12}|. \end{aligned} \tag{1.47}$$

Which give us:

$$\frac{M_{12}}{\Gamma_{12}} \equiv -|\frac{M_{12}}{\Gamma_{12}}|e^{i\phi_{12}} = \frac{\Delta M_K}{\Delta\Gamma_K}(1+i\phi_{12}). \tag{1.48}$$

We go on to note that indirect $\mathcal{CP}$ violation has been observed in the kaon system in complimentary ways.

1. Asymmetries in semi-leptonic K_L^0 decays measure the quantity:

   $$\delta(\ell) = \frac{\Gamma(K_L^0 \to \pi^-\ell^+\nu) - \Gamma(K_L^0 \to \pi^+\ell^-\nu)}{\Gamma(K_L^0 \to \pi^-\ell^+\nu) + \Gamma(K_L^0 \to \pi^+\ell^-\nu)}; \tag{1.49}$$

   and have found:

   $$\delta(\mu) = (3.04 \pm 0.25) \times 10^{-3}, \delta(e) = (3.33 \pm 0.14) \times 10^{-3}[30]. \tag{1.50}$$

2. Asymmetries in the two-pions channels,

   $$\eta_{00} = \frac{A(K_L^0 \to \pi^0\pi^0)}{A(K_S^0 \to \pi^0\pi^0)}, \tag{1.51}$$
   $$\eta_{+-} = \frac{A(K_L^0 \to \pi^+\pi^-)}{A(K_S^0 \to \pi^+\pi^-)},$$

   have also been measured:

   $$|\eta_{00}| = (2.275 \pm 0.019) \times 10^{-3}, \phi_{00} = 43.5 \pm 1.0°, \tag{1.52}$$
   $$|\eta_{+-}| = (2.285 \pm 0.019) \times 10^{-3}, \phi_{00} = 43.7 \pm 0.6°.$$

Given these measurements, it is possible to separate the contributions from different isospin channels and construct two complex parameters ε_K and ε'_K whose real and imaginary parts are sensitive to different types of $\mathcal{CP}$ violation:

$$\varepsilon_K \equiv \frac{1}{3}(\eta_{00} + 2\eta_{+-}), \varepsilon'_K \equiv \frac{1}{3}(\eta_{00} - \eta_{+-})[31].$$

Specifically $\mathcal{R}(\varepsilon_K)$ and $\mathcal{R}(\varepsilon'_K)$ respectively measure $\mathcal{CP}$ violation in mixing and decay, while $\mathcal{I}(\varepsilon_K)$ and $\mathcal{I}(\varepsilon'_K)$ are both measure of $\mathcal{CP}$ violation in interference. As such, the ε_K and ε'_K are can be used to constrain the CKM phase parameter. We will make use of this point in Chapter 7, when we interpret our results within the context of the Standard Model.

1.4.5 The B-Meson System

The lightest neutral B-mesons have quark content $B^0 = b, \bar{d}$, $\overline{B}^0 = \bar{b}, d$. In analogy with the generic case, the mass eigenstates of the neutral B system can be defined as a superposition of the flavor eigenstates:

$$\begin{aligned} |B_L\rangle &= p|B^0\rangle + q|\overline{B}^0\rangle \\ |B_H\rangle &= p|B^0\rangle - q|\overline{B}^0\rangle, \end{aligned} \tag{1.53}$$

and the mass and width differences are defined such that Δm_d is positive:

$$\Delta m_d \equiv M_H - M_L; \Delta\Gamma_B \equiv \Gamma_H - \Gamma_L. \tag{1.54}$$

Because of the large mass of the b quark, the decays of B-mesons are dominated by "spectator" type decays with the quark-level process $b \to cW^+$ and its $\mathcal{CP}$ conjugate. In many cases, such decays will result "tagging" final states such as $B^0 \to D^+\mu^-\bar{\nu}_\mu$ or $B^0 \to D^+\,\pi^-$.

As described above, the difference in width is produced by decays which are common to the B^0 and $\overline{B}^0$. The branching fractions for all of these modes are at or below 10^{-3}. Furthermore, since these modes contribute to $\Delta\Gamma_B$ with varying signs, it is expected that their sum will not greatly exceed the individual level. Thus, since the large majority of neutral B-meson decay modes are specific to either B^0 or $\overline{B}^0$ the relative difference in width is expect to be quite small:

$$\Delta\Gamma_B/\Gamma_B = \mathcal{O}(10^{-2}), \tag{1.55}$$

and has not yet been observed.

In contrast, the mass difference Δm_d arise from the quark masses and the CKM matrix elements, and is comparable to the B^0 width. The current world average is:

$$x_d \equiv \Delta m_d/\Gamma_{B_d} = 0.723 + -0.032. \tag{1.56}$$

From Eqs. (1.56 and 1.14) we integrate of all times and obtains a result for the fraction of $B^0\overline{B}^0$ mesons which decay in a mixed state, χ_d;

$$\chi_d \equiv \frac{1}{2}\frac{x_d}{1+{x_d}^2}. \tag{1.57}$$

Which has been measured to be:

$$\chi_d = 0.174 \pm 0.015. \tag{1.58}$$

Furthermore, from Eqs. (1.55 and 1.56) it is clear that:

$$\Delta\Gamma_B \ll \Delta m_B. \tag{1.59}$$

If we make the approximation that the widths of mass eigenstates are equal ($\Gamma_H = \Gamma_L = \Gamma_B \Rightarrow \Delta\Gamma \equiv 0$), and re-write the time the mixing amplitudes in Eq. (1.14) reduce to:

$$g_+(t) = e^{-iMt}e^{-\Gamma t/2}\cos\Delta m_d t/2 \tag{1.60}$$

$$g_-(t) = e^{-iMt}e^{-\Gamma t/2} i \sin\Delta m_d t/2.$$

Finally, the $\mathcal{CP}$ phase from mixing is dominated by contribution for top quarks in the box diagram and can be calculated quite accurately:

$$\left(\frac{q}{p}\right)_B = \frac{M_{12}^*}{|M_{12}|} = \frac{V_{tb}^*V_{td}}{V_{tb}V_{td}^*}e^{2i\chi_d}. \tag{1.61}$$

These results will be used extensively in the next section to describe how $\mathcal{CP}$ violation arises the in neutral B system.

1.4.6 $\mathcal{CP}$ Violation in the B-System

There exist a myriad of decay channels available to B-mesons, many of which carry contributions from several different diagrams. As such, the overall picture of $\mathcal{CP}$ violation in the B-meson system is very complicated. To broach this subject, we will begin by classifying various types of B decays to $\mathcal{CP}$ eigenstates according to how they might manifest $\mathcal{CP}$ violation.

1. Decays dominated by a single term, such as $b \to s\bar{s}s$ or $b \to c\bar{c}s$. Since the direct $\mathcal{CP}$ violation for such decays is expected to be small, these provide the cleanest method for directly measuring CKM phases via $\mathcal{CP}$ violation in interference.

2. Decays with a large tree level term, and suppressed penguin contributions, such as $b \to c\bar{c}d$ or $b \to u\bar{u}d$. To the extent that direct $\mathcal{CP}$ contribution from the penguin terms can be estimated the asymmetries for these decays can be related to CKM phases.

3. Decays with highly suppressed or null tree contributions, such as $b \to u\bar{u}s$, $b \to s\bar{s}d$ or $b \to /\gamma$. The possibility for relatively large cross terms between various penguins loops and tree diagrams allow several competing $\mathcal{CP}$ violating terms and significantly complicate analyses.

The particular analyses described in this dissertation are of the first type, namely decays with underlying quark content, $b \to c\bar{c}s$. In fact, they are all varieties of $B \to \psi K_S^0$. Such process are all dominated by the internal W tree diagram, and contributes an amplitude ratio:

$$\frac{\bar{A}_{\psi K^0}}{A_{\psi K^0}} = \eta_{\psi k^0}\left(\frac{V_{cb}V_{cs}^*}{V_{cb}^*V_{cs}}\right). \tag{1.62}$$

A critical element of such decays is the subsequent kaon mixing. Since $B^0 \to K^0$ and $\overline{B}^0 \to \bar{K}^0$, we must also consider the contribution to λ from the kaon appearing as a K^0_S rather that a K^0_L:

$$\left(\frac{q}{p}\right)_K = \frac{V_{cs}V_{cd}^*}{V_{cs}^*V_{cd}} e^{-2i\xi_K}. \tag{1.63}$$

So then, taking equations Eqs. (1.62, 1.63 and 1.61) we find:

$$\begin{aligned} \lambda(B \to \psi K^0_S) = &\quad \eta_{K^0_S}\left(\tfrac{V_{td}V_{tb}^*}{V_{td}^*V_{tb}}\right)\left(\tfrac{V_{cb}V_{cs}^*}{V_{cb}^*V_{cs}}\right)\left(\tfrac{V_{cs}V_{cd}^*}{V_{cs}^*V_{cd}}\right) \\ \mathcal{I}\lambda_{\psi K^0_S} = &\quad \sin 2\beta. \end{aligned} \tag{1.64}$$

Alternatively, we can arrive at the result of Eq. (1.64) by observing the relevant $\mathcal{CP}$ phase ϕ_{cp} for such decays is $V_{td}V_{tb}^*V_{cb}V_{cd}^*$. By consulting Fig. 1.4, we see that this corresponds to the angle β. Taking into account a factor of two for the sign change between B^0 and $\overline{B}^0$ finally states, we get:

$$\begin{aligned} \phi_{cp}[\psi K^0_S] = &\quad 2\beta \\ \mathcal{I}\lambda_{\psi K^0_S} = &\quad \sin 2\beta. \end{aligned} \tag{1.65}$$

Finally, we note that it is possible to reproduce the above argument with decays involving an intermediate K^{*0}, provided that the K^{*0} decays to a $\mathcal{CP}$ eigenstate such as $K^0_S\ \pi^0$, rather that a flavor eigenstate such as $K^+\ \pi^-$. However, since the K^{*0} is a vector particle, this decay chain has contributions from different angular momentum states, which must either by separated out or averaged over [33].

1.5 Using B-Meson Decays to Measure $\mathcal{CP}$ Violation

"I thought you just turned on the anti-gravity during earthquakes."
— J. Buetens

Now that we have discussed the origins of $\mathcal{CP}$ violation in the B-meson system, we proceed with a describe of the basic technique used to measure the resulting $\mathcal{CP}$ decay asymmetries.

Some critical observations need to be made at this point.

1. In order to produce coherent $B^0\overline{B}^0$ pairs, the energy in the center of mass (CM) frame must be below the threshold for production of hadronization pions. Otherwise the phase shifts from hadronization process would break the coherence of the B-mesons.

2. Since the lifetimes of B-mesons are too short to resolve temporarily, we can only measure the time structure of $B^0\overline{B}^0$ decays indirectly; by using the distance of flight from creation to decay. In order to do this, the B-mesons must have significant momentum in the lab frame.

Therefore, we immediately conclude that the ideal conditions for studying the time-structure of $\mathcal{CP}$ decays require a CM frame that is boosted relative to the lab frame. This leads immediately to the concept of an asymmetric collider, as discussed in Sec. 2.2.

From that point, these basic steps involved in measuring time-dependent $\mathcal{CP}$ violation with B-mesons.

1. Reconstructing a three samples of B decays, B_{rec}. We reconstruct a measurement sample of B decays to $\mathcal{CP}$ eigenstates (B_{CP}) and two control samples: B^0 decays to flavor eigenstates (B_{flav}), and $B^{\pm}$ decays ($B^{\pm}$). Event selection is described in Chapter 3.

2. Flavor-tagging the non-reconstructed B-meson (B_{tag}) in each event. Flavor tagging is described in Chapter 5.

3. Measuring the proper-time difference Δt between the two B decays (B_{rec} and B_{tag}) in each event. The Δt measurement is described in Chapter 4.

4. Fitting the resulting decay time distributions to extract physics parameters. Various parts of the fitting procedure are discussed in Chapters 3, 4, and 5; however the final fitting procedure and results are presented in Chapter 6.

The rest of this section briefly describes these methods and the experimental issues associated with each part of the process. For clarity and concreteness, we will present this discussion in terms of the decay time Probability Density Functions (PDF's) which will eventually be used to extract sin2β using a maximum likelihood fit.

1.5.1 Decay Time Distributions

The starting point for any eventual fit of the data are the theoretical Δt distribution for different combinations of reconstructed (B_{rec}) and tagged (B_{tag}) B-mesons. In all cases, the Δt distributions for flavor mixing and $\mathcal{CP}$-violating effects that we are studying can be described as complimentary modulations of double-sided exponential $e^{-|\Delta t|/\tau}$.

- For $B^{\pm}$ decays, the decay rate distributions $f_{\pm}$ are simply:

$$\begin{aligned} f_{\pm}(\Delta t, B_{rec}, B_{tag}|\tau_{B^+}) = &\quad (\tfrac{1}{2})_{rec}(\tfrac{1}{2})_{tag}\frac{e^{-|\Delta t|/\tau_{B^+}}}{2\tau_{B^+}} \\ A_{\pm}(\Delta t) = &\quad 0. \end{aligned} \tag{1.66}$$

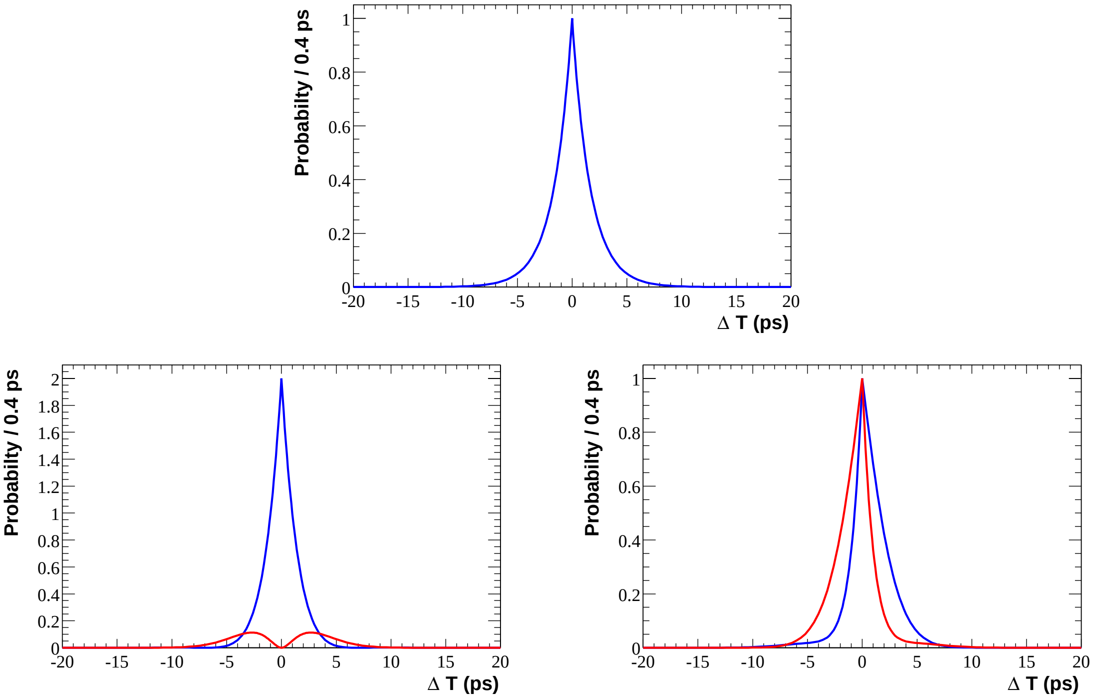

Figure 1.5: *Theoretical decay time difference distributions. Top:* $B^{\pm}$ *events. Bottom left:* B_{flav} *events, unmixed (mixed) event are show as the darker (lighter) line. Bottom right:* $\mathcal{CP}$ *events, events with a* B^0 $(\overline{B}^0)$ *on the tag side are shown as the darker (lighter) line. For all plots we used* $\tau_{B^+} = 1.67$ *ps,* $\tau_{B^0} = 1.54$ *ps,* $\Delta m_d = 0.472 \ \mathrm{ps}^{-1}$ *and* $\sin 2\beta = 0.7$.

- For B^0 decays to flavored states, the decay rate distributions f_{flav} are:

$$\begin{aligned} f_{flav}(\Delta t, B_{rec}, B_{tag}|\tau_{B^0}, \Delta m_d) = & \quad (\tfrac{1}{2})_{rec}(\tfrac{1}{2})_{tag}\frac{e^{-|\Delta t|/\tau_{B^0}}}{2\tau_{B^0}} \\ & \times[1 + S_{mix}\cos\Delta m_d \Delta t] \\ A_{flav}(\Delta t) = & \quad \cos(\Delta m_d \Delta t), \end{aligned} \tag{1.67}$$

  where $S_{mix} = +1(-1)$ for unmixed (mixed) events.

- Finally, for decays to $\mathcal{CP}$ eigenstates, the decay rate distributions f_{cp} are:

$$\begin{aligned} f_{CP}(\Delta t, B_{tag}|\tau_{B^0}, \Delta m_d, \lambda) &= (\frac{1}{2})_{tag}\frac{e^{-|\Delta t|/\tau_{B^0}}}{2\tau_{B^0}} \\ & \times[1 - \eta_f{}^{\cdot}S_{cp}\sin 2\beta\ \sin(\Delta m_d \Delta t)] \\ A_{CP}(\Delta t) &= -\eta_f \sin 2\beta\ \sin(\Delta m_d \Delta t), \end{aligned} \tag{1.68}$$

  where $S_{cp} = +1(-1)$ for events where the B_{tag} is a B^0 ($\overline{B}^0$), and we have made use of the fact that $|\lambda| \sim 1$.

All three of these distributions are shown in Fig. 1.5.

Clearly, all of three of these distributions are of the general form:

$$f(\Delta t) = f_0(\Delta t)[1 \pm f_{mod}(\Delta t)] \tag{1.69}$$

where

$$f_0(\Delta t) = \frac{e^{-|\Delta t|/\tau}}{2\tau} \tag{1.70}$$

and $f_{mod}(\Delta t)$ depends on the type of event. This particular formulation will be quite useful later.

1.5.2 Reconstructing the $\mathcal{CP}$ Sample

As we can see from Eqs. (1.66, 1.67 and 1.68), the decay time distribution of B-mesons varies depending on the $\mathcal{CP}$ and flavor properties of the decay channel of the event.

Furthermore, given the relative rarity (branching ratios of $O(10^{-3})$) of decays to $\mathcal{CP}$ eigenstates, is not possible to extract a completely pure sample of such events. The selected $\mathcal{CP}$ event sample is inevitably contaminated by backgrounds from a variety of sources.

Therefore, from the point of view of extracting physics information from a selected event it is expedient to construct the probability that the event of the signal type as a function of a discrimination variable m. In terms of the signal $\mathcal{G}$ (m) and background $\mathcal{A}$ (m) distributions we have:

$$\begin{aligned} P_{sig}(m) &= f_g \times \frac{\mathcal{G}(m)}{\mathcal{G}(m)+\mathcal{A}(m)} \\ P_{bkg}(m) &= (1-f_g) \times \frac{\mathcal{A}(m)}{\mathcal{G}(m)+\mathcal{A}(m)} \end{aligned} \tag{1.71}$$

where f_g is the fraction of signal events in the entire sample. Furthermore, if we denote the parameters of $\mathcal{G}$ and $\mathcal{A}$ by $\hat{\beta}$ then the combined probability to observe an event with $m, \Delta t$ given a particular set of physics quantities $\hat{\gamma}$ (sin2β, Δm_d, τ) is:

$$F(m, \Delta t\ ; \hat{\beta}, \hat{\gamma}) = P_{sig}(m; \hat{\beta}) \times f_g(\Delta t\ |\hat{\gamma}) + P_{bkg}(m; \hat{\beta}) \times f_{bkg}(\Delta t), \tag{1.72}$$

where $f_{bkg}(\Delta t)$ is the Δt distribution for background events.

Thus, to properly account for the presence of backgrounds in our event sample we will need to:

1. Preselect signal enriched events.

2. Define a variable for discriminating signal events: m.

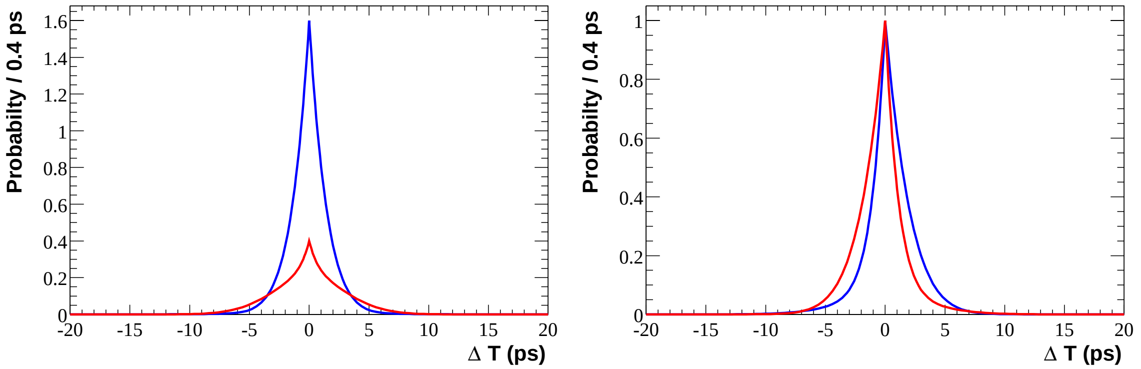

Figure 1.6: *Decay time difference distributions for* $B^0\overline{B}^0$ *with "realistic" tagging performance. The left plot show the distributions for* B_{flav} *events tagged as unmixed (mixed) as the darker (lighter) line. The right plot shows the distributions for* $\mathcal{CP}$ *events with a* B^0 *(*$\overline{B}^0$*) on the tag side as the darker (lighter) line.*

3. Measure the signal and background distributions of m on the preselected events.
4. Model the Δt distributions for background events which pass the pre-selection.

The first three items are described in Chapter 3, while the last is described in Secs. 4.6.1 and 5.5.2.

1.5.3 B Flavor Tagging

After reconstructing a B decay to a $\mathcal{CP}$ eigenstate, we need to determine the flavor of the other B (B_{tag}) in the event. We do this by looking for one of several decay signatures (such as leptons from semi-leptonic decays) which would indicate the flavor of B_{tag}. In practice, tagging is complicated as we must consider a variety of possible decay signature with different power for separating B^0 and $\overline{B}^0$ tag-side decays.

Given a "tagging variable" x derived from such an analysis, we can construct the probability that the B_{tag} in a particular event decayed as a B^0 or as a $\overline{B}^0$ as a function of

x:

$$P(B^0|x) = \frac{f(x)}{f(x)+\bar{f}(x)} \tag{1.73}$$
$$P(\overline{B}^0|x) = \frac{\bar{f}(x)}{f(x)+\bar{f}(x)},$$

where

$$f(x) \equiv f(x|B^0) \tag{1.74}$$

$$\bar{f}(x) = f(x|\overline{B}^0). \tag{1.75}$$

Furthermore, in analogy to Eq. (1.72) the combined probability to observe an event with $x, \Delta t$ given $\hat{\gamma}$ is:

$$\mathcal{F}(x, \Delta t\ |\hat{\gamma}) = f(x) \times f(\Delta t\ |\hat{\gamma}, B^0) + \bar{f}(x) \times f_(\Delta t\ |\hat{\gamma}, \overline{B}^0) \tag{1.76}$$

A significant complication arises because we do not know *a priori* the flavor of the tagging meson or $f(x|B^0)$ and $f(x|\overline{B}^0)$. This is particular important since sin2β is simply the magnitude of the undiluted decay asymmetry. Therefore any error in modeling the tagging performance translates directly to an error on sin2β. In Chapter 5 we describe how we use the data to extract $f(x)$ and $\bar{f}(x)$.

The non-perfect tagging performance has the effect of washing out asymmetries. To illustrate this, decay time difference distribution with the effects of tagging are shown in Fig. 1.6.

1.5.4 Δt Reconstruction

In order to be able to study the decay time distributions it is of course crucial to measure the proper time difference between the decays of the two B mesons. In principle it is not

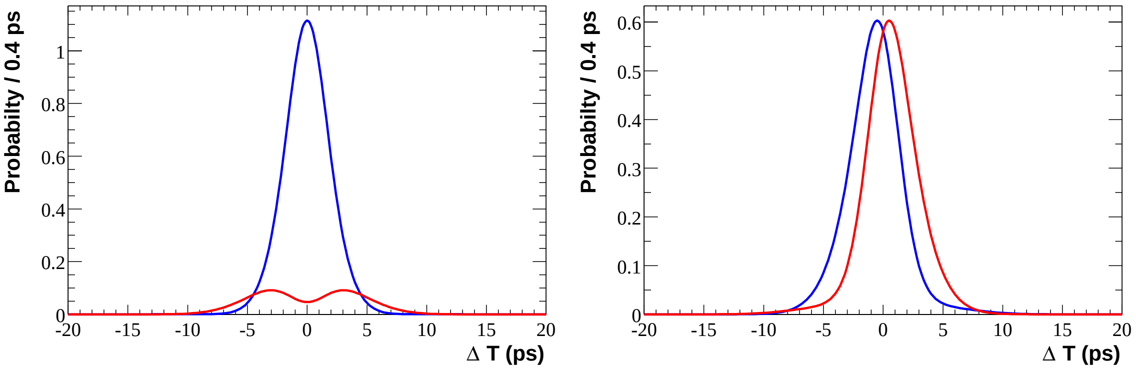

Figure 1.7: *Decay time difference distributions for* $B^0\overline{B}^0$ *with "realistic" vertexing performance. The left plot show the distributions for* B_{flav} *events tagged as unmixed (mixed) as the darker (lighter) line. The right plot shows the distributions for* $\mathcal{CP}$ *events with a* B^0 $(\overline{B}^0)$ *on the tag side as the darker (lighter) line.*

possible to do this with perfect accuracy. Therefore we must model our Δt reconstruction with a resolution function $R(\delta\Delta t)$ and resolution parameters $\hat{\alpha}$.

$$\begin{aligned} \delta t \equiv & \quad \Delta t - \Delta t_{true} \qquad (1.77) \\ R(\delta t;\hat{\alpha}) \equiv & \quad f(\delta t) \\ f(\Delta t) = & \quad R(\delta t;\hat{\alpha}) \otimes f(\Delta t_{true}) \end{aligned}$$

In chapter 4 we describe how we use the data to extract $R(\delta t)$.

The non-perfect vertexing performance has the effect of washing out asymmetries. To illustrate this, decay time difference distributions with the effect of detector resolution are shown in Fig. 1.7.

Parameter	Event Samples	Value
τ_{B^+}	$B^{\pm}$	$1.548 \pm 0.032\,\mathrm{ps}$
τ_{B^0}	B_{flav}, $\mathcal{CP}$	$1.653 \pm 0.028\,\mathrm{ps}$
Δm_d	B_{flav}, $\mathcal{CP}$	$0.472 \pm 0.017\,\mathrm{ps}^{-1}$
sin2β	$\mathcal{CP}$	-

Table 1.2: *Physics parameters measured; with relevant event samples and current world averages..*

1.5.5 Extracting sin2β From the Decay Time Distributions

So the final decay time distribution, accounting for detector resolution and tagging dilutions will have the form:

$$\begin{aligned} f(\Delta t, x, m; \hat{\alpha}|\hat{\gamma}) = \;& f_{sig}(m) \times \mathcal{F}(x, \Delta t\ |\hat{\gamma}) \otimes R_{sig}(\delta\Delta t; \hat{\alpha}) \\ & + f_{bkg}(m) \times [f_{bkg}(\Delta t, x)] \end{aligned} \tag{1.78}$$

We use the $B^0\overline{B}^0$ decays to "tagging" states (B_{flav} sample) to measure the tagging performance. By simultaneously fitting the "mixing" (Eq. (1.67)) and "$\mathcal{CP}$ " (Eq. (1.68)) time distributions, we use the time dependence of the mixed-unmixed asymmetry to the constrain our model of the tagging performance. This technique takes advantage of the knowledge that the mixing asymmetry has unit amplitude.

Furthermore, we also use all three event samples to constrain the Δt resolution function. Doing so takes advantage of precision measurements of B-lifetimes.

In order to correctly use out calibration samples and also to properly fit sin2β we require accurate knowledge of the B lifetimes and Δm_d. In fact, we can also use the B_{flav} and $B^{\pm}$ calibrations samples to help extract these quantities. Tab. 1.5.5 lists the various physics parameters we will consider, as well as sensitive event samples and current world averages for each.

We will use a maximum likelihood fit to extract the physics quantities of interest. In fact, we will use a simultaneous fit to all three data samples ($\mathcal{CP}$, B_{flav}, and $B^{\pm}$). As such, our likelihood function will consist of:

$$\mathcal{L} = \mathcal{L}_{\mathcal{CP}} + \mathcal{L}_{flav} + \mathcal{L}_{\pm}. \tag{1.79}$$

Chapter 2

The *BABAR* Detector

"Green pants"
— M. Bland, "Salient Features of Elephants"

This chapter provides a brief description of the experimental apparatus; namely the PEP-II storage ring and the *BABAR* detector. As such, the main goals of this chapter are:

- to show how the experimental design was motivated by physics goals;
- to detail aspects of detector performance that are relevant to the measurements described in this dissertation;
- to describe those aspects of the data acquisition, processing and storage that are directly relevant to the analyses described in this dissertation.

A much more complete description of the Pep-II storage ring and *BABAR* detector are available in [35].

For now we start with statements of the requirements for both the accelerator and the detector in Sec. 2.1. We then proceed with descriptions of the accelerator and various subdetectors in Sec. 2.2 to Sec. 2.10. We will describe various design considerations, briefly detail the reconstruction algorithms used on the data, and compare measured and expected performance. Finally, we will give a brief overview of the computing infrastructure which transforms the data to a form suitable for physics analysis in Secs. 2.11, 2.12 and 2.13.

2.1 Accelerator and Detector Requirements

> *"Летит, жужжит, сверкает. . ."*
> — I.Zaks and B.Ratinov

Experimentally, the most fundamental point about studying $\mathcal{CP}$ violation in the $b\bar{b}$ system is that such studies require isolating events in rare decay channels. This is a direct consequence of the statement made in Sec. 1.4.5 that only a very small fraction of neutral B-mesons decay to $\mathcal{CP}$ eigenstates.

1. Large $\mathcal{CP}$ asymmetries may be measured at the 10% level with a few hundred events in the appropriate channel.

2. Exclusive B-meson final states useful for $\mathcal{CP}$ measurement smal have branching ratios, *eg.* $\sim 10^{-5}$ for $J/\psi K^0_S$.

3. The cross section for $b\bar{b}$ production at the $\Upsilon(4S)$ resonance is $\sim 1\,\mathrm{nb}$.

4. We expect a 10 year experimental run, with $\sim 10^7$ s of data taken each year.

These numbers imply that the collider should produce in excess of 10^7 $B^0\bar{B}^0$ pairs. Given the cross section and length of the experimental run, this sets a design luminosity of a few $\times 10^{33}\,\mathrm{cm}^{-2}\mathrm{s}^{-1}$. As a figure of comparison, the CESR storage ring at Cornell achieved a record luminosity of $\mathcal{O}(10^{33}\,\mathrm{cm}^{-2}\mathrm{s}^{-1})$.

Independently of the nature of the accelerator, the detector must fulfill certain requirements dictated by the nature of B-meson decays and by the goal of measuring time-dependent

B decays. To understand these requirement, let us first re-iterate the basic ingredients of measuring a time-dependent asymmetry as described in Sec. 1.5.

1. Isolating a sample of B-meson decays both to $\mathcal{CP}$ eigenstates and to "tagging" states by full reconstruction.
2. Flavor tagging the non-reconstructed B-meson in each event by looking at the topology and nature of the remaining particles in the event
3. Reconstructing Δt, the difference in proper time between the decays of the two B-mesons in each event.

Since B-mesons decay in a myriad of channels, only a few of which it is feasible to exclusively reconstruct, good detection and resolution of the energy and momentum of particles in the detector is essential in isolating a clean sample of events for further studies. Thus, exclusive reconstruction implies these requirements.

1. Charged particle tracking down to $p_t \sim 60\,\mathrm{MeV}/c$.
2. Photon and π^0 detection over the range $\sim 20\,\mathrm{MeV} < E <\sim 5\,\mathrm{GeV}$.
3. A minimal amount of material in the active region, so as to avoid resolution loss due to multiple scattering.
4. Particle identification with good π-K separation to distinguish between final states such as $B^0 \to \pi^+\pi^-$ and $B^0 \to K^\pm\pi^\mp$ and to control background in reconstruction of cascade D-meson decays.
5. The ability to identify neutral hadrons for reconstructing channels such as $B^0 \to J/\psi\, K^0_L$.

For the purposes of flavor tagging the crucial requirement is discrimination between e, μ, π, K and p over a wide kinematic range.

The time scale of interest for studying $\mathcal{CP}$ violation is set by the B and D-meson lifetimes, $\mathcal{O}(1\,\mathrm{ps})$. For relativistic particles this implies a length scale of $\mathcal{O}(300\,\mu\mathrm{m})$. Clearly it is desirable for the vertex resolution to be significantly smaller.

2.2 The PEP-II Asymmetric Collider

"Il collisione des montres suisses et parfois ca donne des avions."
— K. Oddoux

There exist several excellent reasons for using an asymmetric e^+e^- collider operating at the $\Upsilon(4S)$ to study $\mathcal{CP}$ violation in the B-meson system [37, 38].

1. The low Q-value of the $\Upsilon(4S) \to B^0\overline{B}^0$ decay implies that the B-mesons are produced essentially at rest in the center of mass frame. This simplifies the event topoplogies.

2. The beam energy asymmetry produces a moving center-of-mass system in the laboratory frame which allows the B meson decay lengths to be measured, as discussed in Sec. 1.5.

3. The $\Upsilon(4S)$ mass is below the threshold for the production of any fragmentation products in decays to $B^0\overline{B}^0$. Cosequently, B-mesons are produced in coherent pairs. As describe in Sec. 1.2.3 this is a huge aide in measuring the decay time structure.

4. The absence of fragmentation products also implies that certain kinematical quatities such as the four-momenutum of the $B^0\overline{B}^0$ system and the momentum magnitudes of the B-mesons in the center-of-mass frame are precisely constrainted. Such constraints are extremely useful in background suppresion.

5. There is a high signal-to-background ratio with $\sigma_{\overline{b}}/\sigma_{TOT} \simeq 0.28$

6. The events are very clean compared to hadronic colliders, having a charged track multiplicity of ~ 11. This allows measurements to be made in many more channels.

7. Even with high luminoisties, the interaction rate is low. Physics events occur at ~ 10 Hz. This reduces the radiation dose suffered by the innermost detector component, the dataflow bandwith requiremenst, and the readout trigger requirements.

These advantages having been enumerated, we proceed with a description of the PEP-II accellerator.

2.2.1 PEP-II Description and Cross-Sections

We list here the basic feature of the PDP-II storage ring.

1. PEP-II consists of two 400 m diameter storage rings with counter-rotating beams. The High Energy Ring (or HER) stores 9 GeV electrons while the Low Energy Ring (or LER) stores 3.1 GeV positrons. These energies produce a boost in the laboratory frame for the resulting B-mesons of $\beta\gamma = 0.56$.

2. Both types of particles are injected into the machine from the SLAC linac.

3. The design luminosity goal is $3 \times 10^{33}\,\mathrm{cm}^{-2}\mathrm{s}^{-1}$. At the densities required to achieve the design luminosity, the beams have a lifetime on the order of ~ 1 hour.

Taking into account the experimental acceptance, the effective cross-sections for the production of fermion pairs at the $\Upsilon(4S)$ are shown in Tab. 2.2.1 [39]. The uncertainty on these value is less than 0.1 nb.

$e^+e^- \to$	Cross-section (nb)
$b\bar{b}$	1.05
$c\bar{c}$	1.30
$s\bar{s}$	0.35
$u\bar{u}$	1.39
$d\bar{d}$	0.35
$\tau^+\tau^-$	0.94
$\mu^+\mu^-$	1.16
e^+e^-	~ 40

Table 2.1: *Production cross-sections at* $\sqrt{s} = M(\Upsilon(4S))$..

Clearly, at a luminosity of $3 \times 10^{33}\,\mathrm{cm}^{-2}\mathrm{s}^{-1}$ these numbers imply a total hadronic event rate of ~ 10 Hz.

Finally, there remains the outstanding issue of the magnitude of the boost from the lab to the center of mass frame. Selecting the best boost for physics performance requires balancing two conflicting effects.

1. The average B flight distance and thus the average Δz is $\sim \gamma\beta c\tau$, where $\gamma\beta$ is the magnitude of the Lorentz boost. Thus increasing the boost increases the B decay vertex separation and makes it easier to resolve the two vertices.

2. The asymmetric beam energies cause the decay products to be boosted forward in the laboratory frame, thus decreasing the acceptance in the center of mass frame. Furthermore, the high luminosity of PEP-II requires accelerator components and produces high radiation levels very close to the interaction region. Both of these facts preclude placing active detector elements very close to the interaction point and limit the detector acceptance. Therefore, choosing too large a boost could degrade physics performance by allowing too many particles to escape undetected through the dead

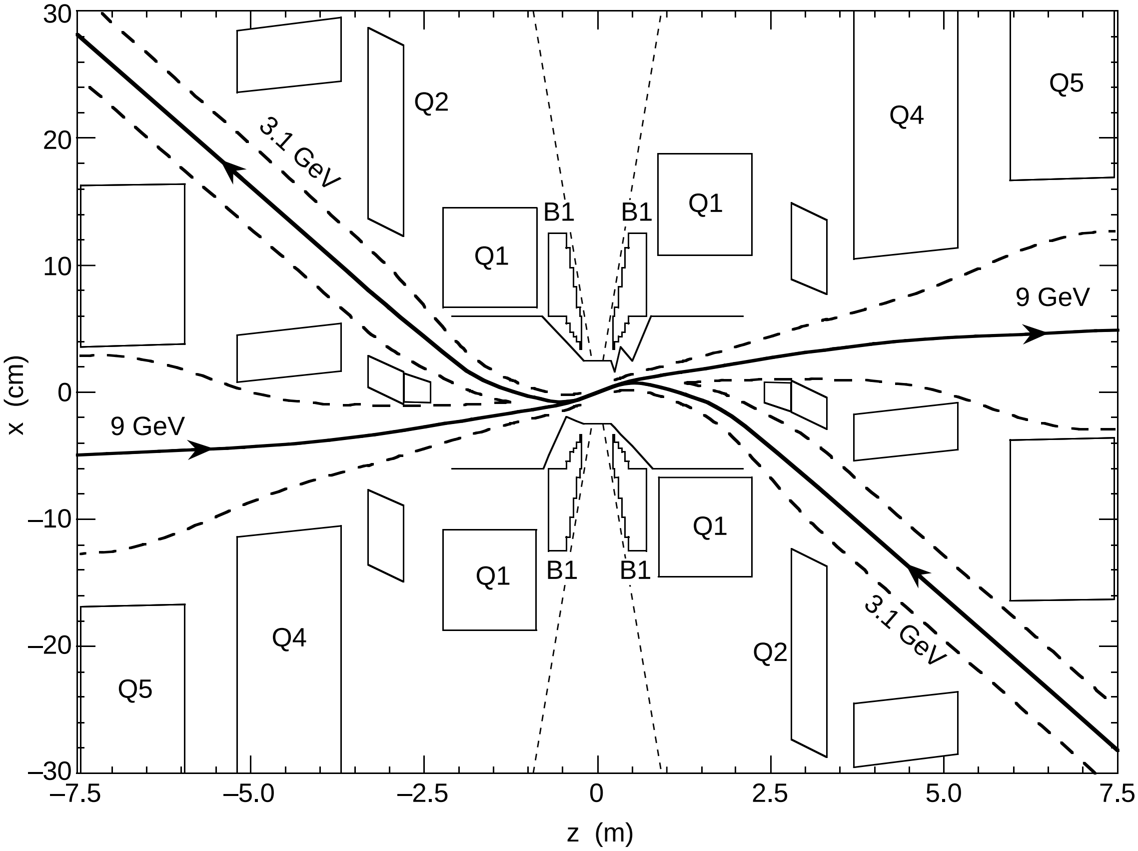

Figure 2.1: *A plan view of the interaction region. The vertical scale is exaggerated. The dashed lines indicate the beam stay-clear envelopes and the detector acceptance cutoff at 300mr.*

region near the forward beam axis.

2.2.2 The Interaction Region

The high luminosity and asymmetry of the PEP-II machine require an unconventional interaction region design. The layout of the interaction region is shown in Fig. 2.1 [36].

From the point of view of the work described in this dissertation, the primary point is that there are several magnets located in what would be active detection volume in most other collider physics detectors.

The reasons for these magnets are.

1. The primary impediment to achieving currents of the required magnitude are beam-beam interference effects and related beam instabilities.
2. Such beam-beam effects can be reduced by dividing the circulating charge into a large number of low charge bunches spaced by 124 cm.
3. Therefore, the two beams must be brought together and re-separated within 62 cm of the interaction point (IP) to avoid spurious collisions between out of phase bunches.
4. Furthermore, strong focusing of the beams near the IP is required to obtain design luminosity.

Collision and re-separation is achieved by placing bending dipoles(B1) 20 cm from the IP in both directions to displace the beams horizontally. Because of the energy asymmetry, the two beams are deflected different amounts and miss each other at the potential spurious interaction points. The B1 magnets are entirely within the *BABAR* detector volume. In fact, the SVT is mounted on them.

Strong focusing of the beams is achieved by an array of focusing quadruples near to the IP. Most importantly, the innermost focusing magnet (Q1) is common to both beams and partially enters the detector volume. Furthermore the support tube for the Q1 magnets runs through the center of the detector between the DCH and the SVT.

Finally we note that the detector axis and the collision axis are not exactly coincident. Rather, the collision axis is offset by 20 mrad about the vertical so as to reduce orbit distortion effects due to the the effect of the detector's solenoidal magnetic field on the outgoing beams.

2.2.3 Machine Backgrounds

As stated above, the beam currents at PEP-II are much larger that in existing accelerators. Consequently, a major challenge to achieve background rates similar to those of existing colliders while circulating an order of magnitude higher beam currents. If the background is too high, the detector can suffer from excessive occupancy and/or radiation damage.

The major points about the machine backgrounds are.

1. The background is not uniform, but much higher in the plane of the PEP-II rings. This is because synchrotron radiation is emitted along the beam direction during bending and focusing.
2. The silicon detector performance will degraded steadily with integrated dose; complete failure due to type inversion is expected at about 2 MRad.
3. While under bias, the various electronics can be damaged by very high instantaneous doses, of the type associated with beam injection and beam loss event.

An interlock and beam abort system has been implemented to monitor the radiation level and protect the detector.

Tab. 2.2.3 lists some important background radiation parameters. In particular we note that the occupancy in the inner layer of the detector can be very high. Such high occupancies significantly increase the difficulty of reconstruction the events and generally degrade performance.

2.3 Detector Overview

"Physicists are so lucky, all those cool toys."

	Silicon Tracker		Drift Chamber	
	Average	First layer	Average	First layer
Occupancy	1.3%	3.0%	0.05%	0.5%
Limit	20%	20%	10%	10%
Rad. dose (yr)	33 krad	82 krad	4×10^{-4} C/ cm	4.5×10^{-3} C/ cm
Limit	1500 krad	1500 krad	0.1 C/ cm	0.1 C/ cm

Table 2.2: *Occupancy levels and radiation doses from lost beam particle backgrounds in the tracking system of the BABAR experiment..*

Parameter	Value [36]
Tracking coverage ($/4\pi$)	0.92
σ_{p_t}/p_t (%) (1 GeV pions at 90°)	0.36
σ_{z_0} (μm) (1 GeV pions at 90°)	52
Calorimetry coverage ($/4\pi$)	0.90
X_0 in front of Calorimeter (at 90°)	0.25
σ_E/E (%) (1 GeV γ at all angles)	1.8
γ efficiency within acceptance (at 100 MeV)	0.92
Charged Hadron ID coverage ($/4\pi$)	0.84

Table 2.3: *Detector design performance parameters. Acceptance coverages are quoted for the center of mass system..*

— C. Perkins

The *BABAR* detector was designed to fulfill all of the requirements describe in Sec. 2.1. A cut-away picture of the detector is shown in Fig. 2.2, and the most salient detector parameters are shown in Tab. 2.3.

There are several *BABAR* subsystems.

1. The Silicon Vertex Tracker (SVT) is a silicon micro-strip detector designed to provide very accurate position information for charged tracks. Additionally, it is the primary tracking device for charged particles with momentum below $\sim 130\,\mathrm{MeV}$, and has some

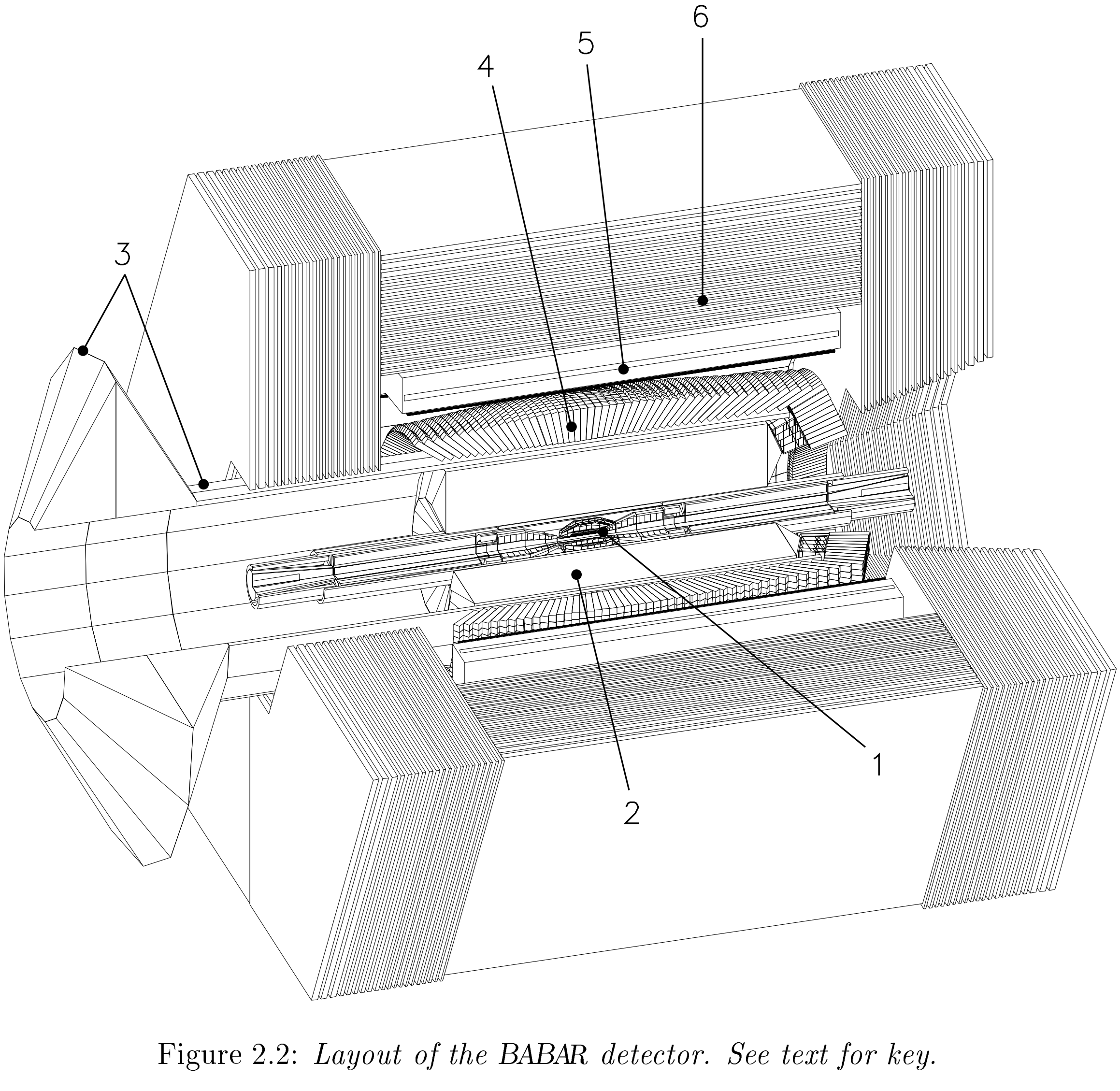

Figure 2.2: *Layout of the BABAR detector. See text for key.*

particle identification power through specific ionization ($\mathrm{d}E/\mathrm{d}x$) measurements.

2. The Drift Chamber (DCH) is a wire chamber with helium based gas mixture. It provides the primary tracking device for most charged particle. It also contributes $\mathrm{d}E/\mathrm{d}x$ information.
3. The Detector of Internally Reflected Cherenkov light (DIRC) is an imaging Cherenkov detector designed for charged hadron particle identification.
4. The Electromagnetic Calorimeter (EMC) is a cesium-iodide crystal calorimeter. It is designed to detect neutral electromagnetic particles and to provide particle identification information based on energy deposition topologies.
5. A super-conducting solenoid produces a 1.5T magnetic field for p_t measurement.
6. The Instrumented Flux Return (IFR), serves as the return yoke for the magnetic field, and provides muon and neutral hadron identification.

In addition to the hardware components of the detector, significant resources are required to be acquire, process, store, and analyze the data.

2.4 The Silicon Vertex Tracker

> *"It will take four months to complete: June, July, September, October."*
> — F. Forti

The innermost *BABAR* sub-detector is the Silicon Vertex Tracker (SVT). The primary purpose of the SVT is to reconstruct the B-meson decay vertices so that the time difference between them can be measured. The active elements of the SVT are silicon microstrip detectors. Their geometry, layout and design parameters are detailed in Sec. 2.4.1. The SVT data readout chain is briefly described in Sec. 2.4.2, and the performance of the SVT is detailed in Sec. 2.4.4.

There are several major design considerations for the SVT.

1. The mean B vertex separation at PEP-II is $\sim 250\,\mu$m. Monte Carlo studies show [41] that measurements of quantities such as time-dependent asymmetries, B flavor mixing and B lifetime measurements require the relative vertex resolution to be better than 50%. This corresponds to a single vertex resolution of better than $80\,\mu$m.

2. Multiple scattering limits the track resolution for the SVT, independent of the point resolution. Studies show that point resolutions 10-15 μm (30-40 μm) in the inner (outer) layers give intrinsic track resolutions comparable to the multiply scattering limit for 700 MeV/c p_T tracks at 90° [42].

3. The innermost points on a track will always provide the most vertex information, owing both to a smaller lever arm and less multiple scattering.

4. Charged particles with $p_T < 130\,\text{MeV}/c$ do not penetrate far enough to be reconstructed in the DCH. Such tracks must be reconstructed using only information from the SVT.

5. The DIRC performance depends crucially on accurately measuring z and polar angles high momentum tracks, so that they may be accurately projected into the DIRC, in order to correctly reconstruct the Cherenkov ring. For many momentum regimes the resolution on these quantities is dominated by the SVT.

To fulfill these goals, SVT has 5 layers of silicon microstrip detectors. The inner two

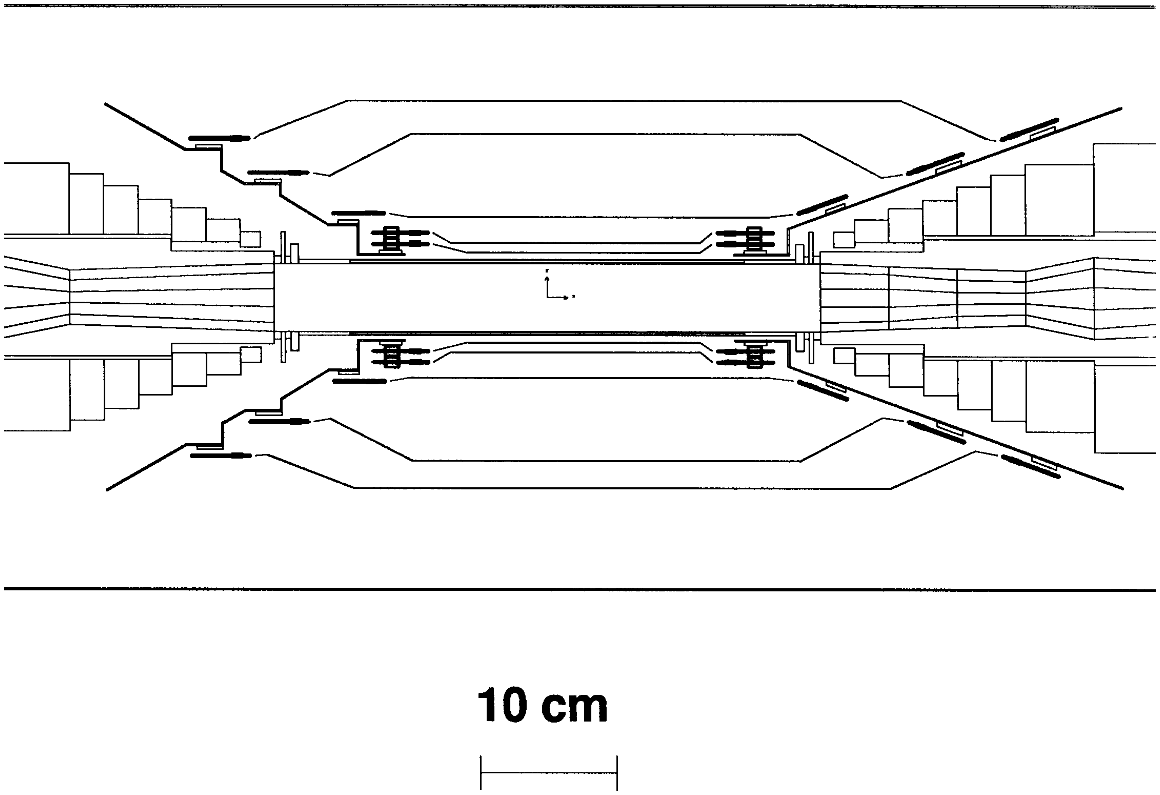

Figure 2.3: *Cross-sectional view of the BABAR Silicon Vertex Tracker in a plane containing the beam axis.*

layers are the most important for impact parameter measurements since they are the closest to the interaction point. The outer two layers are useful for alignment with tracks detected in the drift chamber. The middle layer gives extra tracking information, particularly for charged particles that do not reach the drift chamber. A study was made to determine how best to optimize the resolution of the different layers and can be found in [42].

2.4.1 SVT Detector Layout

As stated about, the SVT consists of five concentric cylindrical layers of double-sided silicon detectors. The layout is shown in Figs. 2.3 and 2.4. There are several important features of

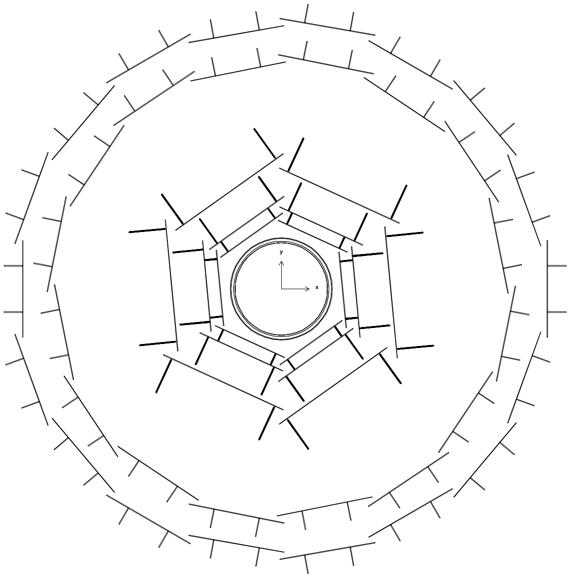

Figure 2.4: *Cross-sectional view of the BABAR Silicon Vertex Tracker in the plane orthogonal to the beam axis.*

the SVT layout.

1. Each layer consists of several modules evenly spaced about the azimuth. The layers have 6, 6, 6, 16 and 18 modules respectively.

2. While the inner layers are fully cylindrical, the modules in the outer layer have an arch-like structure which increases the solid angle coverage and reduces the track incidence angles in the polar regions.

3. Each module is divided into forward and backward half-modules which are kept electrically isolated from one another.

4. The half-modules each contain between two and four detectors, depending on which layer they are situated in.

Layer	1	2	3	4a	4b	5a	5b
Radius (mm)	32	40	54	124	127	140	144
Modules/Layer	6	6	6	8	8	9	9
Wafers/Module	4	4	6	7	7	8	8
Readout pitch (μm)							
ϕ	50	55	55	80–100		80–100	
z	100	100	100	210		210	
Intrinsic Resol.(μm)							
ϕ	10	10	10	10–12		10–12	
z	12	12	12	25		25	

Table 2.4: *Some parameters of the SVT layout..*

5. The inner sides of the detectors have strips running perpendicular to the beam direction to measure the z coordinate, while the outer sides have strips orthogonal to the z strips to measure the ϕ coordinate.

6. In total there are 340 silicon detectors covering an area of $\sim 1\,\text{m}^2$ and about 150,000 readout channels. The parameters of each layer are shown in Tab. 2.4.1.

7. The inner two layers are the most important for impact parameter measurements since they are the closest to the interaction point. Thus they require good point resolution. For this reason the $\phi(z)$ strips in the inner have a inter-strip pitch of $50(100)\,\mu$m.

2.4.2 SVT Readout

Like all silicon microstrip detectors, the SVT modules function by measuring a current induced by the production of ionization electrons in the silicon substrate of the detectors. Each of the SVT detectors is $300\,\mu$m thick, implying an average ionization of about $22000e^-$ or $3.5fC$ for a minimum-ionizing particle.

The induced signals from the strips are amplified and shaped before being compared with a threshold. The time which a signal spends over the threshold is approximately logarithmically related to the charge induced on the strip. An advantage of this "time over threshold"(TOT) method is a re-mapping of the dynamic range due to the logarithm relationship. More information about smaller signals is available, which is exactly what is needed both for better position determination and particle identification.

The number of channels, occupancy from electronics noise and beam-induced backgrounds, and bandwidth limitations preclude transferring every hit of the detector. Rather, the threshold state of each channel is polled every $66ns$ and temporarily buffered in anticipation of a transfer request generated by a level 1 trigger.

Subsequent to a level 1 trigger accept, channel, timestamp and TOT information for each hit is digitized and transferred to the off-detector electronics for inclusion in the event-building process.

2.4.3 SVT Reconstruction

Several steps are performed on the SVT data before they are used in track-making:

1. Application of TOT calibration on the strip level; the ionized charge is calculated separately for every single strip.

2. Clustering of adjacent strips with hits near the trigger time. The cluster position is calculated as the centroid of the charge deposited. Using the centroid has been shown to improve the spatial resolution for two-strip clusters.

3. Rejection of clusters whose total charge is less than about 25% of that expected from a minimum ionizing particle. This rejects hits from electronics noise and low energy

photons from beam-backgrounds.

The use of the SVT data in track finding and fitting is described in Sec. 2.6.

2.4.4 SVT Performance

The SVT has performed very well from the begin of data taking to present. The only significant performance problems are associated with data-readout sections which were failed during the installation process, either from insufficient static-electric precautions, or from broken electrical connections. In all 10 (out of 204) readout sections have failed thus far.

Fig. 2.5 shows the uniform high efficiency throughout the SVT. As stated in Sec. 2.4 the measured efficiency of over 95% permits stand-alone track-finding in the SVT. Furthermore, Fig. 2.5 also show the single hit resolution for z and ϕ hits respectively. These measures are near or better than design specifications.

2.5 The Drift Chamber

"We mentioned that David invented the T.P.C. [Time Projection Chamber] and he started talking about Star Trek."
— B. Cederstrom

The *BABAR* drift chamber is the primary tracking device of the detector. As such, it must be able to accurately reconstruct events having 12 or more charged tracks, even in the presence of beam-related backgrounds. The DCH functions by collecting electrons ionized by the passage of charged particle through a gas mixture [43]. Secs. 2.5.1 and 2.5.2 respectively describe the layout and electronics readout of the DCH. A more detailed description can of these features may found in Ref.[44]. Finally, the current performance of the DCH is described in Sec. 2.5.4.

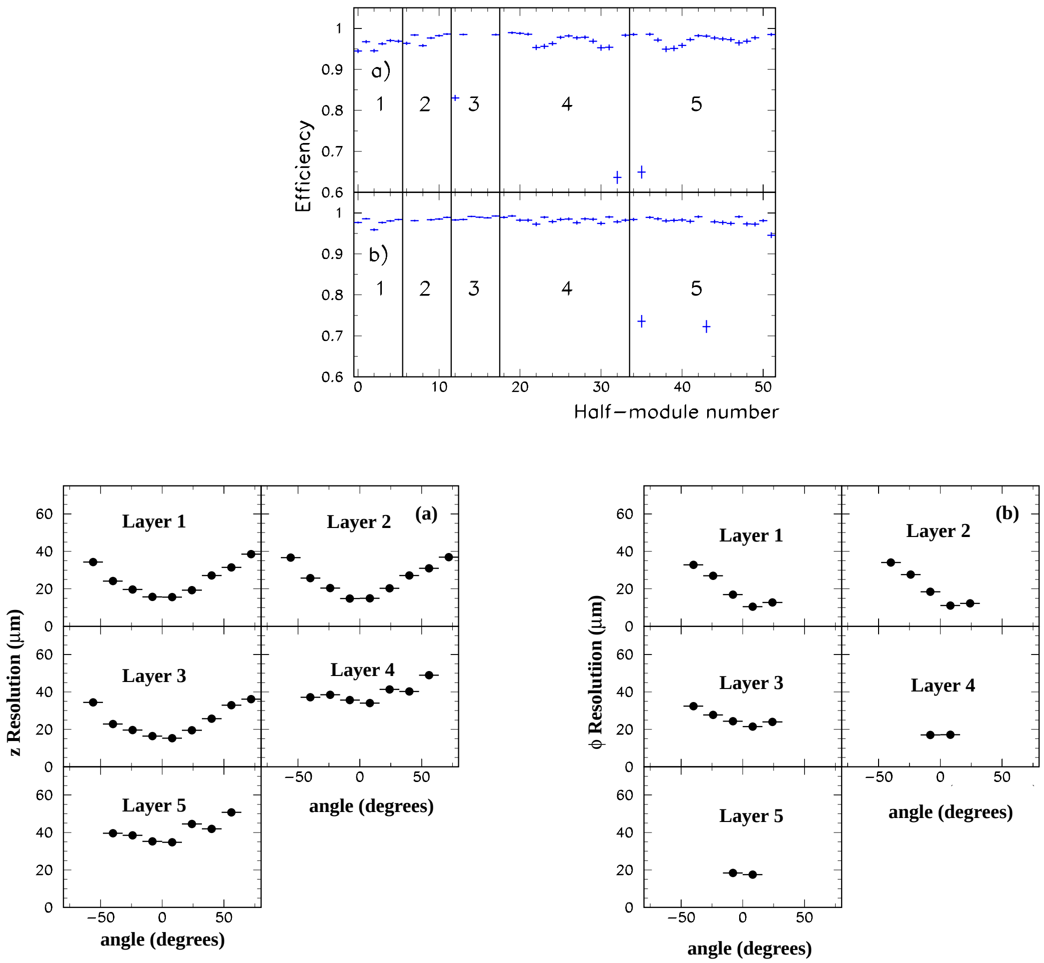

Figure 2.5: *SVT performance plots. The top plot shows the single hit efficiency across the SVT, the bottom plots show the z (left) and ϕ (right) single hit resolutions by layer and incident angle. All three plots are for a typical run (14558)*

Before we move on to the details, we list the major design considerations for the DCH are.

1. It must be highly efficient for charged tracks with a transverse momentum of greater than 130 MeV/c. In part, this means that the DCH must have an angular acceptance right down to the machine components at 300 mrad.

2. In order to be able to accurately propagate tracks both inwards to the SVT and outward to the DIRC, the DCH spatial resolution in $x - y$ for single hits must be better than 140 μm.

3. In order to provide accurate PID information for low momentum tracks which do not reach the outer sub-detectors, the DCH must measure dE/dx through ionization with a resolution of 7%.

4. In order to accurately reconstruct B decays, the DCH must achieve momentum resolution of $\sigma p_T \approx 0.3\% \times p_T$ for tracks with $p_T > 1$ GeV/c.

5. So as not to compromise the performance of the outer sub-detectors, the DCH must present a minimal amount of material. Thus, it was built using lightweight materials and uses a helium based gas mixture. Furthermore, the readout electronics are mounted on the rear end-plate in order to reduce the amount of material in the forward region.

6. Finally, the drift chamber serves as one of the principle inputs for the triggers.

2.5.1 DCH Detector Layout

We list here the basic dimensions of the drift chamber.

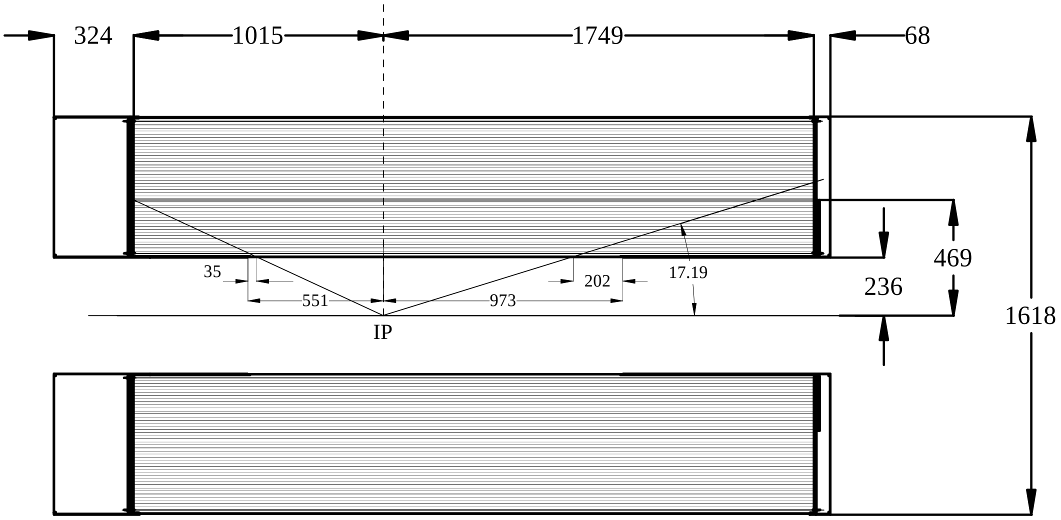

Figure 2.6: *A side view of the BABAR drift chamber. The offset in z with respect to the IP is to take account of the collision asymmetry. All dimensions are in mm.*

1. It is a 280 cm long cylinder.
2. The inner radius is 23.6 cm and an outer radius of 80.9 cm.
3. The end-plates are made of aluminum with the forward (backward) end-plate being 12 mm (24 mm) thick.
4. The inner cylinder is 1 mm or 0.28% X_0 of beryllium.
5. the outer cylinder consists of 2 layers of carbon fiber on a Nomex core, or 1.5% X_0.

A schematic side view of the DCH is shown in Fig. 2.6.

The main details of the drift cells and DCH layout are:

1. The DCH consists of 7104 hexagonal drift cells, whose typical size is 1.2×1.8 cm^2.
2. The drift cells are groups in 10 superlayers, each consisting of 4 layers.

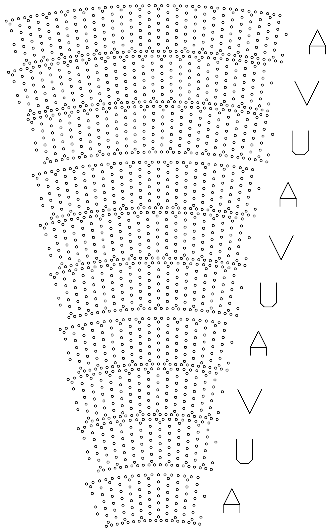

Figure 2.7: *Cell layout in the BABAR drift chamber.*

3. So as to provide so z and polar angle information, Axial(A) and stereo(U,V) superlayers alternate according to the pattern shown in Fig. 2.7

4. The stereo angle increases with radius from 40 mrad to 70 mrad.

5. The sense wires are 20 μm gold-plated tungsten-rhenium and nominally carry 1960 V.

6. The field wires are 120 μm and 80 μm gold-plated aluminum. Field wires at superlayer boundaries carry 340 V, while all others are grounded.

7. The gas mixture is chosen to provide good spatial and $\mathrm{d}E/\mathrm{d}x$ resolution with minimal material and is a helium-isobutane (80%:20%) mixture.

8. The gas and wires correspond to 0.3% X_0 for a track at 90° [45].

2.5.2 DCH Readout

The main requirement of the *BABAR* DCH electronics is that they not degrade the performance of the chamber by more than 10%. When measuring drift-time, the electronics looks for the leading edge of the signal from the charge that arrived at the sense wire. The time is then digitized with a resolution of 1 ns. For $\mathrm{d}E/\mathrm{d}x$ measurements, the total charge in the pulse is summed.

The amplifier, digitizer and trigger interface electronics are mounted on the rear end-plate of the drift chamber, in water-cooled aluminum boxes. The electronics provides trigger information by sending the data from all 7104 channels to the level 1 trigger system with a sampling frequency of 3.75 MHz. The system is designed to maintain good performance even in the presence of high backgrounds with a single-cell efficiency for the trigger signal of greater than 95%.

2.5.3 DCH Reconstruction

Some operations are performed on the DCH data before they are used in track-making:

- feature extraction of the waveform from the sense wire to integrate the total charge and detect the leading pulse edge;
- application of time-to-distance and ionization calibrations on the wire level.

The use of the DCH data in track finding and fitting is described in Sec. 2.6.

2.5.4 DCH Performance

The DCH has performed quite well from the beginning of data taking to present. The only significant performance problems are a period in which the High-Voltage was lowered from

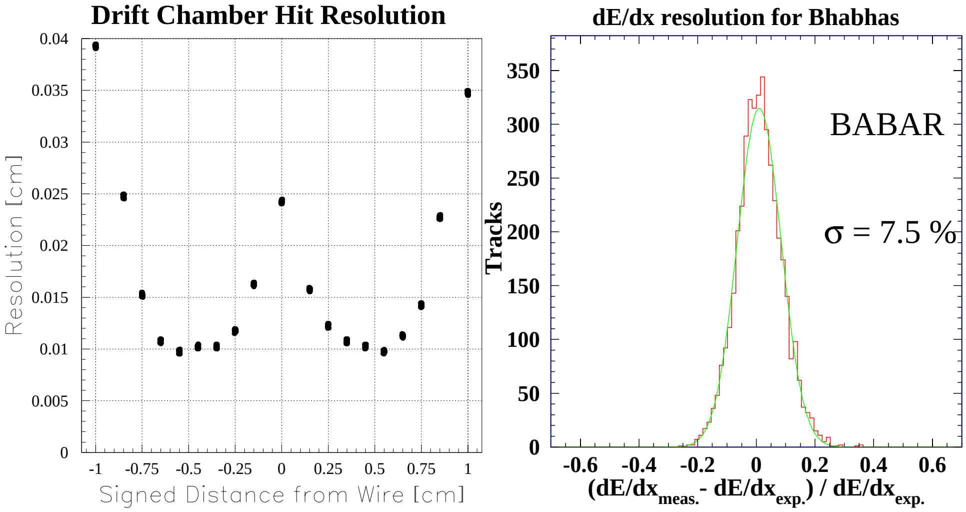

Figure 2.8: *Drift chamber performance plots. The single hit resolution in a typical DCH layer (18) is shown on the left. The DCH* $\mathrm{d}E/\mathrm{d}x$ *resolution is shown on the right.*

1960V to 1900V because of fears about longevity. This voltage change caused a significant ($\sim$ 10%) efficiency drop in the central region of the detector. Otherwise the DCH has performed at or near design specifications. A typical cell's spatial resolution as well as the overall $\mathrm{d}E/\mathrm{d}x$ resolution are shown in Fig. 2.8.

2.6 *BABAR* Tracking

"Have you noticed that Gerry uses his eyebrows to express emotion."
— J. Walsh

Both of the tracking subsystems, SVT and DCH, are capable of stand-alone performance. However, the information they provide is largely complimentary. The *BABAR* tracks are fit to 5-parameter helices. The helix parameters are listed here [46, 47].

1. d_0: the distance of closest approach between the track and the beam axis.

2. z_0: the z value at which d_0 has been calculated.

3. ϕ_0: the azimuthal track direction at the point where d_0 is calculated.

4. ω: the curvature of the track, $\omega \equiv 1/r$ where r is the radius of curvature of the track.

5. $\tan(\lambda)$: the tangent of the dip angle of the track.

The parametric equations in terms of the path-length along the helix l are then:

$$\begin{aligned} x(l) = & \quad \tfrac{1}{\omega}\sin(\phi_0 + \omega l) - (\tfrac{1}{\omega} + d_0)\sin(\phi_0) \\ y(l) = & \quad \tfrac{1}{\omega}\cos(\phi_0 + \omega l) + (\tfrac{1}{\omega} + d_0)\cos(\phi_0) \\ z(l) = & \quad z_0 + l\tan(\lambda) \end{aligned} \tag{2.1}$$

The actually tracking sequence consists of [48, 49]:

1. Several complementary DCH-only track-finding algorithms.

2. Propagating the DCH-only tracks into the SVT and adding SVT hits.

3. Two SVT-only track-finding algorithms.

4. Propagating the SVT-only tracks into the DCH and adding DCH hits.

5. Merging pairs of track found only in one sub-system and remove segments corresponding to return loops.

2.6.1 Tracking Performance

The independence of the two tracking systems allows us to make accurate performance measurements in the regime $p_T > 150\,\mathrm{MeV}/c$ where the DCH is expected to be fully efficient. For example, the efficiency to find a DCH track corresponding to a found SVT track is shown in Fig. 2.9. From these two plots, we can ascertain that the DCH is over 95% efficient

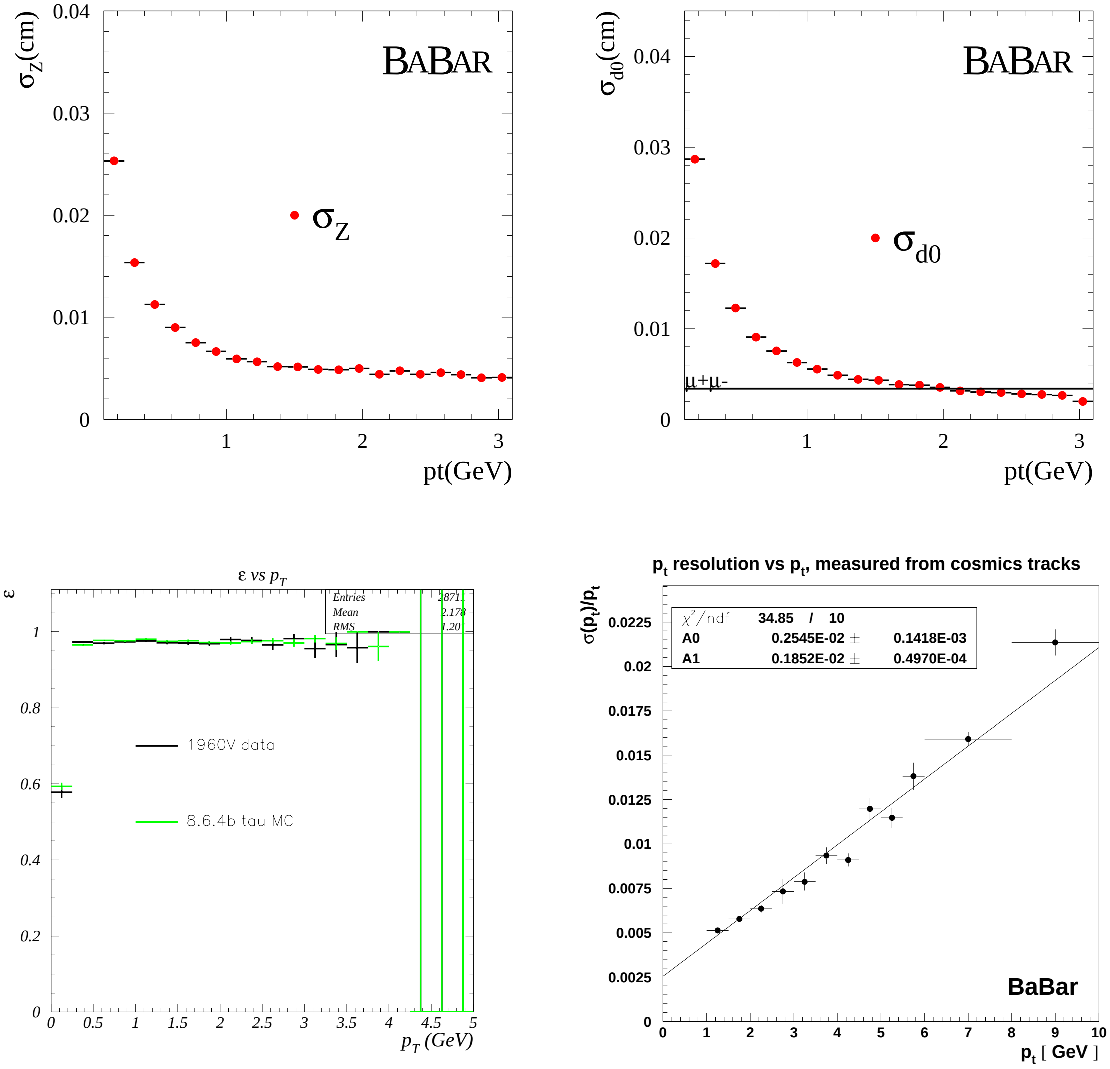

Figure 2.9: *BABAR tracking performance plots. The top plots show the* d_0 *(left) and* z_0 *(right) resolution as a function of* p_T*. The bottom left plot shows the DCH tracking efficiency as a function of* p_T*, while the bottom right plot shows the* p_T *resolution as a function of* p_T*.*

at finding track within the fiducial volume. It is also possible to use events with simple kinematics and well know vertecies, such as $e^+e^- \rightarrow \mu^+\mu^-$, cosmic muons and τ decays, to measure the overall tracking resolution. For example, Fig. 2.9 shows both the spatial resolution and transverse momentum resolution of the tracking system[50].

A somewhat more complicated analysis using known decay topologies is used to measure the SVT tracking performance in the low p_T regime where track do not reach far enough into the DCH to be reconstructed. The conclusions are that the SVT is over 95% efficient down to $p_T < 70\,\mathrm{MeV}/c$ [51].

At this point we must make a final comment about the tracking performance. All of the plots in this section were made with the best available alignments, both of the SVT relative to the DCH, and of the internal geometry of the SVT. However, during the first pass processing of the data described in Sec. 2.12 such a good internal alignment is not always available. Therefore, when studying the vertexing capacities of the *BABAR* detector we must carefully consider the effect of systematic distortions of the SVT from its nominal geometry. Such studies are described in detail in Chapter 4.

2.7 The DIRC

> *"Then you bounce then photons down a quartz bar, shoot them through some water and then make them into a ring. And they gave you money to do this?"*
> — S. Looney

The DIRC, Detector for Internally Reflected Cherenkov light, is a novel particle identification(PID) device. The PID requirements of the *BABAR* experiment are based around the need to tag the flavor of the non-$\mathcal{CP}$ eigenstate B-meson and to distinguish between different decay channels. The need to distinguish between different final states is particularly impor-

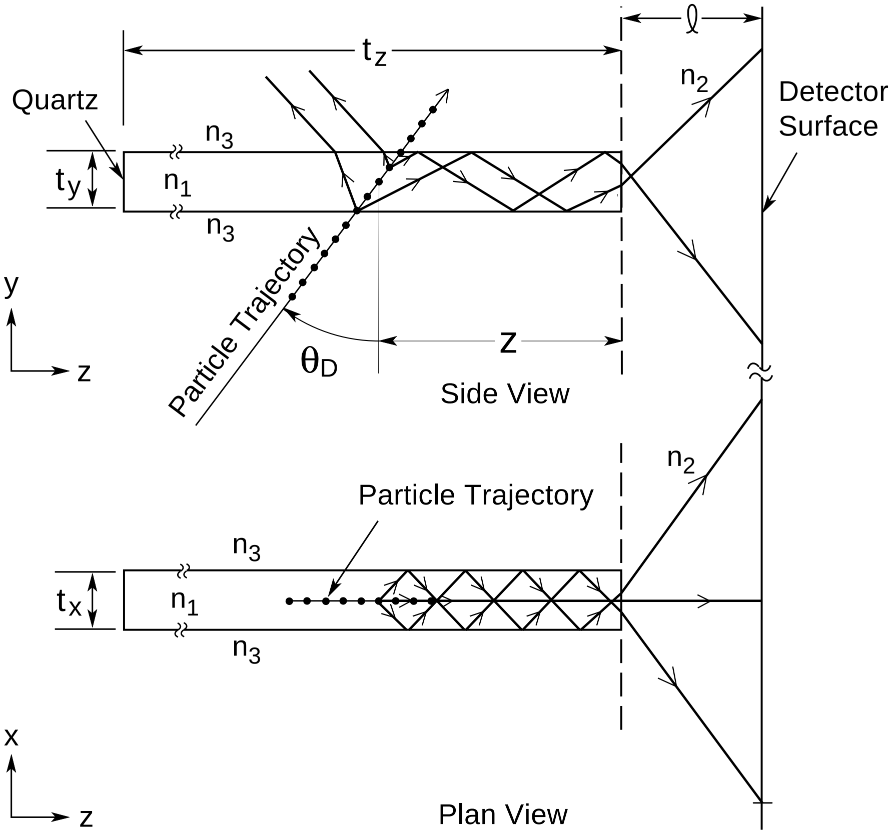

Figure 2.10: *Schematic of a single DIRC radiator bar. The particle trajectory is represented by a series of connected dots. The radiated Cherenkov photons are shown as lines with arrows.*

tant in rare decays such as those used to measure the $\mathcal{CP}$ angle α. For example, it should be possible to separate the channels $B \to \pi^+\pi^-$ and $B \to K^\pm\pi^\mp$ and this needs good K/π discrimination up to 4 GeV/c.

The DIRC concept is the inverse of a traditional ring-imaging Cherenkov counter (RICH); it relies on the detection of photons that are trapped in the radiator through total internal reflection [52]. This principle is shown schematically in Fig. 2.10. The Cherenkov radiation is emitted at a well known angle with respect to the track direction, namely $\theta_c = \cos^{-1}(1/\beta n)$ where n is the refractive index of the radiator medium [53].

The geometric layout and electronics readout of the DIRC are described in Secs. 2.7.1 and 2.7.2 respectively, while the current performance is summarized in Sec. 2.7.4.

These are major design consideration for the DIRC.

1. It must provide excellent kaon identification up to momenta of about 2 GeV/c and reasonable $\pi - K$ separation all the way up to 4 GeV/c . Since the difference in Cherenkov angle between a pion and a kaon at 4 GeV/c is about 6.5 mrad , the DIRC must resolve the Cherenkov angle of a track to 2 mrad or better to achieve $3\sigma K$-π seperation.

2. In turn, 2 mrad resolution on the Cerenkov angle requires single photoelectron resolution of order 9 mrad and with 25-50 photoelectrons per track [54].

3. Because of the beams background and the high-fold (up to 16-fold) reflection ambiguity in the Cerenkov image, single photon time resolution is crucial, both to eliminate background photons and disentange ambiguities.

4. Additionaly, the DIRC addition must assist in muon identification in the range where the IFR is inefficient, below $\sim$ 750 MeV/c.

2.7.1 DIRC Detector Layout

The basic mechanical elements of the DRC are shown schematically in Fig. 2.11 and listed here [54].

1. The DIRC radiator consists of 144 bars of synthetic quartz arranged in a 12-sided polygonal barrel shape.

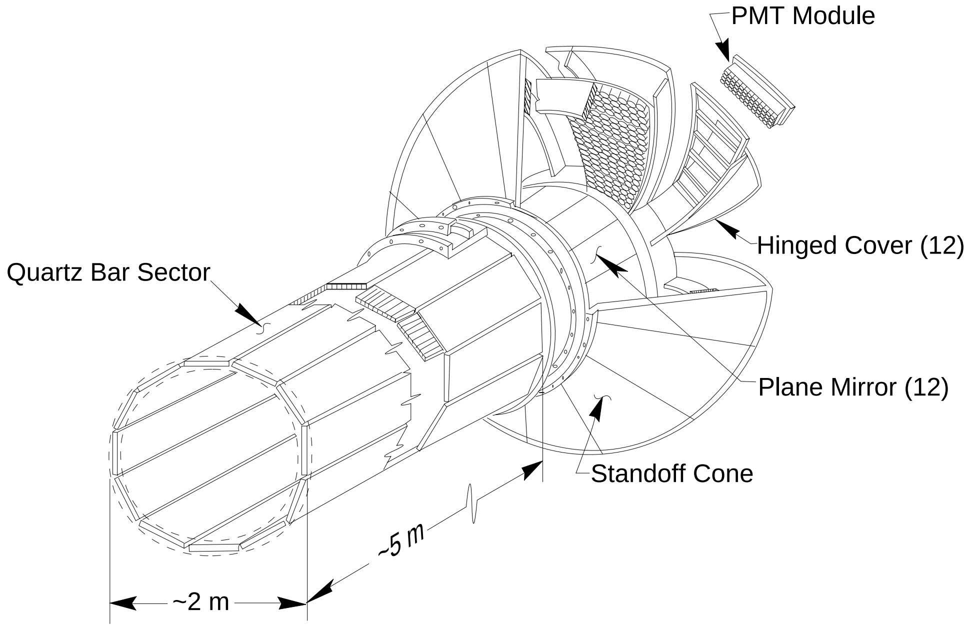

Figure 2.11: *Schematic of the DIRC showing the mechanical elements. Included are the mirrors mounted inside the standoff box, used to reflect Cherenkov light towards the PMTs.*

2. The bars have rectangular cross section; they are 1.7 cm thick by 3.5 cm wide and 4.9 m long.

3. The quartz extends through the magnet flux return in the backward direction in order to bring the Cherenkov light outside tracking and magnetic field volumes.

4. The readout apparatus is located at the backward end to amount of forward material.

5. There are mirrors at the forwards ends of the bars to reflect the light back towards the instrumentation.

6. The outer cylinder consists of 2 layers of carbon fiber on a Nomex core, or 1.5% X_0.

7. It occupies only 8 cm of radial space and represents 14% of an X_0 for a particle at 90°.

8. It covers 87% polar angle in the center-of-mass and 93% of the azimuth.

9. Before detection, the Cherenkov image is allowed to expand in a tank of purified water whose refractive index matches well that of the quartz bars (for which n=1.474).

10. The Cerenkov ring is imaged at the back end of the water tank on an array of about 11,000 photomultiplier tubes (PMTs), each with a diameter of 2.82 cm. The PMTs are disposed on a toroidal surface so as to present a uniform 1.2 m pathlength over most of the angular range.

11. A small trapezoidal piece of quartz is glued to the backward end of each quartz bar. This folds the inner half of the Chernkov ring outward, and also reflect photons with large radial angle back into the detection array.

2.7.2 DIRC Electronics Readout

The DIRC PMT's are held at a voltage of $\sim 1.1kV$. Groups of 64 PMT's are readout by a single custom board which amplifies and shapes the pulses. The shaped pulses are then fed to a zero-crossing discriminator. The motivation for using a zero-crossing discriminator is the improvement in time-resolution over the time-jitter associated with slewing in threshold discrimantors. The digital signals are then buffered in anticipation of a level 1 trigger accept, and which point they are transmitted off detector to the *BABAR* DAQ system.

2.7.3 DIRC Reconstruction

Several steps are performed on the DIRC data during reconstruction.

1. Projection of tracks to their impact point on the DIRC.

2. The expected pattern of PMT hits is calculated for each of the five charged track hypothesis. Timing information is crucial in resolving the multi-fold ambiguity caused

by the various mirrors along the light-path.

3. The best hypothesis, as measured by a χ^2 fit which includes the number of expected and observed photons, is selected. This has the effect of artificially forcing the fitting angle θ_c towards an expected value, though not always the correct one.

2.7.4 DIRC Performance

Although the DIRC installation was slightly behind schedule, owing to delays in polishing the quartz bars to the required smoothness, it has performed very well from the beginning of data taking to present.

Fig. 2.12 shows both the angular and temporal resolution for single photons. Gaussian fits to the two distributions give resolutions of 7.8 mrad and 1.4 ns respectively.

2.8 The Electromagnetic Calorimeter

> *"What did he say?"*
> *"He said, 'We go beer now.' "*
> — P. Strother, S. Gowdy and Y. Kolomensky

The physics that the *BABAR* experiment has been designed to study requires excellent electromagnetic calorimetry. The EMC is a cesium-iodide crystal calorimeter, which functions by measuring the light output from energy deposited by incident particles.

The geometric layout and electronics readout of the EMC are described in Secs. 2.8.1 and 2.8.2 respectively, while the current performance is summarized in Sec. 2.8.4.

Here is a list of the major design consideration for the EMC.

1. Since many of the B decays used to study CP violation contain at least one π^0 , the π^0 and B reconstruction efficiencies to fall off very quickly as the minimum detectable

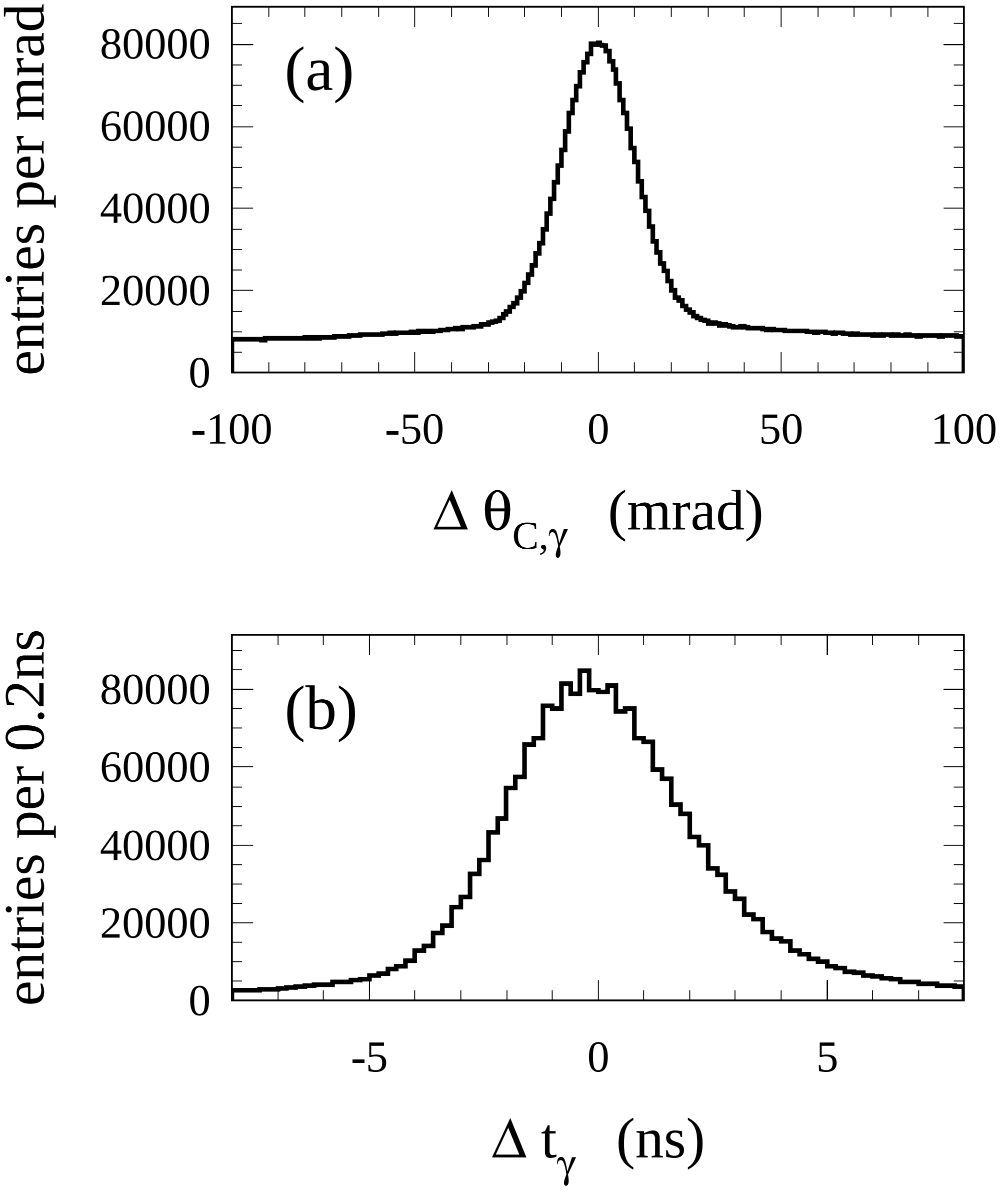

Figure 2.12: *DIRC Cherenkov angle (Θ_c, top) and timing (t_γ, bottom) resolution for single photons. These have calculated from calibration events.*

photon energy increases, thus the EMC must be highly efficient down to energies of 20 MeV, and cover a large solid angle.

2. Good B rescontruction also requires energy resolution of $\frac{\sigma_E}{E} \sim 3\%$ and angular resolutions of $\sigma_\phi \sim \sigma_\theta = 3.9\,\mathrm{mrad}$.

3. Furthermore, the EMC must provide for e and μ identification based on differences in cluster topology.

4. Finally, the EMC serves as the other principle (in addition to the DCH) input for the triggers.

2.8.1 EMC Detector Layout

The basic geometric features of the EMC are shown in Fig. 2.13 and listed here.

1. The *BABAR* calorimeter uses a quasi-projective arrangement of crystals made from thallium doped cesium-iodide covering a range of center-of-mass solid angle of $-0.916 \leq \cos\theta \leq 0.895$.

2. The crystals are divided up into two main sections, the barrel and the forward endcap. The barrel covers the center-of-mass solid angle of $-0.916 \leq \cos\theta \leq 0.715$ and has an inner radius of 91 cm. The endcap is a conic section with the front and back surfaces at an angle of 22.7° to the vertical and covers the center-of-mass solid angle of $0.718 \leq \cos\theta \leq 0.895$.

3. There are 5760 barrel crystals, arranged in 48 θ rows, each row having 120 identical crystals around ϕ. These crystals are grouped in 280 modules of 7×3 in θ and ϕ

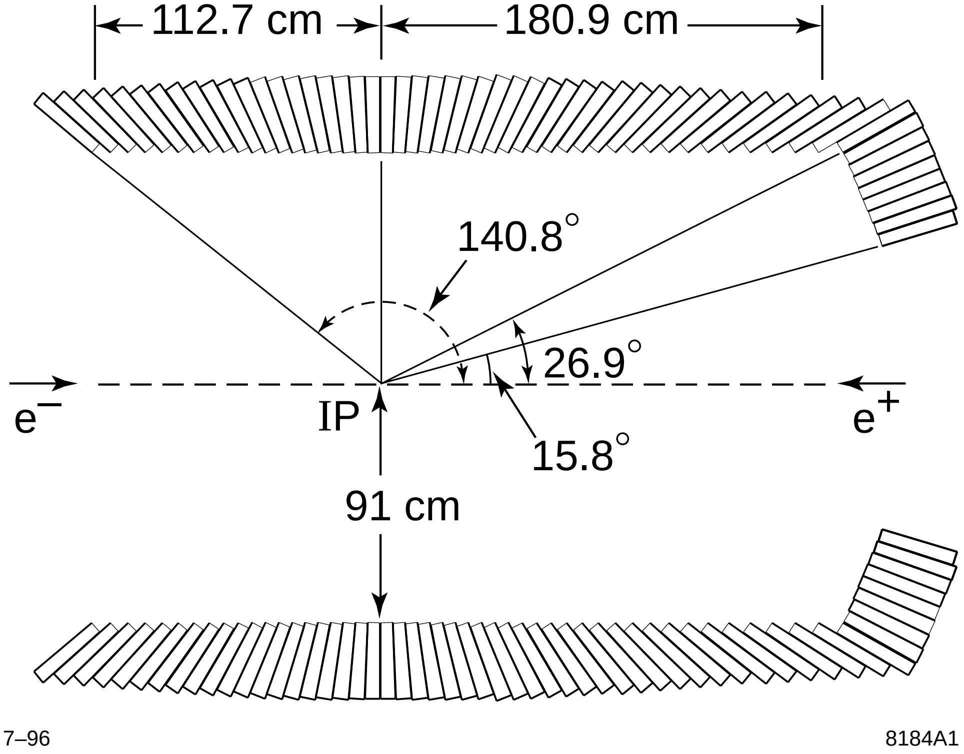

Figure 2.13: *Layout of the EMC showing the barrel and forward endcap.*

respectively. The length of the crystals varies from 29.76 cm (16.1 X_0) at the rear of the barrel to 32.55 cm (17.6 X_0) at the front.

4. There are 820 endcap crystals arranged in 8 rings in theta and in modules so as to give a 20-fold symmetry in ϕ. The ϕ segmentation of the first three rings matches that of the barrel with 120 crystals each. The next three have 100 and the final two rings have 80 crystals each. All the endcap crystals are 32.55 cm ($17.6X_0$) long except for those in the inner two rings which are shorter by $1\,X_0$ due to space limitations.

5. All the crystals are trapezoidal in shape with typical dimensions of $47 \times 47\,\mathrm{mm}^2$ at the front face and $60 \times 60\,\mathrm{mm}^2$.

6. In order to minimize the loss of particles that hit dead material between the crystals, they are arranged to be slightly non-projective in θ with respect to the interaction point. The non-projectivity ranges bewteen ± 15 mrad and 45 mrad across the detector.

2.8.2 EMC Readout

The scintillation light produced in each crystal is picked up by two (for redundancy) 1 cm ×2 cm photodiodes glued to its back face. Their output is sent via a preamplifier circuit (which is also fixed to the back of the crystal in order to reduce pick-up noise) to an ADC board. The digital signal is then sent to a DAQ board in the experiment's electronics house. The information stored here is also sent to the level 1 trigger system. A detailed description of the calorimeter electronics can be found in Refs. [55] and [56].

The average light yield per crystal is 7300 pe/MeV varying between 5000 and 10000. The incoherent electronic noise has been measured at about 900 pe or 150 keV per crystal which makes a negligible contribution to the overall energy resolution [59].

2.8.3 EMC Reconstruction

Several steps are performed on the EMC data [57, 58].

1. Feature extraction of the waveform from each crystal is used to integrate the total current flow and detect the leading pulse edge.
2. Application of electronics and offline calibrations on the crystal level to extract the deposited energy.
3. Clustering alogrithm by which pairs of adjacent crystals with energies above a threshold of a few MeV are recursively joined into clusters.
4. Bump-finding algorithms in which the clusters are searched for local maxima. This is to resolve clusters caused by more than one particle into their respective components.
5. The centroid and various moments are calculated for all clusters and bumps.
6. A final energy rescaling is preformed at the cluster level. This is needed because larger energy clusters tend to lose more energy to leaking throught the rear of the EMC.
7. Finally, a track-cluster matching is perform, using the χ^2 of the expected track impact point with the cluster centroid. All un-associated clusters will then be treated as candidate neutral particles.

2.8.4 EMC Performance

The target EMC energy resolution is $\frac{\sigma_E}{E}\frac{1\%}{E(\,\mathrm{GeV})^{\frac{1}{2}}} \oplus 1.2\%$ where the constant term arises from front and rear leakage, inter-calibration errors and light collection non-uniformity.

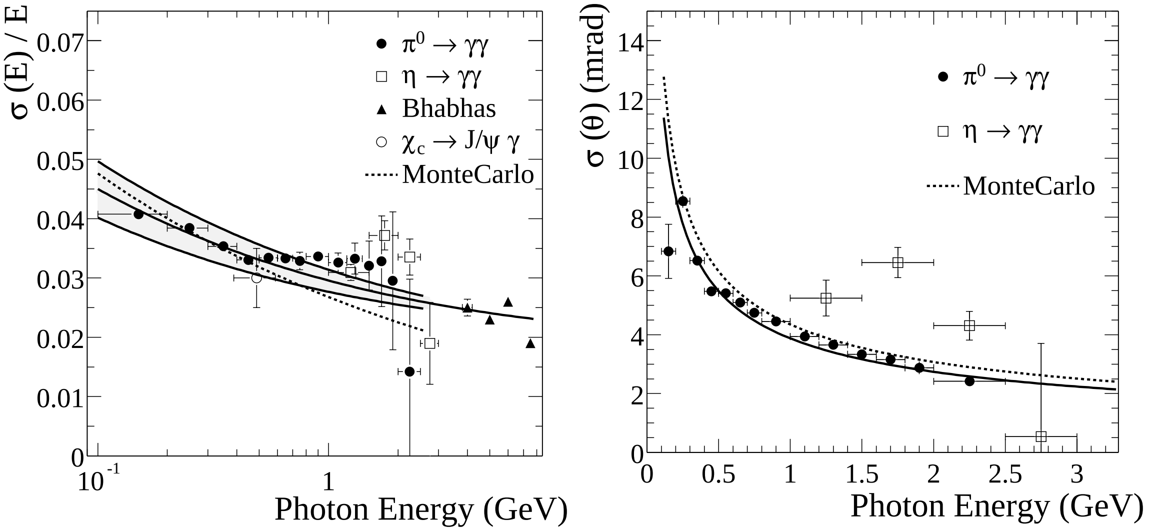

Figure 2.14: *EMC performance plots. The EMC energy resolution is shown on the left, and the angular resoution on the right. Values are shown from several differrent calibration methods for comparison.*

Parameter	Value
Central Field	1.5 T
Maximum Radial Field	< 0.25 T
Mean Solenoid Diameter	3060 mm
Solenoid Length	3513 mm
Stored Energy	27 MJ

Table 2.5: *BABAR magnet parameters..*

This various inputs that have been used to measure both the energy and angular resolution are summarized in Fig. 2.14.

2.9 The *BABAR* Solenoid

> *"Why would I join that experiment, they don't even have a magnet."*
> — Unknown

The *BABAR* solenoid provides a 1.5 T field to allow measurement of the transverse momentum of charged particles. The solenoid is superconducting, and is positioned between the EMC and the IFR.

The main magnet parameters are listed are Tab. 2.9, and the design coniderations are listed here:

1. Large enough field for momentum resolution. A 1.5 T field will cause a track with $p_T = 3\,\mathrm{GeV}/c$ to bend about 3 cm before reaching the outside of the DCH.
2. Since the p_T measurement depends on the value of the field it is crucial that the field stability be better that 1 in 10^{-4}.
3. The field uniformity in the tracking volume is very important. In many cases, it is either implicitly or explicitly assumed that the charged tracks are moving along helicies near the origin. Although field non-uniformities are accounted for in the final track-fitting and extrapolation through the outer detectors, they are ignored in the trigger and pattern recognition algorithms.

2.10 The Instrumented Flux Return

> *"From now on I'm working on beampipes."*
> — D. Fasching

The outermost subdetector in *BABAR* consists of layers of resistive plate chambers or RPCs. It is designed for the identification of muons and the detection of neutral hadrons, as such, it uses the iron of the magnet return yoke to filter charged hadrons and photons.

The geometric layout and electronics readout of the IFR are described in Secs. 2.10.1 and 2.10.2 respectively, while the current performance is summarized in Sec. 2.10.4.

The major design consideration for the IFR are.

1. It is the primary muon identification device. Muons are identified on the principle that they are the only charged particle capable of penetrating far into the IFR volume (since they do not interact hadronically like pions or kaons, and do not shower electromagnetically like electrons).

2. The IFR is also the primary detection device for neutral hadrons, particularly K_L^0, which are often only observed as a small cluster of IFR hits.

3. Since penetration range is momentum dependent, the IFR iron is segmented non-uniformly. The RPCs are radially closer in the inner part of the detector than in the outer parts. This improves performance for lower momenta particles.

4. In order to increase the solid angle coverage, the IFR consists of a barrel section and forward and backward endcaps. The endcaps allow the solid angle coverage to go down to 300 mrad in the forward direction and 400 mrad in the backward direction.

2.10.1 IFR Detector Layout

A cross-section through a *BABAR* RPC is shown in Fig. 2.16 and the general principle of operation is described in [60] and [61]. Basically, the electrodes are 2 mm plates of graphite coated Bakelite, covered by PVC insulating film. One electrode is grounded while the other is held at high voltage (∼8kV). The inter-electrode gap is filled with an argon-Freon-isobutane mixture. Ionization particles induce pulses which are picked up by orthogonal aluminum strips on either side of the chamber.

A cutaway view of the IFR is also shown in Fig. 2.15, and the basic features are listed here.

Missing

Plot

Figure 2.15: *IFR schematic drawings, showing the gradation of the iron layers.*

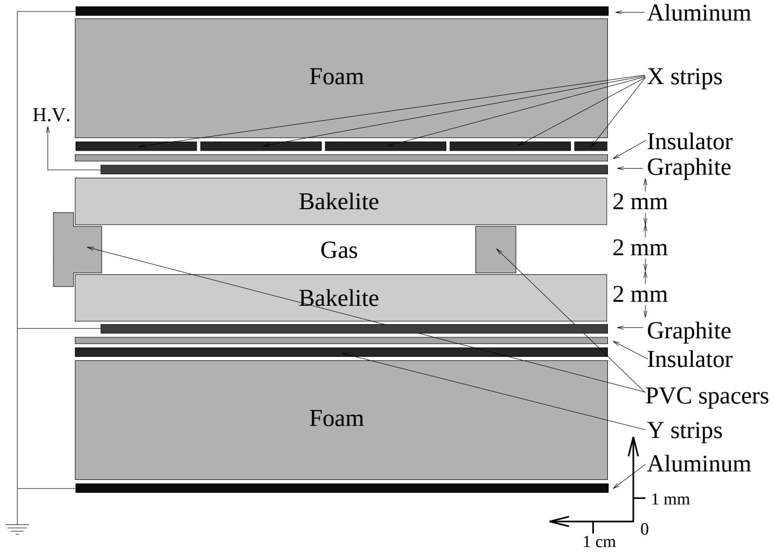

Figure 2.16: *A schematic cross-sectional view of a BABAR RPC.*

1. There are 18 layers of iron in the IFR giving a total thickness of 65 cm in the barrel and 60 cm in the endcaps.

2. The graded segmentation of the iron varies from 2 cm to 10 cm. The innermost nine plates are 2 cm thick, the next four are 3 cm and the next three are 5 cm. The outer two plates are 10 cm thick in the barrel with one 5 cm and one 10 cm in the endcaps.

3. The gaps for the RPCs are 3.2 cm apart from those between the 2 cm barrel plates, which are 3.5 cm.

4. In the barrel region, there are 21 active detector layers: two layers immediately outside the EMC, and 19 layers alternating with the iron.

5. The innermost barrel RPCs are cylindrical, consisting of eight chambers, arranged in two layers for maximum efficiency. They are intended to provide information on particles which lose most of their momentum in the calorimeter. Each RPC cylindrical

covers one quarter of a 147 cm radius cylinder around the beamline.

6. All the other barrel RPCs are planar, comprised of four chambers, and cover one sixth of the azimuth.

7. Both endcap doors are hexagonal, with 18 RPC layers, each consisting of six chambers. The endcaps are split into two halves, which may be separated to allow access to the inner detectors.

8. In the barrel, the readout strips that measure the z-coordinate have a pitch of 38.5 mm and those that measure the ϕ-coordinate vary from 19.7 mm to 33.5 mm.

9. In the endcaps, the strips measuring y position have a pitch of 28.4 mm and for those that measure x position it is 38 mm.

2.10.2 IFR Readout System

The data from sixteen strips are passed to a Front End readout Card(FEC) which then passes the active strips to a TDC circuit. The TDC output is stored in buffers which allow for the trigger latency before being passed along an optical fiber to the *BABAR* DAQ system.

2.10.3 IFR Reconstruction

Several steps are performed on the IFR data.

1. Feature extraction of the output from each RPC is used to integrate the total current flow and detect the leading pulse edge.

2. Clustering algorithm are run which join pairs of adjacent chambers with hits into clusters. Clustering is done in both the $r-\phi$ and the z views separately and then the

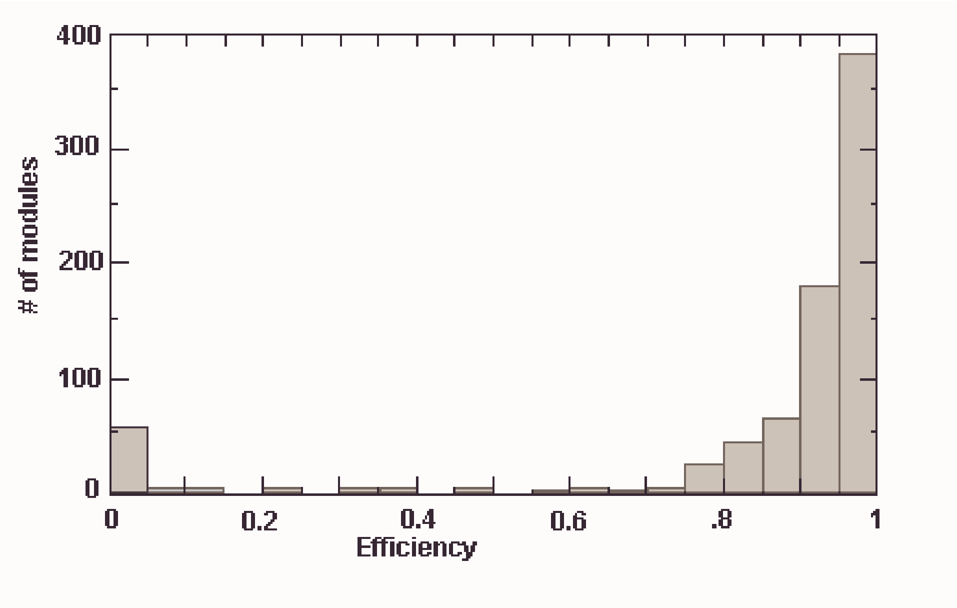

Figure 2.17: *Histogram of the efficiency of IFR modules.*

2D-clusters are joined into full 3D-clusters.

3. Finally, a track-swimming algorithm is performed in with all charged tracks are propagated through the IFR and cluster-matching is performed. All un-associated clusters will then be treated as candidate neutral particles.

2.10.4 IFR Performance

The IFR has performed increasingly poorly from the begin of data taking to present. Fig. 2.17 shows efficiency of the IFR modules. Several modules have failed altogether and many others are degrading rapidly. Although these problems should be fixed during a long shutdown scheduled for sometime in 2002-2003 they do raise significant issues for the analyses described in this dissertation. The main result has been that we use the EMC much more for muon ID and neutral hadron reconstruction than originally intended.

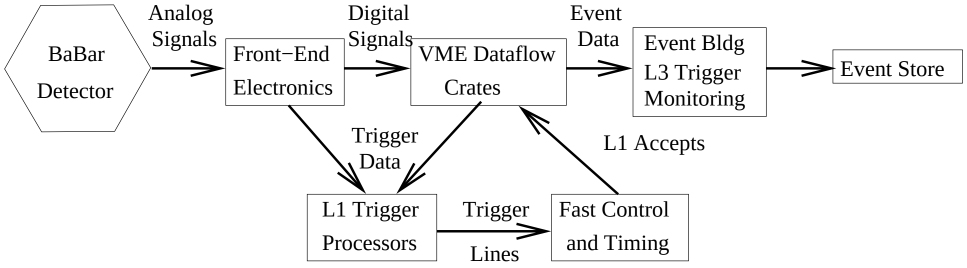

Figure 2.18: *Schematic overview of the BABAR data-acquisition and online computing systems.*

2.11 Online Electronics and Computing

> *"Is he wearing black? Yes.*
> *Did he do any work today? Yes.*
> *Is he a prima donna? Yes.*
> *It's Biff."*
> — T. Dignan and E. Charles, "*BABAR* trigger post-doc taxonomy algorithm."

In order to reliably and efficiently record interesting physics events, which are only present a rate $\sim 100Hz$ from a $\sim 250MHz$ crossing rate, significant hardware instrumentation and software systems are required. We will briefly give an overview of these systems here. In Sec. 2.11.1 we will describe the systems responsible for data flow and data acquisition. In Sec. 2.11.2 we describe the trigger system, which selects interesting events for storage. Finally, in Sec. 2.11.3 we describe the detector control systems. A schematic overview of the online system is shown in Fig. 2.18.

2.11.1 The Data Acquisition System

The *BABAR* data acquisition system must work closely with the trigger system to ensure low deadtimes and efficient performance.

2.11.1.1 Online Dataflow

The basic hardware unit in the dataflows systems is a Read-Out Module (ROM), a VME-based processor connected to the on-detector electronics by 1.2 Gb/s fiber-optic links. The ROMs perform the following tasks.

1. Extracting physical signals from the raw data.
2. Performing gains and pedestal corrections.
3. Data sparsification and formatting.
4. Performing regular calibration of the on-detector electronics.

The main point pertinent to the analyses described herein is that the dataflow system is limited both by bandwidth and processing speed. At best, the dataflow system can handle data rates near 2 kHz.

2.11.1.2 Online Event Processing

In order for the data to be available to the software (level 3) trigger and for storage to disk, the inputs from each of the ROMS must be merged in to a coherent whole. This task is complicated by the fact that during normal operation many events are in different processing stages simultaneously. The OEP application performs event-building and handles communication with the level 3 processors and the data logging manager. Again, from the point of view of this dissertation, the main points are that it works, and that it sets a limit of about $200Hz$ on the data logging rate.

2.11.2 The Trigger System

To be useful for physics, the *BABAR* trigger system must satisfy the following requirements.

1. Select interesting physics events for storage with a high and well known efficiency. This is done in a multi-stage process: level 1 runs in hardware and level 3 is purely software.
2. Because of dataflow limitations it is impossible to read out every event. Rather, all the data is buffered on the detector pending a level 1 decision. Reasonable buffer-sizes allow only for a $12\mu s$ level 1 latency.
3. Because of the limitations in the number of events we are able to reconstruct and store on disk, the level 3 trigger must reduce the event rate to $\sim$ 100 Hz.

The trigger system design requirements are described in detail in [62].

2.11.2.1 Level 1 Trigger

The basic features of the level 1 trigger are:

1. A drift chamber trigger (DCT) which constructs track segments and applies a simple discrimination algorithm to select track segment $p_T > 800\,\mathrm{MeV}/c$.
2. An electromagnetic calorimeter trigger (EMT) which sums the energy of fixed sets of crystal and applies energy threshold cuts.
3. The global trigger (GLT) which then tests the DCT track segments and EMT clusters against various predefined conditions to produce 24 output trigger lines.

4. A level 1 accept signal is asserted if a pre-determined set of trigger lines fire for a given event. In addition the latency in L1 must not be more than $12\,\mu$s with a jitter of less than $1\,\mu$s.

5. Since trigger electronics sampling rates are much slower than the 4 ns crossing time, the trigger is given for a particular time, rather than a specific beam crossing.

6. Since the DCT and EMT are largely independent, they allow for good cross-calibration of the trigger efficiency.

7. Simulation of an 'open trigger' in nominal background conditions generates an output rate of 1.5 kHz and 100% efficiency inside the fiducial region of the detector for B and τ physics events [63].

2.11.2.2 Level 3 Trigger

The level 3 trigger operates after the event has been assembled and employs various tools to reduce backgrounds while still keeping the physics events. More complex algorithms can now be employed since information from the whole event is available. In particular, track impact parameters can be examined to reject events which did not originate from the primary vertex. Also, timing information can be used to reject background events from other beam crossings.

It has been shown under nominal background conditions that the output of level 3 can be kept to the budgeted value of 100 Hz. Of these events, ~ 80 Hz are two-photon processes and Bhabhas leaving less than ~ 20 Hz of potentially interesting hadronic events.

The trigger system is designed to meet the 100 Hz output requirement under a range of background conditions and possible luminosity upgrades to $10^{34}\,\mathrm{cm}^{-2}\mathrm{s}^{-1}$. However, if the situation arises where level 1 can no longer meet the 2 kHz requirement for input to level 3, then it will be necessary to construct a level 2 trigger system as an intermediary stage.

2.11.3 The Detector Control Systems

During normal operation, the *BABAR* detector is controlled by a shift crew of 2 people, who are often non-expert in the particulars of the detector control systems. Therefore, it is crucial that detector control be highly automated, stable and well-protected against unexpected conditions. For completeness, we provide here a very cursory description of these systems. From the point of view of the analyses describe in this dissertation the main point is that they work well enough to ensure lots of data-taking.

2.11.3.1 Online Detector Control

The detector control system provides a set of Graphical User Interfaces running on UNIX workstations which can control any aspect of the *BABAR* detector. For ease of use, the detector control system also defines hierarchical sets of states so that the entire detector and be made ready for data-taking or shutdown by a single command.

2.11.3.2 Online Run Control

The run control systems provide an interface between the detector control and the data acquisition systems, so as to insure that data are taken with reasonable and consistent detector parameters. The run control systems are responsible for storing and apply predefined global detector configures suitable to different data taking conditions, (such as colliding-beams, cosmic-ray data or electronics calibrations). The run control system also stops data-taking if alarms are generated because of unsuitable detector or accelerator conditions.

2.12 Offline Data Processing

"If I get another pint, the pager will go off."
— R. Sloane

This section describes the treatment of the data between being logged to disk, and be readily available for physics analysis. The main aspect of this process is the online prompt reconstruction system (OPR).

The data logged from the detector temporarily stored on disk before being processed by OPR. The jobs of the OPR task are.

1. Process the raw data into objects more appropriate for physics analysis, such as track and calorimeter clusters.

2. Promote those tracks and clusters into candidates for particles. This steps includes associating tracks with calorimeter objects, and performing PID algorithms.

3. Perform physics level filtering. The various candidate particles are used as the input for both inclusive and exclusive searches for particular decay signatures. Based on these results, the events are separated into various analysis specific streams.

4. Perform prompt monitoring, so that feedback on detector performance is available shortly after the data are taken.

5. Perform a set of *rolling calibrations*. Detector parameters such as inter-system alignment and beam-spot position, which change significantly over the course a run ($\sim 2-3$ hours) are calculated using the data from a given run. The extracted parameters are then used as the input for processing the next run.

6. Store all the output data into the *BABAR* event store, an object-oriented database.

Huge processing capabilities are required to keep pace with the data acquisition rate. The prompt reconstruction processing farm consists of 150 Sun SPARC5 CPUs. Furthermore, since the reconstruction algorithms evolve and improve with time, two other processing farms simultaneously re-process older data.

The detector level reconstruction algorithms are described in Sec. 2.12.1. An overview of the physics level reconstruction is provided in Sec. 2.12.2. Finally various calibration mechanisms are briefly described in Sec. 2.13.

2.12.1 Reconstruction Algorithms

A fundamental distinction exists between the representations of data used by the detector subsystem reconstruction algorithms and by the physics analysis software.

When performing reconstruction in the detector subsystems, it is natural to use *geometric* and *uncalibrated* representations of the data. That is to say, during detector reconstruction, tracks are described by helix parameters, calorimeter hits by ADC (analog to digital converter) counts, and SVT hits by clock cycles about threshold.

On the other hand, physics analyses proceed more naturally when treating such quantities as four-vectors, deposited energy and specific ionization per unit length. Therefore, the first step in the physics level analysis of the data re-interpret the output of the detector reconstruction as candidate particles with four-momenta and other associated quantities.

The types particles observed in the detector from the decay modes used in this selection are $K^{\pm}$, $\pi^{\pm}$, $e^{\pm}$, $\mu^{\pm}$, γ, and π^0. The remainder of this section describes the process by which reconstructed tracks and calorimeter hits are converted into these final state particle candidates, which then become the starting point for all physics analyses.

2.12.1.1 Charged Tracks

The following steps are taken to represent charged tracks as candidate particles.

1. The helix parameters are converted to position and four-momentum, assuming that the track is a pion and comes from the beamspot.
2. The $\mathrm{d}E/\mathrm{d}x$ information from both the SVT and DCH, if available, is associated with the candidate.
3. If an EMC cluster is associated with the track, cluster shape and energy deposition information is calculated and associated with the candidate.
4. The Cherenkov angle and number of photons measured in the DIRC is associated with the candidate.
5. The pattern of IFR hits along the track trajectory swim is associated with the candidate.

At this stage in the analysis, all the information required either to 1) use the track as a pion in subsequent parts of the analysis or 2) test other hypothesis (beside pion) for the type of particle which produced the track.

2.12.1.2 Neutral Clusters

The following steps are taken to represent EMC and IFR clusters as candidate particles.

1. Any clusters associated with charged tracks are rejected.

2. The energy and position of all remaining clusters are converted to four-momenta, assuming they are photons produced at the beamspot.

2.12.2 Physics Level Algorithms

BABAR actually runs significantly more of its physics analysis algorithm in the prompt-reconstruction job that many other particle physics experiments. This is because the huge size of the dataset make it infeasible to re-process the entire data-set for several different analyses. Therefore, as much as possible, all the algorithms are run once, and all the various analysis groups use the common results. In this section we briefly describe the parts of the physics analysis which are run in the prompt-reconstruction jobs.

2.12.2.1 Particle Candidates

As described in Sec. 2.12.1, the *BABAR* physics analysis software represents a candidate particle as a four-vector and associated covariance matrix. In addition, information useful for PID, such as the Cherenkov angle in the DIRC, or the $\mathrm{d}E/\mathrm{d}x$ in the SVT are associated with the candidate particles [64].

A novel feature of the *BABAR* software analysis framework is the treatment of reconstructed composite particles such as D^0 and K^{*+} which are observed only via their decay products on a equal footing with final state particle such a π^+ and γ which are seen as tracks or calorimeter hits.

Any given composite particle is defined by the following information:

- particle type (*i.e.*. K^0_S, D^0 or B^0);

- four-momentum and associated covariance matrix;

- genealogy information;
- production and decay vertices, if known;
- it is also possible to associate analysis-specific quantities with the composite particles, in order to speed selection during re-processing or the data.

We make extensive use of this technology in the event selection process, during which we often exclusive reconstruct a complex decay tree by recursively reconstructing the sub-processes all the way up the tree.

2.12.2.2 Event Tag Data

Since the huge amount of data taken by the *BABAR* detector make processing every single event prohibitively slow, certain quantities are calculated as stored in an event header or *Event Tag* database. These quantities can be used to select sub sets of events for subsequent analysis.

Example of such parameters are variables which describe the topology of the event, such as the event thrust, the visible energy or the number of charged tracks. Other quantities stored as tag data include the primary vertex and analysis specific "tag bits" described below.

2.12.2.3 Composites and Tag Bits

As discussed in Chapter 1, many analyses require events in specific decay channels. Therefore, the prompt-reconstruction farm must also identify events that are likely to include such decays. In order to achieve this goal for many separate analysis groups simultaneously, the prompt-reconstruction job calculates a set of "tag-bits" for each event. Each tag bit is intended to flag the presence of a particular physics signature that may classify a certain event as interesting for a given analysis. Examples of tag-bits such tests as the presence of a lepton with $p_T > 1.5\,\mathrm{GeV}/c$ or the exclusive reconstruction of a $J/\psi \to \ell^+\ell^-$ decay.

Since many tag bits require the exclusive reconstruction of particular decay channels, a sequence of exclusive reconstruction algorithms are run during prompt-reconstruction. These algorithms use the composite particle candidate technology mentioned above to progressively reconstruct various intermediate state with loose selection criteria and combinatorially combine them to form more intermediate and initial state candidates. Tag-bits are then assigned based on the presence or absence of a particular decay mode candidate in an event.

2.13 Calibrations

"It will take much longer to get the right numbers; but it is better to tell people the right numbers."
— M. Bona

In order to insure the best performance of the *BABAR* detector, several types of calibrations are required.

1. **Online calibrations** are performed regularly and automatically by the Online Detector Control system.
2. **Rolling calibrations** are performed on rapidly changing quantities which are essential to many aspects of the reconstruction.
3. **Offline calibrations** are performed on slowly changing quantities, often using the full event reconstruction chain.

2.13.1 Online Calibrations

Many of the electronics calibrations are performed automatically by the Online Detector Control system. Such calibrations primarily involve the gains and offset of analog circuits in the on-detector electrons. Furthermore, many of these calibrations are applied either before the data are stored to disk, or in very early stage of the offline reconstruction. Therefore, these calibrations are very closely monitored and frequently checked against existing references to insure that the data is not irreparably damaged by poor calibrations.

2.13.2 Rolling Calibrations

Many quantities, such as the relative position of the various sub-detectors, can change significant over times scales as short as, or shorter than, the 2-3 hours that a run lasts. Therefore, we use a system of rolling calibrations in which these quantities are calculated for a block of data, then used as the input for the next block of data.

2.13.3 Offline Calibrations.

Many of the calibrations require fairly high level inputs, such as the reconstructed invariant mass of a particular decay chain or a very clean Particle ID sample. These calibration are generally performed by the individual or groups responsible for the various subsystems, running over the processed data. The output of such calibrations are then stored for later re-processing of the data.

Chapter 3

Reconstruction of B-Mesons Decays

> *"Comment faire pourri a partir d'un truc bein."*
> — S. Lemaitre

As discussed in section 1.5, the first step towards using B-mesons to measure $\mathcal{CP}$ violation is to isolate a three pure samples of B-meson decays for subsequent study.

1. The $B^{\pm}$ sample: $B^{\pm}$ decays. These decays exhibit neither flavor mixing nor $\mathcal{CP}$ violation through interference and serve to study detector response without the complications of flavor tagging. This sample is also useful as a negative control for the mixing and $\mathcal{CP}$ measurements.

2. The B_{flav} sample: $B^0\overline{B}^0$ decays to non-$\mathcal{CP}$ eigenstates. These decays do exhibit mixing, but do not exhibit $\mathcal{CP}$ violation through interference. In addition to being the signal sample for the Δm_d measurement, this sample is used to calibrate the performance of the flavor tagging algorithms for the $\mathcal{CP}$ measurement.

3. The $\mathcal{CP}$ sample: B decays to $\mathcal{CP}$ eigenstates. This is the signal sample for the $\mathcal{CP}$ measurement.

This chapter will detail the selection of these samples.

3.1 Exclusive B Reconstruction

"He said they used simplest possible method, which was nice until he started talking about N-Dimensional hypercubes."
— J. Boyd

We use *exclusive* selections throughout this analysis. That is to say, we reconstructed the entire decay tree of a B-meson. This requires a different selection for each decay mode, significantly limiting the available data sample. Furthermore, since B-mesons often decay to five or more particles, the selection efficiency can be quite low, ranging anywhere from $1\% - 50\%$ depending on the mode. On the other hand, *exclusive* samples can be made very ($> 90\%$) pure, since the consistency of every aspect of the decay can be tested. Furthermore, once a decay has been fully reconstructed, the four-momentum of the parent B-meson is quite well known, and may be used in later stages of the analysis.

Generally, the more complete knowledge of fully reconstructed B-mesons makes them favorable for complicated analyses; provided that they are available in large enough numbers. In fact, the design luminosity of the PEP-II rings where chosen so as to make full reconstruction viable. Considering efficiencies between 10% and 50% for the most viable decay modes, we expect to reconstruct about 300 B mesons per fb^{-1} in the $B^{\pm}$ and B_{flav} samples, and about 30 B mesons per fb^{-1} in the $\mathcal{CP}$ sample. As such, sufficient samples for world's best measurements of the B lifetimes, Δm_d, and $\sin 2\beta$ are available with an data set of 20-30 fb^{-1} [65, 66].

The next few sections will detail the decay modes used in this analysis.

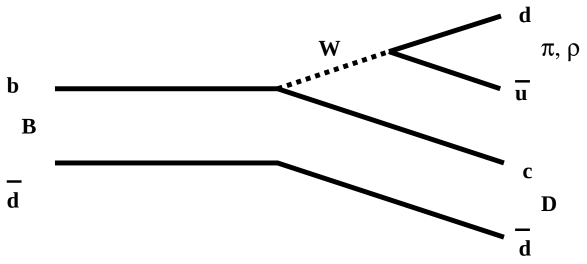

Figure 3.1: *The "spectator" tree-level diagram for B to open charm decays.*

B Mode	Fraction (%)
$\overline{B}^0 \to D^{*+}\pi^-$	0.28
$\overline{B}^0 \to D^{*+}\rho^-$	0.68
$\overline{B}^0 \to D^{*+}a_1^-$	1.30
$\overline{B}^0 \to D^{+}\pi^-$	0.30
$\overline{B}^0 \to D^{+}\rho^-$	0.79
$\overline{B}^0 \to D^{+}a_1^-$	0.60
$B^- \to D^{*0}\pi^-$	0.46
$B^- \to D^{0}\pi^-$	0.53

Table 3.1: *B to open charm decay channels examined in this analysis..*

3.1.1 B to Open Charm Modes

The dominant B decay modes are governed by a tree-level diagram with an external W^- as seen in Fig. 3.1. The easiest of these mode to reconstruct fully are those where the W^- emerges a light hadron state such as π^- or ρ^-. Since the D mesons carry net charm, such decays are said to have "open" charm. Furthermore, such final states are not $\mathcal{CP}$ self-conjugate, meaning that these decays comprise part of either the $B^\pm$ or B_{flav} samples.

In this analysis we reconstruct B decays to open charm in a variety of channels containing a D^{*+}, D^{*0}, D^+, or D^0 and a π^-, ρ^-, or a_1^-. Tab. 3.1.1 lists all the B decay channels reconstructed. Furthermore, Tab. 3.1.1 lists the cascade decays of the charm mesons examined, while Tab. 3.1.1 lists the decay modes of the light hadrons we have used.

$D^{(*)}$ Mode	Fraction (%)
$D^0 \to K^-\pi^+$	3.8
$D^0 \to K^-\pi^+\pi^0$	13.9
$D^0 \to K^0_S\pi^+\pi^-(K^0_S \to \pi^+\pi^-)$	1.8
$D^0 \to K^-\pi^+\pi^+\pi^-$	7.5
$D^+ \to K^-\pi^+\pi^+$	9.0
$D^+ \to K^0_S\pi^+(K^0_S \to \pi^+\pi^-)$	0.9
$D^{*+} \to D^0\pi^+$	67.7
$D^{*+} \to D^+\pi^0$	30.7
$D^{*0} \to D^0\pi^0$	62.0
Total D^0 Fraction	30.6
Total D^+ Fraction	9.7
Total Product D^{*+} Fraction	23.4
Total Product D^{*0} Fraction	19.0

Table 3.2: *Cascade D decay channels examined in this analysis..*

h^+ Mode	Fraction (%)
$\rho^0 \to \pi^+\pi^-$ Mode	100
$\rho^+ \to \pi^0\pi^+$ Mode	100
$a_1^+ \to \rho^0\pi^+$ Mode	“seen”

Table 3.3: *Light hadron decay modes used in this analysis..*

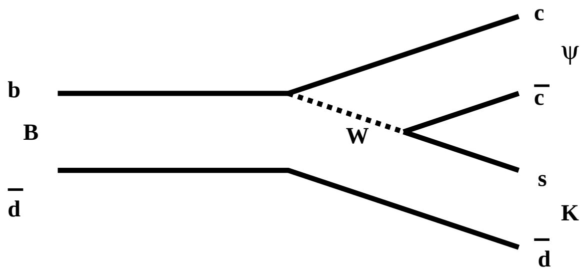

Figure 3.2: *The "internal-W" tree-level diagram for B to charmonium decays.*

We note in passing that the selection involves a total of 32 modes which account for approximately 1% of all $\overline{B}^0$ decays and 0.2% of all $B^{\pm}$ decays. Because of the large number of modes involved, the B candidate reconstruction, selection techniques and background suppression methods have been standardized across modes [70].

3.1.2 B to Charmonium Modes

The dominant B decay modes to $\mathcal{CP}$ eigenstates involve a tree-level diagram with an internal W^- as seen in Fig. 3.2. In the case that the W^- produces a $\overline{c}s$ quark pair, the final state consists of a charmonium particle and a kaon. Should the kaon decay to a $\mathcal{CP}$ eigenstate, the process is $\mathcal{CP}$ self-conjugate; such decays may be used to measure $\mathcal{CP}$ violation.

To isolate samples of such events, we reconstruct decays of B-mesons into two body final states involving a charmonium final states (J/ψ, $\psi(2S)$, or χ_{c1}) and a kaon (K^*, K_S^0 or $K^{\pm}$) [67, 68, 69].

The list of channels that we have considered are shown in Tab. 3.1.2.

3.1.3 Reconstruction Technique

We reconstruct B-mesons by progressively constructing lists of all candidate combinations for each intermediate state particles in the decay chain and using those lists as the input

Channel	Secondary Decay Mode
$B^0 \to J/\psi K_S^0$	$J/\psi \to \ell^+\ell^-$; $K_S^0 \to \pi^+\pi^-$ $J/\psi \to \ell^+\ell^-$; $K_S^0 \to \pi^0\ \pi^0$
$B^+ \to J/\psi K^+$	$J/\psi \to \ell^+\ell^-$
$B^0 \to J/\psi K^{*0}$	$J/\psi \to \ell^+\ell^-$; $K^{*0} \to K^+\ \pi^-$ $J/\psi \to \ell^+\ell^-$; $K^{*0} \to K_S^0\ \pi^0$
$B^+ \to J/\psi K^{*+}$	$J/\psi \to \ell^+\ell^-$; $K^* \to K_S^0\ \pi^-$ $J/\psi \to \ell^+\ell^-$; $K^* \to K^+\ \pi^0$
$B^0 \to J/\psi \pi^0$	$J/\psi \to \ell^+\ell^-$
$B^0 \to \psi(2S) K_S^0$	$\psi(2S) \to \ell^+\ell^-$ or $\psi(2S) \to J/\psi\ \pi^+\pi^-$;$K_S^0 \to \pi^+\pi^-$
$B^+ \to \psi(2S) K^+$	$\psi(2S) \to \ell^+\ell^-$ or $\psi(2S) \to J/\psi\ \pi^+\pi^-$
$B^0 \to \chi_{c1} K_S^0$	$\chi_{c1} \to J/\psi\ \gamma$; $K_S^0 \to \pi^+\pi^-$
$B^+ \to \chi_{c1} K^+$	$\chi_{c1} \to J/\psi\ \gamma$

Table 3.4: *$B \to c\bar{c}\ K$ decay modes considered in this analysis, both the e^+e^- and $\mu^+\mu^-$ decay modes of the ψ are used.*

for the next level of the decay tree. For example, the list of K_S^0 particles is made by taking all pairs of oppositely charged tracks whose invariant mass is at all consistent with the K_S^0 mass. At a later stage in the analysis, the K_S^0 list is combined with the list of charged tracks to construct K^{*+} candidates. At all stages of the analysis care is taken to insure that no reconstructed object is used more than once in the composition of any particle.

In cases where several decay modes of a particular particles are considered, for example $D^+ \to K^-\ \pi^+\ \pi^+$ and $D^+ \to K_S^0\ \pi^+$, each mode is reconstructed separately, then merged into a single list of D^+ candidates which is in turn passed on to later stages of the analysis.

Sec. 3.3 defines and describes the selections used for the final state particles which are directly observed in the *BABAR* detector such as charged pions and kaons, while Sec. 3.6 describes the selections used to define composite particles only indirectly observed.

3.1.4 Cut Selection and Motivation

Since these event samples are being used for a variety of purposes the choice of figure of merit to use for cut optimization is debatable.

As compromise between the need for statistics to characterize the samples and purity to avoid washing out the signature decay-time structures, we chose to minimize the error on the measured branching ration. Thus, we optimized our cut values to maximize the ratio $\frac{S}{\sqrt{S+B}}$ where S and B are the numbers of signal and background events respectively from Monte Carlo which pass the event selection procedure.

Following the channel-by-channel optimization procedure, the cut values were standardized so that for each channel the standard cut was adopted if the impact on $\frac{S}{\sqrt{S+B}}$ relative to the optimal choice was small.

3.2 Data Samples

"The first time he gave a talk, he wasn't sure if he had run on data or Monte Carlo."
— J. Richardson

At this point we describe the data sets used in this dissertation. These data include both real data acquired from the *BABAR* detector (usually simply called "data") and study samples produced by Monte Carlo techniques and processed with a detailed simulated of the *BABAR* detector ("Monte Carlo").

3.2.1 Data

In this analysis we used 29.7 fb^{-1} of data recorded around the peak of the $\Upsilon(4S)$ resonance and 3.7 fb^{-1} recorded $\sim 40\,\mathrm{MeV}$ below [78, 80]. The data were recorded between 22nd October 1999 and 4th July 2001. The sample corresponds to $\times 10^7$ $B\overline{B}$ events.

We only use data approved for analysis by *BABAR* data quality management. The basic requirement for a run to be used are that:

- the PEP-II status was be “Colliding Beams”;
- all *BABAR* sub-detectors were on;
- the data quality monitoring shifter present in the control room during the acquisition of the data marked it as usable;
- the recorded luminosity was non-zero;
- the offline reconstruction for the run was successfully completed [72, 73, 74].

The most significant difference between various data is that the 2001 data were reconstructed with a more accurate measurement SVT internal alignment and thus show better position resolution. This is very important to the measurement of the vertexing performance and is discussed further in Secs. 4.4 and 4.6, thus, we when considering the Δt resolution we explicitly distinguish between 1999-2000 (Run 1, 20.7 fb^{-1}) and 2001 (Run 2, 9.0 fb^{-1}) data. Another significant change in conditions was that the drift chamber high voltage was increased from 1900V to 1960V in July of 2000, as described in Sec. 2.5.4. This resulted in a noticeable increase in tracking efficiency, but does not affect either vertexing or tagging performance enough to warrant further separation of the data [75].

3.2.2 Monte Carlo

We have used Monte Carlo data produced as part of the *BABAR* simulation production [76]. After generation, the simulated particles are decayed and propagated through a full GEANT [77] simulation of the *BABAR* detector.

$B \to c\bar{c}$ modes		
Sample		Events
$B^+ \to (J/\psi,\psi(2S),\chi_{c1})\ K^+$		20 k each
$B^+ \to J/\psi\ K^{*+}$		20 k
$B^0 \to J/\psi\ K^{*0};\ K^{*0} \to K^+\ \pi^-$		20 k
$B^0 \to J/\psi\ K^0_S;\ K^0_S \to \pi^+\pi^-$		100 k
$B^0 \to (\psi(2S),\chi_{c1})K^0_S;\ K^0_S \to \pi^+\pi^-$		20 k each
$B^0 \to J/\psi\ K^0_S;\ K^0_S \to \pi^0\ \pi^0$		20 k
$B^0 \to J/\psi\ K^{*0};\ K^{*0} \to K^0_S\ \pi^0$		20 k
"Tagging" Samples		
$B^0 \to \pi^+\pi^-, \overline{B}^0 \to X$, no mixing		100 k
$B \to D^{(*)}X$ modes		
Sample	Luminosity (fb^{-1})	Events
$B^+ \to D^{(*)0}h+$ Cocktail	680	3,400 k
$B^0 \to D^{(*)-}h+$ Cocktail	450	1,240 k
Background Samples		
J/ψ inclusive	260	700 k
$\psi(2S)$ inclusive	40	146 k
χ_{c1} inclusive	40	120 k
$B^0\overline{B}^0$ Generic	3.4	4,000 k
$B^+\ B^-$ Generic	3.4	4,000 k
$c\bar{c}$ Generic	9.2	12,000 k
uds Generic	8.6	18,000 k

Table 3.5: *Monte Carlo event samples; all Monte Carlo were generated with* $\sin 2\beta = 0.7, \Delta m_d = 0.472\,\mathrm{ps}^{-1}, \tau_{B^0} = 1.54ps$ *and* $\tau_{B^+} = 1.67ps$.

The Monte Carlo events are subject to the same reconstruction and subsequent event processing as the data. The simulation includes conditions data and overlayed background events which were sampled at the same time that the data under consideration were recorded. We have used a luminosity weighted mixture of events processed to match the mixture of conditions in the data sample.

Tab. 3.2.2 lists all the Monte Carlo samples that we used in doing this analysis. The background sample were only used during the cut optimization stage of the event selection. The various signal samples were used to insure that the event selection were correctly implemented, as well as to optimize and judge the performance of the vertexing and tagging algorithms.

3.3 Track and Neutral Particle Reconstruction

"Do you want some tea?"
— N. Chevalier, "Correct British reaction to being woken at 4:30am."

The starting point for our event selection is the lists of charged tracks and neutral EMC and IFR clusters that are the output of the first phase of the prompt-reconstruction job. In this section we briefly describe the fiducial cuts and quality criteria that are applied to these tracks and clusters before they are used in the creation of composite particle candidates.

3.3.1 Track Selection

In order to reduce contributions from beam gas and beam wall backgrounds when appropriate, a sub-selection of well-reconstructed tracks consistent with originating from the beam spot is produced. The criteria for three such selection are listed in Tab. 3.3.1. In most cases the "Loose" selection is used as the starting list of candidate particles from which the

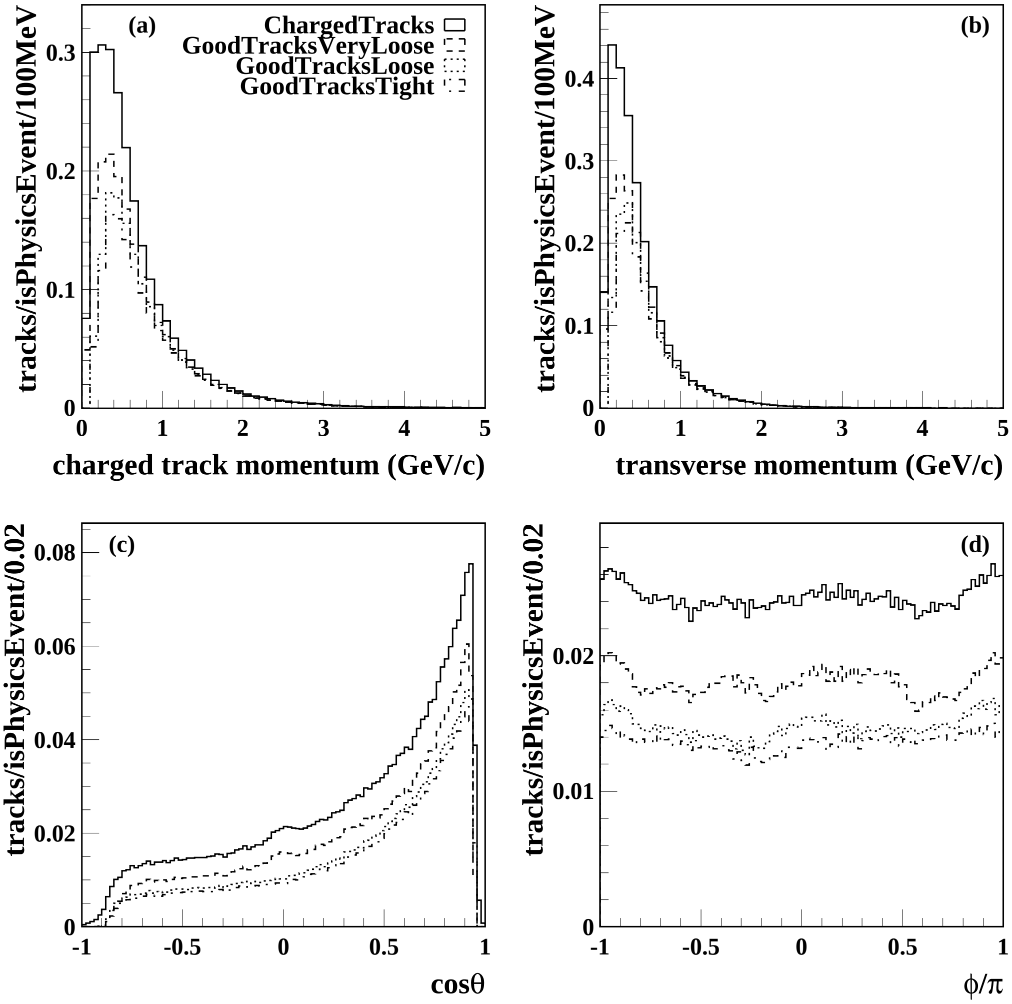

Figure 3.3: *Distributions of (a) total momentum, (b) transverse momentum, (c) cosine of polar angle, and (d) azimuthal angle (all measured in the lab frame) for various track selection criteria: all tracks, “Very Loose”, “Loose” and “Tight”.*

	“Very Loose”	“Loose”	“Tight”
p_T	[0.0,10.] MeV/c	$>$ 0.1 MeV/c	-
d_0	$<$ 1.5 cm	-	$<$ 1.0 cm
z_0	$<$ 10. cm	-	$<$ 3. cm
n_{DCH}	$>$ 12	$>$ 20	-

Table 3.6: *Summary of quality cuts for charged tracks..*

Criteria	Skim	Final Analysis
$E(\gamma\gamma)$	$>$ 200 MeV	-
$m(\gamma\gamma)$	[90.,170.] MeV/c^2	[120.,150.] MeV/c^2

Table 3.7: *Summary of cuts for π^0 selection.*

composite particle are built. However, there are two classes of tracks for which track quality selection is not appropriate: those not originating near the beamspot, and those with momenta too low to penetrate far enough into the DCH. Pions from K^0_S candidates fall into the first category, while the pions from $\psi(2S) \to J/\psi\ \pi^+\pi^-$ are an example of the second [81].

Fig. 3.3 compares some inclusive charged-track distributions for the successively tighter track requirements.

3.3.2 Photon Selection

Isolated photon candidates are subject to the following additional requirements:

- a minimum energy of 30 MeV,
- having a lateral shower shape consistent with the expected pattern of energy deposits for an electromagnetic shower, as determined by a cut of LAT $<$ 0.8.

3.3.3 π^0 Selection

We distinguish between the π^0 s observed as a single cluster in the calorimeter (such π^0 are called *merged* π^0, and occurs at higher energies, usually above 1 GeV), and π^0 s observed as separated γ s (called *composite* π^0).

3.3.3.1 Composite π^0

The composite π^0 selection starts combining pairs of photons with the following requirement:

1. a pair invariant mass in the range of 90–165 (90–170) MeV/c^2, computed at the detector origin and assuming both daughters are photons.

Fig. 3.4 shows the invariant mass and energy distribution and χ^2 probability of the mass-constrained fit for a typical run. The energy and momenta of π^0 candidates are recalculated with a constraint on the π^0 mass calculated at the beam spot position. This re-fitting technique improves the energy resolution of the π^0 candidates from 3.0% to 2.5%. About 80% of all π^0's produced in generic Monte Carlo have both photons within the calorimeter's geometrical acceptance. The fraction of π^0's within the acceptance which are pass the selection varies with π^0 energy: it is $65 - 70\%$ from 0.5–2.0 GeV, and then falls linearly down to 25% at about 5 GeV due to a large fraction of overlapping showers. Details for the π^0 reconstruction can be found in [82].

3.3.3.2 Merged π^0

Merged π^0 selection proceeds by looking for local maxima in each EMC cluster and working from the assumption that local maxima correspond to the location of the decay photons. The photon pair is required to be within ±20 MeV/c^2 of the nominal π^0 mass.

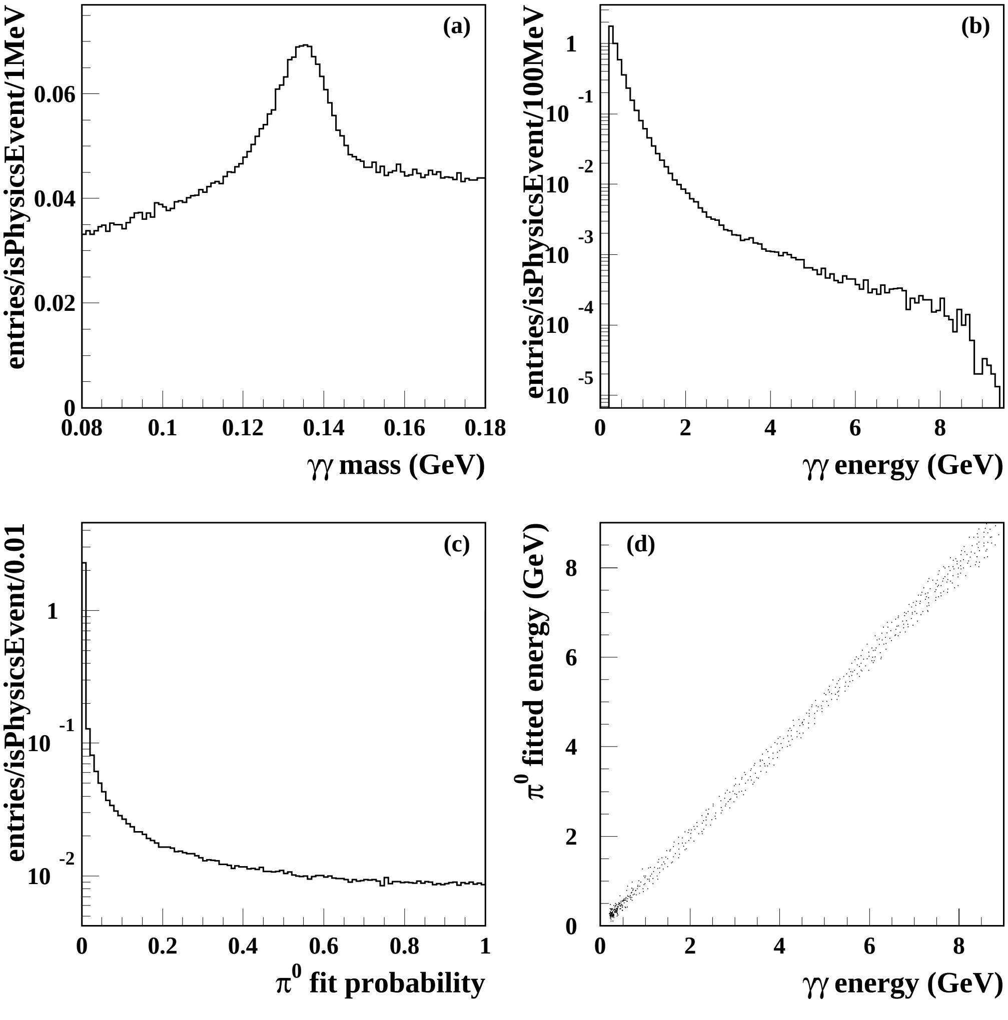

Figure 3.4: *Distributions of (a) invariant mass, (b) total energy for pairs of neutral calorimeter clusters, (c) mass-constraint fit* χ^2 *probability in for a* π^0 *fit, and (d) a scatter plot of energies comparison from a typical run (number 12917).*

3.4 Skims and Pre-Selection

“First you pick the Lady in the Lake.”
— D. Fasching, “How to pick the next King of England”

The PEP-II luminosity makes it infeasible to repeatedly run over the entire data set. Therefore, to expedite data processing, all the data is first “skimmed” and events with potential B-mesons decays in related channels are grouped into event collection for subsequent use for various analyses.

The skims used in this analysis are defined by the following criteria.

- The event must pass the multi-hadron selection used by the B counting analysis:
    - the event must satisfy either the L3 EMC or L3 DCH trigger;
    - the B counting only uses tracks within the restricted angular region $0.41 < \theta_{LAB} < 2.54$ and neutrals with energy $> 30\,\text{MeV}$ in the fiducial volume $0.41 < \theta_{LAB} < 2.409$;
    - a minimum of 3 such tracks which also pass the “Loose” track quality are required;
    - R_2 (the ratio of the second to the zeroth Fox-Wolfram moment) calculated from the tracks and neutrals in the acceptance region must be less than 0.5 [79];
    - the primary vertex which is constructed from these tracks must be within 0.5 cm of the beam spot in x-y and within 6 cm in z;
    - the total energy in the fiducial volume is required to be greater than 4.5 GeV.

  This selection is 95.4% efficient for $B\overline{B}$ events [80].

- The physics level full reconstruction chain is run in a limited manner. As soon any acceptable decays have been found in any particular mode, processing is terminated and the event is flagged for subsequent analysis. Since the output of the skims are used by many analyses, the cuts applied on reconstructed particles are somewhat looser that those applied in the final event selection.

- The reconstruction requirement depends on the process type:

  - for B to open charm selection, the event must have at least one fully reconstructed B decay which passes the "skim" selection criteria in any of the decay modes used for this analysis;

  - for B to charmonium selection the event must have at least one fully reconstructed $J/\psi \to \ell^+\ell^-$ or $\psi(2S) \to \ell^+\ell^-$ decay pass the "skim" selection criteria.

Throughout the rest of this chapter, we distinguish between the selection criteria used in the "skimming" phase of the analysis and in the final analysis.

3.4.1 Post-skim Analysis

At the output of the skimming phase of the analysis all of the composite particles in the decay tree of the exclusively reconstructed B-meson are stored along with the charged track and calorimeter cluster type particle candidates in the standard data format. This make it possible to re-tune the final selection, and modify the algorithms used for subsequent analysis without have to redo the combinatoric searches for composite particle candidates.

3.5 Particle Identification

"I am very excited about selecting some Roys for my analysis."

— D. Azzopardi

As stated in Sec. 3.3.1, the default hypothesis for all charged tracks is that they were caused by pions. However, every track is tested against the hypothesis that it represents each of the five charged particle types commonly seem in the *BABAR* detector: electrons, pions, muons, kaons, and protons.

Many quantities are used from the various sub-detectors for particle identification.

1. *SVT* and *DCH*: measurement of $\mathrm{d}E/\mathrm{d}x$ through ionization. We use the 60% (80% for the DCH) truncated mean of $\mathrm{d}E/\mathrm{d}x$ to lessen the effect of Landau fluctuations [53, 83].
2. *DIRC*: value of the Cherenkov angle (θ_c) and number of photons (N_γ) observed.
3. *EMC*: ratio of Calorimeter energy to track momentum (E/p), the lateral (LAT) and Zernieke A_{42} moments of the Calorimeter cluster, the number of crystals (N_{Xtal}) in the cluster and angular mismatch between the cluster and the track ($\Delta\phi$).
4. *IFR*: pattern of IFR hits, including the last layer hit.

Furthermore, as stated in Sec. 2.12.2 the particle identification algorithms also assign likelihoods for each particle hypothesis based on the data listed above. These likelihoods are calculated separately for each sub-detector and can be combined statistically. In fact, both the kaon identification and flavor tagging algorithms make direct use of the sub-detector likelihoods.

3.5.1 Electrons

There are two main criteria for identifying electrons.

Criteria	“noCal”	“very loose”	“loose”	“tight”	“very tight”
$dE/dx(\sigma)$	[-2.2,4]	[-3,7]	[-3,7]	[-3,7]	[-2.2,4]
N_{Xtal}	-	> 3	> 3	> 3	> 3
E/p	-	[0.50,5.0]	[0.65,5.0]	[0.75,1.3]	[0.89,1.2]
LAT	-	-	-	[0,0.6]	[0,0.6]
A_{42}	-	-	-	[0,0.6]	[0,0.11]
DRC θ_c	-	-	-	-	$\pm 3\sigma$

Table 3.8: *Definitions of electron selection criteria..*

1. Low momentum electrons have very different dE/dx from ionization from heavier particles.

2. Higher energy electrons, (specifically, those which reach the calorimeter) can be recognized by their particular EMC cluster topopoly. Specifically, electrons showers in the calorimeter begin sooner, are more uniform, and deposited a larger fraction of their energy than showers from similar momentum hadrons [85, 84].

Tab. 3.5.1 list increasingly tight sets of electron selection criteria used in different phases of this analysis, while Fig. 3.5 shows the electron selection efficiency as a function of momentum for the “loose” selection.

3.5.2 Muons

We use several criteria for identifying muons [85, 86].

1. A minimum ionizing signature in the EMC. Muons tend to lose about 200 MeV of energy, regardless of their momentum. Owing to the intermittent performance of the IFR, a particular selection criteria “MinIon”, uses only this measure.

2. A pattern of penetrating hits in the IFR. IFR-based muon selection is based on calcu-

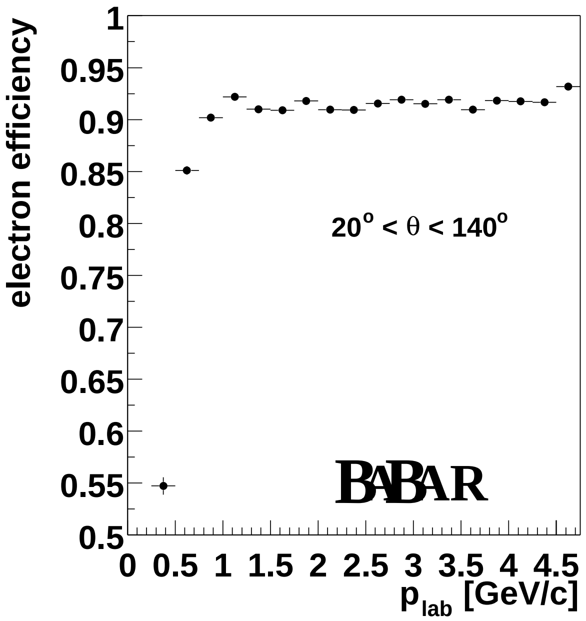

Figure 3.5: *Electron ID efficiency as a function of momentum. This has been calculated for the "Loose" selection using high purity control samples.*

Criteria	"minIon"	"very loose"	"loose'	"tight"	"very tight
E_{EMC}(GeV)	< 0.4	< 0.5	< 0.5	< 0.4	< 0.4
n_{λ}	-	> 2.0	> 2.0	> 2.2	> 2.2
Δn_{λ}	-	< 2.5	< 2.0	< 1.0	< 0.8
$\bar{n}_{hits}$	-	< 10	< 10	< 8	< 8
σn_{hits}	-	< 6	< 6	< 6	< 6
χ^2_{trk}/n_{lay}	-	-	< 7.0	< 5.0	< 5.0
χ^2_{fit}/n_{lay}	-	-	< 4.0	< 3.0	< 3.0

Table 3.9: *Definitions of muon selection criteria..*

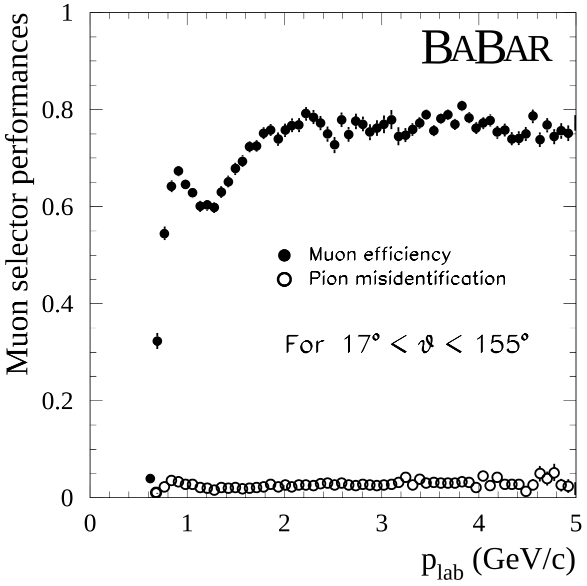

Figure 3.6: *Muon ID efficiency and purity as a function of momentum. This has been calculated for the "loose" selection using high purity control samples.*

lating the likelihood of the observed pattern of hits in the IFR, under the assumption that a track was a muon. The specific variables that we use are:

- n_λ and Δn_λ, respectively the number of hadronic interaction lengths of iron traversed, and difference with the predicted penetration depth for a muon of the same energy and momentum;
- $\bar{n}_{hits}$ and σn_{hits}, the mean and variance of the number of hits per RPC layer; these are used to reject hadronic interactions;
- the quality of fit for fitting a track to the IFR hits (χ^2_{trk}) and fitting the hit pattern for self-consistency (χ^2_{fit}).

Tab. 3.5.2 list increasingly tight sets of muon selection criteria used in different phases of this analysis.

Criteria	"Very Loose"		
Momentum (GeV/c)	< 0.5	[0.5,0.6]	> 0.7
Use SVT	yes	no	no
Use DCH	yes	yes	no
Use DIRC	no	no	yes
$\mathcal{L}_K/\mathcal{L}_\pi$	> 0.1	> 1	> 1
OR $\mathcal{L}_p/\mathcal{L}_\pi$	> 0.1	> 1	> 1

Table 3.10: *Definition of the various kaon selection criteria..*

3.5.3 Kaons

The main criteria for identifying kaons are [87]:

- in the momentum range below 0.7 GeV/c kaons have very different dE/dx from pions;
- the same is true of the Cherenkov angle (θ_c) up to higher momenta.

We select kaons by comparing the likelihood ratios for kaons, pions and protons ($\mathcal{L}_K$, $\mathcal{L}_\pi$ and $\mathcal{L}_p$). Depending on the momentum range, we use either the SVT and DCH, DCH only or DIRC only to construct the likelihood ratios. Tab. 3.5.3 list the kaon selection criteria used in different parts of this analysis. The efficiency and purity of this"Very Loose" selection is shown in Fig. 3.7. A neural network kaon identification algorithm (described in Chapter five) is also used for B flavor tagging, but not for event selection.

3.6 Composite Particle Reconstruction

> *"Open the pod bay doors, PixelDaq."*
> — D. Fasching, "On the complexity of Physics software"

As described in Sec. 2.12.2, the *BABAR* physics analysis software makes extensive use of the concept of composite particle candidates for initial and intermediate state particle not

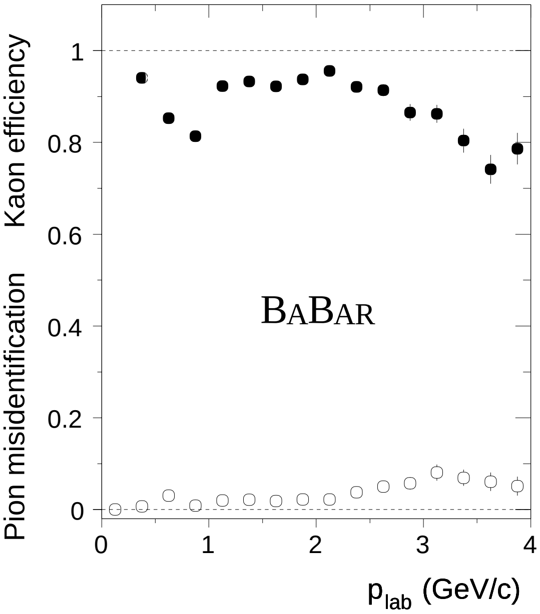

Figure 3.7: *Kaon ID efficiency and purity as a function of momentum. This has been calculated using high purity control samples.*

directly observed in the detector. This section describes how such composite particles are re-built all the way up the decay tree. The analysis algorithms make extensive use of the generality of the treatment of composite particle, *e.g.,* the same combinatorial engine is used throughout the analysis. Furthermore, it is a standard practice to improve mass resolutions by constraining intermediate state particles to their nominal mass.

In Sec. 3.6.1 we will treat the selection of light hadrons for decay chains such as $B \to D^{(*)}X$, where X is a light hadron. Secs. 3.6.2 and 3.6.3 will detail the reconstruction of K_S^0 and various K^* candidates respectively. In Sec. 3.6.4 we will move on to the reconstruction of D-mesons. Sec. 3.6.5 will describe the reconstruction of various $c\bar{c}$ bound states; and finally the construction of B-mesons is treated in Sec. 3.6.6.

Variable	Skim	Final Analysis
π^+		
p_π	> 500 MeV/c	-
ρ^+		
p_π	> 200 MeV/c	-
$\lvert m(\rho^+) - 770\rvert$	< 150 MeV/c^2	-
$p_(\rho^+)$	> 1 GeV/c^2	-
a_1^+		
$p_(a_1^+)$	> 500 MeV/c^2	-
$m(a_1^+)$	$[1.0, 1.6]$ GeV/c^2	-
a_1^+ Vertex	-	$Prob(\chi^2) > 0.1\%$

Table 3.11: *Summary of cuts for high momentum π, ρ and a_1 candidates..*

3.6.1 Light Hadron Reconstruction

In the B to open charm reconstruction channels, the B-meson candidates are obtained by combining a D or D^* candidate, reconstructed as described in Sec. 3.6.4, with a high-momentum π, ρ or a_1 meson.

The light hadrons (π, ρ or a_1) are reconstructed as follows.

1. ρ^+ mesons from $\overline{B}^0 \to D^{*+}\rho^-$ decays are formed by combining a π^0 meson and a charged pion.
2. ρ^0 mesons are formed by combining a pair of oppositely charged tracks.
3. a_1^- mesons from $\overline{B}^0 \to D^{*+}a_1^-$ decays are formed by combining charged pions with ρ^0 mesons.
4. The cuts listed Tab. 3.6.1 are applied.
5. No particle identification is required any of these selections.

Variable	Skim	Final Analysis
$m(\pi^+\pi^-)$	$m(K^0_S) \pm 25$ MeV/c^2	[0.484 – 0.520]
$P(\chi^2)$	-	> 0.001
α_{xy}	-	< 200 mrad (if used)
α	-	< 200 mrad (if used)
r_{xy}	-	> 2 mm (if used)
r	-	> 1 mm (if used)

Table 3.12: *Summary of cuts for $K^0_S \rightarrow \pi^+\pi^-$ selection..*

3.6.2 K^0_S Reconstruction

For the most part, the K^0_S used in this analysis are reconstructed in the decays to charged pions. However, K^0_S decays to neutral pions are used in the exclusive charmonium analyses. The details of both these selections are presented here.

3.6.2.1 $K^0_S \rightarrow \pi^+\pi^-$ Reconstruction

Since K^0_S decays often occur within the active tracking volume of the detector, rather that near the beam spot, specific techniques are needed to reconstruct them. Furthermore, K^0_S decays are used in many separate *BABAR* analyses. Therefore, a standard K^0_S selection process has been chosen for "skim" processing.

1. All pairs of oppositely charged tracks are vertexed, but no cut is applied on vertex quality or convergence.

2. The tracks are assigned the π mass, and the invariant mass of the two tracks is calculated at the vertex. If the vertexing has not converged, four-vector addition of the track parameters at the *BABAR* origin is used.

3. The $\pi^+\pi^-$ invariant mass is required to lie within 25 MeV$/c^2$ of the nominal K^0_S mass. This defines the K^0_S selection used in the "skimming" phase of the analysis.

For the final event selection, these criteria are tightened as shown in Tab. 3.6.2.1.

Furthermore, depending on the mode, additional background reduction is often required. This is done by taking advantage of the flight of the K^0_S $\dot{\text{S}}$pecifically, in some case (detailed later in this chapter) cuts are applied on some additional quantities.

1. The opening angle in the transverse plane between the K^0_S momentum vector and the line of flight connecting the K^0_S decay point to the primary vertex of the event, α_{xy}.
2. A three dimensional version of the same variable is sometimes used. In this case the line of flight is taken between the K^0_S decay point and the other tracks coming from the same fully reconstructed B. This formulation is more appropriate for charmonium decays in which there are no long lived D-mesons in the fully reconstructed decay chain.
3. The transverse flight distance from the primary vertex in the event to the K^0_S decay point, r_{xy}.
4. In charmonium decays the (3-dimensional) flight distance from the charmonium vertex to the K^0_S decay point, r, is used.

The efficiency for a K^0_S with both tracks inside the fiducial volume to satisfy these requirements is $\sim 80\%$ [88].

3.6.2.2 $K_S^0 \to \pi^0\ \pi^0$ Reconstruction

In reconstructing the decay $K_S^0 \to \pi^0\ \pi^0$ we consider cases where the π^0 s are resolved as 2 distinct photons (*composite* π^0) and the cases where the π^0 is observed as a single cluster in the EMC (*merged* π^0). All *composite* π^0 s are considered, as well as all *merged* π^0 above 1 GeV. If the same EMC cluster appears in both forms, preference is given to the composite π^0 candidate.

We use the following $K_S^0 \to \pi^0\ \pi^0$ reconstruction chain.

1. We combine all pairs of acceptable π^0, using the beamspot as the K_S^0 decay point.
2. We require $E_{K_S^0} > 800\,\mathrm{MeV}$ with π^0 and K_S^0 masses in the 110–155 MeV/c^2 and 300–800 MeV/c^2 regions respectively.
3. For each photon pair we perform a constrained fit of their invariant mass to the known π^0 mass and we repeat this assuming different decay points along the K_S^0 flight path, as defined by the beamspot and the initial K_S^0 momentum vector direction.
4. The point where the product fit probability $\mathrm{P}_1(\chi^2) \times \mathrm{P}_2(\chi^2)$ for the two π^0 s is maximum is taken as the K_S^0 decay vertex.
5. All K_S^0 candidates with flight length in the range from -10cm to +40cm and mass at the decay vertex between 440 and 555 MeV/c^2 are retained.

For the final analysis, the invariant mass of the K_S^0 candidate at the optimal vertex point is required to lie in the range 470 to 550 MeV.

Variable	Skim	Final Analysis
$E_{K^0_S}$	$> 800\,\mathrm{MeV}$	-
$m(\pi^+\pi^-)$	[300,800] MeV/c^2	-
$m(\pi^+\pi^-)_vtx$	[440,555] MeV/c^2	[470,550] MeV/c^2
r	[-10,40] cm	-

Table 3.13: *Summary of cuts for* $K^0_S \to \pi^0\ \pi^0$ *selection..*

3.6.3 K^{*0} and K^{*+} Reconstruction

We reconstruct K^{*0} mesons with decays to $K^+\ \pi^-$ and $K^0_S\ \pi^0$ and K^{*+} mesons with decays to $K^0_S\ \pi^+$ and $K^+\ \pi^0$.

We use a common algorithm for reconstructing K^* decay.

1. π^0 s are reconstructed as composite (rather than merged) objects and required to have an invariant mass between 106 MeV and 153 MeV.

2. All candidate K^* s are required to be within 100 MeV of the nominal PDG value.

Depending on the K^* decay mode, additional criteria are applied for the final selection.

1. If there is a K^0_S in the final state we cut on α_{xy} and r as described in Sec. 3.6.2.

2. If these is a π^0 in the final state, we cut on $\cos(\theta_{K^*})$, the cosine of the angle between the kaon momentum vector defined in the K^* rest frame and the K^* momentum defined in the B rest frame.

3. Where there is a charged kaon in the final state it is required to satisfy the "Very Loose" kaon ID criteria.

Variable	Skim	Final Analysis
$m(K\pi)$	$m(K^*) \pm 100$ MeV/c^2	-
$m(\pi^0)$	[106,153] MeV/c^2	-
α_{xy}	-	$< 200\,\mathrm{mrad}$
$\cos(\theta_{K^*})$	-	< 0.95
r	-	> 1 mm
Kaon ID	-	"Very Loose"

Table 3.14: *Summary of cuts for K^* selection..*

3.6.4 D-Meson Reconstruction

The D-mesons used in this analysis are reconstructed in the decays to a single kaon or K^0_S and one or more pions.

3.6.4.1 D^0 and D^+ Reconstruction

D^0 candidates are reconstructed in the modes $D^0 \to K^-\pi^+$, $D^0 \to K^-\pi^+\pi^0$, $D^0 \to K^-\pi^+\pi^-\pi^+$, and $D^0 \to K^0_S\pi^+\pi^-$; while D^+ candidates are reconstructed in the modes $D^+ \to K^-\ \pi^+\ \pi^+$ and $D^+ \to K^0_S\ \pi^+$.

The following procedure is used for these reconstructions.

1. We combine all tracks, K^0_S and π^0 with momenta above 100 MeV/c into D candidates, assign the applicable masses to the tracks, and apply a cut of 40 MeV/c^2 (70 MeV/c^2 for the $D^0 \to K^-\pi^+\pi^0$ channel, to account the poorer π^0 resolution) about the nominal D-meson mass.

2. If the mode includes a charged kaon, we require that it satisfy the "Very Loose" kaon ID criteria.

3. We apply momentum cuts to each D and all its daughters, as listed in Tab. 3.6.4.1.

<table>
<tr><th>Variable</th><th>Skim</th><th>Final Analysis</th></tr>
<tr><td colspan="3">All modes</td></tr>
<tr><td>χ^2</td><td>-</td><td>> 0.001</td></tr>
<tr><td>$p(K^-, \pi^\pm, K^0_S)$</td><td>> 100 MeV/c</td><td>> 150 MeV/c</td></tr>
<tr><td>$p^*(D^0)$</td><td>> 1.3 GeV/c</td><td>-</td></tr>
<tr><td>$m(D)$</td><td>± 0.040 GeV/c^2</td><td>$\pm 3\sigma$ MeV/c^2</td></tr>
<tr><td>Kaon ID</td><td>“Very Loose”</td><td>-</td></tr>
<tr><td colspan="3">$D^0 \to K^- \pi^+$</td></tr>
<tr><td>$p(K^-)$</td><td>> 100 MeV/c</td><td>> 200 MeV/c</td></tr>
<tr><td>$p(\pi^+)$</td><td>> 100 MeV/c</td><td>> 200 MeV/c^2</td></tr>
<tr><td colspan="3">$D^0 \to K^- \ \pi^+ \ \pi^0$</td></tr>
<tr><td>$m(D)$</td><td>± 0.070 GeV/c^2</td><td>$\pm 3\sigma$ MeV/c^2</td></tr>
<tr><td>$m(\pi^+ \pi^0)$</td><td>-</td><td>$m(\rho) \pm 150$ MeV/c^2</td></tr>
<tr><td>$|\cos \theta^*_{K\pi}|$</td><td>-</td><td>> 0.4</td></tr>
<tr><td colspan="3">$D^+ \to K^- \ \pi^+ \ \pi^+$</td></tr>
<tr><td>$p(K^-)$</td><td>-</td><td>> 200 MeV/c</td></tr>
<tr><td colspan="3">$D^+ \to K^0_S \ \pi^+$</td></tr>
<tr><td>$p(\pi^+)$</td><td>-</td><td>> 200 MeV/c</td></tr>
</table>

Table 3.15: *Summary of cuts for D^0 and D^+ selection..*

During the final selection some we also cut on some additional quantities.

1. We vertex the D candidates, and cut on both the D invariant mass relative to the fitted D mass for the inclusive D spectra, as shown in Tab. 3.6.4.1, and the vertex χ^2 probability.

2. For $D^0 \to K^-\pi^+\pi^0$ mode, we attempt to select the dominant resonance, $D^0 \to K^-\rho^+$, $\rho^+ \to \pi^+\pi^0$. To this end, we cut on the $\pi^+\pi^0$ and the angle between the π^+ and K^- in the $\pi^+ \ \pi^0$ rest frame, $\theta^*_{K\pi}$ [91, 92].

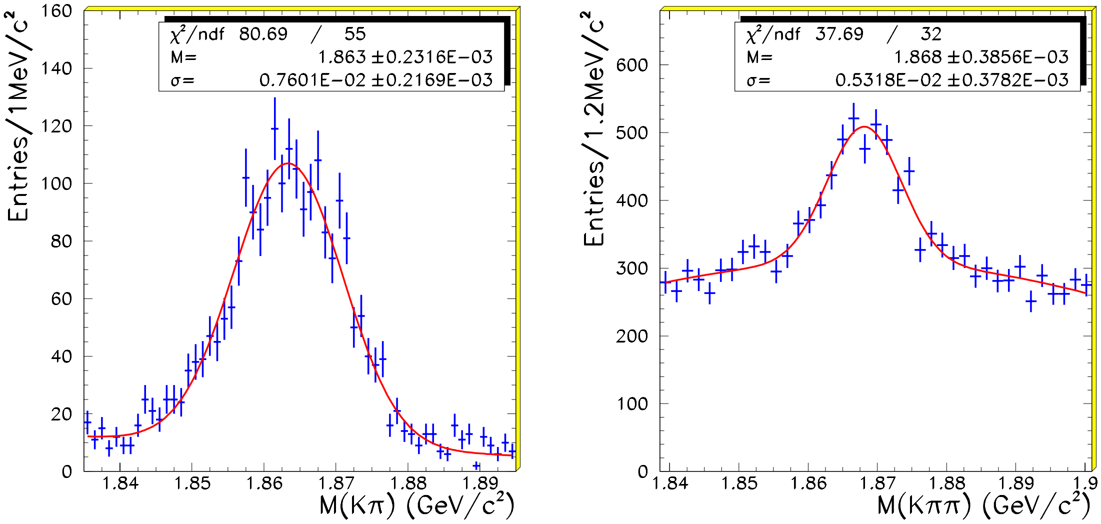

Figure 3.8: *Invariant mass of D candidates. The left plot show* $D^0 \to K^-\pi^+$*candidates, while the right plot shows* $D^+ \to K^-\ \pi^+\ \pi^+$ *candidates*

Mode	m_D (MeV/c^2)	σ_{m_D} (MeV/c^2)
$D^0 \to K^-\pi^+$	1863.1 ± 0.5	6.8 ± 0.6
$D^0 \to K^-\pi^+\pi^0$	1863.1 ± 1.4	11.5 ± 1.4
$D^0 \to K_s\pi^-\pi^+$	1863.3 ± 1.0	8.1 ± 1.0
$D^0 \to K^-\pi^+\pi^-\pi^+$	1863.7 ± 0.5	6.2 ± 0.8
$D^+ \to K_s\pi^+$	1863.2 ± 1.0	7.2 ± 0.9
$D^+ \to K^+\pi^-\pi^+$	1863.3 ± 0.5	6.5 ± 0.7

Table 3.16: *D-meson fitted masses from inclusive spectra..*

Criteria	Skim	Final Analysis
$D^{*+} \to D^+\ \pi^-$		
$\chi^2(beamspot)$	-	convergence
$m(D^0\pi^+) - m(D^0)$	[139,150] MeV/c^2	$\pm 3\sigma$ MeV/c^2
$p^*(\pi^+)$	[70,450] MeV/c	-
$D^{*0} \to D^0\ \pi^0$		
$m(D^0\pi^0) - m(D^0)$	[130,160] MeV/c^2	± 4 MeV/c^2
$p^*(\pi^0)$	[70,450] MeV/c	-

Table 3.17: *Summary of cuts for* D^{*0} *and* D^{*+} *selection.*

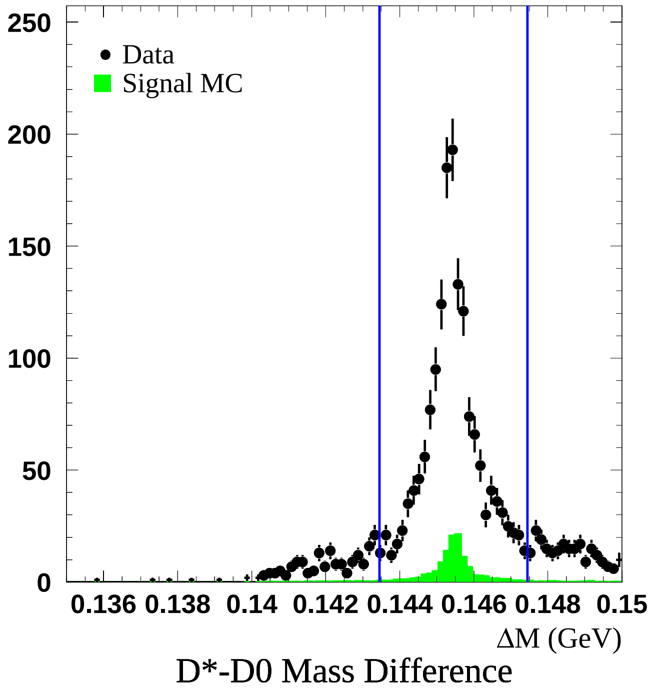

Figure 3.9: $m(D^{*+}\pi^{-}) - m(D^{0})$ *distribution for* D^{*+} *candidates in the* $\overline{B}^{0} \to D^{*+}\pi^{-}$, $D^{0} \to K^{-}\pi^{+}$ *mode. Vertical lines indicate selection criteria*

Mode	Δm (MeV/c^2)	$\sigma_{\Delta m}$ (MeV/c^2)
$D^{*+} \to D^0\pi^+$		
$D^0 \to K^-\pi^+$	145.45	0.8
$D^0 \to K^-\pi^+\pi^0$	145.54	1.1
$D^0 \to K^0_S\pi^+\pi^-$	145.45	0.9
$D^0 \to K^-\pi^+\pi^+\pi^-$	145.54	0.8
$D^{*0} \to D^0\pi^0$	142.2	1.0

Table 3.18: Δm *signal widths used for* D^* *candidate selection.*

3.6.4.2 D^* Reconstruction

We reconstruct D^{*0} mesons with decays to D^0 π^0 and D^{*+} mesons with decays to D^0 π^+ using the following process.

1. We form D^{*+} (D^{*0}) candidates by combining a D^0 with a pion (π^0) having momentum less between 70 and 450 MeV/c in the $\Upsilon(4S)$ frame.

2. For D^{*+} candidates, we perform a vertex fit for the D^{*+} using the constraint of the beam spot to improve the angular resolution for the soft pion and cut on the quantity $\Delta m \equiv m(D^0\pi^0) - m(D^0)$ relative to the fitted value from the inclusive D^{*+} spectrum (see Tab. 3.6.4.2). We use Δm rather than $m(D^0\pi^+)$ as a selection variable because $m(D^0\pi^+)$ is highly correlated with $m(D^0)$, whereas Δm is by construction uncorrelated. A fixed $\sigma = 30$ μm is used to model the beam spot spread in the vertical direction [89].

3. For D^{*0} candidates we cut on Δm without performing the vertex fit.

3.6.5 Charmonium Reconstruction

We reconstruct various charmonium decays involving dileptons; including J/ψ and $\psi(2S) \rightarrow \ell^+\ell^-$, as well as the cascade decays $\psi(2S) \rightarrow J/\psi\ \pi^+\pi^-$ and $\chi_{c1} \rightarrow J/\psi\gamma$, followed by $J/\psi \rightarrow \ell^+\ell^-$.

3.6.5.1 J/ψ and $\psi(2S) \rightarrow \ell^+\ell^-$ Reconstruction

We apply the following algorithm to reconstruct and select J/ψ and $\psi(2S) \rightarrow \ell^+\ell^-$ candidates.

1. Pairs of oppositely charged tracks are assigned the μ (e) mass and combined if their invariant mass calculated from four-vector addition at the origin lies in the range 2.5(2.3) to 3.5 GeV/c^2.

2. Since electrons and positrons undergo both final state radiation, and radiation of bremsstrahlung photons in the detector material, candidates the electron channel are subjected to a bremsstrahlung recovery process in which EMC clusters consistent with the bremsstrahlung hypothesis are combined with either leg of the e^+e^- pair [69].

3. The lepton pair are vertexed but no convergence criteria are required. If the vertexing does not converge four-vector addition is used to calculate the mass.

4. At this stage we cut on the invariant mass and apply particle ID criteria as listed in Tab. 3.6.5.1.

5. If a candidate ψ has the same track combination in both electron and muon channels, the muon channel candidate is discarded.

Variable	Skim	Final Analysis
All modes		
μ ID	1 “Loose” + 1 “MinIon”	-
e ID	1 (“Loose” or “noCal”)	1 (“Tight” or “noCal”)
$J/\psi \to e^+e^-$		
$m(e^+e^-)$	[2.3-3.5] GeV/c^2	[2.95,3.14] GeV/c^2
$J/\psi \to \mu^+\mu^-$		
$m(\mu^+\ \mu\mathrm{m})$	[2.8,3.5] GeV/c^2	[3.06,3.14] GeV/c^2
$\psi(2S) \to e^+e^-$		
$m(e^+e^-)$	[3.3,4.2] GeV/c^2	[3.44,3.74] GeV/c^2
$P^*(\psi(2S))$	-	[1.0,1.6] GeV/c
$\psi(2S) \to \mu^+\ \mu\mathrm{m}$		
$m(\mu^+\ \mu\mathrm{m})$	[3.3,4.2] GeV/c^2	[3.64,3.74] GeV/c^2
$P^*(\psi(2S))$	-	[1.0,1.6] GeV/c

Table 3.19: *Summary of cuts for* J/ψ *and* $\psi(2S) \to \ell^+\ell^-$ *selection..*

Variable	Skim	Final Analysis
$m(\pi^+\pi^-)$	[0.4,0.6] GeV/c^2	-
$m(\psi(2S))$	[3.3,4.2] GeV/c^2	-
$m(J/\psi\pi^+\pi^-) - m(J/\psi)$	-	± 0.015 GeV/c^2
p^*	[1.0,1.6] GeV/c	-

Table 3.20: *Summary of cuts for* $\psi(2S) \to J/\psi\ \pi^+\pi^-$ *selection..*

For the exclusive event selection of $\psi(2S)$ decays we cut on an additional quantity.

1. $P^*(\psi(2S))$, The momentum of the $\psi(2S)$ in the center-of-mass frame which is required to be consistent with the kinematics of $B \to \psi(2S)K$.

3.6.5.2 $\psi(2S) \to J/\psi\ \pi^+\pi^-$ Reconstruction

We also consider $\psi(2S) \to J/\psi\ \pi^+\pi^-$ followed by $J/\psi \to \ell^+\ell^-$ where $\ell^+\ell^-$ is either e or μ. For such decays we apply the following selection.

Variable	Skim	Final Analysis
Muon Id	-	1 “Loose” + 1 “Very Loose”
Electron Id	-	1 “Tight” + 1 (“Loose” or “noCal”)
$E(\gamma)$	> 150 MeV	-
A_{42}	< 0.15	-
$\theta(\gamma)$	[0.41,2.409]	-
$m(J/\psi\,\gamma) - m(J/\psi)$	[0.35,0.45] GeV/c^2	-

Table 3.21: *Summary of cuts for* $\chi_{c1} \to J/\psi\ \gamma$*;* $J/\psi \to \ell^+\ell^-$ *selection..*

1. The J/ψ candidates are mass constrained and combined with any pair of oppositely charged tracks to produce a $\psi(2S)$ candidate.
2. In addition, we require the cut on the $\pi^+\pi^-$ invariant mass and the momentum of the $\psi(2S)$ in the center-of-mass.

For the final selection, the difference in mass between the $\psi(2S)$ and J/ψ candidates is required to be within 15 MeV (again $\sim 3\sigma$) of the expected value.

3.6.5.3 χ_{c1} Reconstruction

χ_{c1} candidates are reconstructed via the decay $\chi_{c1} \to J/\psi\ \gamma$.

The χ_{c1} candidates are formed by combining the J/ψ candidates, after applying a mass constraint, and the photon candidates described in Sec. 3.3.2.

In addition, we tighten the cuts on the photon and the PID requirements. The γ and the J/ψ are then combined geometrically and vertexed and we cut on the reconstructed χ_{c1} and the J/ψ.

A mass constraint is applied to the χ_{c1} candidate for subsequent use.

3.6.6 B Candidate Reconstruction

In the open charm modes, we obtain B-meson candidates by combining a D or D^* candidate with a π, ρ or a_1 meson. In the charmonium modes we combining a J/ψ, $\psi(2S)$ or χ_{c1} candidate with a K^0_S K^* or K meson.

We apply the following additional requirements on the B candidate during the skimming procedure:

- the raw mass lies in the range 5.0 to 5.5 GeV/c^2;
- the reconstructed energy lies within ±300 MeV of one-half the center-the-mass energy.

The final B selection as well as the selection yields and efficiencies are described in the next sections.

3.7 Final B-Meson Selection

"It is hard to find some that has everything you are looking for."
"I just use my personality as a weeder."
— K. Gundersen and S. Looney

The final selection of B mesons to be used in later stages of the analysis is performed by running on the stored B candidates:

1. All the kinematic and particle identification cuts applied on the B decay products are tightened to the values used for the elusive analysis. This is necessary because the "skim" selections are shared with other analyses.
2. For certain decay channels with higher background rates additional cuts are introduced to control the background. All of these selection variables are describe in Sec. 3.7.1.

3. Two independent variables are used to perform the final selection and characterize the remaining background. This step includes selecting a single B from an event should more that one candidate still survive. This process is described in Sec. 3.7.2.

3.7.1 Kinematic Variables for Background Reduction

Our final background reduction cuts are applied to a few variables designed to take advantage of the kinematic difference between B-meson decays and combinatorial background from various sources.

1. We apply cuts on the shape of the event, to distinguish between $B^0\overline{B}^0$ events and light quark events.
2. For $J/\psi\ K_S^0$ and $\psi(2S)\ K_S^0$ events we also cut on helicity angles of the decays.

3.7.1.1 Light Quark Backgrounds

The general principle applied in rejection light quark combinatoric background is that the $\Upsilon(4S) \to B^0\overline{B}^0$ decays are more isotropic that the back-to-back jet-like continuum events. Accordingly, we apply the following cuts.

1. Each event is required to satisfy $R_2 < 0.5$ where R_2 is the ratio of the second Fox-Wolfram moment to the zeroth moment determined using charged tracks and unmatched neutral showers in the $\Upsilon(4S)$ frame.
2. We apply a mode-dependent cut on the cosine of the thrust angle $\cos\theta_{th}$. The thrust angle is defined as the angle between the thrust of the B and the thrust of the rest of the event.

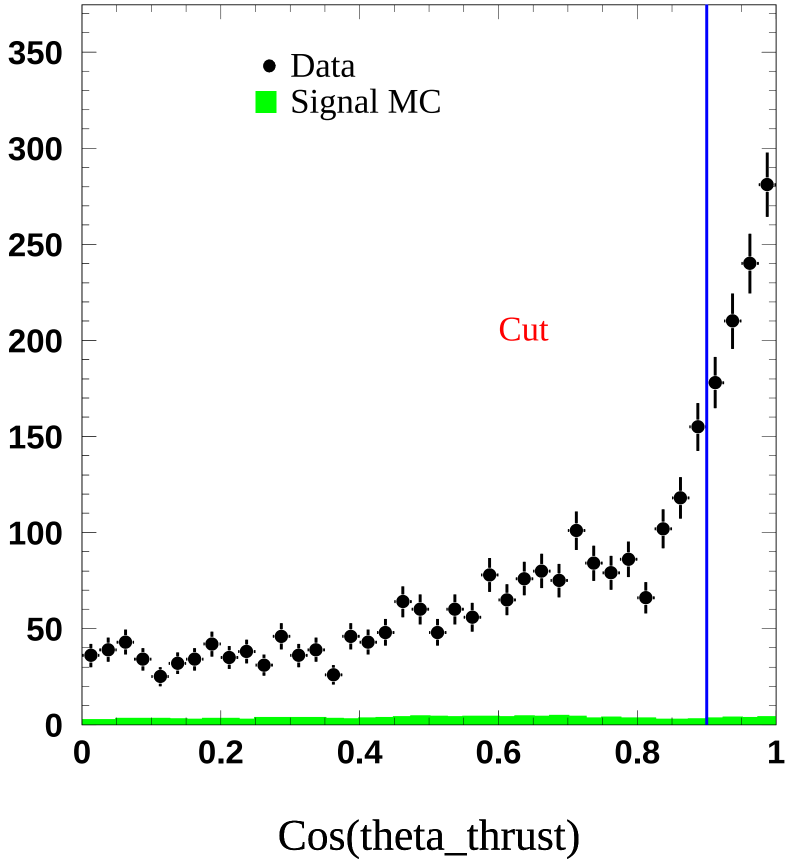

Figure 3.10: *Distribution of the opening angle,* θ_{th}*, between thrust axes for the* B *candidate and the remaining tracks in the event for the mode* $\overline{B}^0 \to D^{*+}\pi^-$, $D^0 \to K^-\pi^+$.

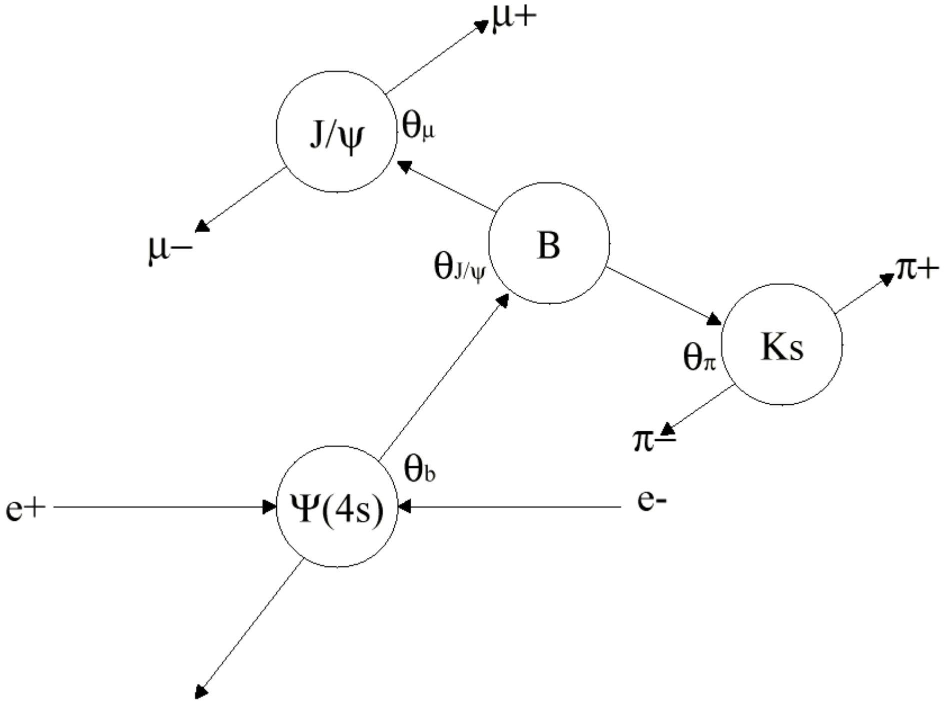

Figure 3.11: *Helicity angles for the decay* $\Upsilon(4S) \rightarrow B\overline{B} \rightarrow J/\psi$ *(*e^+e^- *or* $\mu^+\mu^-$*)+X*

3.7.1.2 Helicity Angles

The relevant kinematic angles for the decay $\Upsilon(4S) \rightarrow B\overline{B} \rightarrow J/\psi$ (e^+e^- or $\mu^+\mu^-$)+X are the helicity angles, θ_B, $\theta_{J/\psi}$, and θ_μ (see Fig. 3.11).

In the reaction, $Y \rightarrow X \rightarrow a + b$, the helicity angle of particle a is the angle measured in the rest frame of the decaying parent particle, X, between the direction of the decay daughter a and the direction of the grandparent particle Y.

For example, in the decay of a pseudo-scalar, $B \rightarrow J/\psi + X$, the helicities must have $\lambda_{J/\psi} = \lambda_X$ and the production angle, $\theta_{J/\psi}$, must be isotropic and the angular distribution is flat.

The backgrounds will tend to have different helicity distribution from the signal. The light quark backgrounds will be more jet like and will peak closer to the beam line direction. The

Mode	$\lvert\cos\theta_{th}\rvert$ cut	$\cos\theta_{\mu} cut$	
		e^+e^-	$\mu^+\ \mu^-$
$B^0 \to D^{*-}\pi^+$	No cut	-	
$B^0 \to D^{*-}\rho^+$	No cut	-	
$B^0 \to D^{*-}a_1^+$	No cut	-	
$B^0 \to D^-\pi^+$	< 0.9	-	
$B^0 \to D^-\rho^+$	< 0.8	-	
$B^0 \to D^-a_1^+$	< 0.7	-	
$B^+ \to D^{*0}\pi^+$	< 0.9	-	
$B^+ \to D^0\pi^+$	< 0.9	-	
$B^0 \to J/\psi\, K_s^0(\pi^+\pi^-)$	No cut	< 0.8	< 0.7
$B^0 \to J/\psi\, K_s^0(\pi^0\pi^0)$	No cut	< 0.9	< 0.8
$B^0 \to \psi(2S)K_s^0$	< 0.9	< 0.8	< 0.9
$B^0 \to \chi_{c1}K_s^0$	< 0.9	-	
$B^0 \to J/\psi\, K^{*0}$	No cut	-	
$B^+ \to J/\psi\, K^+$	No cut	< 0.8	< 0.9
$B^+ \to \psi(2S)K^+$	< 0.9	< 0.8	< 0.8
$B^+ \to \chi_{c1}K^+$	< 0.9	-	
$B^+ \to J/\psi\, K^{*+}$	No cut	-	

Table 3.22: *Thrust and helicity cuts applied in the each B decay channel under study..*

fake B candidates formed from light quark backgrounds will generally follow a $1 + \cos^2\theta_B$ angular distribution. The θ_μ helicity angle is especially useful in rejecting background as its $\cos\theta_\mu$ distribution is highly peaked at ±1 whereas the signal peaks at zero. A likely explanation of this feature is that forming a fake $J/\psi \rightarrow \ell^+\ell^-$ candidate from two random tracks requires the tracks to be back to back in separate jets. The third track (K^+, K^0_S) will lie in one of the two jets and will be close in phase space to one of the candidate leptons. Hence the θ_μ helicity angle for backgrounds will peak at $\cos\theta_\mu \approx \pm 1$.

3.7.2 ΔE and $m_{\rm ES}$

In order to select our final sample of B mesons we introduce two variables which take advantage of the precisely known kinematics of $\Upsilon(4S)$ decays.

1. In the case of a correctly reconstructed B meson produced by the decay of an $\Upsilon(4S)$, the measured energy of the B candidate, E^*_{meas}, must agree with the beam energy, E^*_{beam}. Therefore, we define ΔE to be the difference between the measured B candidate energy and beam energy in the $\Upsilon(4S)$ frame as:

$$\Delta E \;=\; E^*_{meas} - E^*_{beam}. \tag{3.1}$$

2. The B flight direction is correlated with the B momentum. To use this, we define an energy substituted B mass, $m_{\rm ES}$, as:

$$m^2_{ES} \;=\; (E^*_{beam})^2 - (p_B)^2. \tag{3.2}$$

These two constraints and the associated variable are by construction, largely independent of each other.

The resolution on $\sigma_{\Delta E}$ varies from 20 to 40 MeV depending on mode. The list of the modes we have studied and the corresponding values of $\sigma_{\Delta E}$ are given in Tabs. 3.8.2 and 3.8.3. Furthermore, the resolution in $m_{\rm ES}$ is typically about 2.6 MeV/c^2 for decay modes involving all-charged final states. And is usually dominated by the beam energy spread rather that the detector resolution. This is about a factor of 10 better than the resolution in invariant mass [93, 94].

Having defined these selection variables, we use the following method to select signal candidates.

1. We define our signal and background regions in terms of ΔE and $m_{\rm ES}$. For all modes, the region between 5.2 and 5.3 GeV/c^2 in $m_{\rm ES}$ and between ±300 MeV in ΔE is used to study the B candidates. It is often called the "grand sideband" region.

2. We measure the ΔE resolution by fitting a signal Gaussian plus a background polynomial to the ΔE distribution for all events in the grand sidebands.

3. We require ΔE be consistent with zero to within $\pm 2.5\sigma$. For the open charm modes, we fit the ΔE distribution for each mode, and apply cuts based on the the fit results, which are listed along with the yields in Tabs. 3.8.2 and 3.8.3. For the charmonium modes, we simply cut at approximately $\pm 2.5\sigma$; specifically, we cut at ±30 MeV for all the modes except $B^0 \to J/\psi\ K^0_S\ (K^0_S \to \pi^0\ \pi^0)$ which has much worse resolution owing to the π^0's and for which we cut at ±100 MeV.

4. No further cut is applied on $m_{\rm ES}$. The reason for this is that we wish to use $m_{\rm ES}$ during the fitting procedure to distinguish between signal and background events.

5. We allow only one candidate per event; in order to do this we select the candidate with the smallest absolute value for ΔE .

3.8 B-Meson Yields

> *"For me b-quarks are yellow. You said '50 Million B-pairs' and everything went yellow."*
> — P. Elmer

This section first describes the techniques used to measure the size and purity of the final sample of selected B decays. We then go on to use those quote the measured event yields for all of our samples.

3.8.1 Measuring Event Yields

Given the final B samples, we measure m_{ES} resolutions and event yields by fitting to the m_{ES} distribution of the remaining events. We parameterize our m_{ES} distribution for signal events with a Gaussian $\mathcal{G}$, and we use an Argus function [95] to parameterize the background distribution:

$$\begin{aligned} \mathcal{G}(m_{\mathrm{ES}}\ ; m_B, \sigma m_{\mathrm{ES}}) = &\quad \tfrac{1}{\sqrt{2\pi}\sigma m_{\mathrm{ES}}} \times \exp\left(-\tfrac{m_{\mathrm{ES}}\ - m_B}{2\sigma m_{\mathrm{ES}}}^2\right). && (3.3) \\ \mathcal{A}(m_{\mathrm{ES}}\ ; m_0, \xi) = &\quad \Theta(m_0 - m_{\mathrm{ES}}) m_{\mathrm{ES}} \left(1 - \left(\tfrac{m_{\mathrm{ES}}}{m_0}\right)^2\right)^{\frac{1}{2}} && (3.4) \\ & \quad \times \exp\left(\xi\left(1 - \left(\tfrac{m_{\mathrm{ES}}}{m_0}\right)^2\right)\right) \end{aligned}$$

And in terms of the Gaussian Fraction f_g, the combined signal and background distribution is:

$$\begin{aligned} F(m_{\mathrm{ES}}; f_g, m_B, \sigma m_{\mathrm{ES}}, m_0, \xi) = &\quad f_g \mathcal{G}(m_{\mathrm{ES}}\ ; m_B, \sigma m_{\mathrm{ES}}) && (3.5) \\ & \quad + (1 - f_g) \mathcal{A}(m_{\mathrm{ES}}\ ; m_0, \xi). \end{aligned}$$

For brevity, we will often denote by $\hat{\beta}$ all the fit parameters in the Gaussian and Argus functions.

The yield of candidate events in the data is determined using the following procedure [96, 65].

1. We fit the distribution of $m_{\rm ES}$ for candidates in the grand sidebands (see Sec. 3.7.1) which lie within ΔE signal band to Eq. (3.5). Only the Argus function shape parameter, ξ, and the Gaussian width, $\sigma m_{\rm ES}$ are allowed to float in the fit.

2. We count all the candidates inside the 3σ limit in $m_{\rm ES}$ to determine the number of candidates (N_{cand}).

3. We integrate the Argus function is across the 3σ limit in $m_{\rm ES}$ to determine the background (N_{Argus}).

4. The event yield is defined as:

$$N_{signal} = N_{cand} - N_{argus}. \tag{3.6}$$

This formulation does not account for the feed across background from types of decays which peak under the signal in $m_{\rm ES}$. The point is that many such background events come from similar events where a single particle has been mis-reconstructed, for example confusion of at charged pion with a charged kaon. Since such event would have the same time-structure as the signal events, they are treated as signal.

The obvious exception to this treatment is the case where a B^0 is reconstructed as a $\overline{B}^0$ or vice versa, owing to the replacement of a track which a kinematically similar neutral cluster. In general we call such events "peaking" background, and specifically treat to them

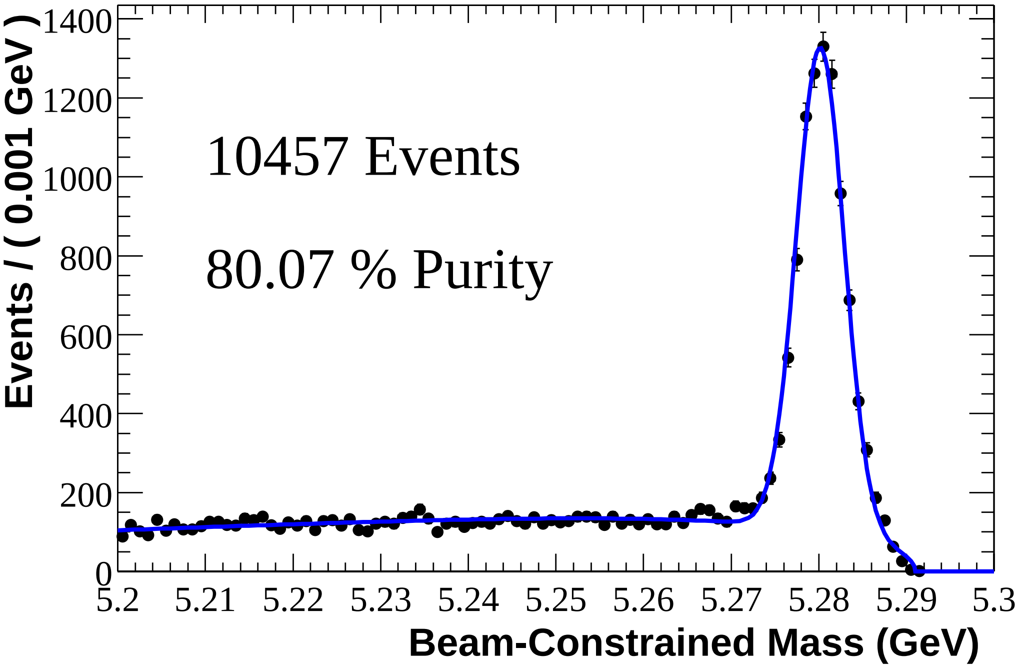

Figure 3.12: *Combined distribution for m_{ES} from all B^0 decay modes to "tagging" final states.*

in fitting the time-structure. In general the fraction of peaking background is determined from inclusive Monte Carlo.

3.8.2 B_{flav} Sample

The fit results for σm_{ES} and $\sigma_{\Delta E}$ as well as the observed yields and purities for B^0 decays to "tagging" final states are summarized in Tab. 3.8.2, and plot of the m_{ES} distribution summed over all the B_{flav} modes is shown in Fig. 3.12.

3.8.3 $B^{\pm}$ Sample

The fit results for σm_{ES} and $\sigma_{\Delta E}$ for B^+ decays are summarized in Tab. 3.8.3, and a plot of the m_{ES} distribution summed over all the B^+ modes is shown in Fig. 3.13.

B^0 mode	Secondary mode	$\sigma_{\Delta E}$ (MeV)	σm_{ES} (MeV)	Yield	Purity
$D^{*-}\pi^+$	$D^0 \to K^- \pi^+$	19.2	26	683 ± 13	96%
	$D^0 \to K^- \pi^+ \pi^0$	22.4	30	447 ± 15	91%
	$D^0 \to K^0_S \pi^+ \pi^-$	16.7	26	568 ± 13	95%
	$D^0 \to K^- \pi^+ \pi^+ \pi^-$	18.0	29	171 ± 8	91%
$D^{*-}\rho^+$	$D^0 \to K^- \pi^+$	23.2	31	511 ± 15	90%
	$D^0 \to K^- \pi^+ \pi^0$	26.7	30	224 ± 14	75%
	$D^0 \to K^0_S \pi^+ \pi^-$	24.1	30	398 ± 17	85%
	$D^0 \to K^- \pi^+ \pi^+ \pi^-$	25.1	35	83 ± 8	81%
$D^{*-}a_1^+$	$D^0 \to K^- \pi^+$	17.0	28	351 ± 14	87%
	$D^0 \to K^- \pi^+ \pi^0$	18.5	33	251 ± 14	82%
	$D^0 \to K^0_S \pi^+ \pi^-$	21.6	26	318 ± 16	73%
	$D^0 \to K^- \pi^+ \pi^+ \pi^-$	12.8	25	89 ± 9	66%
$D^-\pi^+$	$D^- \to K^+ \pi^- \pi^-$	18.5	25	2358 ± 40	83%
	$D^- \to K^0_S \pi^-$	15.6	27	247 ± 11	88%
$D^-\rho^+$	$D^- \to K^+ \pi^- \pi^-$	34.7	34	1577 ± 38	72%
	$D^- \to K^0_S \pi^-$	37.2	32	176 ± 11	75%
$D^-a_1^+$	$D^- \to K^+ \pi^- \pi^-$	12.1	25	1354 ± 35	58%
	$D^- \to K^0_S \pi^-$	12.5	23	164 ± 11	66%
All $B^0 \to D^{(*)-}X^+$			27	9991 ± 80	79%
$J/\psi\ K^{*0}\ (K^+ \pi^-)$	$J/\psi \to e^+e^-$	-	26	203 ± 11	88%
$J/\psi\ K^{*0}\ (K^+ \pi^-)$	$J/\psi \to \mu^+\mu^-$	-	27	221 ± 8	94%
All $B^0 \to c\bar{c}\ K^{*0}$			27	424 ± 14	91%
All B_{flav}			27	10457 ± 88	80%

Table 3.23: *Observed resolutions for* ΔE *and* m_{ES} *and yields for* B^0 *decay modes to "tagging" final states..*

B mode	Secondary mode	$\sigma_{\Delta E}$ (MeV)	σm_{ES} (MeV)	Yield	Purity
$D^{*0}\pi^+$	$D^0 \rightarrow K^- \ \pi^+$	19.2	25	2367 ± 40	92%
	$D^0 \rightarrow K^- \ \pi^+ \ \pi^0$	21.2	28	2367 ± 40	92%
	$D^0 \rightarrow K^0_S \ \pi^+ \ \pi^-$	-	24	2367 ± 40	92%
	$D^0 \rightarrow K^- \ \pi^+ \ \pi^+ \ \pi^-$	15.7	25	2367 ± 40	92%
$D^0\pi^+$	$D^0 \rightarrow K^- \ \pi^+$	17.9	29	2367 ± 40	92%
	$D^0 \rightarrow K^- \ \pi^+ \ \pi^0$	20.2	29	2367 ± 40	92%
	$D^0 \rightarrow K^0_S \ \pi^+ \ \pi^-$	16.3	29	2367 ± 40	92%
	$D^0 \rightarrow K^- \ \pi^+ \ \pi^+ \ \pi^-$	17.3	25	2367 ± 40	92%
All $B^+ \rightarrow D^{(*)0} X^+$			26	8428 ± 71	85%
$J/\psi \ K^+$	$J/\psi \rightarrow e^+e^-$	-	26	1701 ± 19	92%
	$J/\psi \rightarrow \mu^+\mu^-$	-	25	1582 ± 21	92%
$\psi(2S) \ K^+$	$\psi(2S) \rightarrow e^+e^-$	-	33	197 ± 13	80%
	$\psi(2S) \rightarrow \mu^+\mu^-$	-	22	141 ± 5	97%
	$\psi(2S) \rightarrow J/\psi \ \pi^+\pi^- \ (e^+e^-)$	-	24	225 ± 13	65%
	$\psi(2S) \rightarrow J/\psi \ \pi^+\pi^- \ (\mu^+\mu^-)$	-	19	215 ± 10	80%
$\chi_{c1} \ K^+$	$J/\psi \rightarrow e^+e^-$	-	36	363 ± 16	87%
	$J/\psi \rightarrow \mu^+\mu^-$	-	26	331 ± 15	79%
All $B^+ \rightarrow c\overline{c} \ K^+$			26	± 16	%
All $B^{\pm}$			26	14304 ± 87	88%

Table 3.24: *Observed resolutions for ΔE and m_{ES} and yields for $B^{\pm}$ decay modes..*

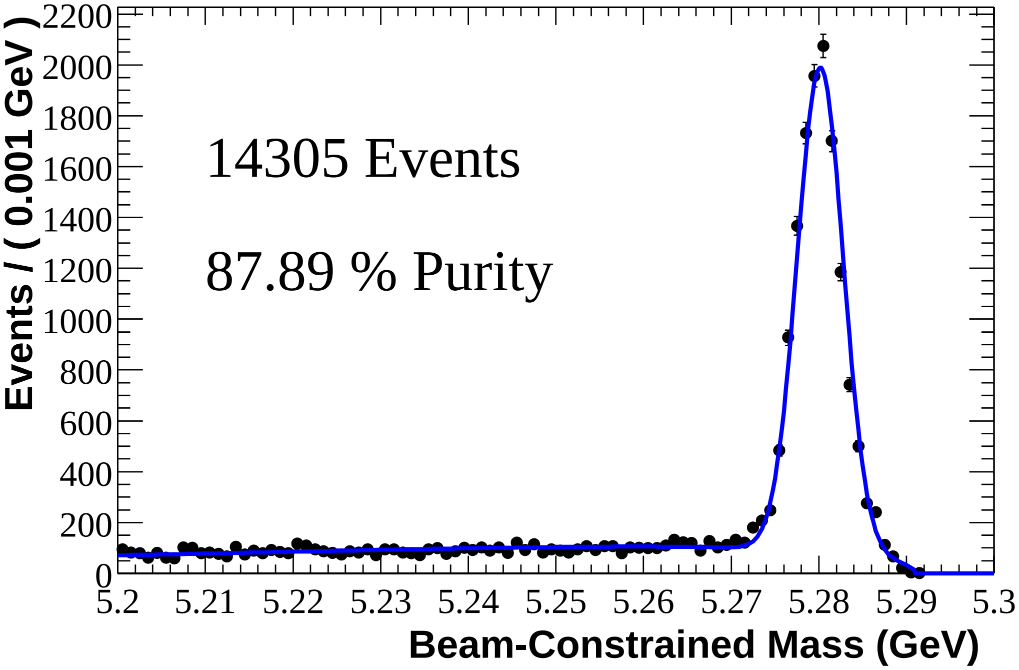

Figure 3.13: *Combined distribution for* m_{ES} *from all* $B^{\pm}$ *modes.*

3.8.4 $\mathcal{CP}$ Sample

The fit results for σm_{ES} for B^0 decays to $\mathcal{CP}$ eigenstates are summarized in Tab. 3.8.4; and a plot of the m_{ES} distribution summed over all the $\mathcal{CP}$ modes is shown in Fig. 3.14.

B^0 mode	Secondary mode	σm_{ES} (MeV)	Yield	Purity
$J/\psi\ K^0_S\ (\pi^+\pi^-)$	$J/\psi\ \to e^+e^-$	26	222 ± 5	98%
	$J/\psi\ \to \mu^+\mu^-$	25	222 ± 6	96%
$J/\psi\ K^0_S\ (\pi^0\ \pi^0)$	$J/\psi\ \to e^+e^-$	33	55 ± 5	92%
	$J/\psi\ \to \mu^+\mu^-$	36	50 ± 4	95%
$\psi(2S)\ K^0_S$	$\psi(2S) \to e^+e^-$	27	30 ± 4	83%
	$\psi(2S) \to \mu^+\mu^-$	23	21 ± 4	77%
	$\psi(2S) \to J/\psi\ \pi^+\pi^-\ (e^+e^-)$	32	38 ± 4	83%
	$\psi(2S) \to J/\psi\ \pi^+\pi^-\ (\mu^+\mu^-)$	26	24 ± 3	89%
$\chi_{c1}\ K^0_S$	$J/\psi\ \to e^+e^-$	28	32 ± 3	87%
	$J/\psi\ \to \mu^+\mu^-$	38	38 ± 4	80%
All $B^0 \to c\bar{c}\ K^0_S$		28	729 ± 15	94%
$J/\psi\ K^{*0}\ (K^0_S\ \pi^0)$	$J/\psi\ \to e^+e^-$	26	40 ± 4	82%
	$J/\psi\ \to \mu^+\mu^-$	26	54 ± 5	76%
All $B^0 \to c\bar{c}\ K^{*0}$		27	92 ± 10	76%
All $\mathcal{CP}$		28	822 ± 17	92%

Table 3.25: *Observed resolutions for m_{ES} and yields for B^0 decay modes to $\mathcal{CP}$ final states..*

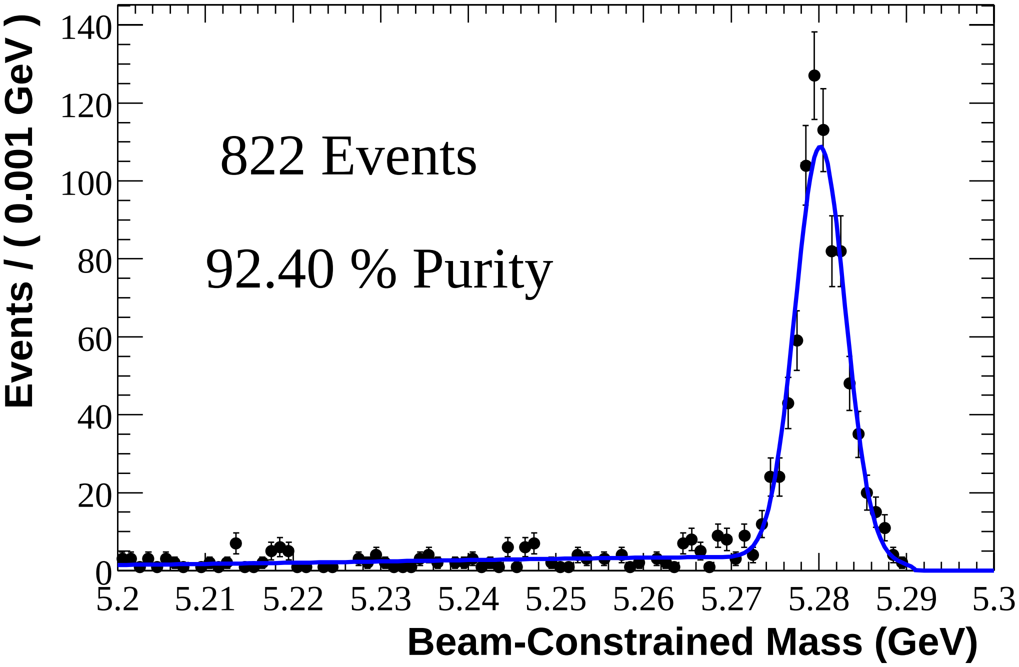

Figure 3.14: *Combined distribution for* m_{ES} *from all* B^0 *decay modes to* $\mathcal{CP}$ *final states.*

Chapter 4

Measuring Δt and the Resolution Function, $R(\delta t;\hat{\alpha})$

“Man who live in glass house; change in basement.”
— R. Miller

As mentioned in Sec. 1.5, precise measurements of decay time difference Δt, as well as an accurate representation of the resolution of those measurements are crucial to time-dependent analyses.

This chapter describes the algorithms used in *BABAR* to measure Δt. Sec. 4.1 provides a brief overview of the subject. Sec. 4.2 provides a brief description of basic vertexing algorithms. Sec. 4.3 then goes on to describe how those algorithms are applied to the specific situation where one B-meson has been fully reconstructed using the methods described in Chapter 3. Sec. 4.4 will describe the parameterization of the resolution function. Sec. 4.5 describes Monte Carlo studies on the vertexing performance and resolution functions, while Sec. 4.6 describes the technique we use to measure vertexing performance in data. Finally, Sec. 4.7 details the major systematic issues pertaining the measurement of Δt and the description of the Δt resolution.

We should point out here that measuring the B-meson lifetimes is a crucial aspect of understanding the vertexing performance. In fact, a cursory measurement of those lifetimes will be described in Sec. 4.6 [97, 98, 99].

4.1 Overview of Vertexing and Δt Measurement

> *"J'ai dit a mon pere, 'tous les copains commence a se marier et faire des gosses.' Il ma repondu, 'les meins commence a mourir.' "*
> — C. Metzger

As described in Sec. 2.2, the asymmetric design of the PEP-II collider, and the boost of $\beta\gamma \approx 0.56$ in the laboratory frame, has the purpose of obtaining a separation of $\langle \beta\gamma c\tau \rangle \approx 250\,\mu$m between the two B vertices. Furthermore, as we described in Sec. 2.1, the *BABAR* detector was designed to achieve a resolution of ~ 130 μm on Δz.

As we have explained in Sec. 1.5 we fully reconstruct only one B and then determine the distance, Δz, between the two B decays. Since the B-mesons are almost at rest in the CM frame, $\Delta t \sim \Delta z/\gamma\beta c$. Because of the absence of fragmentation particles coming from the $\Upsilon(4S)$ decay point, it is not possible to reconstruct the interaction point precisely, and therefore impossible to measure the decay length of each B separately.

The fully reconstructed B-meson (B_{rec}) is kinematically vertexed using all the particles of the decay chain. However, to retain high efficiency the other ("tagging" or "tag-side") B vertex (B_{tag}) must be measured using inclusive techniques. In fact, as we will see in Sec. 4.3 the B_{tag} vertex is reconstructed with the remaining charged tracks in the event.

This inclusive approach is complicated by the possible existence of short and long lived decay products of the "tagging" B , particularly D-mesons. Because of the boost, such particles tend to travel forwards and will thus bias the tag-vertex position forwards. Since

Δt is defined as $\Delta t \equiv t_{reco} - t_{tag}$ this will negatively bias Δt. In fact, the vertexing algorithm described in Sec. 4.3 is specifically designed to minimize the impact of such particles.

As discussed in Sec. 1.5.4 we also need to extract the resolution function $R(\delta t; \hat{\alpha})$. We have three choices as to how to this.

1. We can fit residual ($\delta t \equiv \Delta t - \Delta T_{true}$) distribution from Monte Carlo truth. This is quite simple, but since we hope to measure τ_{B^0} to $\sim 1\%$ and we can not hope to model the details of the SVT intrinsic hit resolution and internal alignment to such precision, this method is not sufficient for our purposes.

2. By fitting the Δt distribution in data for $R(\delta \Delta t)$ with physics quantities such as τ_{B^0} fixed to the world averages. Of course, we can not then later use the same resolution function to measure τ_{B^0}.

3. By simultaneously fitting the physics model and the resolution function. This method allows us to make independent measurements (which are also useful cross-checks) of the B-meson lifetimes. The complication here is that depending on the choice of parameterization, certain resolution function parameters can be highly correlated with the physics quantities. Therefore, some care is need in performing the fit.

In fact, in order to study systematic effects and have good confidence in our measured resolution function, we will use all three of these methods and check that they give consistent results.

Furthermore, in any of these cases, we are sensitive to the parameterization of $R(\delta t)$ that we choose. In fact, the choice of parameterization will be discussed closely is Secs. 4.5 and 4.4.

4.2 Vertexing Algorithms

"You can understand that people wouldn't want to use a physics program called 'Mr. Vertex'."
— I.J.Scott

This section will very briefly treat the basics of vertexing and kinematic fitting. It is intended to provide background to the systematic issues that will be discussed later, rather that to be a full-fledged discussion of vertexing techniques, which can be found in Refs. [100, 101, 102].

The basic point here is that in the *BABAR* physics analysis framework, vertexing is performed as a type of kinematic fitting wherein the measured track parameters are varied until a solution consistent with the tracks and other constraints are found.

4.2.1 Intial Vertex Estimate

A common issue in vertexing is that an initial guess of the location of the vertex is required; usually the primary interaction point can be used, but the convergence radius is of the order of a few centimeters. This is good enough for decays of short-lived particles (B and D) but not for long-lived particles (V^0's).

This problem is handled generally for all cases by solving numerically for the point of closest approach of the two tracks. When more than two tracks appear, the point of closest approach of the closest pair of tracks is used. When this search fails, the *BABAR* origin is assumed and the vertex is still attempted.

4.2.2 Vertexing General Formalism

The general algorithm we use for vertexing is based on the generalized least squares method using the well-known Lagrange multiplier technique [100].

In this formulation the general idea is that we have measured a set of quantities (for instance track parameters) $\boldsymbol{y}$. We allow for normally distributed variations $\boldsymbol{\delta}$ about the measured values. We then summarize unknowns which define the constraints (for example the vertex position) in a vector $\boldsymbol{x}$. The point then is that if we can relate the $\boldsymbol{x}$ and $\boldsymbol{\eta}$ by m constraint functions,

$$f_k(\boldsymbol{x}, \boldsymbol{\eta}) = f_k(\boldsymbol{x}, \boldsymbol{y} + \boldsymbol{\delta}) = 0, \quad k = 1, ..., m \tag{4.1}$$

which can be linearized at $\boldsymbol{x} = \boldsymbol{x}_0$ and $\boldsymbol{\eta} = \boldsymbol{\eta}_0$, the χ^2 can be expressed in terms of the values of the constraints at point $\boldsymbol{x}_0$ ($\boldsymbol{c}$), the derivatives (estimated at point $\boldsymbol{x}_0$, $\boldsymbol{\eta}_0$) of the constraints with respect to the unknowns ($\tilde{A}$) and parameters ($\tilde{B}$), the weight matrix of parameters ($\tilde{W}_y$) and the Lagrange multipliers $\boldsymbol{\mu}$:

$$\chi^2 = \boldsymbol{\delta}^T \tilde{W}_y \boldsymbol{\delta} + 2\boldsymbol{\mu}^T \left(\tilde{A}\boldsymbol{\xi} + \tilde{B}\boldsymbol{\delta} + \boldsymbol{c} \right), \tag{4.2}$$

where

$$\begin{aligned} \boldsymbol{\xi} = & \quad \boldsymbol{x} - \boldsymbol{x_0} \\ \boldsymbol{\delta} = & \quad \boldsymbol{\eta} - \boldsymbol{\eta_0}, \end{aligned} \tag{4.3}$$

Given Eq. (4.2) we can minimize χ^2 using Newton's Method. As a first approximation, we take $\boldsymbol{\eta}_0 = \boldsymbol{y}$. This formulation also requires that we expand about an initial constraint condition $\boldsymbol{x}_0$. In this case of pure geometrical vertexing that is equivalent to saying that we must choose an initial guess vertex point, as discussed in Sec. 4.2.1.

When Eq. (4.1) are already linear, the final solution can be calculated in a single iteration. In general, however, the constraints are not linear, and better approximations are needed for subsequent iterations. These can be obtained by replacing $\boldsymbol{x}_0$, $\boldsymbol{\eta}_0 = \boldsymbol{y}$ by $\boldsymbol{x}$, $\boldsymbol{\eta}$ and recalculating the covariance matrix.

Finally, we note that since we have constructed a proper χ^2, our covariance matrix has physical meaning and we can use it to estimate the error on any of our vertex fit parameters. In particular, we will use $\sigma_{\Delta z}$ (or more exactly, $\sigma_{\Delta t}$) in our treatment of the resolution function.

4.2.3 Vertex Constraints

We use a variety of constraints in fitting $B^0\overline{B}^0$ events for the decay length difference Δt. Complete mathematical detail of these constraints are available in Refs. [103] and [89].

1. Vertex: requiring all the input particles to come from a common vertex. For each input candidate i there are two constraint equations, corresponding to the bend and non-bend planes, respectively.

2. Invariant mass: forcing the output candidate to have an invariant mass M.

3. Beam-spot: forcing the vertex position in the transverse plane (x, y) to be compatible with the beam-spot position. For this constraint, additional parameters (x_{BS}, y_{BS}) are introduced as in the fit and their covariance matrix is used to account for the actual size of the beam.

4. Beam-spot single track: equivalent to the previous one with the difference that it is applied to a single track (or candidate) instead of a vertex. It forces the track to intersect the beam-spot position in the transverse plane.

5. Beam energy: forcing a particle to have half of the beam energy in the reference frame of the $\Upsilon(4S)$, We use the χ^2 of the constraint to account for the energy spread of the beams.

6. Line-of-flight: the decay vertex is required to lie along the line defined by a fixed position (x_0, y_0, z_0) and direction of flight (t_x, t_y, t_z). The length s of the decay point along the line of flight is the only parameter left free.

The main point of this list is to illustrate that the Δt vertex resolution does not only depends on the reconstructed particle in the event, but also requires information about the energy and position of the beams.

4.3 Δz and Δt Algorithms

"You physicists think that you are so clever because you are always calling length 'time' and energy 'mass'."
— M. Frank

In this section we will describe both the algorithm used to measure the decay length difference Δz and the algorithm used to extract the proper time difference between the B-mesons [104, 105].

The single largest specific issue relating to the measurement of Δz is the selection of tracks to be used in the vertex. Because of the forward boost, using tracks which do not come from B decay will tend to bias the tag-side vertex forwards. In order to minimize this bias, we attempt to reject from consideration tracks which are inconsistent with having come directly a B decay vertex. Details of the tag-vertex selection are described in Secs. 4.3.1, 4.3.2 and 4.3.3.

Finally, in Sec. 4.3.4 we describe how we use some particular details of the Δz fitting algorithm to achieve an estimate of Δt which corrects for biases caused by the small momentum of the B-mesons in the CM frame.

4.3.1 Measuring Δz

We adopt a general strategy for finding Δz based on as much of the event information as possible.

1. First we reconstruct the signal B (B_{rec}).
2. We then build a list of all the remaining charged tracks in the event.
3. We remove charged tracks from reconstructed V^0's (K_S^0 and Λ), and add the corresponding composite track. Only V^0's which have SVT information are used, the remaining ones are simply removed.
4. We remove tracks identified as kaons from consideration as they are not likely to come directly from the B decay vertex.
5. Ideally, we should reconstruct D and D_s mesons, and for each successful candidate remove daughter tracks from the list and add the composite track. In practice the fraction of D-mesons we can recover is very small, so the vertex tag reconstruction benefits very little by using exclusive D-mesons. This step of the strategy has never been implemented.
6. We fit the tagging side candidates to a common vertex. During this process we iteratively remove the tracks which we believe came from secondary D-meson decays

because they are geometrically or kinematically inconsistent with coming from the same B decay vertex as the other tag-side tracks.

4.3.2 V^0's and γ Conversions in the Tag-Side Vertexing

Special care is put in the selection of the V^0 candidates since using fake candidates would likely have detrimental effect of the vertex performance. We apply the following cuts for K_S^0 (Λ) selection:

- the probability of the vertex fit (without mass constraint) must be higher than 0.1%;
- the decay length with respect to the primary vertex in the transverse plane must be higher than 2 (5) mm;
- the aperture angle of the daughters must be greater than 200 mrad;
- the mass of the reconstructed candidate must be within 7 (4) MeV of the nominal mass.

The purity within the mass window is estimated to be about 70% for both cases.

We also use a photon-conversion selection to veto tracks for vertexing. The selection cuts are the following:

- the xy (z) distance between the two tracks is required to be less than 5 mm (1 cm);
- the three-dimensional distance between the tracks must be <3 cm;
- the invariant mass of the pair of tracks must be < 10 MeV/c^2.

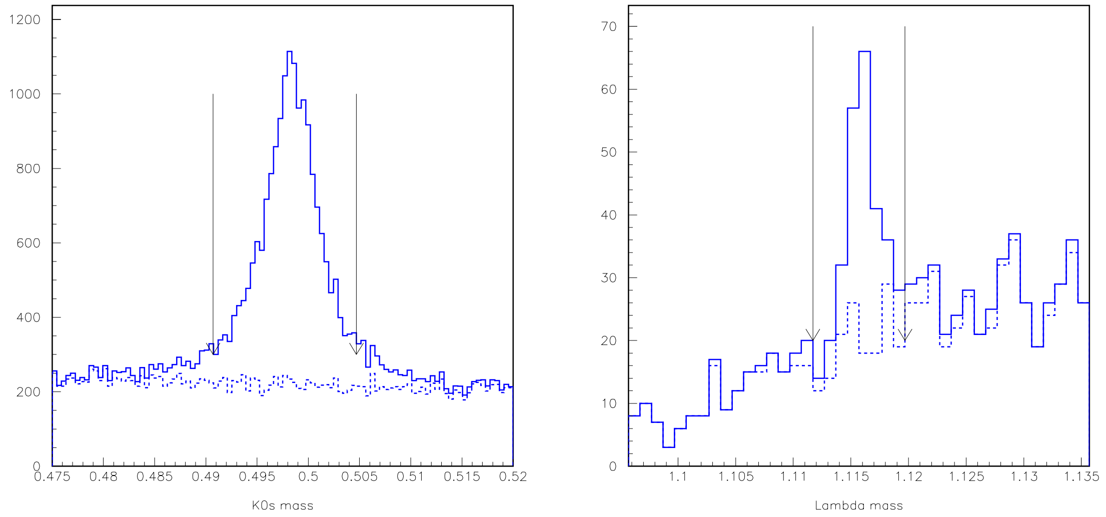

Figure 4.1: *Mass distribution of the* K_S^0 *and* Λ *candidates used for tag-side vertexing. Arrows indicate the mass cut applied.*

From Monte-Carlo truth studies, there is an indication that when using the composite K_S^0 and Λ there is a small (2-3%) reduction of the number of events at large residual and to a lesser extent at large pull. In all cases the vertex tag reconstruction efficiency is the same. The mean number of K_S^0 and Λ used to make a vertex tag is 0.09 and about 0.001, respectively. Furthermore, we see good agreement between the cases when the selection described above are used and when Monte Carlo truth is used, indicating that the above selections are reasonably accurate.

4.3.3 The Tag Vertex Algorithm

This algorithm tries to make use of all the position and kinematic constraints available in the $\Upsilon(4S) \to B^0\overline{B}^0$ decay.

1. The $B^0\overline{B}^0$ pair creation point is reconstructed by intersecting the reconstructed signal B_{rec} with the beam spot ellipsoid, the line of flight of the B_{tag} is given by the (reverse)

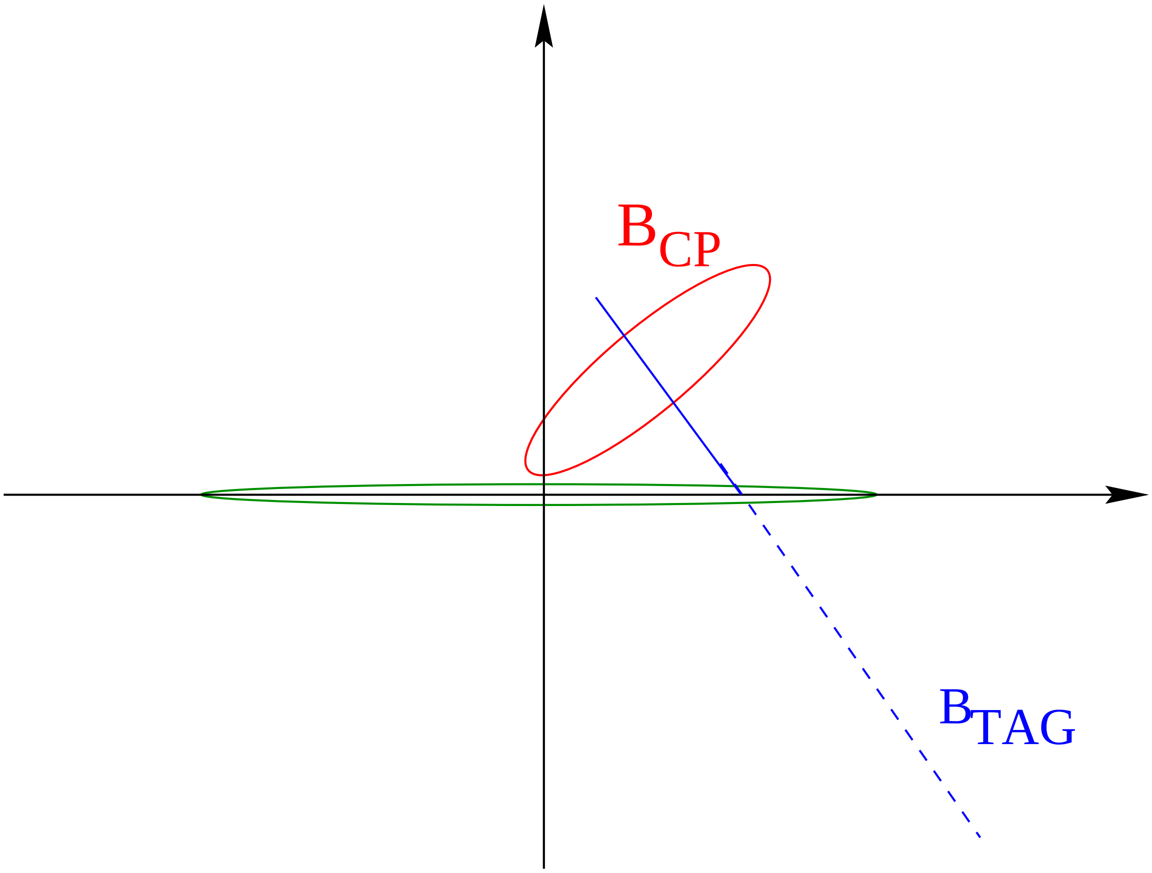

Figure 4.2: *Geometry of* $\Upsilon(4S) \rightarrow B^0\overline{B}^0$ *decay in transverse plane. The line of flight of the* B_{tag} *is given by the (reverse) momentum vector of the reconstructed* B_{rec} *and its vertex. The interaction point is the intersection of this line with the beam spot position in* y*.*

momentum vector of the reconstructed B_{rec} and its vertex in the CM frame, and the interaction point is estimated from the intersection of this line with the beam spot position in y. In practice, the information from the beam spot can be reduced to just the y coordinate. This is shown schematically in Fig. 4.2.

2. Due to the small size of the beam-spot in y, the decay path $L_z^{rec} = z_{rec} - z_{\Upsilon(4S)}$ of the B_{rec} can be extracted,
$$L_z^{rec} \approx \frac{y_{rec} - y_{\Upsilon}}{p_{y,rec}/p_{z,rec}}. \tag{4.4}$$
However, $\sigma(y_{rec}) \approx 45$ μm, the precision on L_z^{rec} is very poor.

3. From momentum conservation, the momentum of the tag B meson, B_{tag}, is known:
$$\boldsymbol{p}_{TAG} = \boldsymbol{p}_{\Upsilon(4S)} - \boldsymbol{p}_{rec}. \tag{4.5}$$

4. From B_{tag} momentum and the $B^0\overline{B}^0$ pair creation point we can form a "pseudo-track" which can be used to fit a common vertex as described in Sec. 4.3.1, above.

5. From the knowledge of $\boldsymbol{p}_{TAG}$ from Eq. (4.5) and the B_{tag} vertex position from the vertex fit, one can get an estimate of the decay path for the tag side, L_z^{TAG}. In the $\sigma_y(\Upsilon(4S)) \approx 0$ limit,
$$L_z^{TAG} \approx \frac{y_{TAG} - y_{\Upsilon}}{p_{y,TAG}/p_{z,TAG}}. \tag{4.6}$$
Unfortunately, as for the case of the B_{rec} case, the precision on L_z^{TAG} is extremely poor.

6. Owing to the pinched geometry, L_z^{rec} and L_z^{TAG} have a positive correlation close to 1. Therefore when we compute the difference $\Delta z = L_z^{rec} - L_z^{TAG}$ the effect of the correlation is basically removed, and this observable becomes much more precise than the separate

decay lengths. In fact, this is just another expression of the fact that we are really measuring Δz rather that the individual decay lengths L_z^{rec} and L_z^{TAG}.

The simultaneous vertex fit involving all the constraints makes the understanding of the algorithm rather difficult. Ref. [114] documents the systematic studies performed which help to understand the details. We list here some of the most important features.

1. When the B_{rec} direction is perpendicular to the y direction, ($\phi \sim 0$), the direct z constraints provided by the reconstructed B_{rec} do not help; rather the beam spot constraint applies directly to the B decay point, providing the whole resolution of the beam spot in y (~ 15 μm).

2. On the other hand, when the B_{rec} direction is along the y direction the B_{rec} constraints directly constraint on z, compensating the loss of beam spot constraint effectiveness as consequence of the B_{rec} transverse flight.

3. As the change of effective resolution of the beam spot from $\phi = 0$ to $\phi = \pi/2$ is not dramatic (from ~ 10 to ~ 30 μm) compared with the tracking resolution, the improvement in resolution (with respect to no constraints) is mostly provided by the beam spot alone.

4. A part of the rather marginal gain in resolution provided by the B_{rec} constraints, their purpose is basically to provide a more robust approach to select the tag side tracks, reducing charm contamination and fraction of outliers. Thus Δz resolution and scales are finally rather insensitive to resolution and scales in B_{rec}, and only $y - z$, $x - z$ correlations from the tagging side tracks and the reconstructed vertex, and the beam

spot determine the improvement in error on the reconstructed Δz, compared to the case when no constraints are applied.

This mechanism allows us to improve Δz track selection and resolution, without spoiling the very basic assumption in all the analyses that the resolution function is independent of the specific B_{rec} mode.

4.3.3.1 Convergence And Quality Criteria

The iterative procedure for track selection removes the candidate with the largest contribution to the total χ^2. The procedure is iterated until there are no tracks contributing more than 6 units to the χ^2. The use of the "pseudo-track" allows us recover events with only a single opposite track, making the algorithm extremely (98+ %) efficient.

However, since a well reconstructed vertex is required of study time distributions, we reject all events with either $|\Delta z| > 3mm$ or $\sigma\Delta z > 400\,\mu$m. These two cuts (particularly the second one) reduces the total vertexing efficiency to about 92 %.

4.3.4 Δz to Δt Conversion

A time-dependent analysis must estimate Δt for each event,

$$\Delta t = t_{rec} - t_{TAG} = M_B[\frac{z_{rec}}{p_{z,rec}} - \frac{z_{TAG}}{p_{z,TAG}}] \tag{4.7}$$

t_{rec} and t_{TAG} are, however, defined in different frames, therefore the transformation from Δz to Δt is not totally straightforward. To better understand these difficulties, we note that the distance Δz can be written in terms of t_{rec} and t_{TAG} as:

$$\Delta z = \beta_z \gamma \gamma^*_{rec} c(t_{rec} - t_{Tag}) + \gamma \beta^*_{rec} \gamma^*_{rec} \cos\theta^*_{rec} c(t_{rec} + t_{Tag}) \tag{4.8}$$

where β_z and γ are the same quantities as defined above. γ^*_{rec}, β^*_{rec} and $\cos\theta^*_{rec}$ are, respectively, the boost factor, velocity and angle with respect to the beam direction of the fully reconstructed B in the $\Upsilon(4S)$ frame. The above expression uses the fact that the two B-mesons are back-to-back in the CM frame.

As we don't know $t_{rec} + t_{Tag}$, we have to neglect it or at best put in some average value. Assuming an experiment with no polar angle bias and neglecting the event-by-event variation of $t_{rec} + t_{Tag}$ (*i.e.*due to changes in Δt, $\langle\cos\theta^*_{rec}\rangle = 0$) on average the second term of Eq. (4.8) vanishes. If we also neglect the energy release of the $\Upsilon(4S) \rightarrow B\overline{B}$ decay, then we have $\gamma^*_{rec} = 1$. These two assumptions lead to the equation

$$\Delta t = \Delta z / \gamma\beta_z c \tag{4.9}$$

where γ is the boost factor of the $\Upsilon(4S)$ in laboratory frame and β_z its velocity projected on the *BABAR* z axis. In *BABAR*, $\beta_z\gamma \approx 0.56$. Using β_z instead of β we account for the rotation in the (x, z) plane of the beam axis with respect to the *BABAR* z axis (tilt angle about 20 mrad), reducing the full boost by about 1.2 MeV (0.02%).

This approximation, for which the B momentum does not need to be measured, is commonly called *boost approximation.* Compared with the experimental resolution on Δz, the effects on Δt produced by this approximation are small (see below). However, this approach is a potential source of bias and systematic error in Δt [106, 107]. In particular, reference [106] shows analytically that for B lifetime measurements the bias introduced by this approach about 0.4%, which is non negligible for a precision measurement as we seek in *BABAR*.

This approach can be corrected, on average, to account for the small momentum of the

B's,

$$\Delta t = \Delta z / \gamma \beta_z c \gamma^*_{rec} \tag{4.10}$$

where $\gamma^*_{rec} \approx 1.002$.

The RMS contribution is then about 30 μm, to be compared to the total resolution of about 110 μm. Therefore, in terms of resolution the effect of neglecting the second term of Eq. (4.8) is small (about 4% in quadrature). Furthermore, if the resolution is extracted from data themselves from B lifetime and mixing fits, this effect is included automatically in any time-dependent analysis.

When one of the B's in the event is fully reconstructed we know with good precision $\cos\theta^*_{rec}$. The problem then is to get an estimate of $t_{rec}+t_{Tag}$. We could take $\langle t_{rec}+t_{Tag}\rangle = 2\tau_B$. This approach, however, does not account for the variation of $\langle t_{rec}+t_{Tag}\rangle$ with Δt. This effect can be taken into account by averaging over the Δt range,

$$\langle t_{rec} + t_{Tag} \rangle \mid_{\Delta t} = \tau_B + \mid \Delta t \mid \tag{4.11}$$

Thus Δt can be extracted combining Eqs. (4.8 and 4.11),

$$\Delta z = \beta_z \gamma \gamma^*_{rec} c \Delta t + \gamma \gamma^*_{rec} \frac{p^*_{z,rec}}{M_B} c(\tau_B + \mid \Delta t \mid). \tag{4.12}$$

This approach corrects for any possible polar angle bias of the experiment and minimizes the additional contribution to the RMS from the per-event variation of $t_{rec} + t_{Tag}$.

4.4 Parameterizing the Δt Resolution

"It doesn't matter how you do it. Nature doesn't have a resolution function.
— G. Raven

As we stated in Sec. 1.5, in order to be able to study time dependence of B-meson decays, we need to parameterize the Δt resolution of the *BABAR* detector. As there is no a priori reason to use a particular parameterization, this is a somewhat arbitrary choice. The only guiding principle are that our resolution parameterization must:

- have enough freedom to accurately describe the data;
- not bias our measurements of physics quantities.

Additionally, since we will need to extract the parameters by fitting to the data, Occam's razor applies: simpler models are preferable over more complicated ones.

4.4.1 Δt Per-Event Errors

In addition of providing a measurement of the Δt, the algorithms described above also give a error estimate, $\sigma_{\Delta t}$. In fact, because of the variety of tag-side topologies we consider, $\sigma_{\Delta t}$ varies widely throughout our sample. Distributions of $\sigma_{\Delta t}$ are shown for both data and Monte Carlo in Fig. 4.3. From top figure, we can also clearly see that the Monte Carlo over-estimates the vertex performance. The bottom figure clearly shows us that the $\sigma_{\Delta t}$ is well correlated with the width of the residual distribution. That is to say, that there is in fact very useful information contained in the value of $\sigma_{\Delta t}$. Therefore, we use it as a dependent parameter in our resolution function, $R(\Delta t, \sigma_{\Delta t})$. That is to say, our resolution function parameterization will depend on both Δt and $\sigma_{\Delta t}$ for each event.

4.4.2 Δt Resolution Function

We have chosen to parameterize our resolution function with three components.

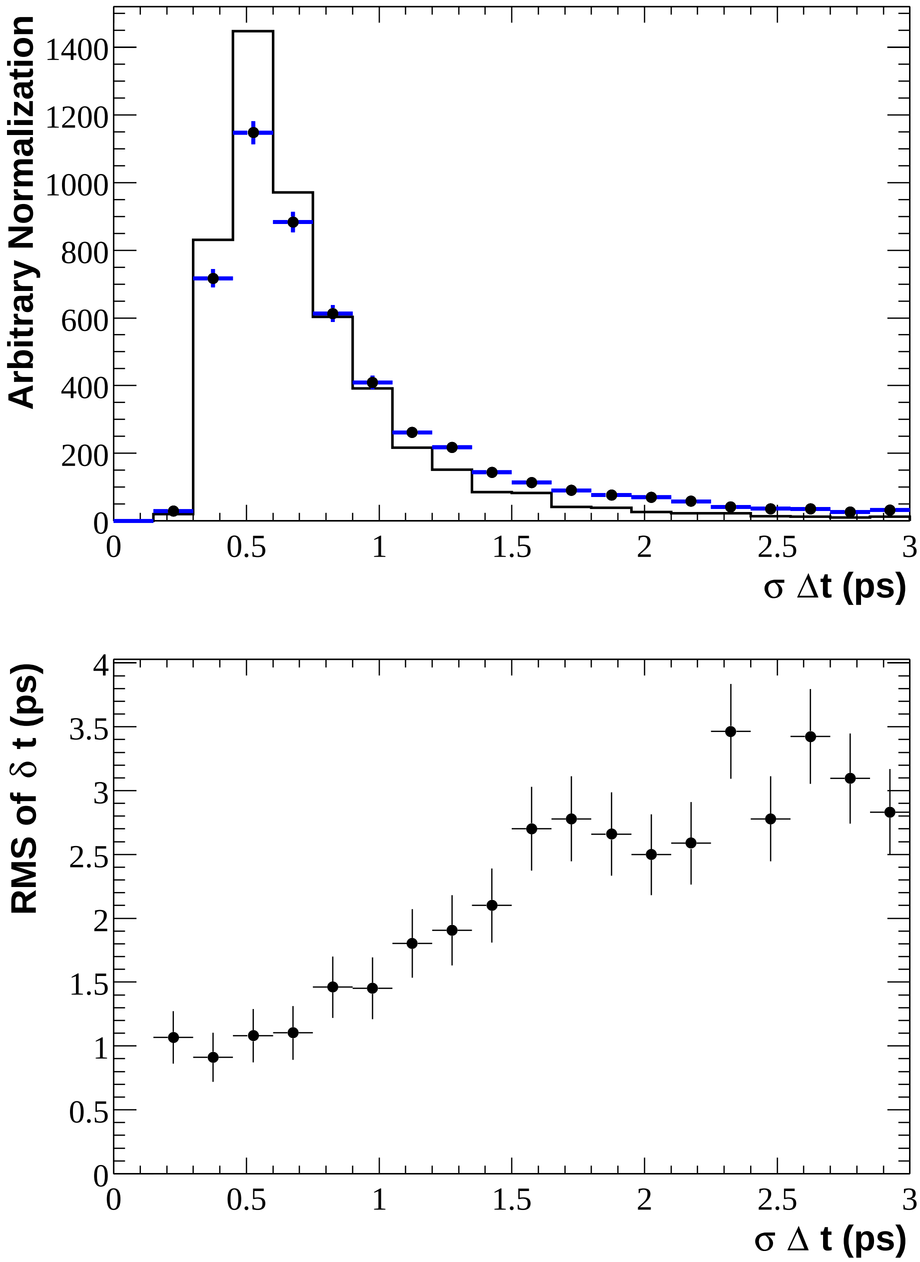

Figure 4.3: *Distributions of* $\sigma_{\Delta t}$. *In the left plot both the Monte Carlo (histogram) and* $B^0\overline{B}^0$ *signal data (points)* $\sigma_{\Delta t}$ *distributions are shown. Both histograms are normalized to 5000 events. In the right plot we show the RMS of the residual distribution plotted for various bins of* $\sigma_{\Delta t}$.

1. A core Gaussian, with width s and mean 0, scaled by the estimated error from the vertex fit.

2. An exponential of lifetime τ_r convoluted with the core Gaussian. The purpose of this component is represent the residual charm bias. This component is also scaled by the vertex error.

3. An outlier Gaussian, with width s_o and mean 0, in general s_o is fixed to be 8 ps. As this component represent poorly reconstructed events, there is no reason to believe that should depend on the vertex error, and is thus left unscaled.

Then, in addition to s, s_o, τ_r, we use the fraction of events in the outlier Gaussian (f_o) and the exponential (f_e) to write the resolution function:

$$\begin{aligned} R(\delta t;\hat{\alpha}) &= \frac{1-f_e-f_o}{\sqrt{2\pi}\cdot\sigma_i s}\cdot\exp\left(-\frac{\delta t^2}{2\sigma_i^2 s^2}\right) \\ &+ \frac{f_e}{2\cdot\sigma_i\tau_\mathrm{r}}\cdot\left[\exp\left(\frac{s^2}{2\tau_\mathrm{r}^2}+\frac{\delta t}{\sigma_i\tau_\mathrm{r}}\right)\cdot\mathrm{erfc}\left(\frac{s}{\sqrt{2}\tau_\mathrm{r}}+\frac{\delta t}{\sqrt{2}\cdot\sigma_i s}\right)\right] \\ &+ \frac{f_o}{\sqrt{2\pi}}\cdot\exp\left(-\frac{\delta t^2}{2{s_o}^2}\right) \end{aligned} \tag{4.13}$$

Extensive Monte-Carlo studies have shown that this parameterization gives less residual bias in fitting the B-meson lifetimes that alternate parameterizations involving only sums of Gaussians, even allowing the Gaussians to have non-zero means [107].

Finally, we note that independent studies have seen that the vertex resolution improved significantly between 1999-2000 (run 1) and 2001 (run 2) data [109]. Therefore we use slightly allow for different values of some of the fit parameters between the two runs. In fact we find that by splitting only the outlier Gaussian fraction f_o and the core scale factor s we are able to accurately reproduce both data sets.

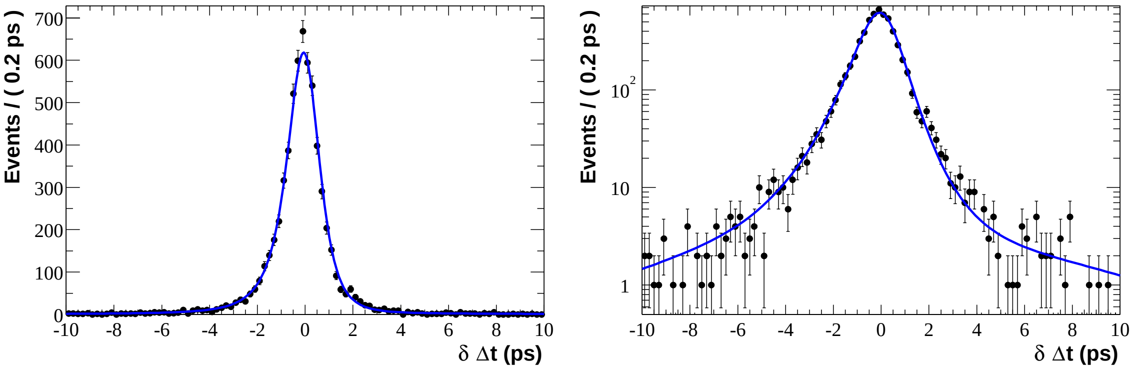

Figure 4.4: *Monte Carlo residual distributions, $R(\delta t)$: a fit (line) is overlayed on the Monte Carlo (points), and the same plot is shown both on linear (left) and logarithmic (right) scales.*

Parameter	Residual	Δt Distribution
Physics Parameters		
τ_{B^0}	-	1.535 ± 0.039
τ_{B^+}	-	1.665 ± 0.041
Resolution Function		
f_e	0.262 ± 0.026	0.260 ± 0.086
f_0	0.034 ± 0.003	0.021 ± 0.005
τ_{r}	1.111 ± 0.088	1.088 ± 0.355
s	1.153 ± 0.016	1.179 ± 0.076

Table 4.1: *Results of the resolution function fits to the Monte Carlo..*

4.5 Vertexing Performance on Monte Carlo

The first step in understanding the performance of the vertexing algorithms is to compare the reconstructed Δt against the true Δt in Monte Carlo.

All the studies performed through this section make use of Monte Carlo events with fully reconstructed B-meson decays into charmonium and open charm modes. The Monte Carlo sample used here is with a 'cocktail' of all those modes together.

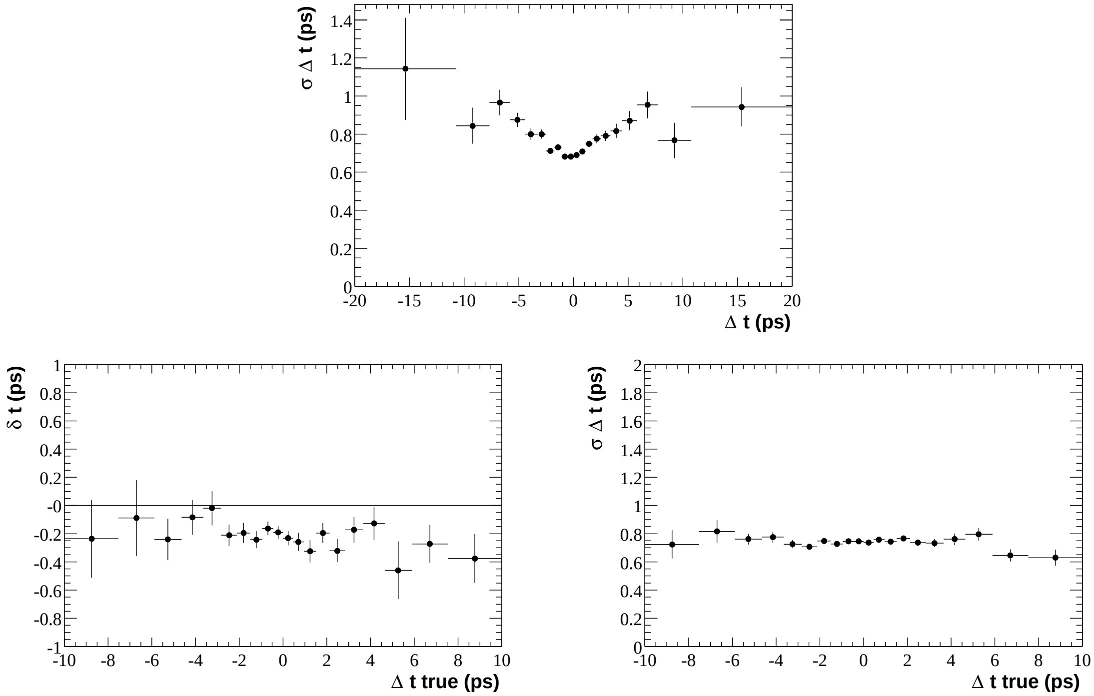

Figure 4.5: *Correlation plots between resolution variables: the top plot shows the average per-event error as a function of* Δt*; the bottom two plots show the average residual (left) and per-event error (right) as functions of* Δt_{true}.

4.5.1 Fitting the Δt Resolution Function in Monte Carlo

We fit the resolution function with Monte Carlo both directly from the residual distribution and by using the Δt distribution. The results both fits for a event sample similar in size to the data are shown in Tab. 4.5.1. Furthermore, the fit result are shown overlayed on the Monte Carlo residual distribution in Fig. 4.4.

4.5.2 Δt Residuals and Pulls

We performed checks to determine the dependence of the mean and width of the δt distribution on various quantities. These are summarized in Fig. 4.5. The bottom two plots show that neither the residual, nor the per-event error show any correlation with the true

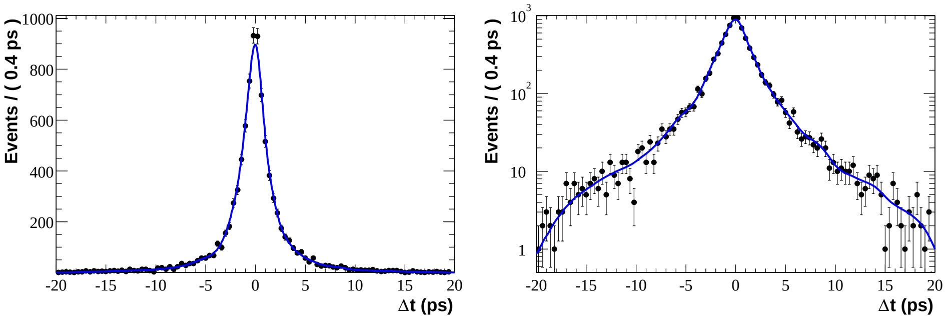

Figure 4.6: Δt *distributions for* $B^0\overline{B}^0$ m_{ES} *sideband events. The kernel estimation technique model is overlayed on the data; the same plot is shown both in linear (left) and logarithmic (right) scales.*

value of Δt. On the other hand the correlation seen in the top plot merely indicates that, as expected, event are large $|\Delta t|$ are more likely to have large per-event errors.

4.6 Vertexing Performance on Data and B Lifetimes

We now move on the discussion of simultaneous fit to the vertex resolution parameters $\hat{\alpha}$ and the B lifetimes, $\tau_{B^0}$and τ_{B^+}. In Secs. 4.6.1 and 4.6.2 we describe our model of the Δt structure of the background events, and in Sec. 4.6.3 we present the fit results. We note in particular that the fit results are not as precise as those from the full combined fit, which we describe in Chapter 6. In particular, our definitive measurements of the B lifetimes are stated in Sec. 6.3.1, while the treatment of systematic error is grouped with the error analyses of the other measurement in Sec. 6.5.

4.6.1 Describing the Δt Distribution for m_{ES} Sideband Events

Since the m_{ES} sideband events do not come from well reconstructed B-meson decays, they exhibit a different decay time-structure. Unless correctly modeled this will bias the lifetime and resolution function measurements on the signal evens. As described in Secs. 1.5 and 3.8

we use m_{ES} to assign as signal probability and construct the product likelihood:

$$f(m_{\mathrm{ES}}, \Delta t, \sigma\Delta t; \hat{\alpha}|\hat{\gamma}) = \mathcal{G}(m_{\mathrm{ES}}; \hat{\beta}) \times f_{sig}(\Delta t\ |\hat{\gamma}) \otimes R(\delta t|\hat{\gamma}) \qquad (4.14)$$
$$+\mathcal{A}(m_{\mathrm{ES}}; \hat{\beta}) \times K(\Delta t);$$

where we have denoted the background Δt distribution by $K(\Delta t)$.

We then use a kernel estimation technique to get an unbiased model of the $K(\Delta t)$ distribution for the background events. Basically, the kernel estimation technique models the Δt distribution as a sum of Gaussians, with one Gaussian at each data point. The Gaussian widths are calculated as function of the data density. As such, the background Δt distribution is an unbiased, parameterless model. As an example, the $B^0\overline{B}^0$ background model is shown overlayed on data is shown in Fig. 4.6. Further description of the use of kernel estimation technique for data modeling can be found in Ref. [110].

4.6.2 Describing the Δt Distribution for Peaking Backgrounds

Another issue we must address is the treatment of the Δt structure of background that peak in m_{ES}. Monte Carlo studies indicate that such backgrounds consist almost entirely of events where two soft particles have been interchanged. Since soft particles do not greatly affect the vertex position, the resolution for these events is very similar to the resolution for correctly reconstructed events. However, depending of which types of particles have been interchanged, it is possible that the true Δt distribution is quite different.

For the purpose of measure the B-lifetimes and the resolution function, we distinguish two cases.

1. Interchange of two charged particles. In this case, the event will remain in the same sample, B^0 or $B^{\pm}$. Therefore, for the time being we consider such events as signal

events. We do note however, that it is possible for such an exchange to change the flavor of the B_{rec}. This will be a more significant issue once we consider flavor tagging.

2. Interchange of a charged particle with a neutral particle. In this case, the event will switch between the B^0 and $B^{\pm}$ samples. Therefore, we consider such events as a separate background. From inclusive Monte Carlo studies [111], we believe that such events correspond to roughly 1.5% of both our B_{flav} and $B^{\pm}$ samples.

Therefore, while fitting, we add a 1.5% contribution of "peaking background" with exactly the same resolution function, but a different lifetime to each of our Δt signal models:

$$\begin{aligned} F_{flav}(\Delta t; \hat{\alpha}, f_{peak}, \hat{\gamma}) &= (1 - f_{peak}) \times f_{flav}(\Delta t; \tau_{B^0}, \hat{\alpha}) \\ &\quad + f_{peak} \times f_{\pm}(\Delta t; \tau_{B^+}, \hat{\gamma}) \\ F_{\pm}(\Delta t; \hat{\alpha}, f_{peak}, \hat{\gamma}) &= (1 - f_{peak}) \times f_{\pm}(\Delta t; \tau_{B^+}, \hat{\alpha}) \\ &\quad + f_{peak} \times f_{flav}(\Delta t; \tau_{B^0}, \hat{\alpha}). \end{aligned} \tag{4.15}$$

Aside from performing systematic studies, we keep f_{peak} fixed to 0.005 throughout the analysis.

4.6.3 Results of the Fit to the Data

Fig. 4.7 shows the Δt distributions for neutral and charged B candidates in the signal region. For the fit above, we do not make an explicit distinction between signal and sideband regions. However, the plots in Fig. 4.7 include only those candidates likely to be signal events ($m_{ES} > 5.27\,\mathrm{GeV}/c^2$). Furthermore, the results of the fit are listed in Tab. 6.3.1.

The resolution function obtained from the fit above is in reasonable agreement with the Monte Carlo (see Tab. 4.5.1). The scale factor obtained for Monte Carlo is about 1.06,

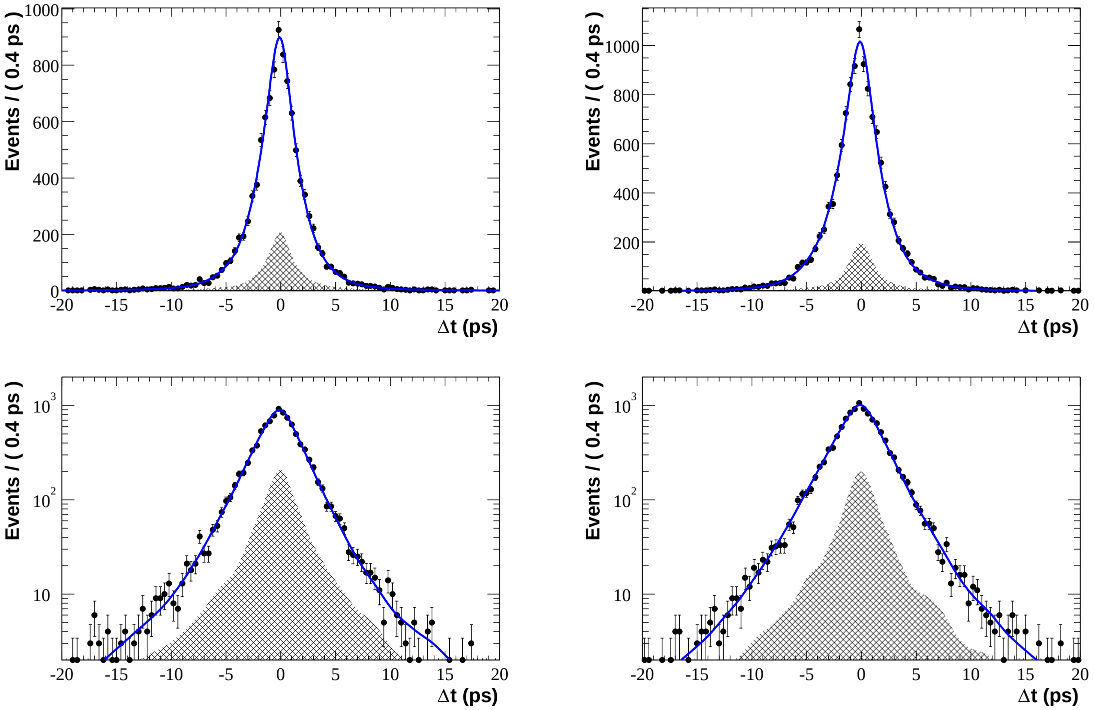

Figure 4.7: *Δt distributions with fit results overlayed. $B^0\overline{B}^0$ ($B^\pm$) candidates in the signal region are shown on left (right), and these plots are shown both on linear (top) and logarithmic (bottom) scales.*

Parameter	Value
Physics Parameters	
$\tau_{B^0}(ps)$	1.557 ± 0.029
$\tau_{B^+}(ps)$	1.679 ± 0.027
Resolution Function	
f_e	0.376 ± 0.128
f_o (run 1)	0.017 ± 0.008
f_o (run 2)	0.007 ± 0.005
$\tau_r(ps)$	0.772 ± 0.217
s_o (run 1)	1.367 ± 0.073
s_o (run 2)	1.197 ± 0.069

Table 4.2: *Summary of lifetime and resolution runction fit results.*

the scale factor obtained for data is 2σ higher than that value. The standard Monte Carlo is produced with perfect detector alignment. Monte Carlo studies of the effect of various misalignments on the Δz reconstruction are documented in [114]. Studies of Δz control samples [147] find the errors on Δz in data to be $\simeq 15$ % worse than in Monte Carlo.

4.7 Vertexing Systematics

> *"And if you set 'doVertex' to 'no' then it does the vertex."*
> — F. Pastore, "How to do the vertexing."

We now move on to a discussion of the systematic effects which may bias our measurement of either the resolution function $R(\delta t; \hat{\alpha})$ or the B lifetimes. In doing this we will separately quantify the possible bias on the resolution function and on the lifetimes. Many of these numbers are taken directly from studies performed for the original *BABAR* publications the B-lifetimes [112].

4.7.1 Resolution Function Parameterization

We have studied several alternative parameterization of the resolution function, including double and triple Gaussians, as well as scaling or not scaling the Gaussian means and/or the exponential lifetime τ_r by the per-event error $\sigma_{\Delta t}$ [143].

4.7.2 Consistency Between Sub-Samples

We have split the samples of B candidates into different subsets.

1. **B species (i.e. fit neutral and charged Bs separately)**, The results of the combined fit and two separate fits to the sample of neutral Bs and to the sample of charged Bs are compared in Tab. 4.7.2.

	combined fit	fit to $B^0/\overline{B}^0$ sample	fit to $B^{\pm}$ sample
$\tau_{B^0}(ps)$	1.557 ± 0.029	1.545 ± 0.0346	-
$\tau_{B^+}(ps)$	1.682 ± 0.027	-	1.693 ± 0.0323
Resolution Function			
f_e	0.376 ± 0.128	0.387 ± 0.117	0.359 ± 0.086
$f_o(run1)$	0.007 ± 0.005	0.007 ± 0.007	0.005 ± 0.005
$f_o(run2)$	0.017 ± 0.008	0.024 ± 0.011	0.012 ± 0.011
$\tau_r(ps)$	0.772 ± 0.217	0.842 ± 0.221	0.668 ± 0.238
$s(run1)$	1.367 ± 0.073	1.451 ± 0.098	1.348 ± 0.099
$s(run2)$	1.197 ± 0.069	1.254 ± 0.083	1.157 ± 0.112

Table 4.3: *Summary of the results of the combined fit and individual fits to the sample of* B^0 *and* $B^{\pm}$ *samples.*

Sample	free resolution function ps	resolution function fixed to result of full combined fit ps
$D^{(*)+}X^-$	1.545 ± 0.045	1.548
$\Psi K^{(*)0}$	1.602 ± 0.101	1.602
B^0	1.546 ± 0.044	1.579
$\overline{B}^0$	1.553 ± 0.042	1.540
All $B^0\overline{B}^0$	1.545 ± 0.036	1.557
$D^{(*)0}\pi^+$	1.784 ± 0.045	1.715
$\Psi K^{(*)+}$	1.678 ± 0.063	1.635
B^+	1.698 ± 0.036	
B^-	1.698 ± 0.036	
All $B^{\pm}$	1.698 ± 0.036	1.675

Table 4.4: *Results of Lifetime fits by subsample, both divided by decay modes and by* B_{rec} *flavor.*

2. B_{rec} **decay mode and flavor**, Tab. 4.7.2 shows the results of lifetime fits to subsamples that contain B candidates in a given subset of decay modes and B_{rec} flavors. Two fits are performed to each subsample. In the first fit, all resolution parameters are free, and in the second fit the three parameters of the signal resolution function are fixed to the values obtained from the full combined fit.

In none of these cases do we find a particularly noticeable effect. However we will later use these numbers to quantify possible systematic errors owing to different resolution function between sub-samples. Much high statistic studies performed with signal Monte Carlo showed differences of a few percent between the resolution function of B^0 and $B^{\pm}$ events, owing primarily to the different kaon content of the events.

4.7.3 Stability of the Vertexing Algorithm

Several studies have been performed to optimize the parameters of the vertexing algorithm [104, 89, 114]. These included turning on and off several features such as the photon conversion and kaon vetoes, removing or loosening various constraints, and changing the track rejection criteria in the tag-vertex algorithm. Although most of these action worsen the vertexing performance, none of them do so in a overly dramatic or unexpected manner. To quantify this statement, none of these algorithm changes result in a loss of more that $2-3\%$ of the selected events. Therefore, we are confident that the vertexing algorithm does not appear to have been over-tuned on Monte Carlo and is robust over the condition variation present in the data.

4.7.4 Beam Spot Effect on Vertexing Performance

Details about how the beam spot is determined can be found in Ref. [115]. The beamspot parameters are stored in the conditions database on a run-by-run basis with rolling calibration. During normal data taking, the rolling calibration can keep up with the slow beamspot movement (typically less than 10 μm/hour) mainly due to the diurnal motion of support tube with respect to the whole BaBar detector.

The average beamspot parameters are:

- position: (0.1,0.33,-0.9) cm;
- widths: (125,4.2,8500) μm;
- xz tilt: -18.8 mrad.

The errors on the mean are typically of the order of 1 μm on x and y. Although the error on the mean y position is typically around 1 μm, the beam position can move significantly compared with 1 μm during a run due to machine operation and diurnal motion.

By using a luminosity based calibration, we observe σ_y to be around $4 - 5$ μm. Furthermore, σ_y decreases from near $8 - 9$ μm as the bunch currents decrease during the course of each run [117]. Since σ_y is much smaller than the BaBar vertexing resolution, it is not monitored online. The 4.2 μm quoted above for σ_y is an estimate from luminosity measurement, smaller than the tracking resolution [118].

These number are very significant because of the role that the y position of the beamspot plays in defining the tag-side vertex [119]. Inaccuracies in modeling the beam-spot have been shown to produce azimuthal dependencies for the D-meson lifetime measurements [97].

4.7.5 Systematic Effects from Beam Energies

The beam energies have spreads of about 5.5 MeV (electrons) and 2.5 MeV (positions). The actual $\Upsilon(4S)$ momentum distribution is a convolution of the Gaussian beam overlap distribution with the Breit-Wigner probability for $\Upsilon(4S)$ production and the phase space for producing $B^0\overline{B}^0$ pairs. Generator level studies [107] show a Gaussian $\Upsilon(4S)$ momentum distribution with a width of about 6 MeV. The effect of the momentum spread is two-fold.

1. At Δz reconstruction level (as the algorithm make use of the total momentum constraint), secondly when estimating Δt, as described in Sec. 4.3.4. The impact of the spread when reconstructing Δz has been evaluated to be completely negligible since errors are dominated by reconstruction.

2. As already mentioned in Sec. 4.3.3, the energy spread of the beams affects the Δt estimation (via the boost parameters β and γ). The accuracy on $\beta_z\gamma$ using 2-prong events [116] has been evaluated to be better than 0.3% [**?**, 118]. Given this accuracy, a generator level study [107] has shown that this is also negligible, provided that a $\cos\theta^{CM}$ correction is used when estimating Δt.

4.7.6 Alignment Effects on Vertexing

In this section we discuss studies of the impact of residual misalignments on the reconstruction of vertices and decay-lengths in the $r\phi$-plane or in the z-direction.

We have performed extensive studies in which we introduced specific misalignment into the Monte Carlo between the full-detector simulation (GEANT) and reconstruction stages. In particular, a sample of 10k $B^- \to D^0\ \pi^-$; $D^0 \to K^-\pi^+$; $B^+ \to X$ Monte Carlo events has been reconstructed several times with different misalignments as well as with perfect alignment. The alignment sets included: perfect alignments, global shifts of the SVT w.r.t. the DCH, global rotations of the SVT, and various deformations of the SVT, included ellipsoidal deformation, systematic expansions, twist and sag distortions, shifts of the outer SVT layers w.r.t the inner layers and finally uncorrelated random translations of SVT wafers.

Most of the corresponding alignments come from a group of people who work on the SVT local alignment, who use them to study the SVT alignment procedure. The preliminary results of their studies [120, 121] indicate that the alignment procedure significantly reduces the systematic deformations listed above, at least after several iterations.

Although the distribution of the number of tracks in the tag-side fit, the error on Δt, and Δt do not change noticeably between these alignment sets; the tag-vertex χ^2 is noticeably affected by the misalignment, with increases of up to 3% in the numbers of tracks having $P(\chi^2) < 0.05$.

Chapter 5

B Flavor Tagging and Δm_d Measurement

"I just didn't want to listen to that terrible man pontificate."
— J. McFall

This chapter describes the algorithms used in *BABAR* to tag the flavor of the non-reconstructed B-meson (B_{tag}). Sec. 5.1 provides a brief overview of the subject. Sec. 5.2 provides a brief description of flavor-tagging algorithms and their inputs. Sec. 5.3 describes the functions that we use to parameterize the tagging performance. Sec. 5.4 describes Monte Carlo studies on the flavor-tagging performance while Sec. 5.5 describes the technique we use to measure flavor-tagging performance in data as well as detailing that performance. Finally, Sec. 5.6 details the major systematic issues pertaining to the measurement flavor-tagging performance.

We should point out here that measuring the B-mixing rate Δm_d is a crucial aspect of understanding the tagging performance [122, 123].. In fact, a cursory measurement of Δm_d will be described in Sec. 5.5 [124].

5.1 Overview of Flavor-Tagging

"It is red olive with a cute little green pimento."

— J. Wood, "Description of an anti-olive."

As we have explained in Sec. 1.5 in measurements of B mixing rates and time-dependent $\mathcal{CP}$-violating asymmetries, we fully reconstruct only one B and attempt to determine the flavor of the other B-meson by looking for a variety of "tagging" signatures.

1. Leptons from $B \rightarrow D\ell\nu$ decays carry the charge of the virtual W boson, thus "tagging" the B. Furthermore, such leptons tend to be highly energetic and are thus easily identified.
2. Single hard pions from $B \rightarrow D\pi$ decays also carry the charge of the virtual W.
3. In many events, there is at least one kaon with the same sign charge as the b quark.
4. Single soft pions from $B \rightarrow D^{*}\pi$, $D^{*} \rightarrow D\pi_{soft}$ decays carry the opposite sign charge from the b quark.

Fig. 5.1 shows the momentum spectrum of the various particle species in "tagging" Monte Carlo samples; we have put in multiplicative factor of -1 for opposite sign tracks to show the clear asymmetry between "right" sign and "wrong" sign particles.

Since our flavor tagging algorithms are not perfectly accurate, in order to extract physics quantities such as Δm_d we need to account for possible tagging errors or "mis-tags". In fact, in analogy with the vertex resolution function, it is possible to extract the resolution function $R(\delta\Delta t)$ in three ways.

1. By measuring the rate of "mistags" from Monte Carlo truth. This is quite simple, but since we hope to measure Δm_d to $\sim 1\%$ and we can not hope to model the details of the B decays to such precision, this method is not sufficient for our purposes.

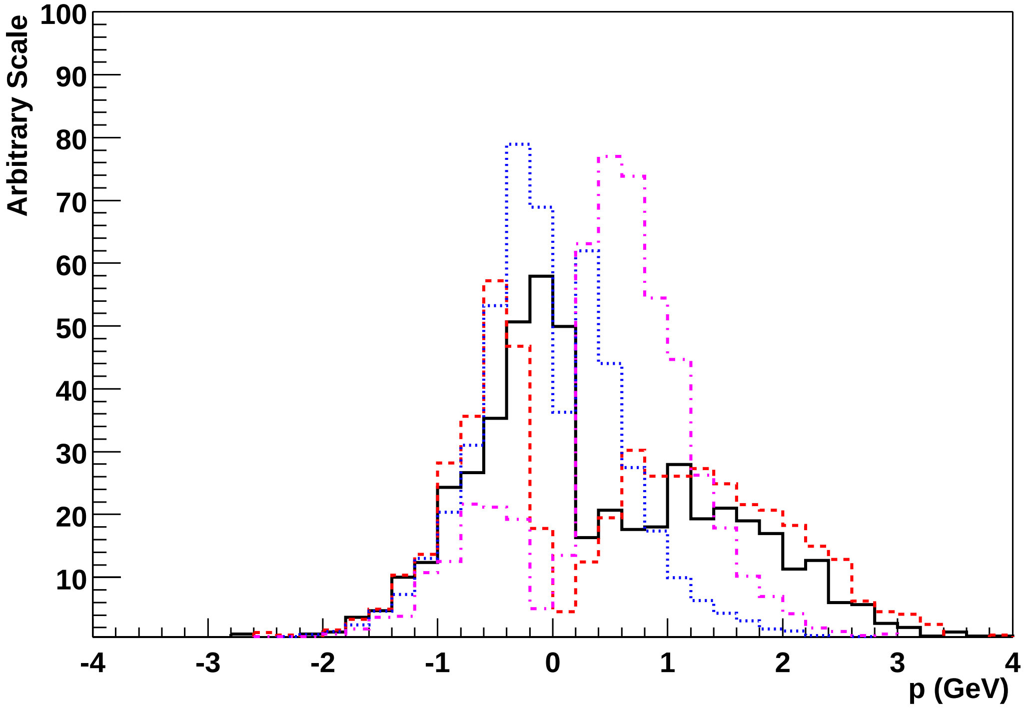

Figure 5.1: *CM momentum spectrum of tagging tracks from Monte Carlo truth. Electrons (solid line), muons (dashed line) pions (dashed line) and kaons (dot-dashed line) are all shown normalized with the same normalization. Wrong sign tracks are shown with negative values.*

2. By fitting the tagging variable and Δt distribution in data with physics quantities such as τ_{B^0} and Δm_d fixed to the world averages. Of course, in this we can not later use the same tagging performance parameters to measure τ_{B^0} or Δm_d.

3. By simultaneously fitting the physics model and tagging performance. We favor this latter method since it allows us to use our independent measurement of the B-mixing rate as a cross check.

5.1.1 Tagging Formalism

In this section we describe the main relations and define the quantities which describe the tagging performance.

As discussed in Sec. 1.5.3 tagging inaccuracies dilute the $\mathcal{CP}$-violating asymmetry A which we use to measure sin2β. Specifically if we define a mistag, w, as the fraction of events which are wrongly tagged by a tagging algorithm, then:

$$(1-2w)\sin 2\beta = A. \tag{5.1}$$

More precisely, w_{B^0} is the fraction of true B^0-decays which are incorrectly tagged as $\overline{B}^0$, and similarly for $w_{\overline{B}^0}$.

Furthermore, the statistical uncertainty on the measurement of A ($\sigma[A]$) is inversely proportional to the square-root of the number of events used in the analysis. Since these must be tagged to be used, $\sigma[A]^2$ is inversely proportional to fraction of events actually tagged, ϵ. As above, we define ϵ_{B^0} as the fraction of true B^0 which are assigned a tag (either a correct or incorrect one), and similarly for $\epsilon_{\overline{B}^0}$.

For later use, we define:

$$\begin{aligned} \epsilon = & \quad \tfrac{1}{2}(\epsilon_{B^0} + \epsilon_{\overline{B}^0}) \\ \Delta\epsilon = & \quad \epsilon_{B^0} - \epsilon_{\overline{B}^0} \\ w = & \quad \tfrac{1}{2}(w_{B^0} + w_{\overline{B}^0}) \\ \Delta w = & \quad w_{B^0} - w_{\overline{B}^0} \\ r = & \quad \tfrac{\epsilon_{\overline{B}^0}}{\epsilon_{B^0}}. \end{aligned} \tag{5.2}$$

We can express the statistical uncertainty on sin2β as: [125, 126]:

$$\sigma[\sin 2\beta] = \frac{const}{\sqrt{Q}} \tag{5.3}$$

where the Q summarizes the tagging performances so far as statistical uncertainty on sin2β is concerned. Q is usually referred to as the “tagging Quality factor”, though it is sometimes called the “absolute separation”.

In the simplest case of a cut-method applied on a single event-category, the quality factor is:

$$Q = \epsilon(1 - 2w)^2 \tag{5.4}$$

When the tagging algorithm uses several event-categories (c) (e.g. electron category, kaon category etc.), each with its own tagging efficiency ϵ_c and mistag rate w_c, the quality factor is the sum of the quality factor per category:

$$\begin{aligned} Q & = \sum_c Q_c \\ Q_c & = \epsilon_c s^2 \\ /_c & = 1 - 2w_c \end{aligned} \tag{5.5}$$

In the case that a continuous variable x_{tag} is used to tag, by extension from Eqs. (5.4 and 5.5) we have:

$$\begin{aligned}
Q &= \int n(x_{tag}) s^2(x_{tag}) dx_{tag} \\
s(x_{tag}) &= S(B_{rec}) \frac{a(x_{tag})}{n(x_{tag})} \\
a(x_{tag}) &= \frac{f(x_{tag}|B^0) - f(x_{tag}|\overline{B}^0)}{2} \\
n(x_{tag}) &= \frac{f(x_{tag}|B^0) + f(x_{tag}|\overline{B}^0)}{2}
\end{aligned} \tag{5.6}$$

where S(B_{rec}) is +1 (-1) for $B_{rec} = B^0$ ($B_{rec} = \overline{B}^0$) decays, $n(x_{tag})$ is the probability of observing an event at x_{tag} and $f(x_{tag}|B^0\ (\overline{B}^0))$ is the probability to observe a B^0 ($\overline{B}^0$) event at x_{tag}. Of course, the $f(x_{tag}|B^0\overline{B}^0)$ are not known a priori, and must be extracted. However, we note that on Monte Carlo it is possible to construct x_{tag} as the difference of probabilities such that:

$$\begin{aligned}
x_{tag} & \quad -1., 1. \\
x_{tag} \equiv & \quad s(x_{tag}).
\end{aligned} \tag{5.7}$$

Although this relationship will not hold exactly on data, we use it as a starting point and define two tagging functions $c(x_{tag})$ such that:

$$\begin{aligned}
f(x_{tag}|B^0) = & \quad c(x_{tag}|B^0) n(x_{tag}) \\
f(x_{tag}|\overline{B}^0) = & \quad c(x_{tag}|\overline{B}^0) n(x_{tag}).
\end{aligned} \tag{5.8}$$

From which we can write:

$$\begin{aligned} n(x_{tag}) = &\quad (c(x_{tag}|B^0) + c(x_{tag}|\overline{B}^0))n(x_{tag}) \\ a(x_{tag}) = &\quad (c(x_{tag}|B^0) - c(x_{tag}|\overline{B}^0))n(x_{tag}) \\ s(x_{tag}) = &\quad S(B_{rec})\dot{(}c(x_{tag}|B^0) - c(x_{tag}|\overline{B}^0)). \end{aligned} \tag{5.9}$$

Clearly the first of these relationships is simply a normalization constraint on the $c(x_{tag})$. Eventually we will parameterize and fit for the $c(x_{tag})$.

In general all of the above formulation assumes that we have equal reconstruction efficiencies r for B^0 and $\overline{B}^0$. If this is not true, we can write the tagging functions in terms of $\Delta r \equiv r(B^0) - r(\overline{B}^0)$ and fraction of mixed events χ:

$$\begin{aligned} n'(x_{tag}) &= n(x_{tag}) + \Delta r(1 - \frac{\chi}{2})a(x_{tag}) \\ a'(x_{tag}) &= a(x_{tag}) + \Delta r(1 - \frac{\chi}{2})n(x_{tag}). \\ s'(x_{tag}) &= \frac{s(x_{tag}) + \Delta r(1 - \frac{\chi}{2})}{1 + s(x_{tag})\Delta r(1 - \frac{\chi}{2})} \end{aligned} \tag{5.10}$$

5.2 Tagging Algorithm

"He is really good, he finds the Higgs anywhere she wants. If she wants the Higgs at 105 GeV*, he finds the Higgs at 105* GeV*."*
— J. Neilsen

We use a neural network based tagging algorithm "NetTagger". The algorithm output a value in the range $[-1, 1]$, and is trained using Monte Carlo truth to return value near $+1(-1)$ for "B^0-like" ("$\overline{B}^0$-like") events. Secs. 5.2.1 and 5.2.2 describe some pre-selection input to the tagging algorithm, and Sec. 5.2.3 describes both the tagging algorithm and its intermediate and final stage outputs.

Particle	Criteria	Additional Cuts
Electron	“Very Tight”	-
Muon	“Tight”	-
Kaon	“Very Loose”	KNet output > 0.45

Table 5.1: *PID selections and criteria used for tagging.*

As systematic cross check, we also use a category-based tagging algorithm, which is a hybrid of the NetTagger algorithm and a cut-based approach. Sec. 5.2.4 describes this hybrid algorithm, the “Elba” tagging algorithm.

5.2.1 Track Selection for Tagging

The tagging algorithms use all the charged tracks with cuts on the distance of closest approach to the beam spot (DOCA). A cut is made at $|\mathrm{Z}_{DOCA}| < 4.0$ cm. A cut is made at $\mathrm{D}_{DOCA} < 0.4$ cm. The comparison between data and Monte-Carlo is good in both cases, and the cuts are reasonably efficient.

Neutral objects are incorporated into the calculation of several quantities used by the NetTagger. They are selected requiring they not match to any charged object and have a minimum energy of 50 MeV. Neutral objects are used to calculate some event shape and missing energy quantities.

5.2.2 Particle ID for Tagging

For the cut-based parts of the tagging algorithm we assign fixed particle type to each track, while for the neural-networks pars we use the likelihoods for the different particle hypothesis from the different sub-detectors as described in Sec. 5.2.3.

In the former case, the electron, muon and kaon PID selectors listed in Tab. 5.2.2 are applied to each track and the choice of a particle type is made as follows.

1. If a track is accepted by only one selector, it is assigned the corresponding particle type.
2. If a track is selected both by the electron and the kaon selector, a cut on the likelihood ratio $\mathcal{L}_K/\mathcal{L}_e > 1.0$ is made to separate kaons and electrons. If there is valid information from the DIRC for $p > 0.6\,\mathrm{GeV}$, then the DIRC likelihood is used alone, otherwise the combined likelihood of the SVT, DCH, and DIRC is used.
3. If a track is selected both by the muon and the kaon selector, it is assumed to be a kaon decay and used as a kaon for tagging purposes.
4. For all other conflicts, or if the track is not selected by any of the PID selectors used for tagging, that track is considered to be a pion.

5.2.3 The NetTagger Algorithm

The NetTagger is a neural network-based flavour-tagging scheme. In NetTagger, all events are treated in the same fashion: a set of neural networks is applied to each event and the flavour of that event is determined by the outputs of these networks.

Flavor tagging is performed via a two-step approach; the first step uses a few specially designed neural networks called “feature nets” to identify potential flavour-carrying sources, and the second step uses a single neural network devoted to separating neutral B-mesons. We employ four feature nets to select potential flavor-carrying sources and a single tagging net uses these sources to tag the flavour of B-mesons. All the neural nets use a feed-forward model whose weights are corrected using back-propagation. Technical detail of the NetTagger neural network can be found in reference [127].

The NetTagger is trained using an Monte Carlo sample of 50k "tagging" events. This allows us to use the other 50k of "tagging" events for performance measurements.

Furthermore, we present here the all of the input variable used for the tagging selection. Primarily we wish to show the tagging power of each variable, and justify its use in the tagging selection. For each variable, the agreement between data and Monte Carlo has been studied, we discuss any notable differenece between data and Monte Carlo.

To study that agreement between data and Monte Carlo we use a background subtraction method.

1. We produce histograms for signal and sideband events, where signal (background) events are defined as events with m_{ES} greater than (less than) $5.27\,\mathrm{GeV}/c^2$.

2. For data, the background contribution to the signal histogram is estimated from the fit of a Gaussian and an Argus function to m_{ES}, and a corresponding fraction of the background histogram is subtracted from the signal histogram for each quantitiy studied.

3. For signal Monte Carlo, we use the tagging ($B^0 \rightarrow \pi^+\pi^-$; $\overline{B}^0 \rightarrow X$) Monte Carlo samples. For these sample the background contribution is very small and no subtraction is made.

We turn now to descriptions of the feature sub-nets.

5.2.3.1 Lepton Net (L-Net)

As seen in Fig. 5.1, the cleanest taggging signature is the presence of the direct lepton from the B_{tag} decay. Such leptons tend to have energies above 1 GeV and are accompanied by the missing energy (carried by the lepton neutrino) on the tag-side of the event.

For electrons the agreement is good, while there is a clear deficit of muons in data with respect to Monte Carlo, which can be explained by the decreased IFR efficiency.

To use these feature, we have designed L-Net, a track-based neural-network used to determine how compatible a track is with having come from a direct semi-leptonic b-decay; that is, L-Net is used to select primary leptons. Currently, this network uses 5 variables:

- eId, a binary variable set according to the "Very Tight" electron selection,
- muId: also a binary variable, set using the "Tight" muon selection,
- p^*, the momentum of the track evaluated in the center-of-mass frame,
- $\cos(\theta_{miss})$, the cosine of the angle which the track makes with respect to the missing momentum (neutrino) of the tagging B side, also evaluate in the CM frame,
- E_{90}^{W}, the energy in the virtual W-boson semi-sphere, assuming this track is the primary lepton.

Both $\cos(\theta_{miss})$ and E_{90}^{W} are intended to correlate lepton candidate with the missing energy and momentum carried by the neutrino.

We have compared the each of these distributions and as well as the multiplicity of positive and negative tracks from $B^0\overline{B}^0$ identified as likely primary electrons and muons. For

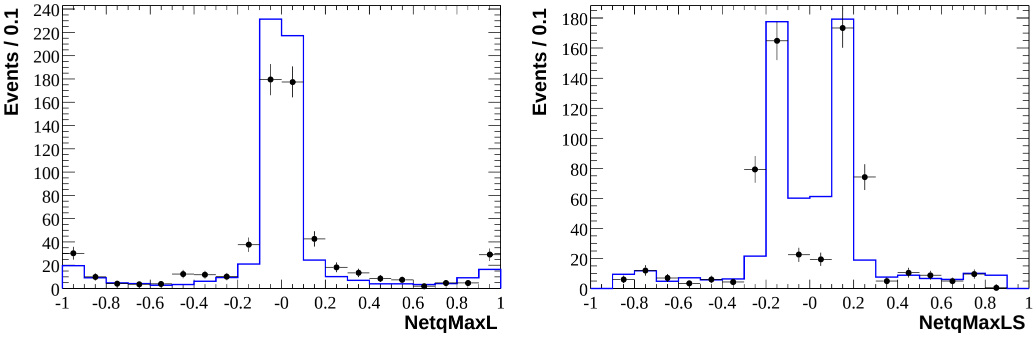

Figure 5.2: *The distributions of the lepton-net variables in Monte Carlo: QmaxL (left) and QmaxLS (right).*

electrons the agreement is good, while there is a clear deficit of muons in data with respect to Monte Carlo, which can be explained by the decreased IFR efficiency.

The L-Net is trained using primary leptons (muons and electrons) against all other charged tracks.

For use in the tagging net, a variable, "QmaxL" is defined which is the product of the charge and L-net output of the track with the largest L-Net output in an event. The distribution and performance of this variable are displayed in Fig. 5.2. We see a noticable difference, with the likilihood having of a good tagging lepton ($|QmaxL| > 0.5$) being $\sim 10\%$ smaller in data.

If only L-Net is used to tag B-mesons, a performance of $Q = 11.4\%$ is obtained.

5.2.3.2 Secondary Lepton Net (LS-Net)

Reverse sign leptons from cascade decays can contribute to tagging at a momentum p^* around 500 MeV/c.

The LS-Net is a track-based neural network used to tag the secondary ("wrong-sign") lepton; it uses the same variables as L-Net. The network is trained only on secondary leptons (muons and electrons) against all other charged tracks.

For use in the tagging net a variable, “QmaxLS”, is defined which is the product of the charge and the neural network output of the track with the largest LS-Net output in an event. The distribution and performance of this variable are shown in the Fig. 5.2.

If B-meson flavors are separated using only lepton information - QmaxL and QmaxLS - the performance is $Q = 14.5\%$.

Although the stand-alone performance of LS-Net is about $\Delta\mathrm{Q} \approx 0.03$, it turns out [128] that much of its performance comes from slow pions and not from cascade leptons. Since slow pion tagging is exploited in a much better way by the Pion net, the LS-Net is not used.

5.2.3.3 Kaon Net (K-Net)

As seen in Fig. 5.1, the presence of kaons of any momentum are more likely to carry the “right” sign than otherwise.

The K-Net is a track-based neural net used to determine how much each track is compatible with being a kaon. It uses as input likelihood ratios, defined as $L = \frac{L(kaon)}{L(kaon)+L(\pi)}$ and momentum information, to wit:

- the kaon likelihood ratios for the SVT, DCH, and DIRC;
- p_{lab}, the momentum of the track evaluated in the laboratory frame.

The K-Net is trained with true kaon tracks against all other charged tracks. After training, kaons produce a neural network output (neural network output) which is close to 1, while other tracks result in a number closer to zero. The K-Net outputs a single variable which determines the “kaon-ness” of a certain track. For use in the tagging net, a variable named “QmaxK” is defined as the product of the charge and the neural network output of

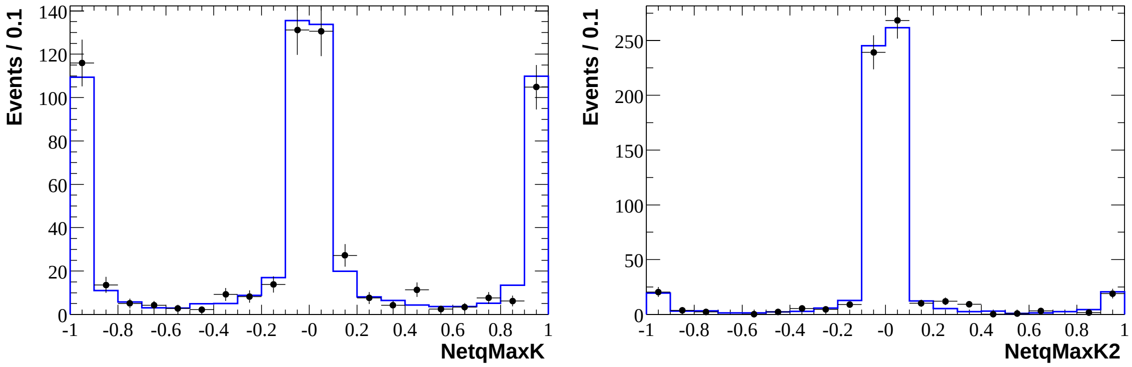

Figure 5.3: *The distribution of Kaon-Net variables in Monte Carlo: QmaxK (left) and QmaxK2 (right).*

the track with the largest K-Net output in an event. The distribution of QmaxK is shown in Fig. 5.3. Given the uncertainty in the rate of kaon from B decays, the excellent agreement between data and Monte Carlo is a pleasant surprise.

A possible secondary kaon can also be considered by defining “QmaxK2”, the product of the charge and the neural network output of the track with the second-largest K-Net output in an event. The distribution of this output is also shown in Fig. 5.3.

If only kaon information is used to tag the flavor of a B-decay, $Q = 20.4\%$ is obtained.

5.2.3.4 Slow Pion Net (Pi-Net)

Another source of tagging information are the slow pions from $D^{*\pm}$ decays, which, compared to lepton or kaon tags, have the opposite charge. The momentum spectrum in the center-of-mass system for any track, from Monte-Carlo $B^0\overline{B}^0$ decays (without mixing), for both charges is shown in Fig. 5.4. The D^* slow π are clearly visible as an excess of low momentum tracks.

The Pi-Net is a track-based neural network used to determine how compatible the track is with being a soft pion coming from D^* decays. The Pi-Net uses three input variables.

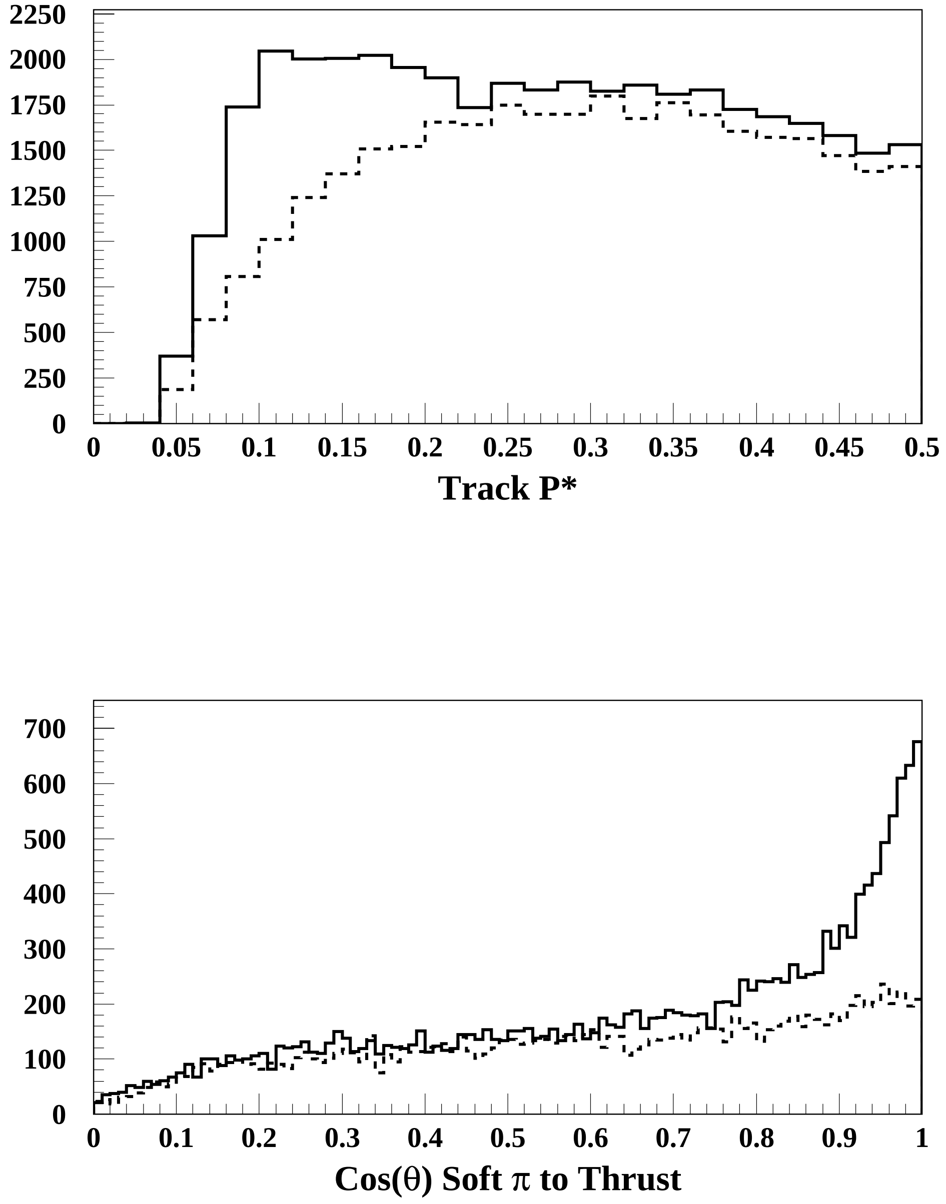

Figure 5.4: *Monte Carlo distributions for slow-pion tagging variables: Center-of-mass momentum* p^* *(top) and the* $\cos\theta$ *between tracks with* $p^* < 0.25$ *GeV and the thrust axis (vottom). In the solid (dashed) histogram is for the right-sign (wrong-sign) tracks.*

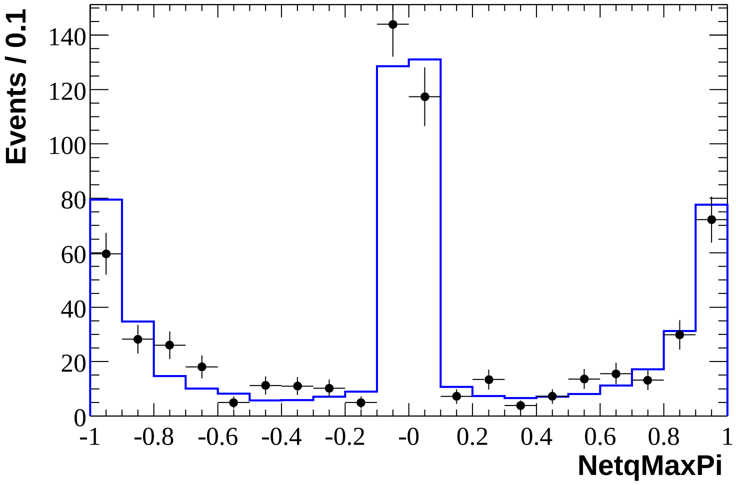

Figure 5.5: *The distribution of soft-pion net variable (QmaxPi) in Monte Carlo.*

- $\cos(\theta_{thrust})$, the cosine of the angle between the track and the thrust vector of the tag-side B, this is calculated using charged and neutral objects;

- Xp_{min}, if this is the lowest momentum track within a DOCA of 0.1cm of the interaction point, this is set to 1; otherwise, it is zero;

- p^*, as above.

The variable $\cos(\theta_{thrust})$ is designed to reduced the substantial background of low momentum tracks by correlating the direction of the slow π and the remaining tracks from the tagging B. Since the slow π and the D^0 are emitted nearly at rest in the D^* frame, they are both boosted in the same direction by the momentum of the $\dot{D^*}$ Thus we expect that the slow π direction in the B rest-frame will be along the direction of both the D^0 decay products and the remainder of the B decay products.

The Pi-Net is trained only on soft pions against all other charged tracks. For use in the tagging net, a variable, “QmaxPi”, is defined which is the product of the charge and the neural network output of the track with the largest Pi-Net output in an event. The output of the network is displayed in figure Fig. 5.5.

5.2.3.5 Event Tagging Net

The second step of NetTagger is to perform the actual flavor tagging. Here, a single neural network is developed with the sole purpose of separating B^0 from $\overline{B}^0$. The inputs to this tagging network are based on the feature net outputs, and two event-based variables.

- $P_{max} * Q_{max}$, the product of the momentum of the most energetic track and its charge.
- N_{imp}, the number of tracks with $d_0 > 0.1cm$.

$P_{max} * Q_{max}$ is intended to take advantage of the kinematics of decays when the virtual W manifests a single track, be it a pion or an un-identified lepton. N_{imp} is somewhat more subtle, it is a measure of the presence of a K_S^0 in the event, which would change the interpretation of any charged kaons also present.

The network is trained on Monte Carlo. Training is performed with B^0 events against $\overline{B}^0$ events. Events with an raw output around 0.5 have little tagging information, while those near 1 (0) are very "B^0-like" ("$\overline{B}^0$-like").

The final step is to convert the raw NetTagger output (x_{raw}) into a pseudo-probability. To do this, we use the Monte Carlo truth from the training sample to construct our tagging variable x_{tag}.

1. x_{tag} lies in the range [-1,1].
2. x_{tag} is defined by the equation:

$$x_{tag}(x_{raw}) \equiv \frac{P(x_{raw}|B^0) - P(x_{raw}|\overline{B}^0)}{P(x_{raw}|B^0) + P(x_{raw}|\overline{B}^0)}. \tag{5.11}$$

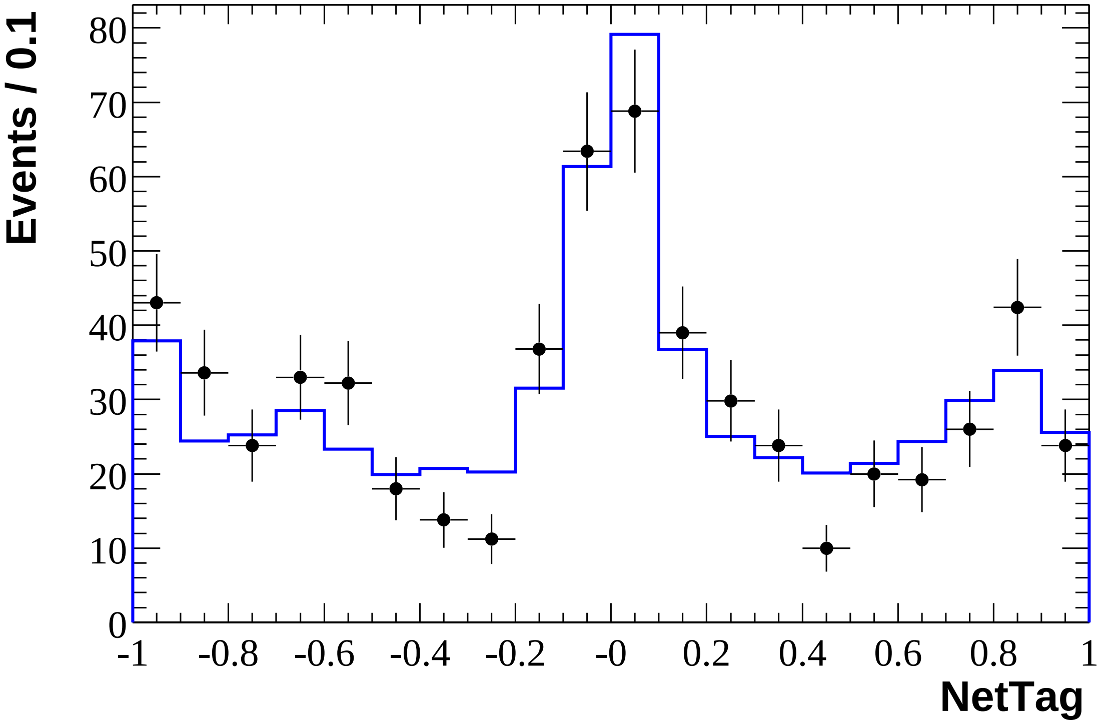

Figure 5.6: *NetTagger output on Monte Carlo.(line) and data (points).*

Fig. 5.6 shows the x_{tag} distribution for Monte Carlo Events. A tagging performance of $Q = 31.9\%$ is obtained. As discussed later, the tagging performance on data will be measured in a fit to Δm_d.

5.2.4 Hybrid Tagging Algorithm

The Elba Tagging algorithm [1] is a hybrid tagging algorithm that tags events with clearly identified tagging electrons, muons or kaons with a cut based algorithm and uses two categories defined by bins of the output of a neural network (NetTagger) to tag the remaining events.

---

[1] The name of the algorithm comes from the fact that this algorithm was chosen as the result of rather convoluted political machinations at the *BABAR* collaboration meeting in Elba (May 28—31, 2000).

	Electron	Muon	Kaon
Track quality	$doca_{xy} < 0.4\,\mathrm{cm}$, $doca_z < 4\,\mathrm{cm}$		
Momentum cut	$p^* > 1.0\,\mathrm{GeV}$	$p^* > 1.1\,\mathrm{GeV}$	none
Tag determination	q of max. p^*	q of max. p^*	sum of q

Table 5.2: *Summary of cuts used by the cut-based part of the Elba tagging algorithm.*

	Bins for NetTagger x_{tag}	
Category	for B^0 tag	for $\overline{B}^0$ tag
NetTagger category 1 (NT1)	[0.5,1.0]	[-1.0,-0.5]
NetTagger category 2 (NT2)	[0.2,0.5]	[-0.5,-0.2]

Table 5.3: *Definition of NetTagger categories for Elba tagging algorithm.*

The motivation for using a hybrid tagging algorithm comes mainly from the fact that for the $\sim 45\%$ of events that can be tagged by the lepton and kaon categories not much tagging performance can be gained with the presently available probability based tagging algorithms [128]. Such events have tagging electrons, muons, and kaons that are identified by the PID selectors used for tagging (see Tab. 5.2.2) and that pass all the corresponding tagging cuts.

The selection criteria used by the Elba tagger are summarized in Tab. 5.2.4 for the cut-based part and in Tab. 5.2.4 for the NetTagger part, respectively. After removing from the event all tracks coming from the reconstructed B_{rec}, cuts on $doca_{xy}$ and $doca_z$, and, except for kaons, on p^* are applied. The tracks passing these cuts are used to derive separate tags for electrons, muons and kaons by taking the charge of the electron or muon with the highest p^*, or by summing the charges of all kaons and taking the sign of the sum. The PID selectors used to identify electrons, muons and kaons are summarized in Tab. 5.2.2, and the algorithm used to assign the particle type if a track is selected by more than one PID selector is described in Sec. 5.2.2.

Depending on the presence of such electron, muon or kaon tags, and on the output of NetTagger for this event, the tagging category and tag for the $B_{tag}$is determined as follows. All categories are mutually exclusive and tagging categories listed first have higher priority.

1. **Lepton** category: If there is both an lepton and a kaon tag, use them to tag B_{tag}if they agree. If they disagree, the event is left for NetTagger. If there is only a lepton tag, use it to tag B_{tag}.
2. **Kaon** category: If there is a kaon tag (and no lepton tag), use it to tag B_{tag}.
3. **NT1** and **NT2** categories: If the NetTagger output falls into the bins defined for the NT1 or NT2 categories, use the corresponding tag.
4. If none of the above criteria is satisfied, the event is not tagged.

The output of NetTagger for events not tagged by the cut based categories is shown in Fig. 5.7, where the definition of the NT1 and NT2 categories is indicated graphically.

5.3 Parameterizing the Tagging Functions

> *"He will be great for your committee, the only time he will even wake up is when you mention Chebychev polynomials."*
> — R. Boutchko and J. Velikina

As we stated in Secs. 1.5 and 5.1, in order to be able to study time dependence of B-meson decays, we need to measure the tagging performance of the *BABAR* detector. As there is no a priori reason to use a particular parameterization, this is a somewhat arbitrary choice. As with the resolution function, the tagging functions must:

- have enough freedom to accurately describe the data,

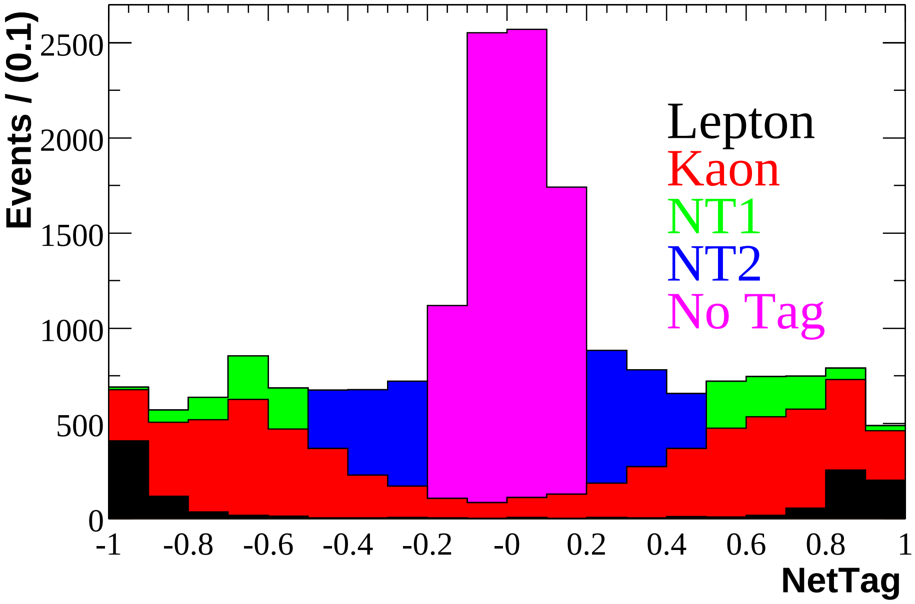

Figure 5.7: *NetTagger output for events by the cut-based categories.*

- not bias our measurements of physics quantities.

We choose to parameterize the tagging functions with Chebychev polynomials:

$$C_{\pm}(x_{tag}) = \sum_n \pm c_n^{\pm} \cos n(\arccos{(x_{tag})}); \tag{5.12}$$

The first five such polynomials are shown in Fig. 5.8.

If we define $C_n \equiv \frac{C_+ + C_-}{2}$ and $\Delta C_n \equiv C_+ - C_-$ then:

$$\begin{aligned} n(x_{tag}) &= \sum_n \Delta C_n P_n^c(x_{tag}) n(x_{tag}) \\ s(x_{tag}) &= \sum_n C_n P_n^c(x_{tag}). \end{aligned} \tag{5.13}$$

Although somewhat arbitrary this parameterization has certain advantages.

1. By construction, the ΔC_n are very small. In fact, in the limit that we are using the correct distribution for $n(x_{tag})$, all the ΔC_n vanish.

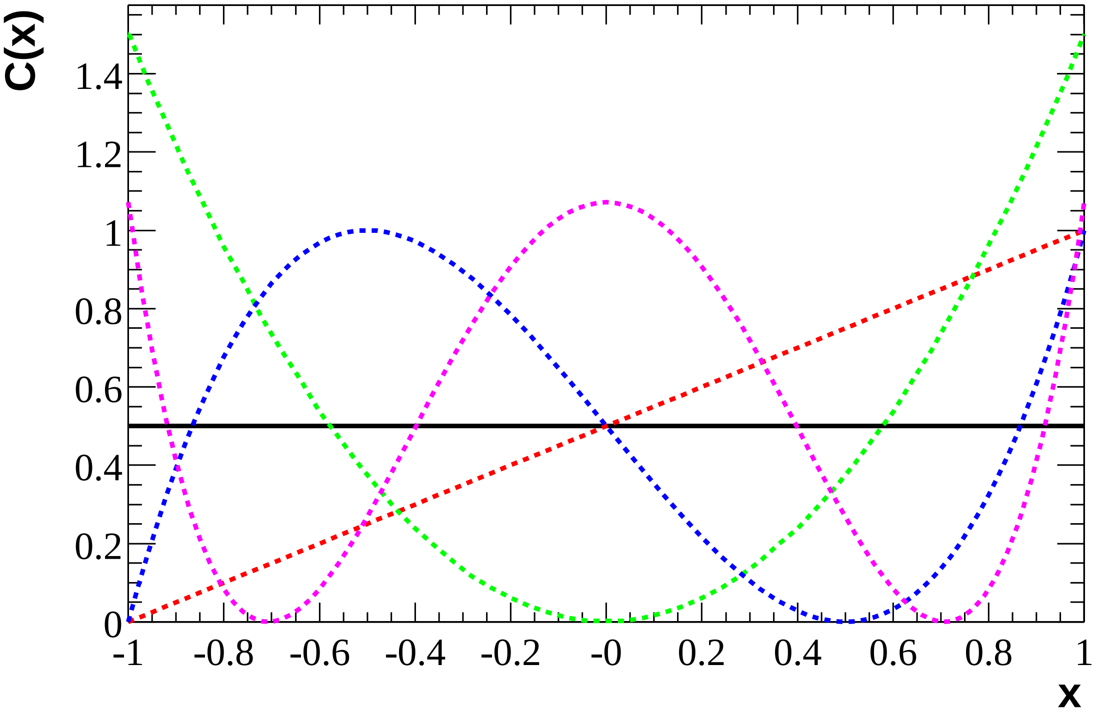

Figure 5.8: *The first five Chebychev polynomials. A constant offset has been added so that the values of the integrals are all normalized to one.*

2. Since x_{tag} was constructed as a pseudo-probability, with $s(x_{tag}) \sim x_{tag}$, $C_1 \sim 1, C_n \sim 0$ for $n \neq 1$. In the limit that the Monte Carlo correctly simulate the tagging separation of the events $(s(x_{tag}))$, all the C_n vanish for $n \neq 1$.

Given this formulation on the tagging functions, we can then express the combined likelihood of observing a event at with Δt, x_{tag}, as:

$$\begin{aligned} \mathcal{F}(\Delta t, x_{tag}; \hat{C}|\hat{\gamma}) = \quad & f_0(\Delta t\ |\hat{\gamma}) \cdot n\prime(x_{tag}) \\ & \times[1 + s\prime(x_{tag}; \hat{C}) \cdot f_{mod}(\Delta t\ |\hat{\gamma})]. \end{aligned} \tag{5.14}$$

We note that $n\prime(x_{tag})$ is exactly the probability to observe an event (of any flavor) at x_{tag}. Therefore, to construct $\prime(x_{tag})$ we simply take the background subtracted x_{tag} distribution. This leaves us with only $\hat{C}$, the Chebychev coefficients, to extract from the data.

5.4 Tagging Performance on Monte Carlo

"You have a telefonino, apartment keys and a friend with a Vespa. You are Italian now."
— C. Bulfon

Measuring the tagging performance on Monte Carlo is simply a matter of comparing the output of the tagging algorithm to the Monte Carlo truth. Or, if we are more ambitious, we can fit for the tagging functions using our Monte Carlo samples.

5.4.1 Fitting Tagging Performance In Monte Carlo

Tab. 5.4.1 lists the tagging function parameters, both as extracted from fitting $f(x_{tag})$ and $\bar{f}(x_{tag})$ directly to the Monte Carlo truth, as from a full fit to the Δt and x_{tag} distributions for signal Monte Carlo.

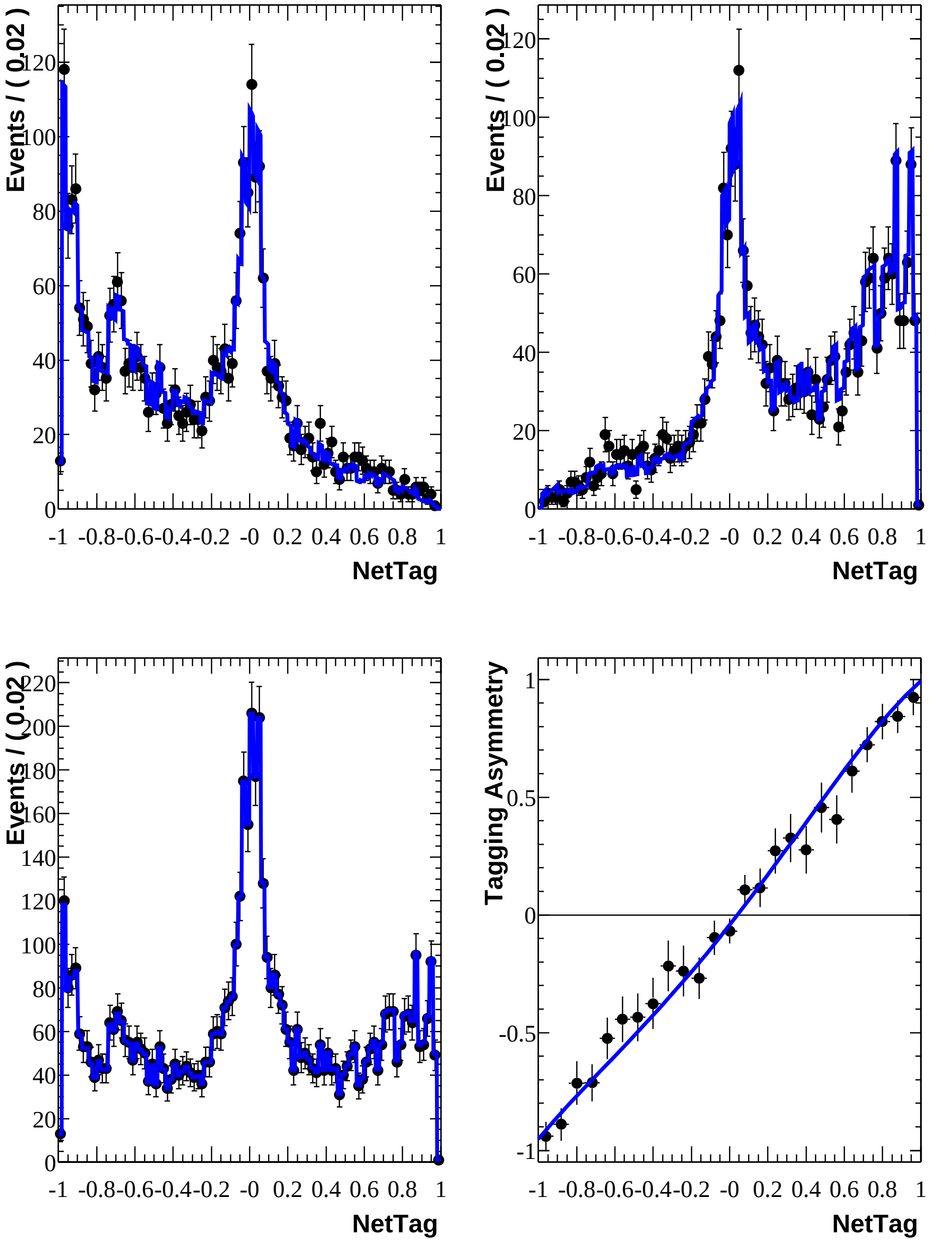

Figure 5.9: *NetTagger tagging performance on Monte Carlo. The top two plots show the NetTagger for Monte Carlo truth* B^0 *(left) and* $\overline{B}^0$ *(right) decays. The bottom left histogram shows distribution the NetTagger output variable* $x_{tag}(n(x_{tag}))$*, while the bottom right plot shows the tagging separation as function of* $x_{tag}(s(x_{tag}))$*. In both cases the fit results are overlayed.*

Parameter	MC Truth	Δt Distribution
Δm_d	-	0.498 ± 0.018 ps^{-1}
Tagging Function		
C_1	1.035 ± 0.028	1.035 ± 0.028
C_2	0.032 ± 0.027	0.032 ± 0.027
C_3	-0.098 ± 0.031	-0.098 ± 0.031
C_4	-0.023 ± 0.028	-0.098 ± 0.031
ΔC_1	0.011 ± 0.019	-0.098 ± 0.031
ΔC_2	-0.021 ± 0.021	-0.098 ± 0.031
ΔC_3	0.014 ± 0.019	-0.098 ± 0.031
ΔC_4	0.012 ± 0.019	-0.098 ± 0.031
Q	30.1 ± 0.3 %	30.2 ± 0.5 %

Table 5.4: *Summary of Δm_d and tagging function fit results on Monte Carlo.*

Category	$\epsilon(\%)$	$w(\%)$	$Q(\%)$
Lepton	12.0 ± 0.1	6.1 ± 0.3	9.2 ± 0.1
Kaon	34.6 ± 0.2	16.4 ± 0.2	15.7 ± 0.2
NT1	7.8 ± 0.1	19.1 ± 0.5	3.0 ± 0.1
NT2	14.6 ± 0.1	34.6 ± 0.5	1.4 ± 0.1
Total	69.0 ± 0.3		29.2 ± 0.3

Table 5.5: *Tagging performance for Monte Carlo.*

Fig. 5.9 details the performance of the NetTagger on Monte Carlo. We see that B^0 and $\overline{B}^0$ tag-side decays are correctly separated by the NetTagger. Most importantly, we see that our fit accurately reconstructs the distributions of $s(x_{tag})$ and $n(x_{tag})$, which are crucial to measuring the flavor asymmetries.

Finally, for comparison, Tab. 5.4.1 lists the tagging performance achieved on Monte Carlo by the "Elba" algorithm for each tagging category.

5.5 Tagging Performance on Data and Δm_d

"Very good, nine-nine percent."

— X. Wu, "My performance on English GRE"

We now move on the discussion of simultaneous fit to the tagging function parameters C_n and the $B^0\overline{B}^0$ mixing frequency, Δm_d. In Sec. 5.5.2 we describe our model of the Δt and x_{tag} structure of the background events, and in Secs. 5.5.4, 5.5.5 and 5.5.1 we present the fit results. We note in particular that the fit results are not as precise as those from the full combined fit, which we describe in Chapter 6. In particular, our definitive measurements of Δm_d is stated in Sec. 6.3.2, while the treatment of systematic error is grouped with the error analyses of the other measurement in Sec. 6.5.

5.5.1 Tagging of Charged B

Although the reconstruction of a charged B already tags the flavor of the other B tagging studies for charged B are very useful for the validation of tagging on data. Also, as discussed in Sec. 4.6.1, $B^{\pm}$ decays peak in m_{ES} and must be specially treated. Finally, the tagging of charged B is required for a measurement of the apparent $\mathcal{CP}$ asymmetry in $B^+ \to J/\psi\ K^+$ as a negative control.

The tagging performance for charged B differs from the one of neutral B in several ways.

1. There are favorable production rates of right sign and wrong sign kaons.
2. No tagging separation is expected from slow pions for charged B (because of the production of neutral instead of charged D^* mesons).
3. Tagging with leptons is expected to be the same.

Fig. 5.10 show that tagging performance on $B^{\pm}$ decays, while Tab. 5.5.1 give the results from the "Elba" tagging algorithm as a comparison. Although the "Elba" algorithm does

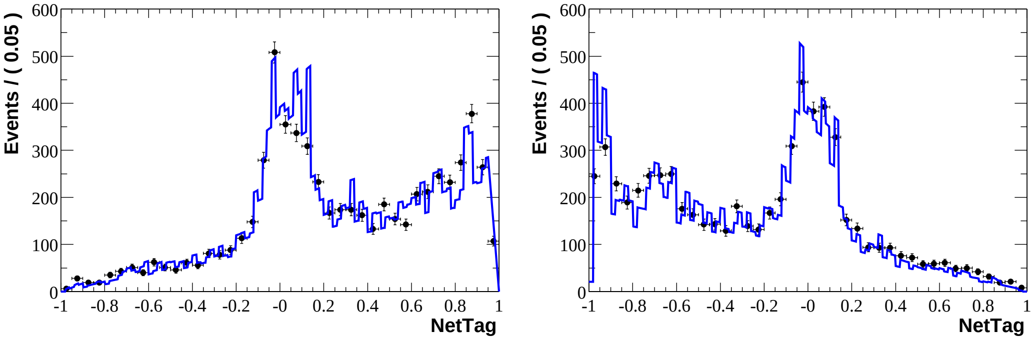

Figure 5.10: *NetTagger tagging performance on the $B^{\pm}$ Sample. The top (bottom) plot shows the x_{tag} distribution for the B^{+} (B^{-}) events (points) as well as the fitting x_{tag} distribution (line).*

Category	$\epsilon(\%)$	$w(\%)$	$Q(\%)$
Lepton	12.1 ± 0.3	4.6 ± 0.6	10.0 ± 0.4
Kaon	38.0 ± 0.5	11.8 ± 0.5	22.2 ± 0.7
NT1	6.5 ± 0.2	21.3 ± 1.6	2.1 ± 0.3
NT2	13.1 ± 0.3	37.2 ± 1.3	0.9 ± 0.2
Total	69.7 ± 0.8		35.2 ± 0.8

Table 5.6: *Tagging Performance for all charged B..*

significantly better on $B^{\pm}$ events, with a $Q = 35\%$, the “NetTagger” algorithm was specifically trained on $B^0\overline{B}^0$ events and only does marginally better on $B^{\pm}$ events than on $B^0\overline{B}^0$ events ($Q \sim 31\%$).

5.5.2 Describing the Time-Structure of $m_{\rm ES}$ Sideband Events

Similarly to the situation described in Sec. 4.6.1, we need to describe combined x_{tag} and Δt structure of the $m_{\rm ES}$ sideband events. Again, we use kernel estimation techniques for these models. We separately model the combined background Δt and x_{tag} distribution, K(Δt,x_{tag}), for each choice of event sample (e) and B_{rec} flavor (b). That is to say:

$$K^{e}(\Delta t, x_{tag}, b; f_{b}^{a,e}) = f_{b}^{a,e} K^{eb}(\Delta t, x_{tag}) \tag{5.15}$$

where $f_b^{a,e}$ is the fraction of events in the Argus background for sample e which have B_{rec} flavor b. Of course, we can take this number directly from the data for the B_{flav} and $B^{\pm}$ samples. Also, in analogy with Sec. 4.6.1, $K^{eb}(\Delta t, x_{tag})$ is the kernel-estimated model of the Δt vs. x_{tag} distribution for the e, b subsample.

For $\mathcal{CP}$ samples the $f_b^{a,e}$ do not mean anything, since $\mathcal{CP}$ decays specifically are not flavored. Since the $\mathcal{CP}$ samples are very small, we use the sum of the $B_{rec} = B^0$ and $B_{rec} = \overline{B}^0$ distributions to model the $\mathcal{CP}$ backgrounds.

5.5.3 Describing the Δt Distribution for Peaking Backgrounds

As in the Sec. 4.6.1, we assume that the peaking background consists of the $B^{\pm}$ decays mis-reconstructed as $B^0\overline{B}^0$ events. In this case, the situation is slightly more complicated in that it is possible to mis-reconstruction a B^0 as $\overline{B}^0$. Fortunately, studies on inclusive signal Monte Carlo show that this is extremely rare in the B_{flav} sample. The point being that the B_{rec} flavor is defined by the sign of the light hadron (the $\pi^{\pm}, \rho^{\pm}$ or $a_1^{\pm}$). Therefore, to mis-reconstruction a B^0 as a $\overline{B}^0$ would require getting the sign of the light hadron wrong. However, unlike the D decay products, which can be very soft, the light hadron decay products are all fairly energetic and thus have fewer possibilities for confusion. Therefore, when working with the B_{flav} sample, we make no changes in treatment of the peaking

Parameter	Value
Δm_d	0.506 ± 0.015
Tagging Function	
C_1	1.032 ± 0.028
C_2	0.032 ± 0.027
C_3	-0.098 ± 0.031
C_4	-0.023 ± 0.028
ΔC_1	0.011 ± 0.019
ΔC_2	-0.021 ± 0.021
ΔC_3	0.014 ± 0.019
ΔC_4	0.012 ± 0.019
Q	27.4 ± 1.4

Table 5.7: *Summary of Δm_d and tagging function fit results to the B_{flav} sample.*

backgrounds. That is to say:

$$\begin{aligned} F_{flav}(\Delta t, x_{tag}; \hat{\alpha}, \hat{c}, f_{peak}, \hat{\gamma}) &= (1 - f_{peak}) \\ &\quad \times F_{flav}(\Delta t, x_{tag}; \tau_{B^0}, \Delta m_d, \hat{c}, \hat{\alpha}) \\ &\quad + f_{peak} \times F_{\pm}(\Delta t; \tau_{B^+}, \hat{\gamma}) \\ F_{\pm}(\Delta t, x_{tag}; \hat{\alpha}, \hat{c}, f_{peak}, \hat{\gamma}) &= (1 - f_{peak}) \times F_{\pm}(\Delta t, x_{tag}; \tau_{B^+}, \hat{\alpha}) \\ &\quad + f_{peak} \times F_{flav}(\Delta t, x_{tag}; \tau_{B^0}, \Delta m_d, \hat{c}, \hat{\alpha}). \end{aligned} \tag{5.16}$$

Aside from performing systematic studies, we keep f_{peak} fixed to 0.015 throughout the analysis.

As we will see latter, the problem is not so simple for the $\mathcal{CP}$ sample, there, a mis-reconstruction could cause a non-$\mathcal{CP}$ event, or event an $\eta_{CP} = +1$ event, to be reconstructed as a $\eta_{CP} = -1$.

5.5.4 Results of the Fit to the Data

The results to the fit to the B_{flav} mixing sample are shown in Tab. 5.5.4. As we can see, all the C_n follow closely to the expected pattern of $C_1 = 1$, $C_{n\neq 1} = 0$, $\Delta C_n = 0$.

5.5.4.1 Displaying the Asymmetry Results

Graphically displaying results the time-dependence of flavor mixing requires a bit of care. What we would like to show is the probability an event occurs with a proper time difference Δt depending on whether the event is mixing or unmixed. However, that is not possible, instead, the best alternative is to show the probability that an event occurs with a proper time difference Δt, weighted by the probability that the event is either mixed or unmixed. To do this, we construct the "tag-weighted" Δt distributions $W_{\pm}(\Delta t)$:

$$\begin{aligned} W_{+}(\Delta t) &= +\int F(\Delta t, x_{tag})\Theta(s(x_{tag}) > 0) \times s(x_{tag}) dx_{tag} \\ W_{-}(\Delta t) &= -\int F(\Delta t, x_{tag})\Theta(s(x_{tag}) < 0) \times s(x_{tag}) dx_{tag}. \end{aligned} \tag{5.17}$$

From these, we can immediately construct the "tag-weighted" asymmetry $A_w(\Delta t)$:

$$A_w(\Delta t) = \frac{W_{+}(\Delta t) - W_{-}(\Delta t)}{W_{+}(\Delta t) + W_{-}(\Delta t)}. \tag{5.18}$$

Fig. 5.11 shows the "tag-weighted" Δt distributions for the fit above. We do not make an explicit distinction between signal and sideband regions. The plots in Fig. 5.11 include candidates in the region $m_{ES} > 5.27\,\mathrm{GeV}/c^2$. The same results are shown together for better comparison in Fig. 5.12. Finally, the "tag-weighted" asymmetry is shown in Fig. 5.13.

5.5.5 Tagging Performance in Data

In addition to having measured Δm_d we have also extracted the tagging function. Fig. 5.14 graphically shows the separation achieved between B^0 and $\overline{B}^0$ decay on the tag side. For

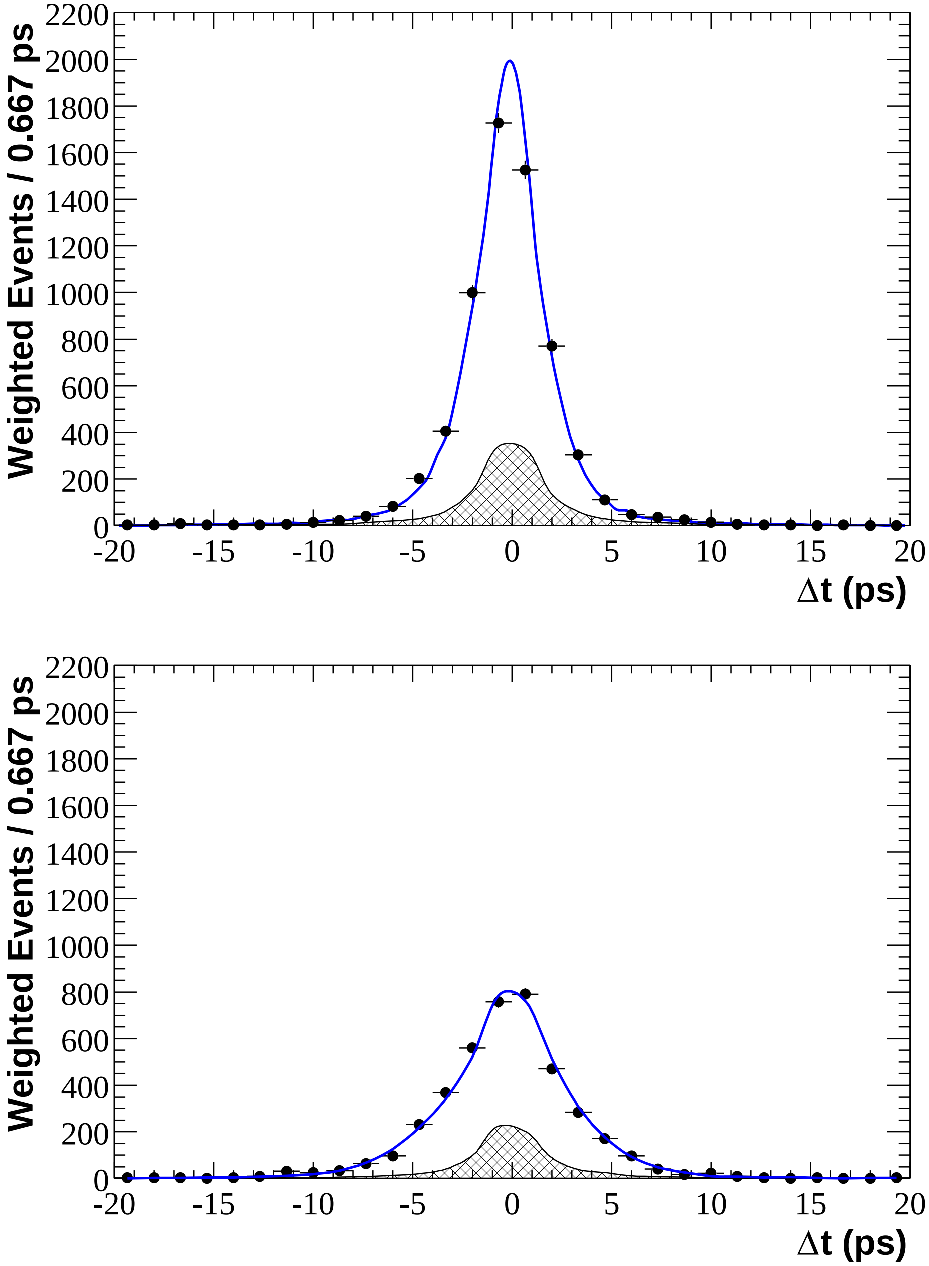

Figure 5.11: *Tag-weighted Δt distributions for the $B^0\overline{B}^0$ mixing sample with fit results overlayed. The unmixed (mixed) events are shown on the top (bottom). In both cases the background contribution (filled curve) is shown.*

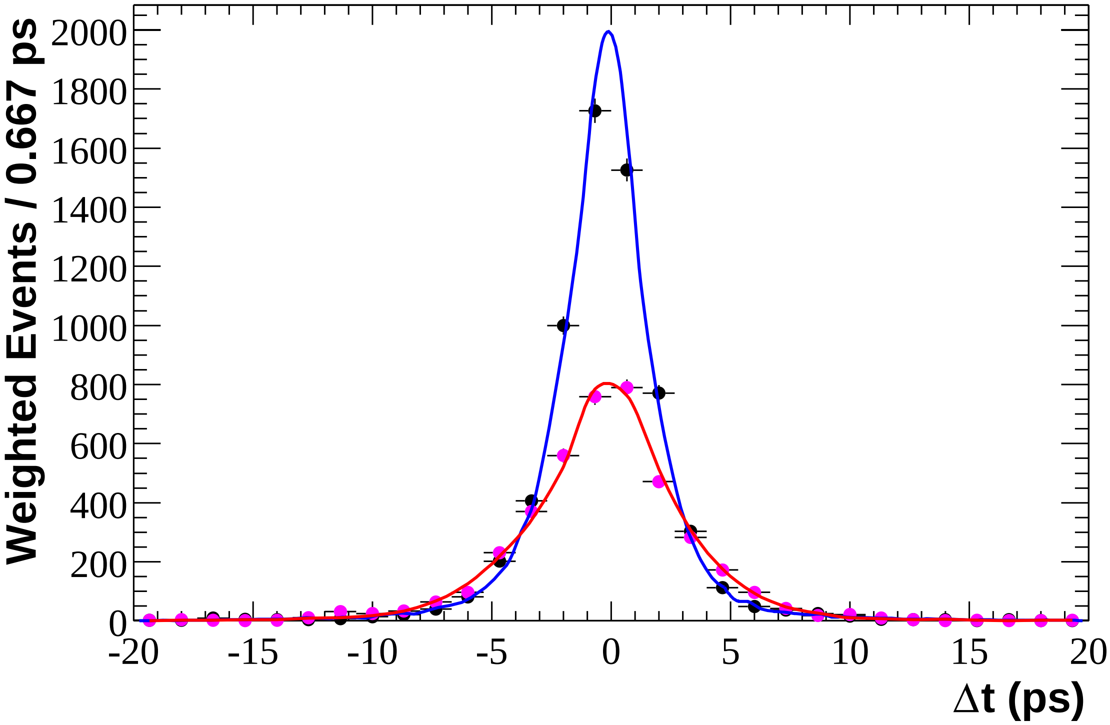

Figure 5.12: *Tag-weighted Δt distributions for the $B^0\overline{B}^0$ mixing sample with fit results overlayed.*

Category	$\epsilon(\%)$	$w(\%)$	$Q(\%)$
Lepton	11.0 ± 0.3	9.3 ± 1.5	7.3 ± 0.6
Kaon	35.7 ± 0.6	17.5 ± 1.1	15.1 ± 1.0
NT1	8.1 ± 0.3	21.9 ± 2.2	2.6 ± 0.4
NT2	13.6 ± 0.4	33.8 ± 2.0	1.4 ± 0.4
Total	68.4 ± 0.9		26.4 ± 1.3

Table 5.8: *"Elba" algorithm tagging performance for data.*

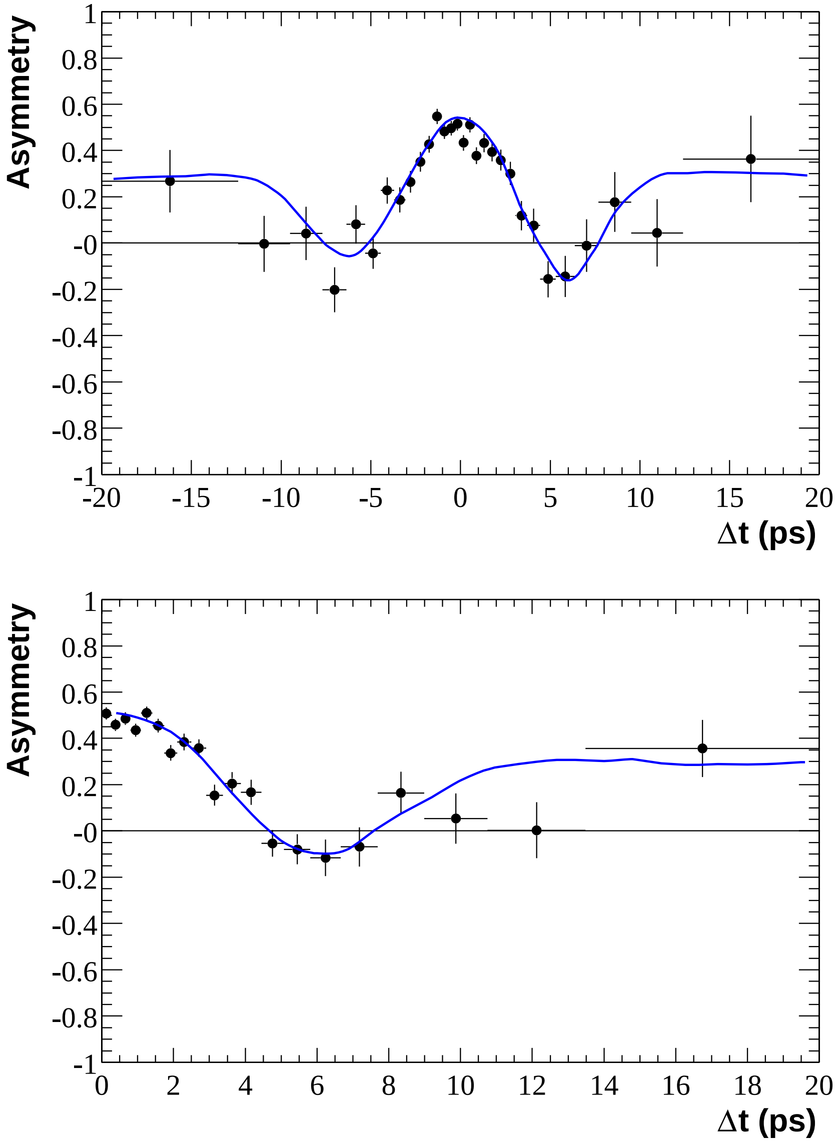

Figure 5.13: *Time-dependent asymmetries for the* $B^0\overline{B}^0$ *mixing samples with fit results overlayed. The top plot full shown the full* Δt *range, while the bottom plot has been folded over and shows the asymmetry as a function of* $|\Delta t|$*.*

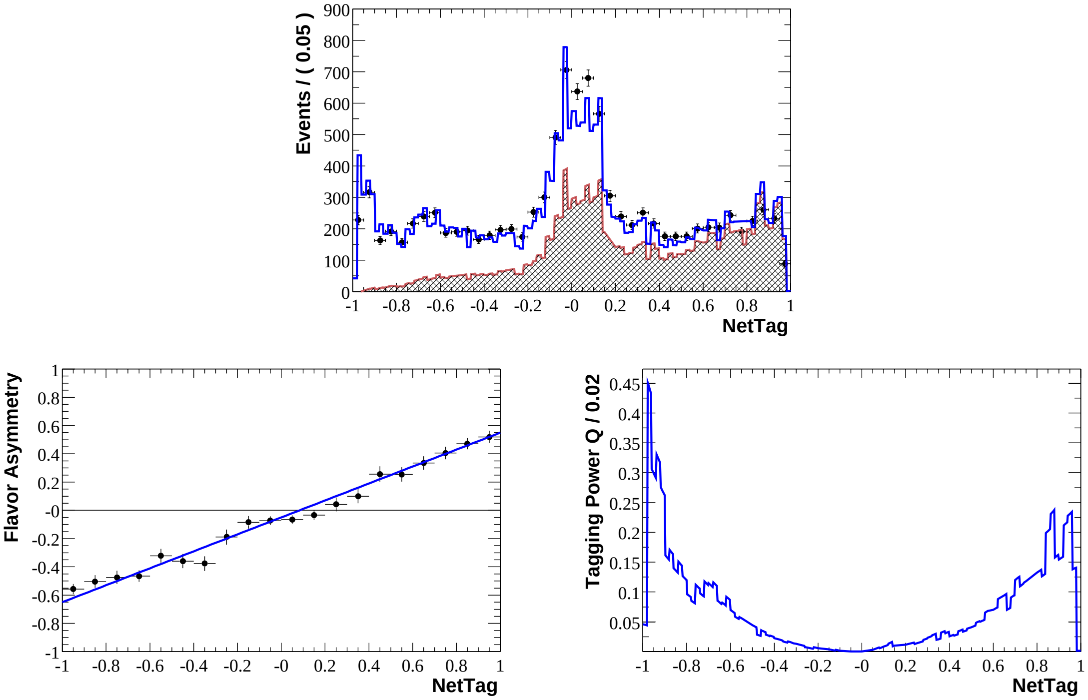

Figure 5.14: *NetTagger tagging performance on the* $B^0\overline{B}^0$ *mixing sample. The top plot shows the* x_{tag} *distribution for the signal events (points) as well as the fitted* x_{tag} *distribution for all events (line) and for with a* B^0 *on the tag side only (filled curve). The bottom left plot shows the asymmetry in* B_{rec} *flavor as a function of* x_{tag}*, which this is roughly equivalent to* $s/(x_{tag}) \times (1 - 2\chi_d)$*. The bottom right plot show the tagging power as a function of the tagging variable* $Q(x_{tag})$*.*

comparison, Tab. 5.5.5 shows the performance of the category based tagging algorithm.

Some comments about the bottom left plot of Fig. 5.14 are in order. This is not a plot of $s(x_{tag})$, rather it is a plot of the asymmetry on the B_{rec} side as a function of x_{tag}. In essence, we have reversed the situation of showing the tagging asymmetry based on the reconstruction flavor. Under ideal circumstance, we expect the line to have a slope of $1 - 2\chi_d$. Of course this is changed both by the presence of background and by differences in the number of B^0 and $\overline{B}^0$ reconstructed.

5.6 Tagging Systematics Studies

"They are the same size. If you call this one signal and that one background you can't be a scientist."
— M. Schmidt

We now move on to a discussion of the systematic effects which may bias our measurement of either the tagging performance or Δm_d. In doing so we quantify both the possible bias on Δm_d and on the tagging power Q. Many of these studies are extensions of studies performed for the original *BABAR* publications of sin2β and Δm_d [129, 130].

5.6.1 Tagging Function Parameterization

The most obvious issue with the technique described here the ability of the tagging function parameterization to reproduce the data. To study this issue, we have performed a series of twenty high statistic toy Monte Carlo (10k events each) studies in which input data was generate with tagging function of arbitrary forms (including polynomials, trigonometric function, large random permutation on straight lines) and subjected to a full mixing fit using our Chebychev parameterization. We also performed a series of twenty toy Monte Carlo studies in which higher order the higher (fifth through eight) order Chebychev coefficients were set to non-zero value for during generation and fixed to zero during the full mixing fit.

In all studies we used a simplified resolution model consisting of two Gaussians with widths fixed to 0.7 and 5 ps respectively. That is to say, we did not model the effect of per-event variation in the Δt resolution. We also ignored background contributions.

We observed five noteworthy trends throughout these studies.

1. The fitted distributions for $n(x_{tag})$ matched the input distributions very well. In fact, the average χ^2 per D.O.F was usually < 0.5. This is no great surprise, as the $n(x_{tag})$ distribution were used in constructing the tagging functions.
2. In some cases, the fitted distributions for $s(x_{tag})$ matched the input distributions rather poorly, with the χ^2 per D.O.F exceeding 20 in a few cases.
3. Likewise, the fitted distributions for $Q(x_{tag})$ did not match the input distributions particularly well.
4. However, the fitted values for $\int |a(x_{tag})| dx_{tag}$ and Δm_d matched the input value with good precision. Specifically, the mean of the pull distributions were $\mu = 0.07$ and -0.10 respectively.
5. We observed qualitatively that smoothly varying input functions were fit much more accurately the more quickly varying ones.

We intemperate these results as showing that our method is fundamentally sound. The poor quality matches of $s(x_{tag})$ and $Q(x_{tag})$ simply reflect the fact that a fourth order Chebychev polynomial can not fully fit rapidly varying distributions. What is important for the purposes of measuring asymmetries is not the local variations in $a(x_{tag})$, but that the overall measure of the asymmetry is accurate. This is equivalent to saying that we can integrate out rapid variations in $a(x_{tag})$ without affecting our with result.

5.6.2 Consistency Between Sub-Samples

One of the fundamental assumptions made for the sin2β analysis is that tagging function $\mathcal{CP}$ events can be measured in data on the B_{flav} sample, i.e. that the tagging performance is independent of the decay mode of the B_{rec} for the decay modes used in the $\mathcal{CP}$ and B_{flav} samples. This assumption can be checked by comparing the tagging performance obtained for different B_{rec} modes in data and Monte Carlo. Possible differences could come from the effect of the higher B_{rec} decay multiplicities in most B_{flav} modes and compared to $\mathcal{CP}$ modes.

Another possible source of problems comes from different performances for tagging B^0 and $\overline{B}^0$ decays. Although such differences would generally be treated correctly within our formalism, it is possible that coupled with other systematic effects they could bias our results.

As with the lifetime measurement, we have split the samples of B candidates:

- by x_{tag}**sign** (for data only),
- by B_{rec} **flavor** (data and Monte Carlo),
- by B_{tag} **truth** (for Monte Carlo only),
- by B_{rec} **decay mode** (for Monte Carlo only).

5.6.3 Tagging-Vertexing Correlations

A dependence of the resolution function $R(\delta t)$ on the x_{tag} would be very dangerous for any time dependent measurement of a $\mathcal{CP}$ asymmetry. We check for such a dependence in two

Sample	Δm_d (ps^{-1})	Q
Monte Carlo Studies		
$B_{rec} = B^0$	0.504 ± 0.022	28.7%
$B_{rec} = \overline{B}^0$	0.453 ± 0.021	28.8%
$B_{tag} = B^0$ (truth)	0.449 ± 0.022	28.9%
$B_{tag} = \overline{B}^0$ (truth)	0.492 ± 0.022	28.5%
$D^{(*)0}\pi^+$	-	28.9%
$\Psi K^{(*)+}$	-	28.5%
Data Studies		
$B_{rec} = B^0$	0.502 ± 0.022	27.3%
$B_{rec} = \overline{B}^0$	0.484 ± 0.021	27.8%
$x_{tag} > 0$	0.473 ± 0.022	27.6%
$x_{tag} < 0$	0.511 ± 0.022	27.3%

Table 5.9: *Results of Δm_d fits for various subsamples, both divided by decay modes and by B_{rec} flavor.*

ways, first, by looking at the correlations between the resolution function variables and x_{tag}. We observe that well tagged events tend to have smaller errors than poorly tagged events. This would be problematic except that the pull distribution shows no correlation. In fact, this plot motivated our choice of scaling the resolution function exponential lifetime by the per-event error.

Since the tagging algorithm specifically looks for high momentum tracks, it is no surprise that well-tagged events are also more often well-vertexed.

We have also used a procedure based on model subtraction to estimate potential bias due to this effect.

1. We make two dimensional histograms of x_{tag} vs. Δt both for the data and directly from the P.D.F. normalized to the size of the data sample.

2. We make a weight histogram by dividing the data histogram by fit histogram.

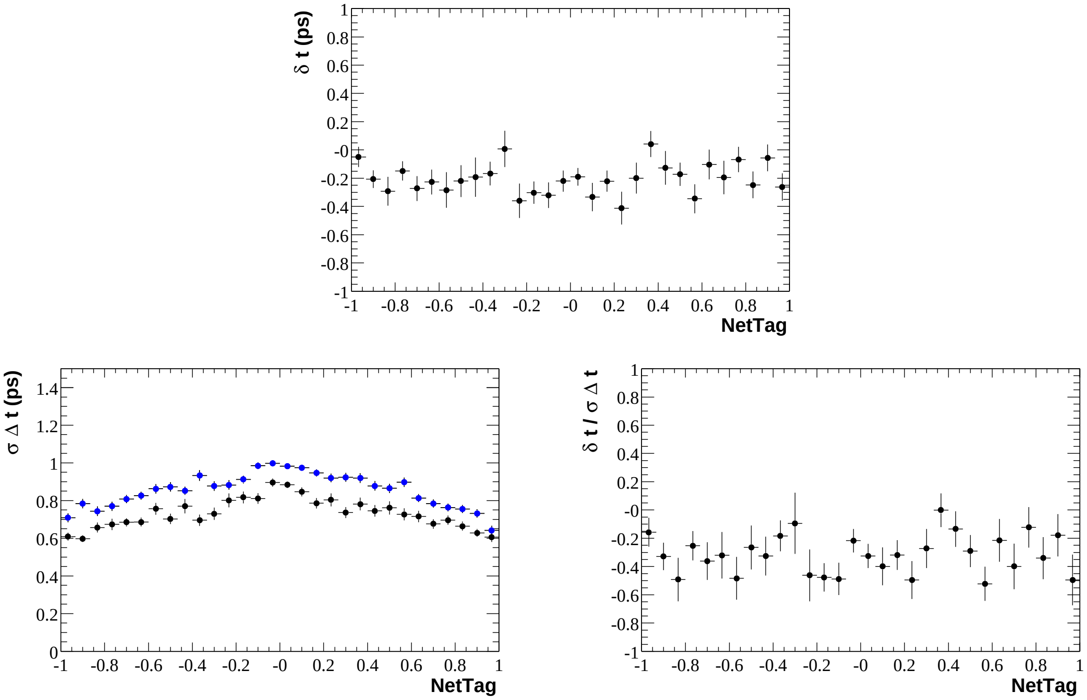

Figure 5.15: *Resolution function variables plotted against x_{tag} for Monte Carlo. The average values of the residual, δt (top), the per-event error, $\sigma_{\Delta t}$ (bottom right), and the pull, $\delta t\ /\sigma_{\Delta t}$ (bottom left), are shown plotted against x_{tag}. In the bottom right left plot, data points (upper curve) are also plotted.*

3. We re-perform the fit with all parameters except for Δm_d fixed and the each event re-weighted by its value from the weight histogram. We then assign the change in fitted value of Δm_d (0.007) as a systematic error.

We also perform a similar study in which we re-weight events based on model subtraction in the $x_{tag} - \sigma_{\Delta t}$ plane. This study shows a smaller effect (0.004) and we choose to quote only the larger value found above.

A related, but not identical, effect arises if the resolution function is correlated with the accuracy of the tag. That is to say, do B^0 decays observed at $x_{tag} = 0.9$ have the same resolution function as $\overline{B}^0$ decays observed at $x_{tag} = 0.9$.

We use the same model subtraction method to quantify this effect with two modification.

1. We perform the study on signal Monte Carlo rather that data.
2. We insert a multiplicative factor of -1 for decays with a true $\overline{B}^0$ decay on the tag side.

From these studies we obtain a assign a systematic error of 0.005 for Δm_d.

Chapter 6

Extracting $\sin 2\beta$

"It would have been more exciting if it were -0.5."
— S. Rahatlou

At this point we have selected events for our $\mathcal{CP}$ sample as well as both the B_{flav} and $B^{\pm}$ control samples. We have also develop good models of both the Δt detector resolution function $R(\delta t; \hat{\alpha})$ and the flavor tagging separation function $s(x_{tag})$. That is to say, we have calibrated everything that we need to calibrate in order to measure $\sin 2\beta$. Therefore we now turn our attention to what is after all, the final goal of this analysis.

In Sec. 6.1 we will describe the details of the full combined likelihood fit which use to extract definitive values for all the physics parameters of interest. Then in Sec. 6.2 we state the results of the combined fit. In Secs. 6.3.1 and 6.3.2 we examine the results for our calibration and cross check measurements of the B-lifetimes and Δm_d respectively. These cross checks are particularly important because of the difficulty in seperating the resolution function from the B-lifetimes and the existence of reasonable prediction of the ratio of the B^0 to B^+ lifetimes [131, 132].

In Sec. 6.4 we go on to examine more closely the final fit results for $\sin 2\beta$. Since the measurement of $\sin 2\beta$ close related to the lifetime and mixing measurements we treat all the

Parameter	World Average
τ_{B^+}	$1.653 \pm 0.028 ps$
τ_{B^0}	$1.548 \pm 0.032 ps$
Δm_d	$0.472 \pm 0.017 ps$

Table 6.1: *Status of physics parameters in the combined fit.*

systematic errors together in Sec. 6.5.

6.1 The Combined Maximum Likelihood Fit

"Even though everyone agrees there is only one way to do a fit, there are still three different fitters."
— W. Bhimji

As stated in Sec. 1.5.5 we use a combined fit to all of the data to extract our physics parameters $\hat{\gamma}$, resolution function parameters $\hat{\alpha}$ and tagging function parameters $\hat{c}$. The fit was performed using the Minuit [133] and RooFitTools [134] software packages.

In this section, we summarize the full P.D.F. used for these fits [135, 136, 137, 138, 139, 140, 141].

6.1.1 Physics Parameters

In addition to sin2β our fit is sensitive to three physics parameters, τ_{B^0}, τ_{B^+} and Δm_d. Tab. 6.1.1 lists the current world averages for these parameters.

6.1.2 Dependent Variables

For completeness, we list here all of the event dependent variable which enter into our fit.

1. Δt, the proper time difference between the B-meson decays.

2. $\sigma \Delta t$, the estimated error on Δt.

Mode	Fraction	$\mathcal{CP}$ Content
$J/\psi\ K^{*0}$	92 %	+0.72
$J/\psi\ K^0_S$	2 %	-1.00
Combinatoric	6 %	0
Total		0.68 ± 0.05

Table 6.2: *Composition and $\mathcal{CP}$ content of events which pass the $J/\psi\ K^{*0}$ selection.*

3. $m_{\rm ES}$, the beam-substituted mass.

4. x_{tag}, the output of the NetTagger tagging algorithm.

5. b, the flavor of the reconstructed B-meson (B_{rec}); clearly this must be either B^0, $\overline{B}^0$, B^+, or B^-. In the case of $\mathcal{CP}$ decays this variable is not relevant.

6. e, the event sample; we distinguish between the "TagMix" sample, the "Charged B" sample, $\eta_{CP} = -1$ $\mathcal{CP}$ modes, and the $B^0 \to J/\psi\ K^{*0}$ $\mathcal{CP}$ decays.

7. r, whether the event is in Run 1 or Run 2. This is necessary since we use different resolution function for the two runs.

6.1.3 Effective η_{CP} for the $J/\psi\ K^{*0}$ $\mathcal{CP}$ Mode

As discussed in Sec. 1.4.6, we can include the decay channel $B^0 \to J/\psi\ K^{*0}$, $K^{*0} \to K^0_S\ \pi^0$ in our $\mathcal{CP}$ sample, provided that we know the effective $\mathcal{CP}$ content of the sample we select [142].

We have performed a study of our selection criteria on various inclusive and signal Monte Carlo samples [65]. The composition of the selected sample is shown in Tab. 6.1.3. Therefore, we assign an effective $\mathcal{CP}$ eigenvalue of $\eta_{CP}^{K^{*0}} = 0.68$ for these decays.

6.1.4 Kernel Estimate Models

We also use some parameter-free models created with kernel estimation techniques to describe certain distributions which enter into our combined fits.

1. For each event sample, e, and B_{rec} flavor, b, we have constructed a model of the Δt vs. x_{tag} distribution using the kernel estimation technique, $K^{eb}(\Delta t, x_{tag})$.
2. We have also built models of the distributions of the x_{tag} variable for all $B^0\overline{B}^0$ decay, $n\prime(x_{tag})$.
3. We have build separate models of the distributions of the x_{tag} variable for B^+ and for B^- decays.

6.1.5 Time Structure of Peaking Background in $\mathcal{CP}$ modes

When treating the time structure of the peaking background for the $\mathcal{CP}$ modes, we must consider the possibility that the peaking background contains some $\mathcal{CP}$ content, possibly with the opposite η_{CP}. To account for these possibilities, we construct a $\mathcal{CP}$ peaking background model, which is identical to the $\mathcal{CP}$ signal model with two modifications.

1. We take the effective $\mathcal{CP}$ of the peaking background (η_{CP}^{peak}) as a fit parameter, though for the time being we fix it to zero. We will assign systematic error based on varying this parameter.
2. Since we do not know the level of $B^{\pm}$ cross-contamination in the $\mathcal{CP}$ signal sample, we also take the lifetime of the peaking background (τ_{CP}^{peak}) as a fit parameter. Bases on estimates of the cross-contamination, we choose $1.60ps$ as a reasonable value for this parameter. Again, we will assign systematic error based on varying this parameter.

Thus, to summarize, the base P.D.F. for our $\mathcal{CP}$ peaking background is:

$$f_{CPpeak} = (\frac{1}{2})_{tag} \frac{e^{-|\Delta t|/\tau_{CP}^{peak}}}{2\tau_{CP}^{peak}} \cdot [1 - \eta_{CP}^{peak} sin \Delta m_d \Delta t]. \tag{6.1}$$

6.1.6 Constructing the Fitting Function

We now list all the parts of the construction of the full P.D.F. used for our combined fit.

1. We perform a simultaneous combined fit to four event samples, the $B^{\pm}$, B_{flav}, $\eta_{CP} = 1$ and $J/\psi\ K^{*0}$ $\mathcal{CP}$ samples. Thus our full likelihood function is:

   $$\mathcal{L} = \mathcal{L}_{flav} + \mathcal{L}_{\pm} + \mathcal{L}_{CP} + \mathcal{L}_{K^{*0}}, \tag{6.2}$$

   where we use the subscript K^{*0} to indicate the $J/\psi\ K^{*0}$ $\mathcal{CP}$ sample.

2. For each event sample and B_{rec} flavor, we define a "Physics" P.D.F. for the "true" Δt distribution in terms of a double sided exponential and a modulation term:

   $$f^e(\Delta t_{true}, b; \hat{\gamma}) = f_0(\Delta t_{true}|\tau_e)[1 \pm f^e_{mod}(\Delta t_{true}, b; \hat{\gamma})], \tag{6.3}$$

   where $\tau_e = \tau_{B^0}(\tau B^{\pm})$ for $B^0\overline{B}^0$ $(B^{\pm})$ events, and $f_0(\Delta t_{true}|\tau_e)$ is the double sided exponential defined in Eq. (1.70). and the various $f^e_{mod}(\Delta t, b; \hat{\gamma})$ are defined in Eq. (6.4), below.

3. We also define a "$\mathcal{CP}$ Peaking Background" distribution as given by Eq. (6.1).

4. In this formulation, the various modulation terms are:

$$\begin{aligned} f^{\pm}_{mod} &= 0 \qquad (6.4) \\ f^{flav}_{mod} &= S_{mix} \cos\left(\Delta m_d \Delta t_{true}\right) \\ f^{CP}_{mod} &= S_{cp} \sin 2\beta \times \sin\left(\Delta m_d \Delta t_{true}\right) \\ f^{K^{*0}}_{mod} &= -S_{cp} \eta^{K^{*0}}_{CP} \sin 2\beta \times \sin\left(\Delta m_d \Delta t_{true}\right) \\ f^{CPpeak}_{mod} &= S_{cp} \eta_{CPpeak} \sin 2\beta \times \sin\left(\Delta m_d \Delta t_{true}\right). \end{aligned}$$

   where $S_{mix} = +1(-1)$ for unmixed (mixed) events, and $S_{cp} = +1$ for events where the B_{tag} is a B^0. We note that at this stage we are still referring to the "true" distributions.

5. To describe the tagging performance of the detector, we consider the probability to observe a measurement of x_{tag} given a true B^0 ($\overline{B}^0$), which we represent with a tagging function $f(x_{tag}; \hat{c}|B^0)$, or just $f(x_{tag}; \hat{c})$,($f(x_{tag}; \hat{c}|\overline{B}^0) \equiv \bar{f}(x_{tag}; \hat{c})$) which has parameters $\hat{c}$.

6. For each type of event, we create a joint x_{tag}, Δt, P.D.F. by summing over the product of the decay and tagging P.D.F.s for each "true" tag. In general this gives us the result:

$$\begin{aligned} \mathcal{F}^e(x_{tag}, \Delta t_{true}, b; \hat{c}, \hat{\gamma}) &= n\prime(x_{tag}; \hat{c}) f_0(\Delta t_{true}; \tau_e) \qquad (6.5) \\ &\quad \times \left[1 + s\prime(x_{tag}; \hat{c}) f^e_{mod}(\Delta t_{true}, b; \hat{\gamma})\right], \end{aligned}$$

   where $n\prime(x_{tag}; \hat{c})$ and $s\prime(x_{tag}; \hat{c})$ are defined by Eq. (5.10).

7. For the B_{flav} and $B^{\pm}$ samples, we must also sum over both possible B_{rec} flavors b. To account possible differences in the reconstruction efficiency for the different flavors, we add the fraction of B^0 and B^+ events reconstructed $f^{sig}_{B^0}$ and $f^{sig}_{B^+}$ as fit parameters.

8. For each event type e, we add a small fraction (f_p^e) of peaking background, so that the combined distribution ($\mathcal{F}^{g,e}$) is:

$$\begin{aligned} \mathcal{F}^{g,e}(x_{tag}, \Delta t_{true}) &= (1 - f_p^e) \times \mathcal{F}^{s,e}(x_{tag}, \Delta t_{true}, b) \\ &\quad + f_p^e \times \mathcal{F}^{p,e}(x_{tag}, \Delta t_{true}, b). \end{aligned} \tag{6.6}$$

   We use the superscripts g,s and p to refer to the summed (or "Gaussian" for Gaussian $m_{\rm ES}$ distribution), signal and peaking background distributions respectively. We use the B_{flav} distribution as peaking background for the $B^{\pm}$ sample and vice versa; we use the "$\mathcal{CP}$ peaking" background for $\mathcal{CP}$ samples.

9. We convolute the Δt_{true} distributions with our resolution function:

$$\mathcal{F}^{g,e}(x_{tag}, \Delta t, b) = R(\delta t; \sigma_{\Delta t}, \hat{\alpha}) \otimes \mathcal{F}^{g,e}(x_{tag}, \Delta t_{true}, b). \tag{6.7}$$

10. For each event sample and B_{rec} flavor we model the x_{tag} vs. Δt distributions for the combinatorical background with the kernel estimation technique: $K^e(\Delta t, x_{tag}, b; f_b^{a,e})$.

11. Finally, for each event type we construct the joint P.D.F. including the $m_{\rm ES}$ distributions:

$$\begin{aligned} F^e(m_{\rm ES}, x_{tag}, \Delta t, b) &= f_g^e \cdot \mathcal{G}^e(m_{\rm ES}) \cdot \mathcal{F}^{g,e}(x_{tag}, \Delta t, b) \\ &\quad + (1 - f_g^e) \cdot \mathcal{A}^e(m_{\rm ES}) \times K^e(\Delta t, x_{tag}, b). \end{aligned} \tag{6.8}$$

6.1.7 Detector Response Parameters

At this point, we have a good estimate of almost all of the parameters we used to describe our data.

1. We have fit various m_{ES} distributions for each of the event sample. Each of these fits has a total of three free parameters: the width of the signal Gaussian (σm_{ES}), the Angus function shape parameter (ξ) and the signal fraction (f_g).
2. We have estimated the cross-contamination between the B_{flav} and $B^{\pm}$ samples, f_p^{flav} and $f_p^{\pm}$.
3. We have also estimated the size of the peaking background in the $\mathcal{CP}$ samples, f_p^{CP} and $f_p^{K^{*0}}$.
4. We have extracted the resolution functions for both runs (r); $R^r(\delta\Delta t|\sigma\Delta t)$. Each resolution function has a total of four free parameters: f_e, f_o, τ_r and σ_g, but we keep f_e and τ_{r} fixed between the two runs for a total of six parameters.
5. We have measured the fraction of events having B_{rec} flavor b in both signal ($m_{\mathrm{ES}} > 5.27$) and background ($m_{\mathrm{ES}} < 5.27$) for both the B_{flav} and $B^{\pm}$ samples.
6. We have measured the tagging function parameters $\hat{c}$ in the B_{flav} sample. There are a total of eight tagging function parameters.

6.2 Results of the Global Fit

"Don't tell [John] Jacobsen you did a 47 parameter fit, he gets off on that stuff and he'll be jealous."
— J. Beacom

Tab. 6.2 lists the fitted value all of the fit parameters. The parameters at the bottom, listed without error, were fixed for the fit.

Physics Parameters			
τ_{B^0}	1.545 ± 0.031 ps		
τ_{B^+}	1.663 ± 0.032 ps		
Δm_d	0.505 ± 0.021 ps^{-1}		
sin2β	0.562 ± 0.165		
Resolution Function		**Tagging Function**	
f_e	0.412 ± 0.112	C_1	1.062 ± 0.034
f_o (run 1)	0.020 ± 0.007	C_2	0.041 ± 0.031
f_o (run 2)	0.007 ± 0.007	C_3	-0.072 ± 0.037
τ_{r} (ps)	1.005 ± 0.243	C_4	-0.005 ± 0.036
s (run 1)	1.355 ± 0.089	ΔC_1	0.006 ± 0.028
s (run 2)	1.210 ± 0.082	ΔC_2	0.003 ± 0.030
		ΔC_3	-0.005 ± 0.027
		ΔC_4	-0.015 ± 0.025
$B^{\pm}$		B_{flav}	
$f^g_{B^+}$	0.505	$f^g_{B^0}$	0.505
$f^a_{B^+}$	0.522	$f^a_{B^0}$	0.505
f_p	0.005	f_p	0.005
f_g	0.616	f_g	0.442
ξ	-41.4	ξ	-34.6
σm_{ES}	2.76	σm_{ES}	2.75
$\mathcal{CP}$ ($\eta_{cp} = -1$)		$\mathcal{CP}$ (J/ψ K^{*0}) $\eta^{eff}_{CP} = 0.68$	
f_p	0.015	f_p	0.015
τ_{peak}	1.60	τ_{peak}	1.60
η^{peak}_{CP}	0.0	η^{peak}_{CP}	0.0
f_g	0.763	f_g	0.518
ξ	-72.8	ξ	-106.3
σm_{ES}	2.75	σm_{ES}	2.62

Table 6.3: *Summary of combined fit to all the data..*

Parameter	Value	Correlation		
		Global	τ_{B^0}	τ_{B^+}
Physics Parameters				
τ_{B^0}	1.561 ± 0.028	0.663	1.000	0.421
τ_{B^+}	1.682 ± 0.026	0.658	0.421	1.000
Resolution Function				
f_e	0.402 ± 0.109	0.964	0.212	0.165
f_o (run 1)	0.018 ± 0.005	0.448	-0.257	-0.240
f_o (run 2)	0.006 ± 0.005	0.566	-0.376	-0.477
τ_r	0.821 ± 0.198	0.969	-0.218	-0.163
s_o (run 1)	1.323 ± 0.060	0.687	-0.297	-0.320
s_o (run 2)	1.121 ± 0.062	0.603	-0.207	-0.139

Table 6.4: *Summary of lifetime fit results.*

6.3 Results for Calibration Measurements

In order to cross check our method, we extract cursory results for the B-lifetimes and Δm_d. The results are presented here, but should be interpreted as systematic cross checks of our sin2β results rather than as definitive measurements of these quantities.

6.3.1 B Lifetimes

To extract measurements for the B-lifetimes we re-perform the global fit these changes:

- we fix all the tagging functions parameters C_n to their values from the combined fit;
- we fix all of the other physics parameters $\hat{\gamma}$ to the current world averages.

Tab. 6.3.1 shows the results of the lifetime fits. These results are fully consistent with the global fit results and reduce the statistical uncertainty on the lifetimes by about 10%. Additionally, Fig. 6.1 shows the likelihood contours contours in the τ_{B^0}-τ_{B^+} plane. From this

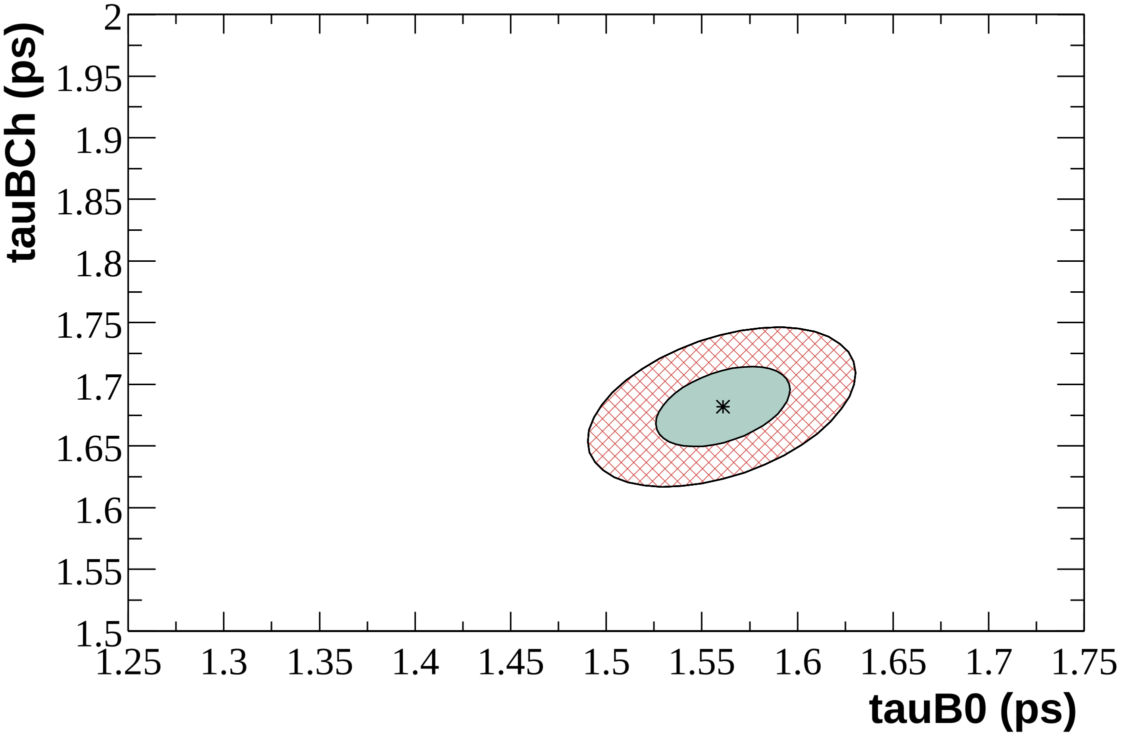

Figure 6.1: *One and two* σ *contours in the* τ_{B^0}-τ_{B^+} *plane.*

second plot we can clearly see the correlation between the two measurement resulting from the shared resolution function.

Although we do not specifically quantify systematic error for our lifetime measurement, we note that our systematics errors are essentially those quoted in the published *BABAR* measurement of the B-lifetimes, which are tabulated in Sec. 6.5. Thus we claim that:

$$\begin{aligned} \tau_{B^0} = &\ 1.561 \pm 0.028(stat) \pm 0.022(syst), \\ \tau_{B^+} = &\ 1.682 \pm 0.026(stat) \pm 0.023(syst) \end{aligned} \tag{6.9}$$

Which are perfectly consistent, although slightly more precise that the published *BABAR* results on the Run 1 data (20.7 fb^{-1}) obtained with slightly different methods [143, 112, 144]:

$$\begin{aligned} \tau_{B^0}(\mathit{BABAR}) = &\ 1.543 \pm 0.032(stat) \pm 0.022(syst) \\ \tau_{B^+}(\mathit{BABAR}) = &\ 1.674 \pm 0.032(stat) \pm 0.023(syst). \end{aligned} \tag{6.10}$$

6.3.2 Δm_d Measurement

To extract a measurement of Δm_d we re-perform the combined fit with all of the other physics parameters, $\hat{\gamma}$ fixed to the current world averages.

Tab. 6.3.2 shows the results of the mixing fits. These results are fully consistent with the global fit results and reduce the statistical uncertainty on on Δm_d by about 10%.

As discussed in Sec. 6.5, for the sake of comparison we adopt the same systematic errors as quoted in the published *BABAR* measurement as far as possible. The primary additionally systematic errors that we quote come from our use of a continuous tagging variable than a category based technique.

$$\Delta m_d \ = 0.498 \pm 0.018(stat) \pm 0.020(syst). \tag{6.11}$$

Parameter	Value	Correlation	
		Global	Δm_d
Physics Parameters			
Δm_d	0.498 ± 0.018	0.445	1.00
Resolution Function			
f_e	0.402 ± 0.109	0.895	0.162
f_o (run 1)	0.018 ± 0.005	0.390	-0.153
f_o (run 2)	0.006 ± 0.005	0.523	-0.282
τ_r	0.821 ± 0.198	0.945	-0.151
s_o (run 1)	1.325 ± 0.060	0.602	-0.233
s_o (run 2)	1.123 ± 0.062	0.582	-0.136
Tagging Function			
C_1	1.045 ± 0.031	0.581	0.414
C_2	0.050 ± 0.028	0.364	0.013
C_3	-0.083 ± 0.032	0.453	-0.188
C_4	-0.025 ± 0.028	0.297	0.038
ΔC_1	0.013 ± 0.023	0.290	0.025
ΔC_2	-0.003 ± 0.023	0.560	-0.023
ΔC_3	0.017 ± 0.021	0.463	0.019
ΔC_4	-0.005 ± 0.022	0.201	-0.010

Table 6.5: *Summary of Δm_d fit to all the data.*

Parameter	Value	Correlation	
		Global	sin2β
Physics Parameters			
sin2β	0.61 ± 0.139	0.072	1.00
Resolution Function			
f_e	0.324 ± 0.012	0.612	0.021
f_o (run 1)	0.021 ± 0.012	0.292	-0.012
f_o (run 2)	0.007 ± 0.007	0.278	0.006
τ_{r}	0.87 ± 0.095	0.419	-0.012
s (run 1)	1.35 ± 0.061	0.330	0.035
s (run 2)	1.19 ± 0.066	0.288	0.032
Tagging Function			
C_1	1.049 ± 0.029	0.094	-0.061
C_2	-0.0315 ± 0.027	0.051	0.006
C_3	-0.0136 ± 0.0318	0.102	-0.034
C_4	-0.009 ± 0.0326	0.032	0.004
ΔC_1	0.0038 ± 0.0032	0.020	0.021
ΔC_2	0.0012 ± 0.0023	0.016	-0.013
ΔC_3	-0.0011 ± 0.0027	0.042	0.013
ΔC_4	-0.0005 ± 0.0030	0.032	-0.021

Table 6.6: *Summary of* sin2β *fit to all the data.*

Again, our results are fairly consistent with, though less precise than the published *BABAR* results:

$$\Delta m_d \ (BABAR) = 0.516 \pm 0.016(stat) \pm 0.010(syst). \tag{6.12}$$

In this case, the method differs fairly significantly, so a larger variation within the errors might be expected.

6.4 Extracting sin2β

Finally, to extract sin2β we redo the fit with all the other physics parameters, $\hat{\gamma}$ fixed to the current world averages.

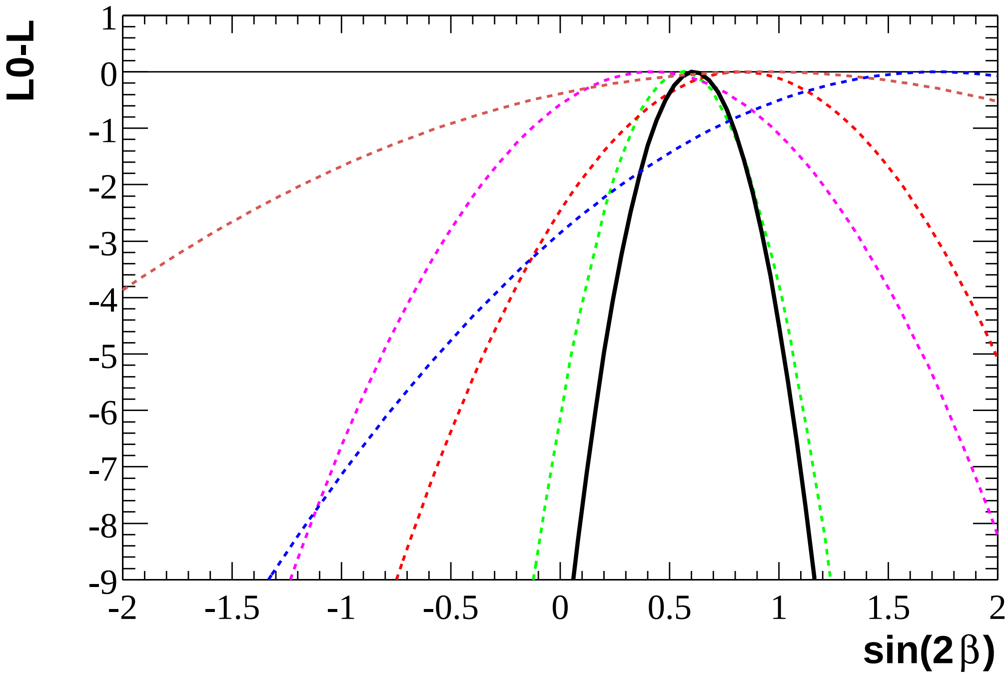

Figure 6.2: *Log-likelihood values as a function of* sin2β*. The combined to all the samples is the solid line, the various dashed lines correspond to the subsamples.*

Tab. 6.4 shows the results of the fit result. These results are again quite consistent with the global fit results and reduce the statistical uncertainty on sin2β by about 10%. Additionally, Fig. 6.2 shows the fit likelihoods for the complete fit, as well as for each decay mode separately.

The contribution to the statistical error from free parameters other than sin2β is fairly large, at 0.036.

6.4.1 Breakdown by Event Samples

As a cross check, we have split the $\mathcal{CP}$ sample in a variety of ways and separately fit each of the sub-samples. For each of this fits, we reconstructed the Argus background Δt model and re-performed the $m_{\rm ES}$ fits to extract the signal fraction. This is particularly important

Sample	Yields	sin2β
$J/\psi\ K^0_S\ (K^0_S \to \pi^+\pi^-)$	410 ± 5	0.55 ± 0.16
$J/\psi\ K^0_S\ (K^0_S \to \pi^0\ \pi^0)$	93 ± 6	0.82 ± 0.37
$\psi(2S)\ K^0_S$	105 ± 9	0.45 ± 0.39
$\chi_{c1}\ K^0_S$	50 ± 5	1.72 ± 0.58
$\eta_{\mathcal{CP}} = -1$	665 ± 14	0.58 ± 0.21
$J/\psi\ K^{*0}\ (K^{*0} \to K^0_S\ \pi^0)$	87 ± 10	0.92 ± 1.05
$\mathcal{CP}$ sample	752 ± 16	**0.61±0.13**
$\eta_{\mathcal{CP}} = -1$ Only		
Lepton	75 ± 6	0.62 ± 0.24
Kaon	264 ± 13	0.58 ± 0.20
NT1	60 ± 5	0.79 ± 0.40
NT2	71 ± 12	-0.02 ± 0.75
‘‘No Tag’’	201 ± 12	1.53 ± 1.25
B^0-Tag	232 ± 7	0.54 ± 0.26
$\overline{B}^0$-Tag	233 ± 6	0.61 ± 0.26
e^+e^-	348 ± 10	0.51 ± 0.21
$\mu^+\ \mu^-$	317 ± 10	0.72 ± 0.20
Control Samples		
B_{flav}	9732 ± 85	0.04 ± 0.04
$B^\pm$	13229 ± 83	-0.03 ± 0.02

Table 6.7: *Result of fitting for $\mathcal{CP}$ asymmetries in the entire $\mathcal{CP}$ sample and in various subsamples. In the fits to only B^0 or $\overline{B}^0$ tags, only the relevant tagging function mass used. In each of the fits to subsamples the background models and fractions were rebuilt and all the parameters excepts* sin2β *were fixed.*

for the fits by tagging category, where the background time distributions vary significantly between the different categories. The only particularly noticeable item is the very unphysical value of sin2β measured with the χ_{c1} K_S^0 events. We can only cite the low statistics and trust that with a larger data sample this value will agree more closely with the others.

We also note an interesting feature if we used only B^0 or $\overline{B}^0$ tagged event to extract the resolution function. This leads to much higher correlation between sin2β and the resolution function, and is oppositely signed for B^0 and $\overline{B}^0$-tagged events. In fact, for certain subsamples we measure the value for sin2β to be lower for both B^0 and $\overline{B}^0$ events than for the combined sample.

Finally, as a negative control, we have fit both the B_{flav} and $B^{\pm}$ samples for $\mathcal{CP}$ asymmetries and obtain the expected null results.

6.4.2 Tag-Weighted Asymmetry

Following the method discussed in Sec. 5.5 we graphically present the $\mathcal{CP}$ asymmetry using the tag-weighting technique.

Fig. 6.3 shows the tag-weighted Δt distributions for both the $\eta_{CP} = -1$ and J/ψ K^{*0} samples with the fit results overlayed. Furthermore, to graphically display $\mathcal{CP}$ asymmetry, we have plotted the tag-weighted Δt asymmetries on Fig. 6.4.

Given the way the likelihood is normalized, the number of B^0 and $\overline{B}^0$ are almost identical, with a small difference due to the Δw. Also very sharp eyed readers may notice that the second oscillation of the curve does not have the same amplitude as the first oscillation (this is much more evident when plotted past 10 ps). This is due to the 8 ps wide outlier Gaussian, which washes out the asymmetry at large Δt. With respect to the data there are also some

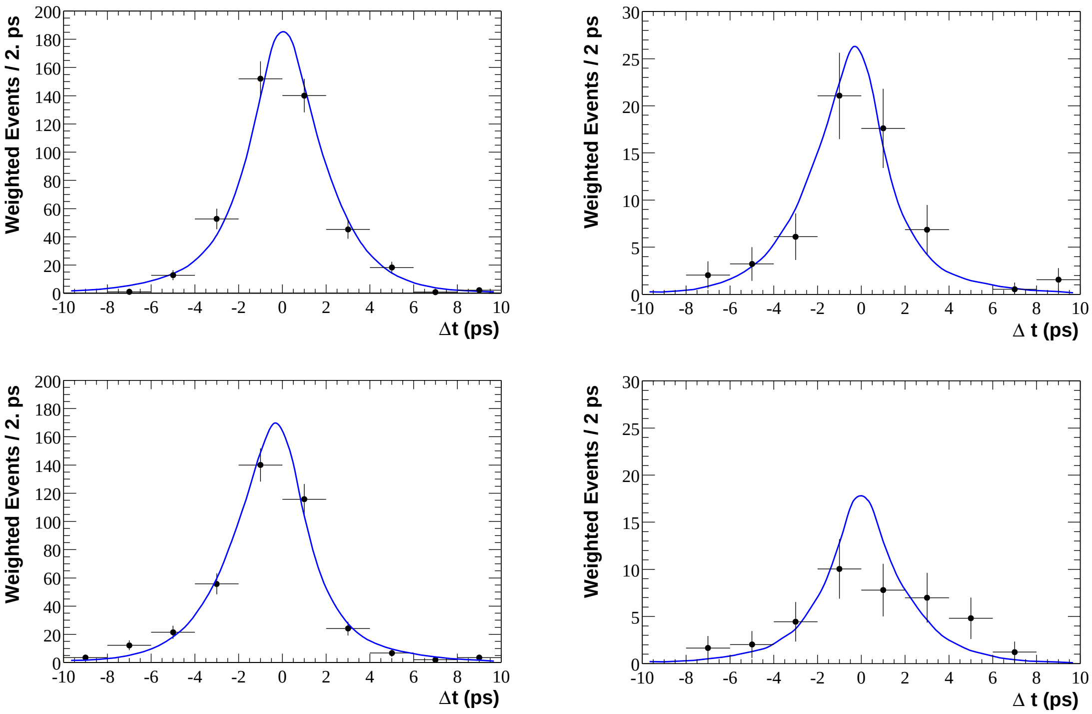

Figure 6.3: *Δt distributions for selected $\mathcal{CP}$ events with $m_{\rm ES} > 5.27\,{\rm GeV}/c^2$. Events with a B^0 ($\overline{B}^0$) on the tagging side are shown on the top (bottom). $\eta_{CP} = -1$ (J/ψ K^{*0}) events are on the left (right). The result from the likelihood fit is overlaid.*

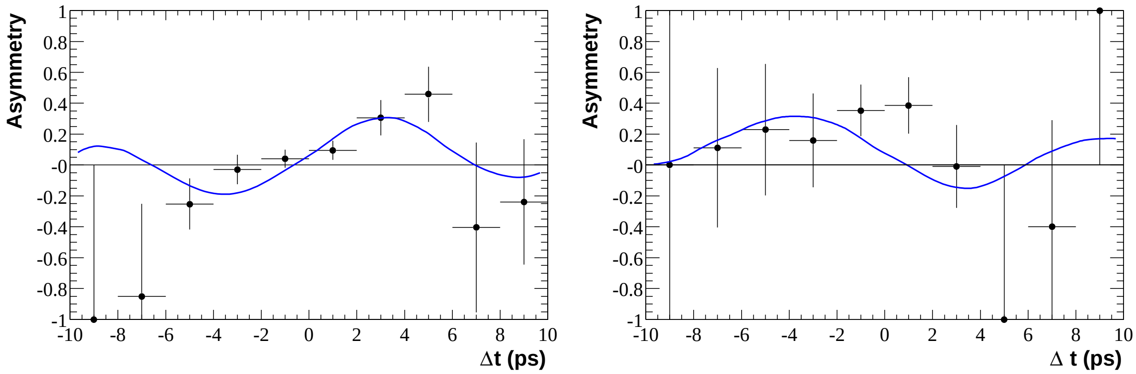

Figure 6.4: *Tag-weighted Δt asymmetry for $\mathcal{CP}$ decays. $\eta_{CP} = -1$ (J/ψ K^{*0}) events are on the left (right).*

comments in order. There are 21 events which fall outside the ±10 ps window of these plots. Also some care has been taken in the evaluation of the errors for each data point, due to the low statistics present in some of the bins.

6.4.3 The $\mathcal{K}in$ Variable

The fact that we are measuring an asymmetry allow for a very useful alternative to performing the full likelihood fit [145]. We define a variable $\mathcal{K}in$:

$$\mathcal{K}in \equiv \frac{F(\hat{c},\hat{\alpha};\hat{\gamma}_{+}) - F(\hat{c},\hat{\alpha};\hat{\gamma}_{-})}{F(\hat{c},\hat{\alpha};\hat{\gamma}_{+}) + F(\hat{c},\hat{\alpha};\hat{\gamma}_{-})}, \tag{6.13}$$

where $\hat{\gamma}_{\pm}$ is the physics model, with $\sin 2\beta$ set to ± 1. It can be shown that the maximum likelihood will occur when the fitted asymmetry, that is to say $\sin 2\beta$ given by:

$$\sin 2\beta \ = \frac{\sum_i \mathcal{K}in_i}{\sum_i \mathcal{K}in_i{}^2}, \tag{6.14}$$

where the subscript i is to remind us that we are calculating $\mathcal{K}in$ separately for each event and summing over all the events.

Thus, once we have extracted all the the resolution and tagging function parameters once, we can consider the effects of small changes among them on $\sin 2\beta$, or among the input events for the fit, without re-fitting the entire sample. This is ideal for studying systematic effects, since they represent, by definition, small potential differences between the fitted model and reality.

6.5 Systematic Errors

"It has been shown that systematic errors tend to be under-estimated by a factor of three."
— R. Jacobsen

This section describes each contribution to the systematic error as well as other cross checks performed. For some sources, we also quote the systematic assigned in the lifetime and mixing from studies performed within the *BABAR* collaboration for related publications [112, 130] for the sake of comparison. Furthermore, many of the sources of systematic error have already been discussed in the context of the B-lifetime and Δm_d measurements in Secs. 4.7 and 5.6. Finally, in those cases where our method does not differ from the method in the published *BABAR* sin2β measurement [130], we simply cite the relevant studies.

In general, we divide our potential systematic bias into five types.

1. Bias coming from inaccuracies in our modeling of the signal and detector effect on the signal. This includes our models of the tagging and resolution functions, as well as possible biases caused by un-modeled correlations between dependent variables in our likelihood fits. These issues are treated in Sec. 6.5.1.

2. Bias coming from inaccuracies in our modeling of the background. Essentially, we question how well the m_{ES} sideband events and our model of the "peaking" background components describe the non-signal which are used in the likelihood fits. These effects are treated in Sec. 6.5.2.

3. Since our Δt distributions depend on a combination of several physics parameters, changes in the favored value of one will cause changes in the measured values of the other. This is discussed in Sec. 6.5.3.

4. It is also possible that there are some detector biases with are not absorbed by the resolution and tagging functions (*e.g.,*an overall inaccuracy in the z-scale of the experiment). Some potential biases of this type are treated in Sec. 6.5.4.

5. Finally, we must quantify the accuracy to which our fitting technique is in fact able to measure physics quantities. This subject is treated in Sec. 6.5.5.

6.5.1 Signal Properties

Certain systematic biases can be introduced because of limitations in our modeling of the signal distributions for the event dependent variables Δt x_{tag} and m_{ES}. Our results are only as accurate as the parameterizations of the resolution and tagging function that we have used. Furthermore, our technique has three underlying assumptions.

1. That the resolution functions are the same for all the signal events samples.
2. That the tagging functions are the same for the $\mathcal{CP}$ and "mixing" events.
3. There is no correlation between the resolution function and the tag value.

Deviations from each of these assumptions are considered in the systematic errors.

6.5.1.1 Parameterization of the Resolution Function

As discussed the Sec. 4.7.1, we have studied alternative parameterization of the resolution function. By changing between various resolution functions and using the $\mathcal{K}in$ technique to gauge the effects on sin2β we estimate that possible effect for the parameterization of the central part of the resolution function is $\delta\sin2\beta = 0.012$. Furthermore, we independently estimate that the effect of changing the outlier contribution and model is $\delta\sin2\beta = 0.003$.

We note in passing that these are the two dominant sources of systematic error in the B-lifetime measurements, giving in quadrature a total of $0.014ps$ out of a total systematic error of $0.022ps$ [147].

6.5.1.2 Resolution Differences Between Event Samples

The variation of the resolution function between the $B^{\pm}$, B_{flav} and $\mathcal{CP}$ samples was studied in Secs. 4.7 and 5.6. To quantify the possible bias from these effects, we change each of the resolution parameters by ±1 times the difference observed in the separate fits to the $B^0\overline{B}^0$ and $B^{\pm}$ event samples. In Monte Carlo, the difference between $B^{\pm}$ and $B^0\overline{B}^0$ resolution functions is significantly larger that the difference between different B^0 modes, therefore, we find this to be very conservative error assignment. The largest variation ($\delta\sin 2\beta = 0.003$) comes with the scale factor s, which we assign as a systematic error.

6.5.1.3 Resolution Correlation with $\sigma_{\Delta t}$

Although the correlation between δt and $\sigma_{\Delta t}$ is an issue in the lifetime and mixing measurements, we find much less of an effect on $\sin 2\beta$ (< 0.0005) when performing a Monte Carlo study in which we re-weight events based on their likelihood in the δt-$\sigma_{\Delta t}$ plane. Since these correlation might be slightly underestimated in the Monte Carlo, we take 0.001 as a systematic error from this source.

6.5.1.4 Resolution Correlation with x_{tag}

As with the Δm_d measurement, we are worried about any correlation between the resolution function and x_{tag}[146]. Using the model subtraction technique discussed is Sec. 5.6, with the simple change of using the $\mathcal{K}in$ technique to estimate the changes, rather that a complete re-fit, we estimate potential variation of $\delta\sin 2\beta = +0.007$. Furthermore, we have observed that increasing the correlation between $\sigma_{\Delta t}$ and x_{tag} always increases the measured value of $\sin 2\beta$. That is to say, that this source of error seems to slightly bias the $\sin 2\beta$ measurement towards higher values.

In Monte Carlo studies, we also noted that if we change the resolution function so that the exponential term is not scaled by the per-event error, we see similar effect, but with the opposite sign and somewhat larger (-0.013).

We interpret these results as follows.

1. Since we fit the resolution function, and perform a series of cross check, we have every reason to believe that, on average, the resolution function is accurate. What we are concerned with here is the case where we systematically overestimate the resolution (*i.e.* we model the data with a function with a resolution function that is too narrow) for some types of flavor tags and underestimate the resolution for others.
2. As far as measuring sin2β is concerned, the key issue is if we are overestimating or underestimating the vertex resolution of well-tagged (high $|x_{tag}|$) events, since these dominate the fit.
3. If we do not scale the exponential term in the resolution function by the per-event error, we know that we are underestimating the resolution of well-tagged events.
4. On the other hand, if we do scale the exponential term by the per-event errors, we seem to be over-correcting for the differences between events.

Given the uncertainty on the number and the relatively small size of the effect, we do not attempt to correct for this bias. But rather we take size of the larger difference 0.013 as a systematic error.

We also note that this effect is does not exist in the published *BABAR* measurement of Δm_d. As stated in Sec. 5.6 we estimate the possible effect on Δm_d to by ± 0.009.

6.5.1.5 Tagging Function Parameterization

As we discussed in Sec. 5.6, there a possibility that our parameterization of the tagging function could cause a systematic bias in measuring asymmetry rates. To quantify the size of such effect, we repeat the toy Monte Carlo studies performed with for Δm_d, with the change of fitting for sin2β instead of Δm_d. We then take the mean error on sin2β (0.012) from those studies as a systematic error.

6.5.1.6 Tagging Function Difference between Event Samples

We also considered possible differences between the tagging performance on difference event samples. Specifically, in high statistics full Monte Carlo studies we found a 0.035 change in sin2β when we varied the tagging function parameters by the difference measured from Monte Carlo truth between the $\mathcal{CP}$ and B_{flav} samples.

We also accounted for possible resolution function differences between "accurately" and "inaccurately" tagged events, as discussed in Sec. 5.6.3 [140]. We observed a 0.014 changed in sin2β when we only used events where the favored tag was the true tag, as opposed to events where the favored tag was incorrect.

We assign both of these variations as systematic errors.

6.5.1.7 Signal Probability Parameterization

We study the effect of the uncertainty on the m_{ES} shape parameterization by simply assigning equal signal probability to all the events with $m_{\mathrm{ES}} > 5.27$ based on the measured purities, a zero signal probability to all others. That is to say, we replace the m_{ES} signal Gaussian with a step function. From these studies we quote an error of sin2β of ±0.006.

We have also performed studies to account for an error in m_{ES} fit results due to the uncertainty in the beam energy by varying the end-point of the Argus background shape by $\pm 2\,\mathrm{MeV}$ around the nominal value of $5.291\,\mathrm{GeV}$. From which we estimate the systematic uncertainty due to the m_{ES} endpoint to be ± 0.001.

Finally, we account for the possibility that signal probabilities are correlated with x_{tag}. That is to say that better-tagged events are also cleaner. This is not unexpected, as requiring a high-energy track on the tag side is known to reduce light-quark backgrounds. To study this, we split the sample by x_{tag}, measure the background level for each sub-sample and re-weight the event accordingly. From these studies we assign an error of $\delta\sin 2\beta = 0.005$.

Thus, in total we assign an error of ± 0.008 from uncertainties in the signal probabilities.

6.5.1.8 Effective $\mathcal{CP}$ of the $J/\psi\ K^{*0}$ Sample

To take into account our uncertainty of the effective $\mathcal{CP}$ content of the $J/\psi\ K^{*0}$ $\mathcal{CP}$ sample, we simply quote a relative error of $\frac{\delta\sin 2\beta}{\sin 2\beta} = 12\%$, equal to our uncertainly of the effective η_{CP}. This corresponds to an error of 0.08 for the $J/\psi\ K^{*0}$ mode only. Giving an error of 0.001 for the full sample.

6.5.2 Background Properties

It is also possible to introduced biases in the measurement of $\sin 2\beta$ by incorrectly modeling either the size of the shape of the backgrounds which contribute to the fit. Fortunately, these effect are reduced by the high purity of the $\mathcal{CP}$ sample [148].

All of the background parameters we used were either measured on data from independent fits (*e.g.,*fitting the m_{ES} shapes) or evaluated from Monte Carlo.

6.5.2.1 Peaking Background Component

As discussed in Secs. 4.6.1 and 5.5.2, background contributions that peak in m_{ES} were estimated by running on the inclusive Monte Carlo samples. In general, we assign error corresponding to a 100% change in the size of the peaking background. From these studies, we assign a total error of ± 0.004 on sin2β.

6.5.2.2 Peaking Background Content

It is also possible that the peaking background has a significant $\mathcal{CP}$ component to. To account for this possibility, we vary the effective $\mathcal{CP}$ asymmetry of that model over the full $[-1, 1]$ range. From these studies, we assign a total error of 0.008 on sin2β.

6.5.2.3 Argus Background Content

To account for the unknown $\mathcal{CP}$ content of the Argus background, we replace the kernel-estimated background model with the model used for the peaking $\mathcal{CP}$ background and vary the $\mathcal{CP}$ content over the range $[-1, 1]$. This yields a systematic error of sin2β ± 0.017.

The lifetime of the $\mathcal{CP}$ background has been varied from 0.7 to 2.5 ps, and gives negligible (< 0.0005) systematic uncertainty on sin2β. However, separate studies have found a shift (0.002) in sin2β observed when a different resolution function is used is for this background. Therefore, we quote 0.002 as the possible systematic error from the peaking background Δt resolution. In either case this is negligible compared to the 0.017 assigned for the unknown $\mathcal{CP}$ content.

	Global	Δm_d	sin2β	τ_{B^0}	τ_{B^+}
Δm_d	0.68602	1.000	-0.153	-0.335	-0.206
sin2β	0.24508	-0.153	1.000	-0.038	-0.012
τ_{B^0}	0.52391	-0.335	-0.038	1.000	0.269
τ_{B^+}	0.60727	-0.206	-0.012	0.269	1.000

Table 6.8: *Correlation matrix for the physics parameters.*

6.5.2.4 Modeling the B_{flav} Background

Finally, we consider the possible error in estimating the tagging performance caused by errors in modeling the B_{flav} background. This uncertainty gives a systematic error on sin2β of ±0.003, coming primarily from the uncertainties in the fraction and possible mixing content of the Argus background.

6.5.3 External Physics Parameters

Probably the most accurate analysis of the potential errors arising from the correlation between various physics parameters is simply to measure their correlation in the combined fit.

In fact, we see that sin2β is largely decoupled from the other physics parameters. Intuitively, this is because while all of the other three parameters manifest in Δt (*i.e.*, the horizontal axis in a asymmetry plot such a Fig. 6.4, sin2β is a measure of the asymmetry, (*i.e.*, the vertical axis).

From Tab. 6.5.3 we can immediately assign errors on sin2β of ±0.009, and ±0.005 from the uncertainties on Δm_d and τ_{B^0} respectively.

6.5.4 Detector Effects

As in Sec. 4.7, we have also considered the possibility of forms of mis-reconstruction of the data that might not be properly accounted by the measurement technique. We note that many detector effects, (*e.g.,*momentum dependence the kaon ID algorithm), are implicitly absorbed in our studies or the Δt resolution and tagging functions and the correlation therein.

6.5.4.1 Location and Size of the Beam Spot

As discussed in Secs. 4.3 and 4.7.4, the vertexing algorithm uses the y position and size of the beam spot to constrain the line of flight of the B_{tag}. For the magnitude possible biases due to this effect, we quote the results of both data and Monte Carlo studies in which the the various beam spot and beam-energy constraints used in the tag-vertex algorithm were both weakened and completely removed. In total, we use an error of ± 0.002 for this source.

6.5.4.2 Uncertainty on z Scale and Boost

Since a measurement of $\sin 2\beta$ is primarily a measurement of the amplitude of asymmetry, it is not directly sensitive to the changes in the Δt scale that would arise for inaccuracies in either the z length scale the magnitude of the CMS boost [149].

However, since we are fixing the B lifetimes and Δm_d to the world averages in our fit for $\sin 2\beta$, we are effectively fixing the frequency of the asymmetry oscillations. If we do so incorrectly, we will bias our measurement of the their amplitude.

In order to evaluate a possible effect from the uncertainty on the boost, the measurement of Δt has been rescaled by 0.3% upwards and downwards in fit. This results in a change of $\delta \sin 2\beta = 0.003$, which is taken as a systematic error.

6.5.4.3 SVT Internal Misalignment

As discussed in Sec. 4.7.6, possible local misalignment have been studied by reconstructing the same sample of Monte Carlo events with different sets of alignment constants. The largest systematic offset from a realistic (elliptical) distortion is $\delta \sin 2\beta = 0.027$, which we take as a possible error.

6.5.5 Validation of Measurement Method

We have performed high statistics Monte Carlo studies of all of the measurements described in this dissertation using the Monte Carlo samples listed in Sec. 3.2.2. None of these studies shows significant bias from the input Monte Carlo values. We have also used Monte Carlo samples with different input values of $\sin 2\beta$ in the range [0.1,0.9] and confirmed that we extract the correct value of $\sin 2\beta$ in all cases [70, 150, 151].

Furthermore, we have also performed an extensive (100 tests of 50000 events total, split in the same proportions as the data sample) toy Monte Carlo study of the combined likelihood fit to confirm our ability to correctly measure the input values. From these experiments, we have measured a mean discrepancy -0.017 with and error of 0.013, which we assign as a systematic error. Given more processor time, we could reduce this number considerably.

6.5.6 Summary of Systematic Errors

Tab. 6.5.6 summarizes our estimate of the total systematic error on all the measurements presented here.

Source	τ_{B^0}	$\tau_{B^\pm}$	Δm_d	sin2β
	$10^{-3}ps$		10^{-3} ps^{-1}	10^{-2}
Signal Parameterization				
Signal Probability	3	3	2	0.8
Δt Signal Resolution	8	4	3	0.9
$R(\delta t), \sigma\Delta t$ Correlation	NQ	NQ	3	0.1
$R(\delta t)$ by Sample	4	5	-	0.3
$R(\delta t), x_{tag}$ Correlation	-	-	9	1.3
$R(\delta t)$ by Tag Accuracy	-	-	1	1.4
$C(x_{tag})$ Parameterization	-	-	2	1.2
$C(x_{tag})$ by Sample	-	-	-	3.5
Background Modeling				
Peaking Fraction	NQ	NQ	2	0.4
Peaking Content	NQ	NQ	NQ	0.8
Argus Content	5	11	3	1.7
B_{flav} Background Effect on $C(x_{tag})$	-	-	-	0.3
Detector Effects				
SVT Alignment	8	8	4	2.7
Beamspot	2	2	1	0.2
z Scale and Boost	10	10	2	0.3
External Parameters				
τ_{B^0}	-	NQ	7	0.5
Δm_d	NQ	-	-	0.9
Monte Carlo Limitations	9	7	3	1.3
Total in Quadrature	22	23	14	5.6

Table 6.9: *Full list of systematic errors for all analyses. Many of the errors the the B-lifetime and Δm_d measurements are taken from studies for the published BABAR results. In the cases in which various sources of error are merged, we list the error under its dominant contribution and mark the other parts are "NQ".*

Parameter	Measurement	Value
τ_{B^0}(ps)	This Analysis (*BABAR*) (World Average)	$1.560 \pm 0.028(stat) \pm 0.022(syst)$ $1.546 \pm 0.032(stat) \pm 0.022(sys)$ 1.548 ± 0.032
τ_{B^+}(ps)	This Analysis (*BABAR*) (World Average)	$1.676 \pm 0.026(stat) \pm 0.023(syst)$ $1.673 \pm 0.032(stat) \pm 0.023(sys)$ 1.653 ± 0.028
Δm_d (ps^{-1})	This Analysis (*BABAR*) (World Average)	$0.498 \pm 0.018(stat) \pm 0.022(syst)$ $0.516 \pm 0.016(stat) \pm 0.010(sys)$ 0.472 ± 0.017
sin2β	This Analysis (*BABAR*) (World Average)	$0.61 \pm 0.14(stat) \pm 0.06(syst)$ $0.59 \pm 0.14(stat) \pm 0.05(syst)$ -

Table 6.10: *Final values for all the measurements. The systematic error for the three calibration measurements, τ_{B^0}, τ_{B^+} and Δm_d are largely taken from relevant BABAR publications.*

6.6 Summary of Results

Tab. 6.6 summarizes all of our measured results, as well the current world averages and published *BABAR* measurements for each. We note that the *BABAR* measurement of sin2β also includes the $\eta_{CP} = +1$ channel $J/\psi\ K^0_L$.

Chapter 7

Interpretation of Results

"It was a lot easier for me, since you got all your balls out of the way."
— T. Dignan

Having measured sin2β and $|\lambda|$ can now interpret our results in the context of the Standard Model.

We distinguish between three possible goals of such an interpretation.

1. To achieve the best determination of the CKM parameters within the Standard Model.
2. To set a confidence level (CL) for the agreement between data and the Standard Model as a whole.
3. To search for specific signatures of new physics by measuring additional parameters of a particular theoretical extension of the Standard Model.

Only the first two goals are dealt with in the following, a discussion of the third can be found in [154].

7.1 Fitting in the ρ-η Plane

"Tu preferais pas les plots en bleu, blanc, rouge. Je peux le faire si tu le veux."
— S. Laplace

As discussed in Secs. 1.4.2 and 1.4.3 $\mathcal{CP}$ violation in the Standard Model can be summarized by the unitarity triangles and fully parameterized by the four CKM matrix parameters. Accordingly, we will show the effects of our measurements on fits for these parameters.

7.1.1 Statistical Treatment

The current knowledge of many theoretical parameters and measurement systematics relating to CKM observable are not Gaussian-distributed. Rather, they are none to lie with in fixed ranges, but in most cases we do not have an a priori knowledge of which parts of the range are more favored.

Given this situation, we prefer a frequentist, (rather than Bayesian) statistical treatment [152, 153].

The entire statistical analysis, the results of which are presented here, is realized by means of the program package *CkmFitter*. A detailed description of the methods it employs and the presentation of state of are results are the subject of Ref. [154].

The statistical treatment used to combine the available measurements in order to set constraints, *e.g.*,, in the $\bar{\rho}$–$\bar{\eta}$ plane is based on a frequentist approach.

A global χ^2 is built as a sum of individual contributions. This χ^2 receives no contribution due to non-accountable theoretical uncertainties.

For a given point in the ρ-η plane, a confidence level (CL) is computed as:

$$\mathrm{CL} = \mathrm{Prob}(\chi^2 - \chi^2_{\mathrm{min}}, N_{\mathrm{dof}} = 2). \tag{7.1}$$

In this formulation χ^2 is obtained by minimizing the global χ^2 with respect to all parameters except for ρ and η, which are fixed to the point under consideration. During the χ^2 minimization, the parameters which suffer from theoretical uncertainties can vary freely within their pre-defined ranges (so-called *allowed* ranges).

Theoretical uncertainties are attributed to most of the theoretical input parameters, in particular those related to strong interaction (QCD). Moreover, the extraction of some of the CKM elements (*e.g.*,, $|V_{ub}|$) inserts theoretical uncertainties due to the model assumptions made. The theoretical parameters fall into two different types.

1. Parameters whose allowed ranges are is irrelevant since the available measurements are powerful enough to determine them, (*e.g.*,λ).
2. Parameters whose allowed ranges determine the usefulness of measurements of CKM observables (*e.g.*,, Δm_d), (*e.g.*,, f_{B_d}). This second type corresponds to QCD quantities and is denoted y_{QCD}.

Finally, $\chi^2_{\min}$ is the absolute minimum of the global χ^2, obtained when all parameters (including ρ and η) are let free to vary.

7.1.2 Constraints in the ρ-η Plane

As discussed in Sec. 1.4, constraints on the CKM elements come from a variety of sources. For example, the Wolfenstein parameters λ and A are obtained from measurements of semileptonic decay rates of K-mesons, and B-meson decays involving $b \to c$ transitions, respectively.

More specifically, constraints in the ρ-η plane are obtained from several measurements.

1. Semileptonic B decays yield $|V_{ub}|$ as well as the ratio $|V_{ub}/V_{cb}|$.
2. Standard Model predictions of B_d and B_s oscillations depend of the CKM phase parameter.

3. Standard Model predictions of indirect $\mathcal{CP}$ violation in the neutral kaon sector also depend on the CKM phase parameter.

However, as discussed in Sec. 1.4, theoretical predictions for both flavor mixing and ϵ_K are limited by uncertainties which mainly stem from long distance QCD. Therefore, these measurements predictive power in the ρ-η plane is limited.

7.1.3 Input Parameters

Tab. 7.1.3 shows a listing of the input values used in the global CKM fit which are allowed to vary during the fit. In cases where the theoretical error has been deduced by more or less educated guess work or its size is questionable it is considered as a range (see previous section) [155, 156].

7.1.4 Effects of These Results In the ρ-η Plane

For the graphical display of the results, lines of constant CL (32% and 5%) are represented in the $\bar{\rho}-\bar{\eta}$ plane together with the most favored domain (MFD) where the CL is close to one. The size of the MFD is determined by the size chosen for the allowed-ranges of y_{QCD} parameters.

The results of the global fit in the $\bar{\rho}-\bar{\eta}$ plane are shown in Fig. 7.1 with the BaBar measurement of sin2β as fit input. The darker shaded (central) and lighter shaded (outer) areas correspond to $> 32\%$ CL and $> 5\%$ CL, respectively. The outer regions receive lower CL's which expresses the fact that they leave the range where a simple modification of the fit parameters produces maximal compatibility (*i.e.*, where they approximately reproduce the global χ^2_{min}). In the $\geq 5\%$ CLregion, several ellipses are shown as dashed lines: they

Parameter	Value ± Error(s)	χ^2	Free	Prop.
Experimentally Measured CKM Elements				
$\|V_{ud}\|$	0.97394 ± 0.00089	*	-	-
$\|V_{us}\|$	0.2200 ± 0.0025	*	-	-
$\|V_{ub}\|$	$(3.48 \pm 0.23 \pm 0.55) \times 10^{-3}$	*	-	-
$\|V_{cd}\|$	0.224 ± 0.014	*	-	-
$\|V_{cs}\|$	0.969 ± 0.058	*	-	-
$\|V_{cb}\|$	$(40.8 \pm 0.4 \pm 2.0) \times 10^{-3}$	*	-	-
Experimentally Measured Observables				
$\|\epsilon_K\|$	$(2.271 \pm 0.017) \times 10^{-3}$	*	-	-
Δm_d	$(0.487 \pm 0.014)\ \text{ps}^{-1}$	*	-	-
sin2β	0.49 ± 0.18	*	-	-
Expirementally Measured Standard Model Parameters				
$m_t(\overline{\text{MS}})$	$(166.0 \pm 5.0)\ \text{GeV}/c^2$	*	*	-
m_K	$(493.677 \pm 0.016)\ \text{MeV}/c^2$	-	-	*
Δm_K	$(3.4885 \pm 0.0008) \times 10^{-15}\ \text{GeV}/c^2$	-	-	*
m_{B_d}	$(5.2794 \pm 0.0005)\ \text{GeV}/c^2$	-	-	*
m_{B_s}	$(5.3696 \pm 0.0024)\ \text{GeV}/c^2$	-	-	*
m_W	$(80.419 \pm 0.056)\ \text{GeV}/c^2$	-	-	*
f_K	$(159.8 \pm 1.5)\ \text{MeV}/c^2$	-	-	*
Theoretically Predicted Standard Model Parameters				
m_c	$(1.3 \pm 0.1)\ \text{GeV}/c^2$	-	*	-
B_K	$0.87 \pm 0.06 \pm 0.13$	*	*	-
η_{cc}	1.38 ± 0.53	-	*	-
$\eta_B(\overline{\text{MS}})$	0.55 ± 0.01	-	*	-
$f_{B_d}\sqrt{B_d}$	$(230 \pm 28 \pm 28)\ \text{MeV}$	*	*	-
ξ	$1.16 \pm 0.03 \pm 0.05$	*	*	-

Table 7.1: *Input observables and parameters for the global CKM fit. Quantities that contribute to the* χ^2 *of the global CKM fit are marked as "*χ^2*" with an asterisk. Quantities that vary freely in the fit are marked as "Free" and quantities with smaller errors that are statistically propagated are marked as "Prop.".*

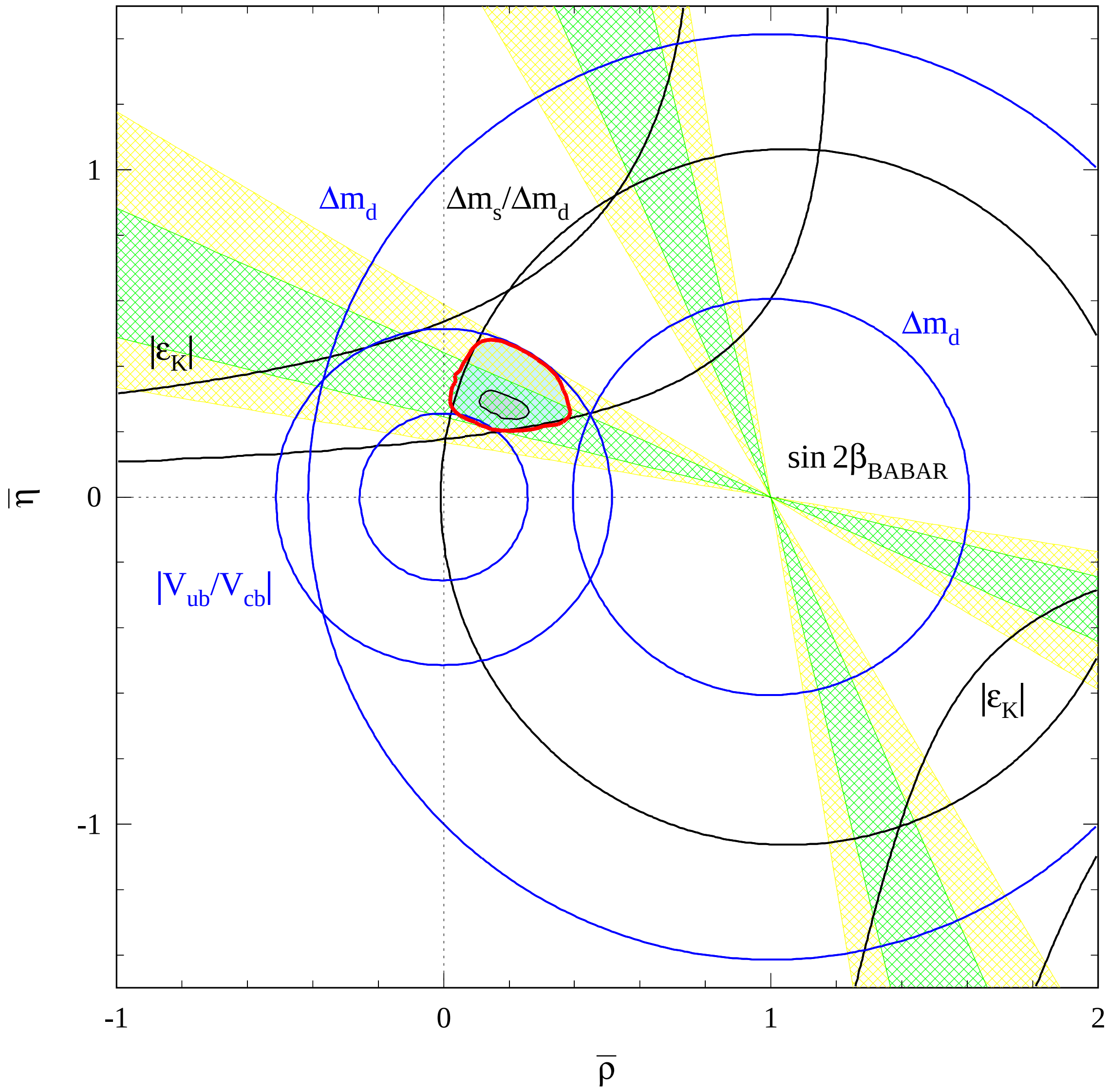

Figure 7.1: *Confidence levels in the* $\bar{\rho}$*−*$\bar{\eta}$ *plane obtained from the global CKM fit. Results are shown both with the measurements describe in this dissertation. The shaded areas indicate the regions of* $\geq 32\%$ *and* $\geq 5\%$ *CL's, respectively. The dashed ellipses represent the* 95% CL *contours one would obtain if the* $y_{\rm QCD}$ *values were exactly known. Also shown are the* 5% *CL contours of the individual constraints. The* $\geq 32\%$ *and* $\geq 5\%$ *CL constraints from the BABAR* sin2β *measurement are depicted by the dashed areas.*

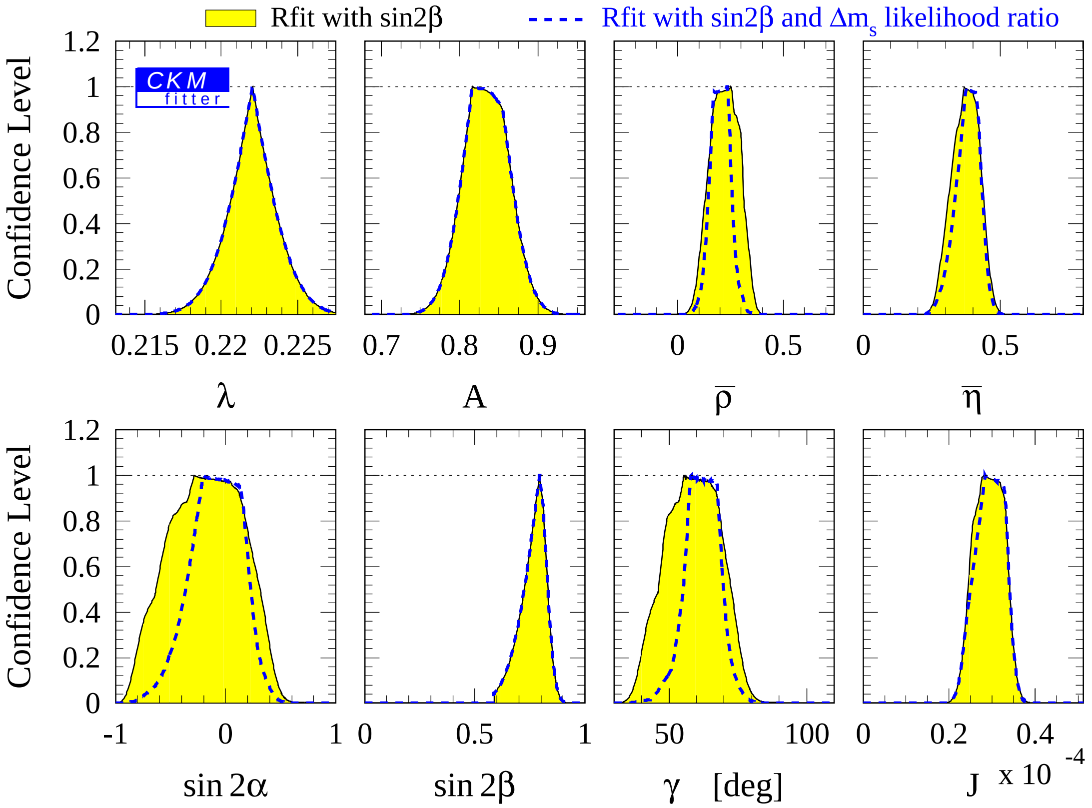

Figure 7.2: *Confidence levels for the one-dimensional parameter fits of the unitarity Triangle Angles and the Jarlskog parameter. The shaded area (dashed line) gives the result without (with) our* $\sin 2\beta$ *measurement as fit input. For* $\sin 2\beta$*, the fit constraint without the BABAR measurement of* $\sin 2\beta$ *as fit input can be directly compared to the CL of the BaBar measurement.*

represent the 95% CL contours one would obtain if the y_{QCD} values were exactly known. Shown in addition are the 5% CL contours of the individual constraints.

According to the frequentist approach adopted here, the CL's have to be interpreted as *upper bounds for the best theoretical model at a given point in the $\bar{\rho}$–$\bar{\eta}$ plane.*

Hence, one shall *not* interpret the CL's given as relative probabilities, *i.e.*, infer equal probabilities from equal shades. Instead, the CL's express the probability that for a given coordinate $\{\bar{\rho}, \bar{\eta}\}$, we find a set of fit parameters that has the same statistical confidence level as that of the best fit confidence level (ξ^2_{min}) in the $\bar{\rho} - \bar{\eta}$ plane. Moreover, although the CL's have a well defined statistical meaning, one must be careful when interpreting them; a modification of the range of the somewhat arbitrary theoretical uncertainties moves the shaded borders of the allowed $\bar{\rho}$–$\bar{\eta}$ region accordingly. As described in the statistics section of Ref. [154], the CL's obtained do not constitute a test of goodness of the theory. A probe of the Standard Model is obtained from an interpretation of the numerical value of χ^2_{min}, as discussed in the next section.

For the numerical analysis, one can derive one-dimensional constraints for all parameters involved, such as the CKM parameters or the CKM matrix elements. As an example, Fig. 7.2 shows the CL's obtained for the unitarity triangle angles and the J parameter. In perfect analogy to the two-dimensional case, the CL's shown constitute upper bounds, corresponding to the most compatible theory for a given value of the parameter considered.

A short compilation of the allowed 95% CL ranges for the CP violating CKM parameters is given in Tab. 7.1.4, without and with the new BaBar value for sin2β. A complete list of the results that can be obtained from the global fit is provided in Ref. [154].

Parameter	Without sin2β		With sin2β	
	$\geq 5\%$ CL	half width	$\geq 5\%$ CL	half width
λ	0.2220 ± 0.0041		0.2220 ± 0.0041	
A	0.76 - 0.90	0.07	0.76 - 0.90	0.07
$\bar{\rho}$	0.04 - 0.38	0.17	0.04 - 0.37	0.16
$\bar{\eta}$	0.20 - 0.48	0.14	0.20 - 0.40	0.10
J	(1.6 - 3.9) $\times 10^{-5}$	1.2×10^{-5}	(1.6 - 3.2) $\times 10^{-5}$	0.8×10^{-5}

Table 7.2: *Fit results for the unitary CKM parameters. Ranges are given for the quantities that are limited by theoretical errors. The left (right) data column gives the constraints when not using (using) the current BaBar measurement of* sin2β *as input into the global fit.*

7.1.5 Probing the Standard Model

Since Eq. (7.1) removes the information contained in $\chi^2_{\rm min}$ by construction, it can not be used directly to measure the consistency of the Standard Model with the observed data. Rather, this value is a measure of the best possible agreement between data and theory. To interpret this result we use a Monte Carlo simulation.

The fits in the previous section yield for the point of best compatibility

$$\chi^2_{\rm min} = 2.3 \ (3.2) \tag{7.2}$$

for the data set without (with) sin2$\beta_{\rm BaBar}$. Taking the theoretical predictions of the input measurements for this point as reference measurements, and fluctuating these within the experimental errors leads to the histograms shown in Fig. 7.3. Integrating the distributions according to

$$\text{Prob(SM)} \ = \text{CL}(\chi^2_{\rm min}) = \int\limits_{\chi^2 > \chi^2_{\rm min}} \mathcal{F}(\chi^2) \ d\chi^2 \ . \tag{7.3}$$

gives the corresponding CL. We find

$$\text{Prob(SM)} = 85\% \ (86\%), \tag{7.4}$$

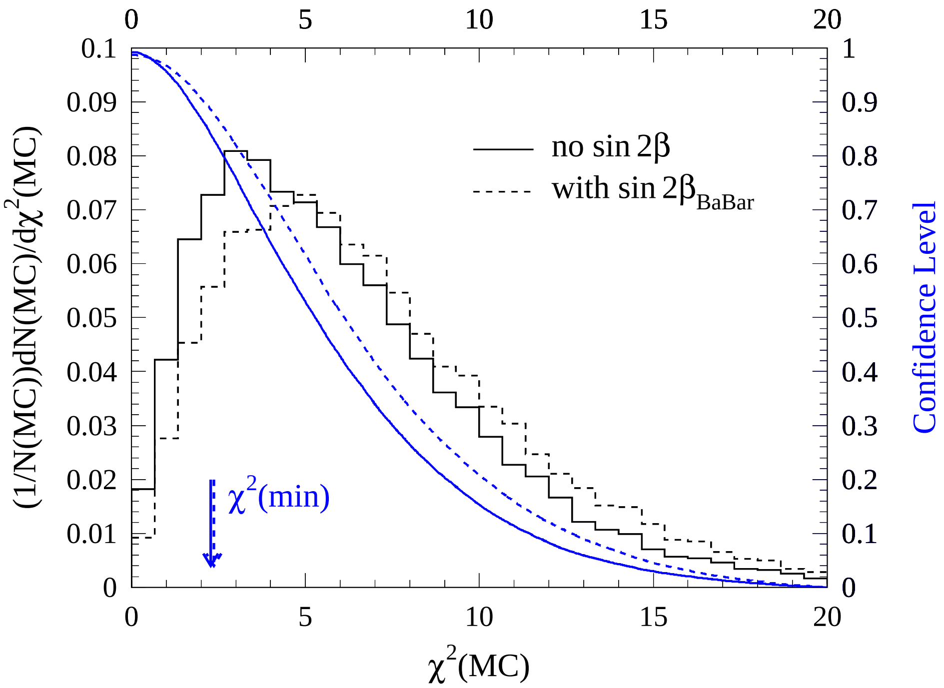

Figure 7.3: *Simulated* $\mathcal{F}(\chi^2)$ *distributions and corresponding CL's without (solid lines) and with* sin2β *(dashed lines). Indicated by the arrow is the minimal* χ^2_{min} *found in the analysis.*

for the validity of the Standard Model without (with) our measurement of sin2β.

7.2 Conclusions

> *"I've finished, here's the proof. . ."*
> — J. Boyd

The central work of this dissertation is that we have measured:

$$\sin 2\beta \; = 0.61 \pm 0.13(stat) \pm 0.04(syst). \tag{7.5}$$

From which we claim unambiguous observation of indirect $\mathcal{CP}$ violation in the B-meson system. Furthermore, we have examined our results in the context of the Standard Model, with which they are highly consistent, having an 85% Confidence Level.

Bibliography

[1] P.F.Harrison and H.R.Quinn eds. [BABAR Collaboration], "The BaBar Physics Book: Physics at an Asymmetric B-Factory," SLAC-R-0504 (1998).

[2] D.N.Brown, D.A.Roberts and E.Charles, "The *BABAR* Track Fitting Algorithm," *Presented at Computing in High Energy Physics 2000 (CHEP 2000) by D.N.Brown*, Padova, Italy, 7-11 February 2000.

[3] A.Hoecker *et al.*, "A New Approach to a Global Fit of the CKM Matrix," Eur. Phys. J.**C21**, 225 (2001).

[4] C.Caso *et al.* [Particle Data Group], "Review of Particle Physics," Phys. Rev. Lett. **D3**, 1 (1998).

[5] D.E.Groom *et al.* [Particle Data Group], "Review of Particle Properties," Eur. Phys. J.**C15**, 1 (2000).

[6] J.H.Christenson, J.W.Cronin, V.L.Fitch and R.Turlay, "Evidence For the 2π Decay of the K_0^2 Meson," Phys. Rev. Lett. **13**, 138 (1964).

[7] A.D.Sakharov, "Violation of $\mathcal{CP}$ Invariance, $\mathcal{C}$ Asymmetry, and Baryon Asymmetry of the Universe," Pisma Zh. Eksp. Teor. Fiz.**5**, 32 (1967).

[8] M.Kobayashi and T.Maskawa, "$\mathcal{CP}$ Violation In the Renormalizable Theory of Weak Interaction," Prog. Theor. Phys. **49**, 652 (1973).

[9] A.Alavi-Harati *et al.* [KTeV Collaboration], "Observation of Direct $\mathcal{CP}$ Violation in $K_{S,L} \to \pi\pi$ Decays," Phys. Rev. Lett. **83**, 22 (1999).

[10] V.Fanti *et al.* [NA48 Collaboration], "A New Measurement of Direct $\mathcal{CP}$ Violation in Two Pion Decays of the Neutral Kaon," Phys. Lett. **B465**, 335 (1999).

[11] C.N.Yang and T.D.Lee, "Question of Parity Conservation in Weak Interactions," Phys. Rev. **104**, 254 (1956).

[12] C.S.Wu *et al.*, "Experimental Test of Parity Conservation in Beta Decay," Phys. Rev. **105**, 1413 (1957).

[13] J.Schwinger, “Spin, Statistics, and the TCP Theorem,” Proc. Nat. Acc. Sci.**44**, 223 (1958).

[14] L.Wolfenstein and T.G.Trippe [for the Particle Data Group], “Tests of Conservation Laws” Eur. Phys. J.**C15**, 67 (2000).

[15] P.F.Harrison and H.R.Quinn eds. [BABAR Collaboration], “The BaBar Physics Book: Physics at an Asymmetric B-Factory,” SLAC-R-0504 (1998), Sec 1.3.

[16] A.Einstein, B.Poldosky and N.Rosen, “Can Quantum Mechanical Description of Physical Reality be Considered Complete?” Phys. Rev. **47**, 777 (1935).

[17] P.F.Harrison and H.R.Quinn eds. [BABAR Collaboration], “The BaBar Physics Book: Physics at an Asymmetric B-Factory,” SLAC-R-0504 (1998), Sec 1.3.

[18] M.Neubert, “B Decays and $\mathcal{CP}$ Violation,” Int. J. Mod. Phys.**A11**, 4173 (1996).

[19] B.Aubert *et al.* [*BABAR* Collaboration], “Measurement of $\mathcal{CP}$ Violationg Asymmetries in B^0 Decays to $\mathcal{CP}$ Eigenstates,” Phys. Rev. Lett. **86**, 2515 (2001).

[20] A.Abashian *et al.* [Belle Collaboration], “Measurement of the $\mathcal{CP}$ Violation Parameter $\sin(2\phi_1)$ in B_d^0 Meson Decays,” Phys. Rev. Lett. **86**, 2001 (2509).

[21] K.Ackerstaff *et al.* [OPAL Collaboration], “Investigation of $\mathcal{CP}$ Violation in $B^0 \to J/\psi$ K_s^0 Decays at LEP,” Eur. Phys. J.**C5**, 1998 (379).

[22] J.D.Lewis *et al.* [CDF Collaboration], “Measurements of the $\mathcal{CP}$-Violation Parameter sin2β in $B^0 \to J/\psi\ K_s^0$ Decays,” FERMILAB-CONF-99-124-E.

[23] L.-L.Chau and W.-Y.Keung, “Comments on the Parameterization of the Kobayashi-Maskawa Matrix,” Phys. Rev. Lett. **53**, 1802 (1984).

[24] L.Wolfenstein, “Parametrization of the Kobayashi-Maskawa Matrix,” Phys. Rev. Lett. **51**, 1945 (1983).

[25] N.Cabibbo, “Unitarity Symmetry and Leptonic Decays,” Phys. Rev. Lett. **10**, 531 (1963).

[26] C.Jarlskog, “A Basis Independent Formulation of the Connection Between Quark Mass Matrices, $\mathcal{CP}$ Violation and Experiment,” Z. Phys. **C29**, 491 (1985).

[27] C.Jarlskog, “Commutator of the Quark Mass Matrices in the Standard Electroweak Model and a Measure of Maximal $\mathcal{CP}$ Violation,” Phys. Rev. Lett. **55**, 1039 (1985).

[28] C.Jarlskog and R.Stora, “Unitarity Polygons and $\mathcal{CP}$ Violation Areas and Phases in the Standard Electroweak Model,” Phys. Lett. **B208**, 268 (1988).

[29] F.J.Gilman, K.Kleinknecht and B.Renk [for the Particle Data Group], "The Cabbibo-Kobayashi-Maskawa Quark-Mixing Matrix" Eur. Phys. J.**C15**, 110 (2000).

[30] H.H.Williams *et al.*, "A Measurement of the Lepton Charge Asymmetry in $K_L^0 \to \pi^{\pm} l^{\mp} \nu$ Decays," Phys. Rev. Lett. **31**, 1521 (1973).

[31] M.Fabbrichesi, "The $\Delta I = 1/2$ Selection Rule," hep-ph/9607348.

[32] P.F.Harrison and H.R.Quinn eds. [BABAR Collaboration], "The BaBar Physics Book: Physics at an Asymmetric B-Factory," SLAC-R-0504 (1998), Sec 1.4.

[33] M.Gronau and D.London, "Isospin Analysis of $\mathcal{CP}$ Asymmetries in B Decays," Phys. Rev. Lett. **65**, 3381 (1990).

[34] B.Aubert *et al.* [*BABAR* Collaboration], "The First Year of the *BABAR* Experiment at PEP-II" hep-ex/0012042 (2000).

[35] B.Aubert *et al.* [*BABAR* Collaboration], "The *BABAR* Detector" Submitted to Nucl.Instrum.Meth. hep-ex/0105044 (2000).

[36] D.Boutigny *et al.* [*BABAR* Collaboration], "*BABAR* Technical Design Report" SLAC-R-0457 (1995).

[37] [PEP-II B-Factory Working Group], "An Asymmetric B-Factory Based on PEP: Conceptual Design Report" SLAC-0372 (1991).

[38] [PEP-II B-Factory Working Group], "PEP-II: An Asymmetric B-Factory. Conceptual Design Report. June 1993" SLAC-0418 (1993).

[39] P.F.Harrison and H.R.Quinn eds. [BABAR Collaboration], "The BaBar Physics Book: Physics at an Asymmetric B-Factory," SLAC-R-0504 (1998), Sec 3.1.

[40] D.C.Carey, K.L.Brown and F.C.Iselin, "Decay Turtle (Trace Unlimited Rays Through Lumped Elements): A Computer Program For Simulating Charged Particle Beam Transport Systems, Including Decay Calculations," SLAC-0246 (1982).

[41] A.Snyder, "BaBar Note #177: Effect of Vertex Cuts on $\mathcal{CP}$ Reach," (1994).

[42] F. Forti, "BaBar Note #195: TRACKERR Studies for Optimization of Vertex Detector Resolution," (1994).

[43] F.Sauli, "Principles Of Operation Of Multiwire Proportional And Drift Chambers," CERN-77-09 (1977).

[44] G. Sciolla *et al.* [*BABAR* Drift Chamber Collaboration], "The *BABAR* Drift Chamber," Nucl. Instr. and Meth. **A419**, 310 (1998).

[45] A.Boyarski, D.Briggs and P.Burchat, "Studies of Helium Based Drift Chamber Gases for High Luminosity low-Energy Machines," Nucl. Instr. and Meth. **A323**, 267 (1992).

[46] R.Kerth *et al.*, "BaBar Note #230: The *BABAR* Coordinate System and Units," (1995).

[47] G.Lynch, "A Proposal for *BABAR* Track Parameterization," (1996). *http://www.slac.stanford.edu/BFROOT/www/Computing/Offline/Reconstruction/-Tracking/TrackParProposal.ps*

[48] P.Billoir, R.Fruhwirth and M.Regler, "Track Element Merging Strategy and Vertex Fitting in Complex Modular Detectors," Nucl. Instr. and Meth. **A242**, 115 (1985).

[49] D.N.Brown, "An Object-Oriented Extended Kalman Filter Tracking Algorithm," *Presented at Computing in High-energy Physics (CHEP 1997) by D.N.Brown*, Berlin, Germany, 7-11 Apr 1997.

[50] G.Raven, G.Cavoto, "BaBar Analysis Document #61: Determination of the Tracking Efficiency for High Momentum Tracks," (2000).

[51] O.Long, "BaBar Analysis Document #54: Measurement of the Slow Pion Relative Efficiency Using Helicity Distributions," (2000).

[52] B.Ratcliff, "The B-Factory Detector for PEP-II: A Status report," *Presented at 26th International Conference on High Energy Physics (ICHEP 92) by B.Ratcliff*, Dallas, TX, 6-12 Aug. 1992.

[53] W.W.Allison and P.R.Wright, "The Physics Of Charged Particle Identification: $\mathrm{d}E/\mathrm{d}x$, Cerenkov And Transition Radiation," OXFORD-NP-35-83 (1983).

[54] P.F.Harrison and H.R.Quinn eds. [BABAR Collaboration], "The BaBar Physics Book: Physics at an Asymmetric B-Factory," SLAC-R-0504 (1998), Sec 3.5.

[55] G.M.Haller and D.R.Freytag, "BaBar Note #285: Analog Floating Point BiCMOS Sampling Chip and Architecture of the *BABAR* CsI Calorimeter Front End Electronics System at the SLAC B Factory," (1996).

[56] J.Dowdell, "*BABAR* Calorimeter DAQ System Overview," *BABAR* Calorimeter Internal Note, (1996).

[57] J.Button-Shafer *et al.*, "BaBar Note #322: Use of Radioactive Photon Sources with the *BABAR* Electromagnetic Calorimeters," (1996).

Yu.I.Skovpen, "BaBar Note #356: Calibration of Calorimeter with Bhabha Events," (1995).

Yu.I.Skovpen, "BaBar Note #357: Calibration of Photon Energy with Radiative Bhabha Events," (1995).

A.Bukin and H.Marsiske, "BaBar Note #339 and 433: Absolute Photon Energy Calibration in the *BABAR* Calorimeter Using π^0's," (1996).

[58] P.D.Strother, PhD thesis (1998), University of London (Imperial College).

[59] P.F.Harrison and H.R.Quinn eds. [BABAR Collaboration], "The BaBar Physics Book: Physics at an Asymmetric B-Factory," SLAC-R-0504 (1998), Sec 3.6.

[60] R.Santonico, R.Cardarelli, A.DiBiagio and A.Lucci, "Progress In Resistive Plate Counters," Nucl. Instr. and Meth. **A263**, 20 (1988).

[61] R.Santonico and R.Cardarelli, "Development Of Resistive Plate Counters," Nucl. Instr. and Meth. **187**, 377 (1981).

[62] N.Dyce *et al.* [*BABAR* Trigger Collaboration], The *BABAR* Trigger System Design Requirements (1997).

[63] S.Gehrig, "BaBar Note #380: Design and Simulated Performance of the Level 1 Trigger System," (1997).

[64] J.Izen *et al.*, "BaBar Note #422: Some Statistics for Particle Identification," (1999).

[65] D.Lange (contact), "BaBar Analysis Document #115: Supporting Document for the Run 1 sin2β Analysis," (2000).

[66] C.P.Jessop *et al.* [CLEO Collaboration], "Measurement of the Decay Amplitudes and Branching Fractions of $B \to J/\psi K^*$ and $B \to J/\psi K$ decays," Phys. Rev. Lett. **79**, 4533 (1997).

[67] R.Faccini (contact), "BaBar Analysis Document #12: Exclusive B Reconstruction into Charmonium Final States: Status Report," (1999).

[68] S.McMahon, T.McMahon, "BaBar Analysis Document #69: Exclusive B Reconstruction into Charmonium Final States," (2000).

[69] C.Hearty (contact), "BaBar Analysis Document #139: Measurement of Inclusive Production of Charmonium States in B Meson Decays," (2000).

[70] B.Brau (contact), "BaBar Analysis Document #150: Exclusive B Reconstruction to Open Charm Final States," (2000).

[71] P.Robbe (contact), "BaBar Analysis Document #105: BRecoUser User's Guide," (2000).

[72] E.Robutti, "*BABAR* datasets," (2000).
http://www.slac.stanford.edu/BFROOT/www/Physics/BaBarData/GoodRuns/-dataSets.html

[73] P.Hart, “Elements of Selecting Good Runs,” (2000).
http://www.slac.stanford.edu/~philiph/rqm/7mar.pdf

[74] E.Robutti (contact), “BaBar Analysis Document #123: Data Quality Monitoring,” (2000).

[75] S.Wagner, G.Raven and M.VanHoek, *Private Disscussions About Drift Chamber Performance,*, (2000).

[76] A. Ryd *et al.*, “EvtGen: A Monte Carlo Generator for B-physics,” (2000).

[77] [CERN CN Division, Application Software Group], “GEANT: Detector Description and Simulation Tool; User Guide and Reference Manual,” CERN Program Library Long Writeup Q123, CERN(1993).

[78] C.Touramanis, “Luminosity,” *Presented at Feb. 2001 BABAR Collaboration Meeting*, SLAC, Feb. 2001.

[79] G.Fox, S.Wolfram, “Event Shapes in e^+e^- Annihilation,” Nucl. Phys. **B149**, 413 (1979).

G.Fox, S.Wolfram, “Observables for the Analysis of Event Shapes in e^+e^- Annihilation and Other Processes,” Phys. Rev. Lett. **41**, 1581 (1978).

[80] C.Hearty (contact), “BaBar Analysis Document #134: Measurement of the Number of $\Upsilon(4S)$ Mesons Produced in Run 1 (B Counting,)” (2001).

[81] E.Varnes (contact), “BaBar Analysis Document #157: Measurement of the GoodTrackLoose Efficiency using SVT tracks,” (2000).

[82] C.Touramanis (contact), “BaBar Analysis Document #20: Reconstruction of π^0 in *BABAR*,” (1999).

[83] H.D.Maccabee and D.G.Papworth, “Correction to Landau’s Energy Loss Formula,” Phys. Lett. **30A(4)**, 241 (1969).

[84] U.Langenegger (contact), “BaBar Analysis Document #90: Cut-based Electron Identification,” (2000).

[85] M.Marko, “BaBar Analysis Document #126: Lepton Identification Efficiencies and Systematic Errors,” (2000).

[86] L.Lista (contact), “BaBar Analysis Document #60: Muon Identification in the *BABAR*Experiment,” (2000).

L.Lista, “BaBar Note #413: Muon Identification in the IFR,” (1998).

[87] S.Spanier (contact), “BaBar Analysis Document #116: Kaon Selection at *BABAR*,” (2000).

[88] M.Bona (contact), "BaBar Analysis Document #19: Studies on $K_S^0 \to \pi^+\pi^-$ Reconstruction," (1999).

[89] F.Martinez-Vidal (contact), "BaBar Analysis Document #102: The *BABAR* Vertexing," (2000).

[90] M.S.Alam *et al.* [CLEO Collaboration], "Exclusive Hadronic B Decays to Charm and Charmonium Final States," Phys. Rev. **D50**, 43 (1994).

[91] J.C.Anjos *et al.* [E691 Collaboration], "A Dalitz Plot Analysis of $D \to K\pi\pi$ Decays," Phys. Rev. **D48**, 56 (1993).

[92] C.Cheng, "Dalitz Distribution Function for $D^0 \to K\pi\pi^0$," (2000). *http://www.slac.stanford.edu/~chcheng/talk/kpipi0DalitzFunc/index.html*

[93] J.Smith, A.Soffer and R.Waldi, "BaBar Note #497: Recommendation for Exclusive B Reconstruction Analysis Variables," (1999).

[94] W.T.Ford, "BaBar Analysis Document #53: Choice of Kinematic Variables in B-Meson Reconstruction–Take 3," (2000).

[95] H.Albrecht *et al.* [ARGUS Collaboration], "Search for Hadronic $b \to u$ Decays," Phys. Lett. **B241**, 1990 (278).

[96] E.Varnes, "BaBar Analysis Document #113: Measurement of Exclusive Charmonium Branching Ratios Using Data from *BABAR*'s First Run," (2000).

[97] J.Chauveau, F.Martinez-Vidal, J.Stark, "BaBar Analysis Document #37: B Lifetime Measurement Using Exclusively Reconstructed Hadronic B Decays," (2000).

[98] C. De la Vaissiere (contact), "BaBar Note #436: Lifetimes with Full B Reconstruction," (1998).

[99] R.Muller-Pfefferkorn, R.Waldi, "BaBar Note #373: Monte Carlo Study of the Vertex Resolution in *BABAR* $C\!\!\!/P$ Violation Measurements," (1997).

[100] S.Brandt, "Statistical and Computational Methods in Data Analysis", *North Holland Publishing, Amsterdam 1976, 414p.*

[101] P.Avery, "Data Analysis and Kinematic Fitting With the KWFIT Library," CSN 98-355, (1998).

[102] P.Billoir, S.Qian, "Fast Vertex Fitting with a Local Parametrization of Track," Nucl. Instr. and Meth. **A311**, 139 (1992).

[103] R.Faccini, F.Martinez-Vidal, "Vertexing/Kinematic Fitting User's Guide," (1999). *http://www.slac.stanford.edu/BFROOT/www/Physics/Tools/Vertex/VtxGuide/-index.html*

[104] F.Martinez-Vidal, "VtxTagBtaSelFit: a Vertex Tag Reconstruction Tool. User's Guide" (1999).
http://www.slac.stanford.edu/BFROOT/www/Physics/Tools/Vertex/VtxGuide/-VtxTagBtaSelFit.html

[105] S.Plaszczynski, "FastVtx How-To" (1999).
http://www.lal.in2p3.fr/recherche/babar/Analyse/FastVtx/HowTo/index.html

[106] S.Metzler (contact), "BaBar Analysis Document #65: Measurement of B Lifetimes at *BABAR*," (2000).

[107] D.Kirkby, "Generator Level Studies for $B^0\overline{B}^0$ Mixing," (2000).
http://www.slac.stanford.edu/~davidk/BBMix/GenStudy

[108] A.Synder, "Δz vs Δt," (2000).
http://babar-hn.slac.stanford.edu:5090/HyperNews/get/recoTracking/386/4.html

[109] S.Rahatlou, private communication, (2001).

[110] K.Cranmer, "Kernel Estimation in High-Energy Physics," Comp. Phys. Comm. **136**, 198 (2001).

[111] B.Brau, private communication, (2000).

[112] B.Aubert *et al.* [*BABAR* Collaboration], "Measurement of the B^0 and B^+ Meson Lifetimes With Fully Reconstructed Hadronic Final States," Phys. Rev. Lett. **87**, 201803 (2001).

[113] J. Stark, "B^0/B^+ lifetimes with Fully Reconstructed Hadronic B Decays and the Δz Resolution Function," *Presented at April 2000 BABAR Physics Week*, SLAC, April 2000.

[114] F.Martinez-Vidal (contact), "BaBar Analysis Document #130: Performances and Control Samples of the *BABAR* Vertexing," (2000).

[115] U.Egede (contact), "BaBar Analysis Document #13: Beam Spot Determination and Use in *BABAR*," (1999).

[116] J.Blouw, A.Soffer and S.Dong, "BaBar Analysis Document #14: Measuring the PEP-II Boost," (1999).

[117] C.Cheng, "'Flat' Beam Spot," (2000).
http://babar-hn.slac.stanford.edu:5090/HyperNews/get/pubboard01/25.html
C.Cheng, "Beam Spot Variation Within a Run (14459)," (2000).
http://babar-hn.slac.stanford.edu:5090/HyperNews/get/sin2beta/210.html

[118] A.Soffer, “Beam Parameters in Data and Monte Carlo,” *Presented at Nov. 2000 BABAR*sin2β *WorkShop by A.Soffer*, SLAC, 3rd Nov. 2000.

[119] S.Plaszczynski, “Reults Concerning the Right “y” Beamspot Size to Use for Vertexing,” (2000).
http://babar-hn.slac.stanford.edu:5090/HyperNews/get/VertexTools/173/1/1/1.html

[120] A. Gritsan, “SVT Local Alignment Diagnostics,” (2000).
http://www.slac.stanford.edu/~gritsan/svt/index.html A.V.Gritsan, “SVT Local Alignment Systematics,” (2000).
http://babar-hn.slac.stanford.edu:5090/HyperNews/get/physAnal/1023.html

A.V.Gritsan, “SVT Local Alignment Systematics for Run1 Data” *Presented at Feb. 2001 BABAR Collaboration Meeting*, SLAC, Feb. 2001.

[121] J.Schieck, private communication, (2000).

[122] R.Cahn, “BaBar Analysis Document #17: TagMixZ and its Application to the Analysis of $\mathcal{CP}$ Violation,” (1999).

[123] S.Plaszczynski, L.Roos, M-H.Schune, “BaBar Analysis Document #151: Measurement of the Mistag Fractions with Counting Methods,” (2000).

[124] G.Raven (contact), “BaBar Analysis Document #125: Measurement of B^0 Mixing using Fully Reconstructed Hadronic B^0 Decays,” (2000).

[125] R.Cahn, “Useful Formulae,” (2000).
http://phyweb.lbl.gov/~rncahn/www/babar/useful_formulae.ps

[126] A.Gaidot (contact), “BaBar Note #461: $B^0\overline{B}^0$ Tagging Studies,” (1998).

[127] H.Hu (contact), “BaBar Analysis Document #103: The NetTagger,” (2000).

[128] J.Beringer, “Studies of N.O.T.,” (2000).
http://www.slac.stanford.edu/BFROOT/www/Organization/CollabMtgs/elba2000/-Mon4a/beringer.pdf

J.Beringer (contact), “BaBar Analysis Document #16: B-Tagging in *BABAR*: Status for ICHEP 2000 (Osaka),” (2000).

J.Beringer (contact), “BaBar Analysis Document #118: Cut Based Tagging,” (2000).

J.Beringer (contact), “BaBar Analysis Document #119: B Tagging in BaBar: Status for the sin2β Journal Publication,” (2000).

J.Beringer (contact), “BaBar Analysis Document #242: A User’s Guide to the *BABAR* B Flavor Tagging Tools,” (2001).

[129] B.Aubert *et al.* [*BABAR* Collaboration], “Measurement of B^0 - anti-B^0 Flavor Oscillations in Hadronic B^0 Decays,” Submitted to Phys.Rev.Lett. (2001) hep-ex/0112044.

[130] B.Aubert *et al.* [*BABAR* Collaboration], “A Study of Time Dependent $\mathcal{CP}$ Violating Asymmetries and Flavor Oscillations in Neutral B Decays at the $\Upsilon(4S)$,” hep-ex/0201020 (2002).

[131] I.I.Bigi, “Lifetimes of Heavy Flavor Hadrons: Whence and Whither?” Nuovo Cim. **A109**, 713 (1996).

[132] M.Neubert, C.T.Sachrajda, “Spectator Effects in Inclusive Decays of Beauty Hadrons,” Nucl. Phys. **B483**, 339 (1997).

[133] F.James, “Minuit. Function Minimization and Error Analysis” CERN program library long writeup D506 (1994).

[134] D.Kirkby (contact), “BaBar Analysis Document #18: A User’s Guide to the RooFitTools Package for Unbinned Maximum Likelihood Fitting,” (2000).

[135] *BABAR* Collaboration, “A Measurement of the $B^0\overline{B}^0$ Oscillation Frequency and Determination of Flavor Tagging Efficiency Using Semileptonic and Hadronic B^0 Decays,” BABAR-CONF-00/08 (2000).

[136] *BABAR* Collaboration, “A Study of Time-Dependent $\mathcal{CP}$-asymmetries in $B^0 \to J/\psi\ K^0_S$ and $B^0 \to \psi(2S)\ K^0_S$ Decays,” BABAR-CONF-00/01 (2000).

[137] D.Lange (contact), “BaBar Analysis Document #205: Supporting Document for the Summer 2001 sin2β Analysis,” (2001).

[138] S. Prell (contact), “BaBar Analysis Document #101: `tFit` — A Program to Fit Decay Time (Difference) Distributions to Study $B^0/B^\pm$ Lifetimes, $B^0\overline{B}^0$ Oscillations and $\mathcal{CP}$ Asymmetry Parameters,” (2000).

[139] G. Raven, “Counting Mixed/Unmixed Events,” (2001).
http://www.slac.stanford.edu/BFROOT/www/Physics/Analysis/AWG/-BBMixingHadr/Meetings/29Mar2001/mix.ps

[140] R.Cahn, “If Tag and Reco Efficiencies Differ for B0 and B0Bar,” (2000).
http://babar-hn.slac.stanford.edu:5090/HyperNews/get/sin2beta/159.html
R.Cahn, “Effect of Efficiency Differences on CP Analysis,” (2000).
http://babar-hn.slac.stanford.edu:5090/HyperNews/get/sin2beta/183.html

[141] D.Lange, “I Didn’t Learn Anything That Gerhard Didn’t Already Know,” (2000).
http://babar-hn.slac.stanford.edu:5090/HyperNews/get/Bmixing/258/1/1.html

[142] D.Bernard (contact), “BaBar Analysis Document #35: Amplitude Measurement in the $B \to J/\psi K^*$ Channels,” (1999).

[143] J.Stark (contact), "BaBar Analysis Document #144: Measurements of the Charged and Neutral B-Meson Lifetimes Using Fully Reconstructed B Decays," (2000).

[144] B.Aubert *et al.* [*BABAR* Collaboration], "A Measurement of the Charged and Neutral B-Meson Lifetimes using Fully Reconstructed Decays," *BABAR*-CONF-00/07 and hep-ex/0008060 (2000).

[145] S.Henrot-Versille and F.Le Diberder, "Kin: The Optimal Variable for $\not{CP}$ Violation," hep-ex/0007025 (2000).

[146] S.Plaszczynski, "Tagging/Vertexing Correleations" *Presented at* $\sin 2\beta$ *Workshop*, 3rd Nov. 2000.

[147] F.Martinez-Vidal (contact), "BaBar Analysis Document #183: Vertexing Control Samples," (2000).

[148] P.Robbe, "Breco modes - Background studies," *Presented at Breco Meeting*, Nov 16, 2000.

[149] P.Robbe and C.Hast, "z-Scale of the Detector" (2000).
http://babar-hn.slac.stanford.edu:5090/HyperNews/get/recoTracking/334.html

W.Dunwoodie, P.Robbe and C.Hast, "Radial and Longitudinal Length Scale from Beampipe Structure" (2000).
http://www.slac.stanford.edu/~wmd/beampipe/dec00.talk

W.Dunwoodie (contact), "BaBar Analysis Document #106: Study of Material Interactions with Gamma Conversions and Protons," (2000).

W.Dunwoodie, private communication, (2000).

[150] M-H.Schune, "Re: DECAY File Updates for SP4: χ_d for Signal $D^* l\nu$??" (2001).
http://babar-hn.slac.stanford.edu:5090/HyperNews/get/phys-anal/1058.html

[151] G.Raven, "Exclusive B^0 Cocktail MC Decay File Updated, Wrong χ_d in SP3," (2001).
http://babar-hn.slac.stanford.edu:5090/HyperNews/get/Bmixing/228/1/1.html

[152] F.Porter, "Interval Estimation Using the Likelihood Function," Nucl. Instr. and Meth. **A368**, 1996 (793).

[153] M.Ciuchini *et al.*, "2000 CKM-Triangle Analysis: A Critical Review with Updated Experimental Inputs and Theoretical Parameters," LAL 00-77, ROME1-1307/00, RM3-TH/00-16, (2000).

[154] H.Lacker (contact), "BaBar Analysis Document #153: Constraining the CKM Matrix," (2000).

[155] G.Eigen (contact), “BaBar Analysis Document #92: Inputs for the Unitarity Triangle Fits,” (2000).

[156] H.Lacker *et al.* [*BABAR* CKM Working Group], “Input Values for a Global CKM fit: SUMMARY,” (2000).
http://babar-hn.slac.stanford.edu:5090/HyperNews/get/ckmfit/5.html